Biwojno, Konrad P. (2006) Embedding of fine features in multi-scale electromagnetic models. PhD thesis, University of Nottingham.

Embedding of Fine Features in Multi-Scale Electromagnetic Models

By

Konrad P. Biwojno, MSc

Thesis submitted to the University of Nottingham for
the degree of Doctor of Philosophy, April 2006

Acknowledgments

I would like to extend my deepest gratitude to my supervisors, Professor Christos Christopoulos and Professor Phillip Sewell, for their excellent supervision and guidance throughout this project. There is no doubt that this work would not be accomplished without their patience and constant motivation.

I am also very grateful to Dr Chris Smartt from BAE Systems for all the fruitful discussions and helpful advice.

No acknowledgement would be completed without a mention of those who worked with me inside the George Green Institute for Electromagnetics Research and the School of Electrical and Electronic Engineering. Special thanks to James, Jim, Ahmed, Carl, John, Ella and Steve for sharing their knowledge and experience and also for all the jokes that made the labs a very enjoyable working environment.

I give sincere appreciation to all my friends, here in England and back home in Poland, for encouragement and help to make my stay in Nottingham pleasurable and the jovial moments outside the labs.

Last but not least, I thank my family for their unconditional love, support, understanding and strong belief in me.

I dedicate this thesis to my grandparents, Józefa and the late Stanisław.

Pracę tę dedykuje moim dziadkom, Józefie i śp. Stanisławowi.

Abstract

Modelling detailed electromagnetic interactions in Electromagnetic Compatibility predictions is an extremely demanding task, made more difficult by the increasing complexity of modern engineering problems. Over the last decade major innovations in numerical models and methods have been introduced to reduce demands on computational resources or render the simulations of large systems containing a diverse range of physical features possible.

This thesis presents one of the methods of dealing with large systems which utilises the concept of sub-cells containing fine geometrical objects. A general approach to embedding fine features into a coarse numerical time-domain techniques such as the Transmission Line Modelling (TLM) method is proposed. A non-standard node has been developed that mimics the electro- magnetic behaviour of virtually any object or group of small objects wholly or partially enclosed by a volume of space represented by the numerical cell.

The core of this scheme is to identify a suitable set of local field solutions to Maxwell's equations within the vicinity of the enclosed objects and, by correctly sampling the fields on the boundary of the cell, to integrate these with field solutions represented by the neighbouring nodes, ensuring both field continuity

and power conservation. The idea whilst simple leads to an algorithm that is both explicitly stable and conservative as well as only incurring a minor computational overhead compared to a conventional TLM algorithm. It is noted that, as the required identification and evaluation of the local field solutions occurs as a pre-processing stage prior to the main TLM run and that the non-standard nodes are a small proportion of the coarse grid, a significant overall reduction in computational requirements is achieved in comparison to direct fine meshing of the features. Another advantage of this approach lies in the fact that the local solutions to Maxwell's equations calculated in the pre-run process can be obtained by any suitable means. Analytical formulations, numerical results of another simulation or simply experimental measurements are some of the possibilities.

The approach is employed to investigate a variety of EMC problems. An analysis of the field scattered from multiple cylindrical geometries embedded within a single two-dimensional cell is presented. Multiple conducting and lossy wires, dielectric rods and dielectric coated wires, conducting strips and slots are also studied. Three-dimensional simulations are shown for an arbitrarily orientated wires, small dielectric and conducting spheres and other canonical shapes. The approach is also successfully applied to other disciplines where modelling plays an important role. The flexibility of the algorithm is demonstrated for simulations of photonic structures with the primary focus placed upon photonic band-gap materials.

List of Publications

The following publications have arisen out of the work presented in this thesis and are listed in two categories:

Journal Papers:

[1] Biwojno, K., Sewell, P., Liu, Y., Christopoulos, C., *"Electromagnetic Modelling of Fine Features in Photonic Applications"*, Optical and Quantum Electronics, Special Issue on Waveguide Theory and Numerical Modelling, Vol. 38, No. 1-3, pp. 187-201, 2006

[2] Liu, Y., Sewell, P., Biwojno, K., Christopoulos, C., *"Accurate Representation Of Thin Metal Strips And Narrow Slot Apertures In Transmission Line Modelling (TLM) Simulations"*, Microwave and Optical Technology Letters, Vol. 48, No. 1, pp.178-180, 2006.

[3] Liu, Y., Sewell, P., Biwojno, K., Christopoulos, C., *"A Generalized Node for Embedding Sub-Wavelength Objects into 3D Transmission Line Models"*, IEEE Transactions on Electromagnetic Compatibility, Vol 47, No. 4, pp. 749-755, 2005

[4] Govan, D., Bekker, E., Paul, J.D., Greedy, S., Liu, Y., Biwojno, K., Wykes, J., Vukovic, A., Thomas, D.W.P, Benson, T.M., Sewell, P., Christopoulos, C., *"Computational Electromagnetics: Current Applications and Future Trends"*, IEEE Microwave Review, No. 2, Vol. 10, pp. 16-25, 2004,

[5] Biwojno, K., Smartt, C.J., Sewell, P., Liu Y., Christopoulos, C., *"General treatment of TLM node with Embedded Structures"*, accepted to International Journal of Numerical Modelling.

Conference Papers:

[6] Christopoulos, C., Thomas, D.W.P., Sewell, P., Paul, J., Biwojno, K., Wykes, J., Greedy, S., *"Simulation Methodologies for Electromagnetic Compatibility (EMC) and Signal Integrity (SI) for System Design"*, EPTC 2005, 7th Electronics Packaging Technology Conference, 7-9 December, Grand Copthorne Waterfront, Singapore. Proceedings EPTC, pp. 406-411, 2005

[7] Benson, T.M., Christopoulos, C., Thomas, D.W.P., Vukovic, A., Greedy, S., Liu, X., Biwojno, K., Liu, Y., *"Simulation for Electromagnetic Compatibility (EMC) and Signal Integrity (SI) in an Integrated Environment"*, Euro DesignCon, Munich, Germany, Paper 5-TA2, Oct 2005

[8] Benson, T. M., Govan, D., Wykes, J., Biwojno, K., Sewell, P., Greedy, S., *"Time Domain Techniques for the Accurate Description of Fine Features"*, OWTNM05, Sydney Australia, pp 23, July 2005

[9] Christopoulos, C., Sewell, P., Thomas, D.W.P., Benson, T.M., Vukovic, A., Biwojno, K., Liu, Y., Paul, J., *"Full-Field Electromagnetic Models and Complexity in EMC "*, 9th International Conference on Electromagnetics in Advanced Applications, ICEAA '05, Torino Italy, pp 375-378, 2005

[10] Liu, Y., Biwojno, K., Sewell, P., Christopoulos, C., *"A General Approach for Embedding Local Field Solutions into TLM Simulations"*, XXVIII General Assembly of the Union of Radio Science (URSI), Delhi, E-proceedings, EB.1(0433), Oct 2005

[11] Christopoulos, C., Sewell, P., Biwojno, K., Liu, Y., Smartt, C. J., *"Hierarchical Models of Complex Systems in Time-Domain"*, XXVIII General Assembly of the Union of Radio Science (URSI), Delhi, E-proceedings, EB.1(0433), Oct 2005

[12] Biwojno, K., Smartt, C.J., Sewell, P., Liu, Y., Christopoulos, C., *"General treatment of TLM node with Embedded Structures"*, IEEE Proceedings of CEM-TD 2005, Atlanta, Georgia, USA, pp.52-54, 2005

[13] Biwojno, K., Sewell, P., Liu, Y., Christopoulos, C., *"Electromagnetic Modelling of Fine Features in Photonic Applications"*, OWTNM 2005 Grenoble, France, Proceedings, Grenoble, France, April 2005

[14] Biwojno, K., Sewell, P., Liu, Y., Christopoulos, C., *"Embedding Multiple Wires Within a Single TLM Node"*, EUROEM, Magdburg, Germany, pp. 173-174, July 2004

[15] Biwojno, K., Sewell, P., Liu, Y., Christopoulos, C., *"Embedding Multiple Wires Within a Single TLM Node"*, to appear in Ultra-Wideband, Short-Pulse Electromagnetics 7 Book (UWB SP 7)

Other Author's Publications:

[16] Sewell, P., Biwojno, K., Sujecki, S., Benson, T.M., *"A thermal model for silicon-on-insulator waveguide modulators"*, ICTON'02 Conference, Warsaw, Poland, pp. 55-58, 2002

[17] Biwojno, K., Sujecki, S., Vukovic, A., Benson, T.M., Sewell P., *"Thermal models for silicon-on-insulator-based optical circuits"*, Optica Applicata, Vol. 34, No. 2, pp. 149-161, 2004,

[18] Biwojno, K., Sujecki, S., Sewell, P., Benson, T.M., *"Analiza Przelaczania Termicznego W Ukladach Optyki Zintegrowanej Wykonanych Na Podlozu Krzemu"*, Elektronika, No.10 pp 73-76, Nov 2002

[19] Biwojno, K., Sujecki, S., Sewell, P., Benson, T.M.,, *"Numerical Analysis Of Thermal Switching In Silicon Based Integrated Optical Devices"*, Proceedings of SPIE: Photonics Applications in Astronomy, Communications, Industry, and High-Energy Physics Experiments, Vol. 5125, pp. 252-258, 2003

[20] Sewell, P., Biwojno, K., Sujecki S., Benson, T.M., *"A thermal model for silicon-on-insulator-based waveguide modulators"*, Transparent Optical Networks, 2002. IEEE Proceedings of the 2002 4th International Conference on, Vol. 1, pp 151 –154, 2002

Awards

Student prize awarded by The Publisher and Editorial Advisory Board of International Journal of Numerical Modelling, Electronic Network, Devices and Fields for the paper *"General treatment of TLM node with Embedded Structures"* selected as the best student paper in Numerical Modelling at the Computational Electromagnetics in Time Domain (CEM-TD) Workshop in Georgia Tech, Atlanta, Georgia, USA, September 2005.

Contents

Chapter 1

Multi-Scale Modelling

The material presented in this thesis is primarily concerned with the development of modelling techniques and simulation tools for multi-scale environments such as those encountered in Electromagnetic Compatibility (EMC) predictions. An introduction to the problems found in this kind of system will now be given with the main focus placed upon EMC applications. The state-of-art in this area will be covered and the main techniques and solutions proposed to-date will be reviewed. Subsequently, an overview of the work described in this thesis will be presented.

1.1. The General Nature of Multi-scale Systems

A broad range of scientific and engineering problems involve multiple scales. Traditional mono-scale models for this kind of system have proven to be inadequate, even with the fast growing computational power of modern supercomputers. This is due to the wide variety of scales and the prohibitively large number of variables involved in actual systems. In addition, it is often the case that none of the elements in the system, regardless of their size, can be easily simplified nor neglected in the design, as they all contribute significantly to the overall response of the modelled structure. More difficulties arise when one deals with a variety of scales distributed over a large system which cannot be divided into parts that are considered separately, and subsequently connected. Thus, there is a great demand to develop systematic modelling and simulation approaches for such large multi-scale configurations. One of the disciplines where multi-scale features are commonly encountered is Electromagnetic Compatibility (EMC).

1.2. Multi-scale Problems in Electromagnetic Compatibility (EMC)

Electromagnetic Compatibility (EMC) is the branch of electrical sciences which studies the unintentional generation, propagation and reception of electromagnetic disturbances with reference to the unwanted effects that the energy carried by such disturbance may induce. EMC is also defined as the ability of different electrical and electronic components to function together in the same environment without suffering the effects of mutual electromagnetic interference (EMI) or introducing the intolerable disturbance to that environment. Thus, this implies a limit on radio frequency (RF) emissions from the device or system, as well as a certain level of immunity (susceptibility) to interference that must be expected from other devices and systems in the surroundings. The susceptibility to EMI is determined by the strength of signals coupled into the equipment and the impact they have on its operation, whereas emission from the equipment is described by the radiation from elements of the system such as wires, circuits and its propagation in the external environment [1.1].

The proliferation of electronic devices in the modern world and constant pursuit of higher circuit integration and dense packaging increases the likelihood that sensitive and "noisy" devices are operated in close vicinity. This is especially observed with the rapid growth of technologies that utilise frequencies above the gigahertz band; broadband and wireless telecommunication and electronic components present in almost every aspect of everyday life and every household. Therefore, EMC compliance became not only a matter of increasing interest but in fact a practical necessity. Indeed, it has been already widely recognised in the defence/military, information technology (IT), rail, medicine, radio, telecoms and power industries, [1.2-1.5]. Due to its breadth, it is impossible to cover every aspect of EMC here and therefore the focus will now be placed upon a number of illustrative examples that are important from the point of view of the work presented in this thesis.

1.3. Areas of EMC Applications

Signal transmission at high speed and high capacity has been substantially increasing in the mobile communication industry over recent years. In this area, EMC faces challenging problem due to the coexistence of many sources utilising the same frequency bandwidth. One particular example is the use of the 2.45 GHz band, where such activity as Bluetooth, cordless phones, home RF, and transmissions of other systems are all present and must work with close proximity to each other [1.2].

EMI radiating from and coupling to signal transmission cables inside equipment cabinets is one of the particularly critical issues for compliance with EMC requirements. It is recognized that these cable assemblies can be EMI sources radiating significant electromagnetic fields often due to discontinuities between signal cables and terminal connectors. From the view point of providing shielding from these electromagnetic fields, this issue not only concerns individual assessment of the cable and connectors but also the influence of the equipment enclosures, [1.6, 1.7].

When operating at frequencies above 1 GHz, most structures in the system, including cabinets, enclosures, cabling, and others can act as effective radiators due to the wavelength being comparable to the size of the components [1.8]. At such frequencies a ventilation slot, a chassis door without correctly installed radio-frequency-interference (RFI) gasketing, a gap due to improper fitting or even a card cage can potentially become an antenna. For such scenarios little shielding attenuation exists, hence, once an emission from the product escapes through the slots or gaps, it spreads out affecting devices in both its near and far-field region [1.8]. Similarly, the slot is a receiving aperture or antenna that passes RFI environmental noise into the system [1.9, 1.10]. This in effect, moves EMC design down to the printed circuit board (PCB) level [1.11].

A relatively new area of concern involves the generation of power frequency harmonics by electronic equipment. Due to the large number of new electronic equipment with switched-mode power supplies, these harmonics can be significant enough to propagate within the power network and cause interference to other equipment connected to it [1.5].

The aerospace industry has long been aware of EMC-related functional safety issues, due to their long-term use of electronics in mission-critical and safety-critical applications such as autopilots and automatic landing systems [1.4]. The modern aircraft is vitally dependent on electronics, even for manual controls the pilot's movements of his controls are mediated by computers and servo-systems before being applied to the aircraft systems or control surfaces. In addition, all aircraft are exposed to very powerful EM disturbances, e.g. from airfield radars, radio broadcasting transmitters, and direct lightning strikes. The latter results in huge pulsed currents flowing through the airframe and therefore through the systems. Once again, EMC compliance necessitates the demonstration of continued operation of all systems during high induced pulsed currents. Military aircraft have the further burdens of electronic warfare and countermeasure equipment to take into consideration [1.4].

The difficulty in performing EMC or EMI predications in the aerospace area arises from the fact that aircraft are highly integrated. Hence, it is hard to divide the problem up into distinct parts from an electromagnetic point of view and be confident that synergistic effects have not been missed.

An issue closely connected to dealing with large system such as aircraft or ships is the analysis of radiation and scattering from the thin wire structures that form a wide range of antennas. Such analysis is very challenging when only free space environment is considered. In practice, however, the problem is exacerbated as antennas are installed on structures which influence their ideal "free-space" radiation characteristics. The objective is to design antennas, determine the influence of the platform on the antenna's radiation characteristics and their best position and orientation. Also of great importance is to estimate the impact of the radiated beams on other elements of the platform, such as cabling systems that link and enable communication between components of the aircraft or ship; malfunction or failure of which can have irreversible consequences.

1.4. Numerical Modelling and Measurements in EMC

Rather than waiting for interference to happen and then fixing the problem, which is a very expensive process, it is advisable to specify electromagnetic requirements for devices before they are installed, to ensure they are compatible when operated in their intended environment. For this purpose, both measurements and numerical modelling are typically conducted to enable better understanding of electromagnetic interference mechanisms. For both methods size is a very important factor, especially in measurements since test facilities such as screen rooms, are very expensive to build. Immunity testing in open-field environments requires large test generators and produces "threats" to other equipment that are not under test. Even in the case of emissions testing, it can be difficult to establish the level of emissions from a particular piece of equipment after it has been installed in an operating platform. Other complications arise when moving to high frequencies concerning narrow emission beamwidths from products that can be hard to identify. Measuring antennas also tend to have narrow beamwidths, making it hard to capture the radiated signal at the limit distance away from the product [1.12].

Numerical modelling offers the potential for obtaining accurate results for complex systems without the problems associated with direct measurements. However, the increasing demand to model fields in a large three-dimensional (3D) space while at the same time keeping a fine mesh resolution around small features (wires, slots, gaps, gaskets, etc.) makes conventional methods computationally expensive and in many cases prohibitive. In order to make differential equation methods such as Transmission Line Modelling (TLM) [1.13] or Finite Difference (FD) [1.14] more suitable for EMC problems, so-called *compact models* must be developed. Compact models take into account the electromagnetic presence of fine features without resorting to an extremely fine mesh. Since these compact models are often implemented locally, within a single cell, or a tube of cells, they are also referred to as *sub-cell models*. In order to maintain time synchronism with the rest of the problem, compact models must always be integrated into the main time-marching process.

The work presented in this thesis describes new developments in numerical approaches for sub-cell models embedded in a coarse mesh for simulation of large platforms such as aircrafts and ships. Of particular interest is the modelling of thin wires for antenna design and for studying the phenomenon of fields scattered from antennas positioned on large platforms. To appreciate the scale of the difficulties encountered when dealing with large platforms two examples are illustrated in Figure 1.1. In Figure 1.1(a) a spiral antenna is positioned on a wing pod whereas in Figure 1.1(b) an antenna is placed on the top of the fuselage.

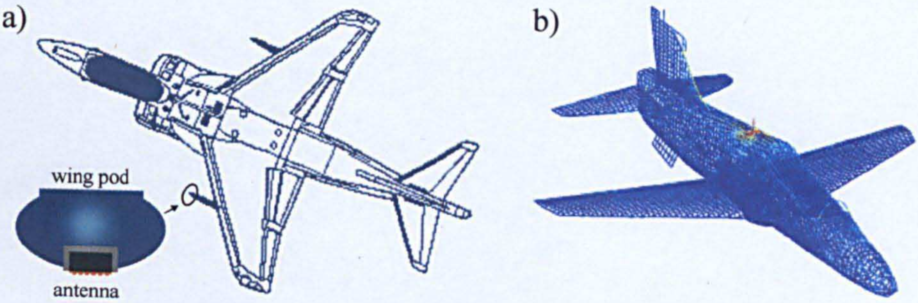

Figure 1.1. Aircraft models with different positions of antenna

It should be clear that discretising the whole platform with a fine mesh that describes in detail the small geometry of the wire antenna will result in extensive computational requirements that may not be satisfied by available resources. Therefore, over the years a substantial effort has been made to develop models of thin wires that can be embedded in a coarse simulation grid. These models will be next briefly overviewed.

1.5. History of Thin Wire Models

As discussed in the previous section, Electromagnetic Compatibility (EMC) prediction often requires dealing with electrically large systems that are characterised by a diverse range of physical scales, all of which discernibly affect the overall behaviour of the body under consideration. A practically important and commonly occurring example of such a scenario arises whenever thin wires are present. As demonstrated above, whenever the wire is in a close proximity to large-scale objects, it is usually prohibitively expensive in terms of computational resources to employ direct fine meshes with resolution sufficient to describe the geometry of the wire in detail. The difficulty is further exacerbated when a number of wires, wire looms or bundles, are placed in close vicinity, each of different insulation. In addition, the elements of the system interact and interfere through a large volume of empty space, which introduces another very substantial level of complexity to an otherwise challenging problem. Therefore, all the aspects over last decade have become a factor driving innovations and new developments in numerical models of thin wires that can be applied to such a multi-scale environment utilising the best available computational resources.

One of the techniques that have been considered and widely investigated is multi-gridding or the use of graded meshes. These methods deploy a distortion of the numerical grid in the region where small wires and other small objects are highly concentrated to give accurate description of those features [1.13-1.18]. However, it is common that the extent of the finely meshed region continues to the edges on the computational window in order to prevail the one-to-one connection between the numerical cells. This is done to avoid both problems with stability and to maintain a structured grid, which is computationally efficient. Therefore, in the realm of EMC applications, the computational requirements may not actually be that significantly reduced. Whenever the grid is locally refined using multi-grid approaches, the connection of one-to-many nodes has to be considered. The issues regarding flexibility, stability and conservation of energy which relate to that fact, are not yet completely resolved but are under severe examination [1.15-1.18].

The use of completely unstructured meshing has also been proposed for modelling multi-scale environments. This approach allows a significantly graded mesh to be employed, albeit at the cost of computational efficiency per mesh element [1.19-1.20]. These schemes also have the attraction of providing piecewise linear approximation of smooth geometrical boundaries and material interfaces to alleviate the staircasing that is inevitable with structured schemes.

Separated or integrated solution techniques [1.20] or diakoptics [1.22] have also been employed in the past to model conducting thin wires. Here, the conductors are treated separately from the rest of the problem, allowing for field coupling to the wires by introducing equivalent sources derived from knowledge of the incident field. Although this method is simple, it involves several restrictions, the most important being that any electromagnetic interaction of the wires with the rest of the structure must be negligibly small thus questions of the applicability of such methods to EMC environment arise.

Another scheme that has recently attracted a lot of attention is the use of the sub-cell models previously mentioned. This results in a small number of non-standard nodes embedded within the large-scale model whose macroscopic behaviour is engineered to account for the presence of a small scale object enclosed within the FDTD [1.23-1.28] or TLM [1.29-1.37] cell. It is noted that using this concept, the majority of the computational space is described with conventional coarse nodes thus significantly reducing the memory consumption and calculation run-times.
The early design of such elements or nodes for thin wires was based upon physical approximations and involved the use of empirically fitted parameters [1.24-1.26]. Specifically, for the case of the TLM method, the emphasis was on

modifying the capacitance and inductance of the TLM node to take into consideration the presence of the wire. By using an arbitrarily defined outer return radius, the capacitance and inductance of a particular thin wire was calculated and then the return radius scaled using the empirical factors to recover the node step size [1.29-1.31]. Furthermore, for TLM, these models have also been developed to include thin wire junctions and multi-wire systems [1.32, 1.33]. Generally, the empirical factors have been determined either experimentally or by fine numerical meshing.

As the use of empirical factors is neither robust nor sufficiently flexible, an innovative formulation, the so called macro-node, was subsequently developed from the theoretically known local field behaviour in the proximity of the wire. Taking into account an appropriate set of lowest order field solutions, a thin wire has been embedded within a single cell of the TLM method without the use of empirical factors [1.34-1.37]. In particular, this variant describes a straight wire placed at the centre of the node in 2D and 3D TLM. This approach has been found to be very accurate for applications to EMC problems, incurring only slight computational overheads compared to the conventional coarse TLM node and subsequently better that using fine meshes. It also has been extended to the case of a wire offset from the centre of the node for two-dimensional simulations. However, this previous work is restricted to straight wires orientated along one of the Cartesian axes. Another limitation that preludes its use for the important case of wires clustered in close proximity, or for modelling of wire looms, bundles and cables, is the fact that it allows the embedding of only one wire per numerical cell.

1.6. Aims of the Work Described in the Thesis

This thesis substantially extends the concept of macro-nodes or sub-cell models incorporated within time-domain numerical networks. It significantly extends the scope of the approach and removes all the restrictions and limitations listed above. It allows features of arbitrary geometry to be arbitrarily positioned within the cell. In addition these fine objects may be wholly enclosed within a single cell or pass across several cells. The approach also accounts for multiple objects inserted into a single numerical cell, recognising at the same time the interaction of near fields scattered from the encased bodies. The technique combines a rigorous field approach with the simplicity and versatility of the network approach, while maintaining second order accuracy which is acceptable for the simulation of EMC problems.

1.7. Overview of the Thesis

Chapter 2 introduces the fundamentals of electromagnetic theory required to understand the phenomenon of waves propagating in the presence of potential scatterers. From a general statement of Maxwell's equations, the wave equation is derived. As the majority of the work presented in this thesis is concerned with cylindrical and circular-shaped scatterers the solution to the cylindrical wave equation is demonstrated. In addition, this solution is presented from the point of view of field decomposition into different local modes. Finally, the principles of TLM method are discussed, a technique widely used in electromagnetic field modelling and which is also employed throughout this project.

Chapter 3 describes the generic algorithm for embedding fine feature into a single cell of TLM method. The procedure for identifying a suitable set of field solutions so they can be incorporated within a time-domain network is detailed. Finally, the algorithm that maps the field solutions to passive components of a network consisting of short transmission lines is studied.

A two-dimensional analysis of the generic algorithm from Chapter 3 is presented in Chapter 4, based initially on the example of a single infinitely long conducting wire placed at the centre of numerical cell. An insight into the process of selecting appropriate modal solutions from the general field is given. Following this, the approach is employed to embed multiple conducting wires within a single TLM cell. In both cases the results are validated against analytical solutions.

Chapter 5 shows the flexibility of the approach for modelling fields scattered from cylindrical media of various characteristics. This includes a cluster of dielectric rods, dielectric coated wires and conductors with multi-layered dielectric insulation.

An important group of EMC problems that involves field distribution in the presence of cylindrical lossy wires is illustrated at the beginning of Chapter 6. The second part of this chapter demonstrates the applicability of macro-nodes in disciplines other than EMC. Of special interest is a prediction of the macroscopic behaviour of nanostructures in photonic applications with a primarily focus placed on photonic band-gap materials.

The two-dimensional simulations are extended in Chapter 7 to include objects described by elliptical coordinates. At first, the solution to the wave equation in an elliptical coordinate system is derived in the form of superposition of angular and radial Mathieu functions. Instead of presenting the canonical problem of field scattering from elliptical cylinder, this solution is applied to design a node that mimics the presence of thin conducting strips or a narrow slots. These particular features are of great importance in EMC problems as previously discussed.

Finally, in Chapter 8 three-dimensional simulations are presented. The practical illustration of the power of this technique is demonstrated for the case of arbitrarily routed wires. Another example considers a conducting ring constructed from piecewise linear segments of wire. For both of these problems the local field solutions are evaluated analytically in a pre-processing stage. Next, the use of numerical estimation of the local field solutions prior to the main TLM simulation is demonstrated based on a canonical problem of field scattering from a small metal cube. A simplification of the method for scatterers of symmetrical geometries is given and illustrated for both conducting and dielectric small spheres embedded in a single 3D TLM cell.

The work described in this thesis is summarised in Chapter 9.

1.8. References

[1.1] Paul, C.R., *"Introduction to Electromagnetic Compatibility"*, John Wiley Interscience, New York, 1992.

[1.2] IEE Guidance Document on EMC & Functional Safety; available at http://www.iee.org/Policy/Areas/Electro/core.pdf

[1.3] Konefal, T., Pearce, D.A.J., Marshman, C.A., McCormack L.M., *"Potential Electromagnetic Interference to radio Services from Railways"*, a report for the Radio communications Agency by York EMC Services Ltd, University of York; available at http://www.yorkemc.co.uk/research/railways/report.pdf

[1.4] IEE Colloquium on *"EMC and Medicine"*; Digest No. 1993/098, 1993

[1.5] Philips, J.K., Nelson, J.P., Sen, P.K., *"Power Quality and Harmonic Distortion and Distribution Systems"*, IEEE Trans on Industry Applications, Vol. 30, No. 2, pp. 476-483, 1994

[1.6] Vance, E.F., *"Coupling to Shielded Cables"*, Wiley-Interscience, John Wiley & Sons, New York, 1978

[1.7] Hoeft, L.O., and Hofstra, J.S., *"Measured Electromagnetic Shielding Performance of Commonly used Cables and Connectors"*, IEEE Trans. Electromagn. Compat., Vol. 30, No. 3, Part 1, 1988.

[1.8] Christopoulos, C., *"Principles and Techniques of Electromagnetic Compatibility"*, CRC Press Inc., 1995

[1.9] Robinson, M.P., Benson, T.M., Christopoulos, C., Dawson, J.F., Ganley, M.D., Marvin, A.C., Porter, S.J., and Thomas, D.W.P., *"Analytical* *formulation for the shielding effectiveness of enclosures with apertures",* IEEE Trans. Electromagn. Compat., Vol. 40, pp. 240–248, 1998

[1.10] Cerri, G., De Leo, R., De Rentiis, R., and Mariani, V., *"ESD field penetration through slots into shielded enclosures: A time domain approach",* IEEE Trans. Electromagn. Compat., Vol. 39, pp. 377–386, 1997

[1.11] Montrose, M. I., *"EMC and the Printed Circuit Board: Design, Theory, and Layout Made Simple",* Wiley-IEEE Press, New York, 1998

[1.12] Williams, T., and Armstrong, K., "*EMC Testing*" a series of seven articles in the EMC Compliance Journal, 2001 - 2002, available at: www.compliance-club.com/KeithArmstrongPortfolio

[1.13] Christopoulos, C., *"The Transmission-Line Modeling Method: TLM".* Piscataway, NJ: IEEE Press, 1995

[1.14] Taflove, A. Hagness, S.S, , *"Computational Electrodynamics: The Finite Difference Time-Domain Method",* 2nd ed, Norwell, MA: Artech House, 2000,

[1.15] Wlodarczyk, J., "*New multigrid interface for the TLM method,*" Electron. Lett., Vol. 32, No. 12, pp. 1111–1112, 1996

[1.16] Herring, J. L. and Christopoulos, C., *"Multigrid transmission-line modeling method for solving electromagnetic field problem, ",* Electron. Lett., Vol. 27, No. 20, pp. 1794–1795, 1991

[1.17] Sobhy, M. I. , Abd El-Azeem, M. H. , and Royer, K.W., *"A new multi-grid 3-D TLM algorithm for simulation of microwave FSS", IEEE MTT-S Int. Microwave Symp. Dig.,* Vol. 2, pp. 439–442, 1996

[1.18] Sewell, P., Wykes, J. G., Benson, T.M., Christopoulos, C., Thomas, D.W.P. and Vukovic, A., *"Multi-Grid Interface in Computational Electromagnetics"*, Electron. Lett., Vol. 40, No. 3, pp. 162-163, 2004

[1.19] Sewell, P., Wykes, J. G., Benson, T.M., Christopoulos, C., Thomas, D.W.P. and Vukovic, A., *"Transmission-Line Modeling Using Unstructured Triangular Meshes"*, IEEE Trans. Microwave Theory Techniques., Vol. 52, pp. 1490–1497, 2004

[1.20] Sewell, P., Benson, T. M., Christopoulos, C., Thomas, D. W. P., Vukovic A. and Wykes, J. G., *"Transmission Line Modeling (TLM) Based Upon Unstructured Tetrahedral Meshes"*, IEEE Transactions on Microwave Theory and Techniques, Vol. 53, No. 6, pp. 1919-1928, 2005

[1.21] Naylor, P., Christopoulos, C., and Johns, P. B., *"Coupling between electromagnetic field and wires using transmission-line modeling"*, Proc. Inst. Elect. Eng. 134, pp. 679–686, 1987

[1.22] Johns, P.B., and Akhtarzad, K., *"The use of time domain diakoptics in time discrete models of fields"*, International Journal of Numerical Methods in Eng, 17, pp. 1–14, 1981

[1.23] Cascio, L., Tardioli, G., Rozzi, T., and Hoefer, W. J. R., *"A quasi-static modification of TLM at knife edge and 90° wedge singularities,"* IEEE Trans. Microwave Theory Techniques., Vol. 44, pp. 2519-2524, 2002

[1.24] Holland, R., and Simpson, L., *"Finite-difference analysis of EMP coupling of thin struts and wires"*, IEEE Trans. Electromagn. Compat., Vol. 23, pp. 88–97, 1981

[1.25] Umashanker, K.R., Taflove, A., and Beker, B., *"Calculation and experimental validation of induced currents on coupled wires in an arbitrary shaped cavity"*, IEEE Trans. Antennas Propagation, Vol. 35, No. 11, pp. 1248–1257, 1987

[1.26] Makinen, R.M., Juntunen, J.S., and Kivikoski, M.A., *"An improved thin-wire model for FDTD"*, IEEE Trans. Microwave Theory Techniques, Vol. 50, pp. 1245–1255, 2002

[1.27] Railton, C.J. , Koh, B.P., and Craddock, I.J., *"The treatment of thin wires in the FDTD method using a weighted residuals approach"*, IEEE Trans. Antennas Propagation, Vol. 52, pp. 2941-2949, 2004

[1.28] Edelvik, F., *"A new technique for accurate and stable modeling of arbitrarily oriented thin wires in the FDTD method"*, IEEE Trans. Electromagn. Compat., Vol. 45, pp. 416-423, May 2003

[1.29] Wlodarczyk, A. J., and Johns, D. P., *"New wire interface for graded 3D TLM"*, Electron. Lett., Vol. 28, pp. 728–729, 1992

[1.30] Naylor, P., and Christopoulos, C., *"A new wire node for modeling thin wires in electromagnetic field problems solved by transmission line modeling"*, IEEE Trans. Microwave Theory Techniques, Vol. 38, pp. 328–330, 1990

[1.31] Porti, J. A., Morente, J.A., Khalladi, M., and Callego, A., *"A comparison of thin-wire models for TLM method"*, Electron. Lett., Vol. 28, pp. 1910–1911, 1992

[1.32] Jorge, A.P., Khalladi, M., Morente, J.A., Giménez, G., Carrión, M.C., *"Wire junction Matriz Model for the TLM Method"*, IEEE Trans. Antennas and Propagation, Vol. 42, No. 2, pp. 282-285, 1994

[1.33] Wlodarczyk, A.J., Trenkic, V., Scaramuzza, R.A., Christopoulos, C., *"A fully integrated multi-conductor model for TLM"*, IEEE Trans. Microwave Theory Techniques, Vol. 46, No. 12, pp.2431-2437, 1998

[1.34] Choong, Y.K., Sewell, P., and Christopoulos, C., *"Accurate wire representation in numerical models for high-frequency simulation"*, Electron. Lett., Vol. 37, No. 5, pp. 280–282, 2001

[1.35] Choong, Y.K., Sewell, P., and Christopoulos, C., *"New thin-wire formulation for time-domain differential-equation models"*, in Proc. 4th Int. Workshop Computational Electromagnetics, U.K.: Univ. Nottingham, Sept. 17–19, pp. 187–194, 2001

[1.36] Choong, Y.K., Sewell, P., and Christopoulos, C., *"Accurate modeling of arbitrary placed thin wire in a coarse mesh"*, in Proc. IEE, 4th Int. Conf. Computational Electromagnetics, CEM'02, Bournemouth, U.K., Apr. 8–11, pp. 158-159, 2002

[1.37] Sewell, P., Choong, Y. K., and Christopoulos, C. *"An accurate thin-wire model for 3-D TLM simulations"*, IEEE Trans. Electromagn. Compat., Vol. 45, pp. 207–217, 2003

Chapter 2

Principles of Electromagnetic Field Theory and the TLM Method

This chapter introduces the fundamentals of electromagnetic theory. In order to understand field scattering phenomena, the wave equation is derived from a general form of Maxwell's equations. Due to the fact that the majority of the work presented in this thesis is concerned with circular-shaped scatterers the solution to the cylindrical wave equation is also considered. Decomposition of this general field solution into different local solutions is presented. Finally, the principles of Transmission Line Modelling method are given as this technique is widely used in EMC predictions and also is the main numerical means employed in this thesis.

2.1. Basic Theory of Electromagnetism

Electromagnetic fields are time dependent fields, in the general harmonic time form given by:

$$\mathbf{E} = \mathrm{Re}\left\{\mathbf{E}\,e^{j\omega t}\right\} \qquad \text{and} \qquad \mathbf{H} = \mathrm{Re}\left\{\mathbf{H}\,e^{j\omega t}\right\} \tag{2.1}$$

where ω is the angular frequency. The behaviour of such fields is fully described by the set of Maxwell's equations. In a source free and lossless region these are:

$$\nabla \cdot \mathbf{D} = 0 \tag{2.2}$$

$$\nabla \cdot \mathbf{B} = 0 \tag{2.3}$$

$$\nabla \times \mathbf{E} = -\frac{\partial \mathbf{B}}{\partial t} = -j\omega\mu\mathbf{H} \tag{2.4}$$

$$\nabla \times \mathbf{H} = \frac{\partial \mathbf{D}}{\partial t} = j\omega\varepsilon\mathbf{E} \tag{2.5}$$

The vector quantities denoted above in bold are: **D** (C/m) – the electric flux density, **B** (T) – the magnetic flux density, **E** (V/m) – the electric field intensity, and **H** (A/m) is the magnetic field intensity. Two constitutive relationships that provide the dependence between the fields and the medium the fields exist in, have been introduced in Equation (2.2) and (2.3). For linear isotropic media these are:

$$\mathbf{D} = \varepsilon\mathbf{E} \tag{2.6}$$

$$\mathbf{B} = \mu\mathbf{H} \tag{2.7}$$

where ε is a dielectric permittivity and μ magnetic permeability usually expressed as:

$$\varepsilon = \varepsilon_r\varepsilon_o \qquad \mu = \mu_r\mu_o \tag{2.8}$$

In Equation (2.8) ε_r and μ_r are the relative permittivity and permeability of the medium and ε_o, μ_o; of the free space respectively. This work involves isotropic and non-magnetic materials only, hence $\mu_r = 1$.

The wave equation for electric field $\mathbf{E}$ is readily obtained by taking the curl of Equation (2.4) and substituting for the curl of $\mathbf{H}$ on the right-hand side with Equation (2.5), thus

$$\nabla \times \nabla \times \mathbf{E} = -j\omega\mu\nabla \times \mathbf{H} = \omega^2\mu\varepsilon\mathbf{E} = k^2\mathbf{E} \tag{2.9}$$

where $k = \omega\sqrt{\mu\varepsilon}$ is the wavenumber.

Using the vector identity (A.1) given in Appendix A the following can be formulated:

$$\nabla \times \nabla \times \mathbf{E} = \nabla\nabla \cdot \mathbf{E} - \nabla^2 \mathbf{E} \tag{2.10}$$

Substituting Equation (2.6) into Equation (2.2) and utilising identity (A.2) it should be clear that in a homogenous and isotropic medium, the component of $\nabla\nabla \cdot \mathbf{E}$ from Equation (2.10) equals zero and Equation (2.9) simplifies to:

$$\nabla^2 \mathbf{E} + k^2 \mathbf{E} = 0 \tag{2.11}$$

which is the Helmholtz equation [2.1].

In a cylindrical structure where $\frac{\partial \varepsilon}{\partial z} = \frac{\partial \mu}{\partial z} = 0$ separation of the variables permits the substitution $\frac{\partial^2}{\partial z^2} = -\beta_z^2$ in which case

$$\nabla_t^2 \mathbf{E} + (k^2 - \beta_z^2)\mathbf{E} = 0 \tag{2.12}$$

In the above equation $\nabla_t^2 \left(\nabla^2 = \nabla_t^2 + \frac{\partial^2}{\partial z^2} \right)$ operates now only on two variables (x,y) or (r, ϕ) depending which coordinate system is under consideration.

Similarly, taking the curl of Equation (2.5) and substituting on the right-hand side for $\nabla \times \mathbf{E}$ from Equation (2.4), then by analogy to the process presented above, the equation for $\mathbf{H}$ field can be derived in the form:

$$\nabla_t^2 \mathbf{H} + (k^2 - \beta_z^2)\mathbf{H} = 0 \tag{2.13}$$

Equations (2.12) and (2.13) are vector Helmholtz equations in which permittivity and permeability are assumed to be constants. These equations are solved subject to the field boundary conditions at any discontinuity surface as will be discussed in section 2.5.1.

2.2. Wave Equation in Cylindrical Coordinates

The majority of the work presented in this thesis is dedicated to systems of a cylindrical configuration. Therefore, it advisable to solve the boundary-value problem for the **E** and **H** fields using cylindrical coordinates. Thus, Maxwell's equations and the Helmholtz equation presented in the previous section will be now expressed using cylindrical coordinates. The solution for the **E** field is considered in a source-free and lossless medium. A similar procedure can be used for the **H** field formulations.

In cylindrical coordinates, a general solution to the vector Helmholtz equation for electric field and conditions mentioned above can be written as [2.2]:

$$\mathbf{E}(r,\phi,z)=\hat{a}_r E_r(r,\phi,z)+\hat{a}_\phi E_\phi(r,\phi,z)+\hat{a}_z E_z(r,\phi,z) \tag{2.14}$$

where r, ϕ, z are the cylindrical coordinates and $\hat{a}_r,\hat{a}_\phi,\hat{a}_z$ are unit vectors.

Substituting Equation (2.14) in Equation (2.11) leads to:

$$\nabla^2(\hat{a}_r E_r+\hat{a}_\phi E_\phi+\hat{a}_z E_z)=-k^2(\hat{a}_r E_r+\hat{a}_\phi E_\phi+\hat{a}_z E_z) \tag{2.15}$$

According to the formula (A.12) shown in Appendix A, one of the three scalar equations which Equation (2.15) provides is:

$$\nabla^2 E_z+k^2 E_z=0 \tag{2.16}$$

In the above equation the scalar Laplacian is defined in Appendix A in Equation (A.11) which allows Equation (2.16) to be generalised to:

$$\nabla^2\psi(r,\phi,z)+k^2\psi=\frac{\partial^2\psi}{\partial r^2}+\frac{1}{r}\frac{\partial\psi}{\partial r}+\frac{1}{r^2}\frac{\partial^2\psi}{\partial\phi^2}+\frac{\partial^2\psi}{\partial z^2}+k^2\psi=0 \tag{2.17}$$

where ψ is a scalar function that can represent a field or a vector potential component.

The second order partial differential equation presented in Equation (2.17) is highlighted as its solutions will be shown to lead to the transverse electric (TE) and transverse magnetic (TM) fields.

Assuming a separable solution for $\psi(r,\phi,z)$ defined as:

$$\psi(r,\phi,z) = R(r)\Phi(\phi)Z(z) \tag{2.18}$$

it can be shown [2.2] that Equation (2.17) reduces to three independent solutions

$$r^2\frac{d^2R}{dr^2} + r\frac{dR}{dr} + \left(\beta_r^2 r^2 - n^2\right)R = 0 \tag{2.19}$$

$$\frac{d^2\Phi}{d\phi^2} = -n^2\Phi \tag{2.20}$$

$$\frac{d^2Z}{dz^2} = -\beta_z^2 Z \tag{2.21}$$

where n, β_r and β_z are separation constants and the wavenumber *k* equals

$$k^2 = \beta_r^2 + \beta_z^2 \tag{2.22}$$

The general solution to Equation (2.17) is formulated as [2.2]:

$$\begin{aligned}\psi(r,\phi,z) &= R(r)\Phi(\phi)Z(z)\\ &= \left[A_1J_n(\beta_r r) + B_1H_n^{(2)}(\beta_r r)\right]\times \qquad (2.23)\\ &\quad \left[A_2e^{-jn\phi} + B_2e^{+jn\phi}\right]\left[A_3\cos(\beta_z z) + B_3\sin(\beta_z z)\right]\end{aligned}$$

and *n* is of integer order.

In this solution the Bessel functions $J_n(\beta_r r)$ represent radial standing waves, whereas the Hankel functions $H_n^{(2)}(\beta_r r)$ represent waves carrying energy away from the origin. It should be noted that the particular form of the solution can be modified depending on the application. The exponential functions of ϕ can be substituted by trigonometric cosine and sine functions to form a periodic wave solution and similarly exponential functions of z can be used to describe travelling waves. Also, the kind of Bessel functions can be chosen appropriately for the physical solution they are to represent.

As mentioned previously the solution presented in Equation (2.23) can represent a vector potential function and can be applied to decoupled general field solution into different types of transverse modes. It is noted that general Maxwell's equations are valid for all space and boundary conditions. However, by deriving the fields from vector potential functions, the transverse modes can be expressed in terms of a single scalar solution which in practice is easier to obtain than the full vector fields. Therefore, a brief introduction to vector potentials will be given.

2.3. Vector Potentials

2.3.1. Vector Potential A

In a source-free region the magnetic density $\mathbf{B}$ satisfies $\nabla \cdot \mathbf{B} = 0$. It can be therefore represented as a curl of another vector as it obeys the vector identity

$$\nabla \cdot (\nabla \times \mathbf{A}) = 0 \tag{2.24}$$

where $\mathbf{A}$ is an arbitrary vector. Thus,

$$\mathbf{B}_A = \mu \mathbf{H}_A = \nabla \times \mathbf{A} \quad \text{or} \quad \mathbf{H}_A = \frac{1}{\mu} \nabla \times \mathbf{A} \tag{2.25}$$

where the subscript A indicates the fields present due to the potential $\mathbf{A}$. Hence Maxwell's equations can be written as:

$$\nabla \times \mathbf{E}_A = -j\omega\mu \mathbf{H}_A \tag{2.26}$$

$$\nabla \times \mathbf{H}_A = j\omega\varepsilon \mathbf{E}_A \tag{2.27}$$

By mathematical manipulation of the above equations and Equation (2.25) it can be shown that [2.2]:

$$\mathbf{E}_A = -j\omega \mathbf{A} - j\frac{1}{\omega\mu\varepsilon}\nabla(\nabla \cdot \mathbf{A}) \tag{2.28}$$

where $\mathbf{A}$ is the solution of

$$\left(\nabla^2 + k^2\right)\mathbf{A} = 0 \tag{2.29}$$

Once the vector potential $\mathbf{A}$ is known both $\mathbf{H}_A$ and $\mathbf{E}_A$ can be calculated from Equations (2.25) and (2.28) respectively.

2.3.2. Vector Potential F

In a source-free region the magnetic density $\mathbf{D}$ satisfies $\nabla \cdot \mathbf{D} = 0$. It can be therefore represented as a curl of another vector as it obeys the vector identity

$$\nabla \cdot (-\nabla \times \mathbf{F}) = 0 \tag{2.30}$$

where $\mathbf{F}$ is an arbitrary vector. Thus,

$$\mathbf{D}_F = -\nabla \times \mathbf{F} \quad \text{or} \quad \mathbf{E}_F = -\frac{1}{\varepsilon}\nabla \times \mathbf{F} \tag{2.31}$$

where a subscript F indicates the fields present due to the potential $\mathbf{F}$. The Maxwell's equations can be formulated as:

$$\nabla \times \mathbf{H}_F = j\omega\varepsilon \mathbf{E}_F \tag{2.32}$$

$$\nabla \times \mathbf{E}_F = -j\omega\mu \mathbf{H}_F \tag{2.33}$$

By mathematical arrangements of the above equations and Equation (2.31) it can be shown that [2.2]:

$$\mathbf{H}_F = -j\omega\mathbf{F} - j\frac{1}{\omega\mu\varepsilon}\nabla(\nabla\cdot\mathbf{F}) \tag{2.34}$$

where $\mathbf{F}$ is the solution of

$$\left(\nabla^2 + k^2\right)\mathbf{F} = 0 \tag{2.35}$$

Once the vector potential $\mathbf{F}$ is known both $\mathbf{E}_F$ and $\mathbf{H}_F$ can be obtained from Equations (2.31) and (2.34) respectively.

It should be clear that the vector potentials $\mathbf{A}$ and $\mathbf{F}$ must satisfy the vector Helmholtz equation. It is also noted that the total fields can be expressed as a superposition of both vector potentials, i.e.

$$\mathbf{E} = \mathbf{E}_A + \mathbf{E}_F = -j\omega\mathbf{A} - j\frac{1}{\omega\mu\varepsilon}\nabla(\nabla\cdot\mathbf{A}) + \frac{1}{\varepsilon}\nabla\times\mathbf{F} \tag{2.36}$$

$$\mathbf{H} = \mathbf{H}_A + \mathbf{H}_F = \frac{1}{\mu}\nabla\times\mathbf{A} - j\omega\mathbf{F} - j\frac{1}{\omega\mu\varepsilon}\nabla(\nabla\cdot\mathbf{F}) \tag{2.37}$$

In practice, rather than constructing three components of $\mathbf{A}$ or $\mathbf{F}$ it is more convenient to use for example $\mathbf{A} = \hat{z}A_z$ or $\mathbf{F} = \hat{z}F_z$ as the unknowns.

2.4. Modal Solutions

The aim of this section is to present the field configurations (modes) that are used in this work as local field solutions. These are: Transverse ElectroMagnetic (TEM) modes whose electric and magnetic field components are both transverse to the direction of propagation; Transverse Magnetic (TM) mode whose magnetic field components are transverse to the direction of propagation and finally Transverse Electric (TE) mode with electric field components transverse to the direction of propagation. Again the focus is placed upon cylindrical modes.

For any z-directed field potential defined by:

$$\mathbf{A}(r,\phi,z)=\hat{a}_z A_z(r,\phi,z) \tag{2.38}$$

$$\mathbf{F}(r,\phi,z)=\hat{a}_z F_z(r,\phi,z) \tag{2.39}$$

the total electric and magnetic field solutions can be derived from Equations (2.36) and (2.37) utilising the differential operators detailed in section 3 of Appendix A and are expressed by:

$$\begin{aligned}\mathbf{E}=&\,\hat{a}_r\left\{-j\frac{1}{\omega\mu\varepsilon}\frac{\partial}{\partial r}\frac{\partial A_z}{\partial z}-\frac{1}{\varepsilon}\frac{1}{r}\frac{\partial F_z}{\partial \phi}\right\}+\hat{a}_\theta\left\{-j\frac{1}{\omega\mu\varepsilon}\frac{1}{r}\frac{\partial}{\partial \phi}\frac{\partial A_z}{\partial z}+\frac{1}{\varepsilon}\frac{\partial F_z}{\partial r}\right\}\\&+\hat{a}_z\left\{-j\frac{1}{\omega\mu\varepsilon}\left(k^2+\frac{\partial^2}{\partial z^2}\right)A_z\right\}\end{aligned} \tag{2.40}$$

$$\begin{aligned}\mathbf{H}=&\,\hat{a}_r\left\{-j\frac{1}{\omega\mu\varepsilon}\frac{\partial}{\partial r}\frac{\partial F_z}{\partial z}+\frac{1}{\mu}\frac{1}{r}\frac{\partial A_z}{\partial \phi}\right\}+\hat{a}_\theta\left\{-j\frac{1}{\omega\mu\varepsilon}\frac{1}{r}\frac{\partial}{\partial \phi}\frac{\partial F_z}{\partial z}-\frac{1}{\mu}\frac{\partial A_z}{\partial r}\right\}\\&+\hat{a}_z\left\{-j\frac{1}{\omega\mu\varepsilon}\left(k^2+\frac{\partial^2}{\partial z^2}\right)F_z\right\}\end{aligned} \tag{2.41}$$

where $k^2=\beta_r^2+\beta_z^2$

Utilising this general solution for total fields the transverse modes will be next discussed.

2.4.1. Transverse Magnetic (TM) Mode

For a TM mode the magnetic field components are transverse to the direction of propagation. The expression that is valid for TM fields will be derived here for any general field in the form of $e^{j(\omega t-\beta_z z)}$. To accomplish this, the following is assumed:

$$\begin{aligned}\mathbf{A}&=\hat{a}_z A_z(r,\phi,z)\\ \mathbf{F}&=0\end{aligned} \tag{2.42}$$

Recognising the fact that for exponential variation of field as described above

$$\frac{\partial}{\partial z} = j\beta_z \text{ and } \frac{\partial^2}{\partial z^2} = -\beta_z^2 \tag{2.43}$$

and furthermore that for TM mode there is no variation along z-direction, hence $\beta_z = 0$, the wave equation given in Equation (2.17) that must be satisfied by the vector potential $\mathbf{A}$ reduces to:

$$\frac{\partial^2 A_z}{\partial r^2} + \frac{1}{r}\frac{\partial A_z}{\partial r} + \frac{1}{r^2}\frac{\partial^2 A_z}{\partial \phi^2} + k^2 A_z = 0 \tag{2.44}$$

where $k^2 = \beta_r^2 = \omega^2 \mu\varepsilon$.

Separating this equation to an ordinary differential equation, as shown above, the vector potential can be identified in the form [2.3]:

$$A_z(r,\phi,z) = \left[A_1 J_n(\beta_r r) + B_1 H_n^{(2)}(\beta_r r)\right] \times \left[A_2 e^{-jn\phi} + B_2 e^{+jn\phi}\right] \tag{2.45}$$

The remaining field components are found using Equation (2.40) and (2.41) and are respectively:

$$\begin{aligned} E_r &= 0 & H_r &= \frac{1}{\mu}\frac{1}{r}\frac{\partial A_z}{\partial \phi} \\ E_\theta &= 0 & H_\theta &= -\frac{1}{\mu}\frac{\partial A_z}{\partial r} \\ E_z &= -j\frac{k^2}{\omega\mu\varepsilon} A_z & H_z &= 0 \end{aligned} \tag{2.46}$$

2.4.2. Transverse Electric (TE) Mode

For a TE mode the electric field components are transverse to the direction of propagation. The TE mode can be derived by analogy to the TM polarisation presented above by assuming:

$$\begin{aligned} \mathbf{A} &= 0 \\ \mathbf{F} &= \hat{a}_z F_z(r,\phi,z) \end{aligned} \tag{2.47}$$

Similarly, the vector $\mathbf{F}$ must satisfy the Helmholtz equation:

$$\frac{\partial^2 F_z}{\partial r^2} + \frac{1}{r}\frac{\partial F_z}{\partial r} + \frac{1}{r^2}\frac{\partial^2 F_z}{\partial \phi^2} + k^2 F_z = 0 \tag{2.48}$$

where $\beta_z = 0$ and $k^2 = \beta_r^2 = \omega^2\mu\varepsilon$.

Utilising the separation of variables method the following solution can be obtained:

$$F_z(r,\phi,z) = \left[A_1 J_n(\beta_r r) + B_1 H_n^{(2)}(\beta_r r)\right] \times \left[A_2 e^{-jn\phi} + B_2 e^{+jn\phi}\right] \tag{2.49}$$

and remaining field components are found using Equation (2.40) and (2.41)

$$\begin{aligned} E_r &= -\frac{1}{\varepsilon r}\frac{\partial F_z}{\partial \phi} & H_r &= 0 \\ E_\theta &= \frac{1}{\varepsilon}\frac{\partial F_z}{\partial r} & H_\theta &= 0 \\ E_z &= 0 & H_z &= -j\frac{k^2}{\omega\mu\varepsilon}F_z \end{aligned} \tag{2.50}$$

2.4.3. Transverse Electro-Magnetic (TEM) Mode

The Transverse Electro-Magnetic mode is defined by existence only of electric and magnetic field components that are transverse to the direction of propagation. Hence $E_z = 0$ and $H_z = 0$. From Equation (2.43) and the definition of z-components given in Equation (2.40) and (2.41) it is clear that the E_z and H_z can be forced to zero when $\beta_r = 0$. Hence $k^2 = \beta_z^2 = \omega^2\mu\varepsilon$. The transverse field elements are:

$$
\begin{aligned}
E_r &= -j\frac{1}{\omega\mu\varepsilon}\frac{\partial}{\partial r}\frac{\partial A_z}{\partial z} - \frac{1}{\varepsilon}\frac{1}{r}\frac{\partial F_z}{\partial \phi} \\
E_\theta &= -j\frac{1}{\omega\mu\varepsilon}\frac{1}{r}\frac{\partial}{\partial \phi}\frac{\partial A_z}{\partial z} + \frac{1}{\varepsilon}\frac{\partial F_z}{\partial r} \\
H_r &= -j\frac{1}{\omega\mu\varepsilon}\frac{\partial}{\partial r}\frac{\partial F_z}{\partial z} + \frac{1}{\mu}\frac{1}{r}\frac{\partial A_z}{\partial \phi} \\
H_\theta &= -j\frac{1}{\omega\mu\varepsilon}\frac{1}{r}\frac{\partial}{\partial \phi}\frac{\partial F_z}{\partial z} - \frac{1}{\mu}\frac{\partial A_z}{\partial r}
\end{aligned}
\qquad (2.51)
$$

where A_z and F_z can be proven to be in the form:

$$
\begin{aligned}
A_z(r,\phi,z) = F_z(r,\phi,z) &= \left[A_1 r^n + B_1 r^{-n}\right] \\
&\times\left[A_2 e^{-jn\phi} + B_2 e^{+jn\phi}\right]\left[A_3\cos(\beta_z z) + B_3\sin(\beta_z z)\right]
\end{aligned}
\qquad (2.52)
$$

It is noted that for the case of $k=\beta_z$ the Helmholtz equation presented in Equation (2.12) or (2.13) reduces to the Laplace equation. Therefore, the solution presented in Equation (2.52) represents static field. Hence, the solution of R(r) is no longer represented by Bessel and Hankel functions as in the case of TM and TE mode but is given by:

$$
R(r) = A_1 r^n + B_1 r^{-n} \qquad (2.53)
$$

It can be interpreted as a limiting case of Bessel and Hankel functions when $\beta_r = 0$. It is can be shown that in such scenario $J_n(\beta_r r) = C_1 r^n$ and $H_n^2(\beta_r r) = C_2 r^{-n}$ where C_1 and C_2 are constants. It is also underlined that in Equation (2.51) only one of the vector potentials needs to be used to calculate the transverse field components, as in this static problem potentials **A** and **F** give rise to the same **E** and **H** fields.

2.5. Plane Wave Scattering from a Cylinder

The aim of this section is to describe the problem of plane wave scattering by cylindrical structures in a homogenous space as this configuration often recurs in the models presented in this thesis. Consider an infinitely long cylinder is placed along the z-axis, as presented in Figure 2.1. A plane wave travelling in the +x-direction is incident normally upon the structure with electric field:

$$E^i = \hat{a}_z E_z^i = \hat{a}_z E_0 e^{-j\beta x} = \hat{a}_z E_0 e^{-j\beta r\cos\phi} \tag{2.54}$$

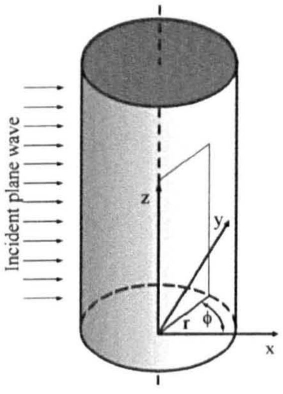

Figure 2.1. Plane wave incident normally upon cylinder

To satisfy the boundary conditions on the cylinder it is convenient to express the plane wave in terms of cylindrical functions. Specifically, the incident field can be expressed as an infinite sum of cylindrical wave functions using the Jacobi-Anger expansion of the form:

$$E_z^i = e^{-j\beta r\cos\phi} = \sum_{n=-\infty}^{\infty} (-j)^n J_n(\beta r) e^{-jn\phi} \tag{2.55}$$

$J_n(\beta r)$ are Bessel functions of the first kind and order n and the propagation constant $\beta = k$ as the field is invariant in the z-direction, where k is the wavenumber of the medium, for free space assigned as k_0.

To represent the outgoing or scattered wave the Bessel functions of the second kind, known also as Hankel functions are employed and the expansion takes the form:

$$E_z^s = \sum_{n=-\infty}^{\infty} B_n H_n^{(2)}(\beta r) e^{-jn\phi} \tag{2.56}$$

Therefore the total field, defined as the superposition of the incident field E_z^i and the scattered field E_z^s, is given by:

$$E_z^t = E_z^i + E_z^s = \sum_{n=-\infty}^{\infty} \left[(-j)^n J(\beta r) + B_n H_n^{(2)}(\beta r)\right] e^{-jn\phi} \tag{2.57}$$

To determine the total field, the unknown so far scattered field coefficients, B_n, need to be calculated. To accomplish this, the boundary conditions at the surface of the cylinder must be applied.

2.5.1. Boundary Conditions at the Surface of Cylinder

Consider an infinitely long z-directed cylinder as presented in Figure 2.1. The surface of the cylinder divides the space into two regions of parameters (ε_1, μ_1) outside cylinder and (ε_2, μ_2) enclosed by the cylinder. Faraday's law for electric and magnetic field enforces the continuity of the tangential field components at the interface [2.3], which is defined as:

$$E_{1t} = E_{2t} \quad \text{and} \quad H_{1t} = H_{2t} \tag{2.58}$$

where the subscript t denotes tangential field and the numbers 1 and 2 regions outside and inside the cylinder respectively. In vector form the above can be expressed as:

$$\hat{n} \times (E_1 - E_2) = 0 \quad \text{and} \quad \hat{n} \times (H_1 - H_2) = 0 \tag{2.59}$$

where $\hat{n}$ is a vector normal to the cylinder surface.

To sum up, the tangential components of electric and magnetic field must be equal on the two sides of any boundary between physical media. This condition however may be modified for an idealised case such as perfect conductor. In such model, since the electric field is zero within the perfect conducting cylinder, continuity of tangential electric field at the boundary requires that the surface tangential electric field be zero just outside the boundary, hence

$$E_{1t} = 0 \tag{2.60}$$

From the integral form of Gauss's law for a charge-free region the following can be concluded [2.3]:

$$D_{n1} = D_{n2} \quad \text{or} \quad \varepsilon_1 E_{n1} = \varepsilon_2 E_{n2} \tag{2.61}$$

$$B_{n1} = B_{n2} \quad \text{or} \quad \mu_1 H_{n1} = \mu_2 H_{n2} \tag{2.62}$$

That is, normal components of electric and magnetic flux density are continuous at the boundary. For the case of perfect conductor the magnetic field vanishes inside the cylinder, hence

$$B_{1n} = 0 \tag{2.63}$$

These boundary conditions will be discussed in detail when practical configurations are studied in the following chapters and calculations of scattered field coefficients will be shown.

In the above sections the analytical solution to Maxwell's equations has been introduced based on the problem of electromagnetic field scattered from a cylindrical structure. However, in many engineering problems the analytical solution is intractable and Maxwell's equation can only be solved by numerical means. Therefore, in the next section the numerical techniques will be discussed with the main focus placed on the Transmission Line Modelling method.

2.6. Transmission Line Modelling (TLM) Method

There are a variety of numerical methods available for obtaining the solution to Maxwell's equations. The two that have become widespread due to their flexibility and relative ease of use are the Finite Difference Time Domain (FDTD) [2.5] and Transmission Line Modelling (TLM) methods [2.6]. Both these techniques have been successfully applied to a variety of complex electromagnetic problems. Owing to the time-domain nature of these algorithms, a response containing a wide range of frequencies can be obtained in a single computational run. In the well-known FDTD method, the problem space is overlayed by a system of meshes and the derivatives in Maxwell's equations are directly approximated in terms of difference quotients over a small interval [2.7]. Hence, field at each point of the mesh is calculated with relation to its neighbours. The TLM method is based on a discrete representation of Huygens' principle [2.8, 2.9] which is implemented by the scattering of voltages impulses in a mesh of short commensurate transmission lines interconnected at junctions called nodes. The pulses are partially reflected and transmitted according to transmission line theory and the scattered pulses at a particular time step become incident at the adjacent nodes at the next time step. In this way the disturbance propagates and spreads in space. Therefore, the TLM method exhibits a clear isomorphism between the field quantities and the lumped circuit equivalents of transmission lines which results in an explicit scheme.

TLM also offers two important advantages over FDTD. Whilst in FDTD the electric and magnetic fields are separated in space and time by a half of the cell size and a half of the time step respectively, all fields in TLM coincide at the same point in time and space. This makes TLM highly applicable for simulations of EM wave propagation in complex materials, such as frequency-dependent [2.10], anisotropic [2.11], and nonlinear materials [2.12]. An additional advantage when developing TLM algorithms comes from the fact that the field quantities are mapped onto a passive electrical circuit equivalent which ensures that TLM is provably stable and conservative at a local level. Furthermore, the circuit representation allows a high level of hybridisation of TLM with other techniques [2.13] and lumped circuit models of components and devices.

A detailed formulation of the TLM method which has been employed throughout this project is available in [2.6, 2.8, 2.9]. However, the necessary fundamentals are presented below.

2.6.1. Two-Dimensional TLM

In two-dimensional problem with $\frac{\partial}{\partial z} = 0$, Maxwell's equations can be decoupled into two field configurations, namely Transverse Magnetic (TM) and Transverse Electric (TE) modes. Depending on the mode selection, two different nodal implementations of TLM circuit are considered, i.e. the shunt and series node models.

2.6.1.1. Shunt Node

To maintain consistency with the notation common in TLM literature [2.8] and the derivations given in previous sections, the fields are taken to propagate in the x-y plane with no variation along the z-direction. Hence, the Transverse Magnetic (TM) modes comprise only three non-zero components, i.e. H_x, H_y and E_z. Maxwell's equations presented in general form in section 4 of Appendix A, now reduce to:

$$\frac{\partial E_z}{\partial y} = -\mu \frac{\partial H_x}{\partial t}, \quad -\frac{\partial E_z}{\partial x} = -\mu \frac{\partial H_y}{\partial t} \quad \frac{\partial H_y}{\partial x} - \frac{\partial H_x}{\partial y} = \varepsilon \frac{\partial E_z}{\partial t} \tag{2.64}$$

The rearrangement carried out by differentiating and then eliminating the magnetic field component gives the 2D wave equation:

$$\frac{\partial^2 E_z}{\partial x^2} + \frac{\partial^2 E_z}{\partial y^2} = \varepsilon\mu \frac{\partial^2 E_z}{\partial t^2} \tag{2.65}$$

The shunt lumped element model, which is the building block or unit cell of two-dimensional TLM network for TM polarisation is presented in Figure 2.2(a). It will be now argued that the voltage and current in the circuit are analogous to electric and magnetic field in Maxwell's equations.

Setting $\Delta l = \Delta x = \Delta y = \Delta z$ very small compared to the shortest wavelength of interest, the size of each mesh element can be considered infinitesimal, then the voltages and currents change according to Kirchhoff's and Ampere's laws:

$$\frac{\partial V_z}{\partial x} = -L \frac{\partial I_x}{\partial t}, \quad \frac{\partial V_z}{\partial y} = -L \frac{\partial I_y}{\partial t}, \quad \frac{\partial I_x}{\partial x} + \frac{\partial I_y}{\partial y} = -2C \frac{\partial V_z}{\partial t} \tag{2.66}$$

It is noted that the node capacitance is twice that of an individual line section due to the parallel connection at the node where L and C are assumed to be the inductance and capacitance per unit length of 1. Differentiating the above equations in pairs with respect to x and t or y and t, and combining them together leads to a similar expression to Equation (2.65):

$$\frac{\partial^2}{\partial x^2}\left(\frac{V_z}{\Delta l}\right)+\frac{\partial^2}{\partial y^2}\left(\frac{V_z}{\Delta l}\right)=(2C)\,L\frac{\partial^2}{\partial t^2}\left(\frac{V_z}{\Delta l}\right) \tag{2.67}$$

Thus, comparing Equation (2.67) with Equation (2.65), the following equivalences are established:

$$V_z \equiv E_z,\quad I_y \equiv H_x \quad I_x \equiv H_y \quad \mu \equiv L \quad \varepsilon \equiv 2C \tag{2.68}$$

As observed, the shunt node models a medium of parameters $(2\varepsilon, \mu)$.

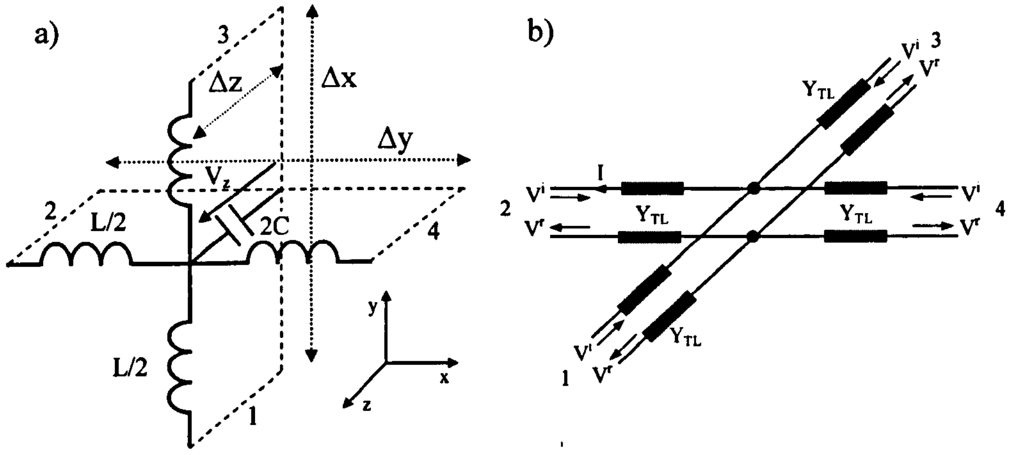

Figure 2.2. TLM shunt node (a) and its transmission line equivalent (b)

Figure 2.2(a) shows a circuit representation of Maxwell's equations in a shunt configuration. In principle, this LC circuit can be solved using any circuit technique. However, an explicit algorithm, which is computationally simpler can be obtained by replacing the LC circuit with an equivalent transmission line model, as presented in Figure 2.2(b). To achieve this, the equivalences between the LC components and characteristic impedance of a transmission line need to be identified.

TLM Models of Inductor and Capacitor

The models of capacitors and inductors that form the basic components of TLM network will now be developed. Let the capacitance and inductance per unit length of a transmission line of Δl presented in Figure 2.3(a) be C_d and L_d and the propagation delay be defined as Δt,

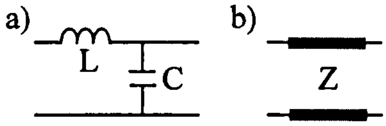

Figure 2.3. A segment of LC circuit (a) and its transmission line equivalent (b)

The components of the LC circuit shown in Figure 2.3(b) are:

$$C_d \Delta l = C \qquad L_d \Delta l = L \tag{2.69}$$

As the velocity of propagation along the line is given by:

$$u = \frac{\Delta l}{\Delta t} = \frac{1}{\sqrt{L_d C_d}} \tag{2.70}$$

the capacitance and inductance per unit length are determined as:

$$L_d = \left(\frac{\Delta t}{\Delta l}\right)^2 \frac{1}{C_d} \quad \text{and} \quad C_d = \left(\frac{\Delta l}{\Delta t}\right)^2 \frac{1}{L_d} \tag{2.71}$$

The transmission line characteristic impedance is:

$$Z = Z_C = \sqrt{\frac{L_d}{C_d}} = \frac{\Delta t}{C} \quad \text{and} \quad Z = Z_L = \sqrt{\frac{L_d}{C_d}} = \frac{L}{\Delta t} \tag{2.72}$$

Hence, the capacitor can be modelled by a transmission line of characteristic impedance Z_C but with associated inductance equal to

$$L_e = L_d \Delta l = \frac{(\Delta t)^2}{C} \tag{2.73}$$

whereas the inductor can be replaced by a line of impedance Z_L with associated capacitance of

$$C_e = C_d \Delta l = \frac{(\Delta t)^2}{L} \tag{2.74}$$

Both, L_e and C_e can be regarded as a modelling error and could be minimised by decreasing the time step Δt. It is therefore argued that a transmission line with large impedance value can represent an inductor of $L = Z\Delta t$, with the second order accurate approximation and a line with small impedance corresponds to a capacitor of $C = \Delta t / Z$. Such models are known in the literature as link models. Based on the above discussion special cases can be derived, for instance when a capacitor or inductor terminates the LC circuit. In such scenarios, a capacitor is modelled by an open-circuited transmission line and an inductor by a short-circuited transmission line. Such models are referred to as stubs and their characteristic impedances can be derived analogously to the link line impedances. The propagation velocity on a line is now defined as:

$$u = \frac{\Delta l}{\Delta t / 2} = \frac{1}{\sqrt{L_d C_d}} \tag{2.75}$$

from which

$$L_d = \frac{(\Delta t)^2}{4C\Delta l} \quad \text{and} \quad C_d = \frac{(\Delta t)^2}{4L\Delta l} \tag{2.76}$$

Hence, the characteristic impedances of capacitive and inductive stubs are:

$$Z = Z_c = \sqrt{\frac{L_d}{C_d}} = \frac{\Delta t}{2C} \quad \text{and} \quad Z = Z_L = \sqrt{\frac{L_d}{C_d}} = \frac{2L}{\Delta t} \tag{2.77}$$

with associated errors in the form of inductance and capacitance respectively given by:

$$L_e = L_d \Delta t = \frac{(\Delta t)^2}{4C} \quad \text{and} \quad C_e = C_d \Delta l = \frac{(\Delta t)^2}{4L} \tag{2.78}$$

Although identifying the corresponding series inductor-capacitor combinations required in the equivalent transmission line model is perfectly valid, in this thesis the transmission line parameters are often implemented as the input impedance to the stub. Using a general formula for an input impedance of a transmission line loaded with impedance Z_l of the form:

$$Z_{in} = Z_0 \frac{Z_l + jZ_0 \tan(\beta\Delta l)}{Z_0 + jZ_l \tan(\beta\Delta l)} \tag{2.79}$$

and assuming open circuit termination which requires that $Z_l = \infty$ the input impedance looking into a capacitive stub can be calculated as:

$$Z_{in} = \frac{Z_c}{j\tan(\beta\Delta l)} \tag{2.80}$$

where

$$\beta\Delta l = \frac{\omega}{u}\Delta l = \omega\frac{\Delta t}{2} \tag{2.81}$$

As for the short-circuited stub the inductor model can be examined in the frequency model when the input impedance for a transmission line of Equation (2.79) is considered with the load impedance $Z_l = 0$. Thus, the input impedance looking into an inductive stub model takes the form of:

$$Z_{in} = jZ_L \tan(\beta\Delta l) \tag{2.82}$$

Having established equivalences between LC circuit and a transmission line the shunt node from Figure 2.2(a) is then replaced by a model shown in Figure 2.2(b).

A time domain algorithm is recovered using principles of transmission line theory.

The voltages and currents at port 1 to 4 presented in Figure 2.2(b) are defined in terms of the incident and reflected voltages on the transmission lines utilising:

$$V_n = V_n^i + V_n^r \quad \text{and} \quad I = Y_{TL}^n (V_n^i - V_n^r) \tag{2.83}$$

where V_n^i and V_n^r are the incident and reflected voltages respectively on line *n* and Y_{TL}^n is the link line admittance of line n; in case of free space being considered as a medium this admittance is $Y_{TL} = (120\pi)^{-1}$ S. Computations in a shunt node are then performed by introducing the relationship between the incident and reflected voltages in the form:

$${}_k\underline{V}^i = \underline{\underline{S}} \cdot {}_k\underline{V}^r \tag{2.84}$$

where ${}_k\underline{V}^i$ and ${}_k\underline{V}^r$ are vectors of the four incident and reflected voltages respectively at the ports at time step k, and scattering matrix $\underline{\underline{S}}$ is defined as:

$$\underline{\underline{S}} = 0.5 \begin{bmatrix} -1 & 1 & 1 & 1 \\ 1 & -1 & 1 & 1 \\ 1 & 1 & -1 & 1 \\ 1 & 1 & 1 & -1 \end{bmatrix} \tag{2.85}$$

Pulses incident on the ports of the node defined in space by (x,y) at the time step k+1 are the pulses reflected from adjacent nodes at the previous time step k. Therefore, the incident voltages on node (x,y) for vacuum depend entirely on the nodes connected to it and the so-called connection process is described as:

$$\begin{aligned} {}_{k+1}V_1(x,y) &= {}_kV_3(x,y-1) \\ {}_{k+1}V_2(x,y) &= {}_kV_4(x-1,y) \\ {}_{k+1}V_3(x,y) &= {}_kV_1(x,y+1) \\ {}_{k+1}V_4(x,y) &= {}_kV_2(x+1,y) \end{aligned} \tag{2.86}$$

where x, y are the space indices of the mesh cells and this is schematically illustrated in Figure 2.4.

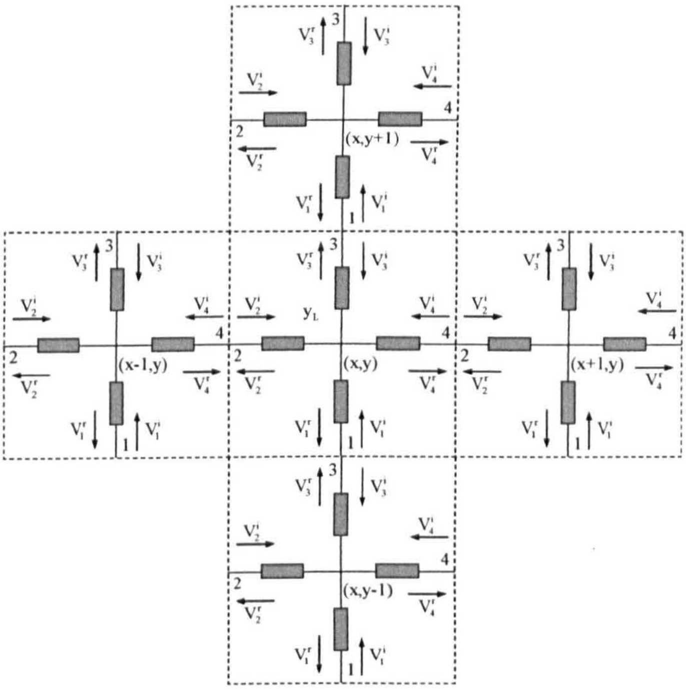

Figure 2.4. A diagram illustrating connection process for empty space two-dimensional TLM mesh

2.6.1.2. Series Node

The Transverse Electric (TE) modes consist of only the three non-zero components, i.e. E_x, E_y and H_z, and hence, Maxwell's equations reduce to:

$$\frac{\partial H_z}{\partial y} = \varepsilon \frac{\partial E_x}{\partial t}, \qquad -\frac{\partial H_z}{\partial x} = \varepsilon \frac{\partial E_y}{\partial t}, \qquad \frac{\partial E_y}{\partial x} - \frac{\partial E_x}{\partial y} = -\mu \frac{\partial H_z}{\partial t} \tag{2.87}$$

These can be rearranged by differentiating and eliminating the electric field component to give the 2D wave equation:

$$\frac{\partial^2 H_z}{\partial x^2} + \frac{\partial^2 H_z}{\partial y^2} = \varepsilon\mu \frac{\partial^2 H_z}{\partial t^2} \tag{2.88}$$

The structure referred to as a series node is presented in Figure 2.5(a).

It is desirable to devise circuits in which the variation of the circuit quantities exhibit isomorphic behaviour to those in Equation (2.88). From Kirchhoff's voltage and Ampere's current law the following can be formulated:

$$\frac{\partial I_z}{\partial y} = -C\frac{\partial V_x}{\partial t}, \quad \frac{\partial I_z}{\partial x} = -C\frac{\partial V_y}{\partial t}, \quad \frac{\partial V_x}{\partial y} + \frac{\partial V_y}{\partial x} = -2L\frac{\partial I_z}{\partial t} \tag{2.89}$$

Differentiating the above equations in pairs with respect to x and t or y and t, and combining them together gives the required isomorphism to Equation (2.88):

$$\frac{\partial^2}{\partial x^2}\left(\frac{I_z}{\Delta l}\right) + \frac{\partial^2}{\partial y^2}\left(\frac{I_z}{\Delta l}\right) = (2L)\,C\frac{\partial^2}{\partial t^2}\left(\frac{I_z}{\Delta l}\right) \tag{2.90}$$

Comparing Equation (2.90) with wave Equation (2.88) the following equivalences are determined:

$$I_z \equiv H_z, \quad V_x \equiv E_x \quad V_y \equiv E_y \quad \varepsilon \equiv C \quad \mu \equiv 2L \tag{2.91}$$

Thus, the series node models a medium of parameters $(2\mu, \varepsilon)$.

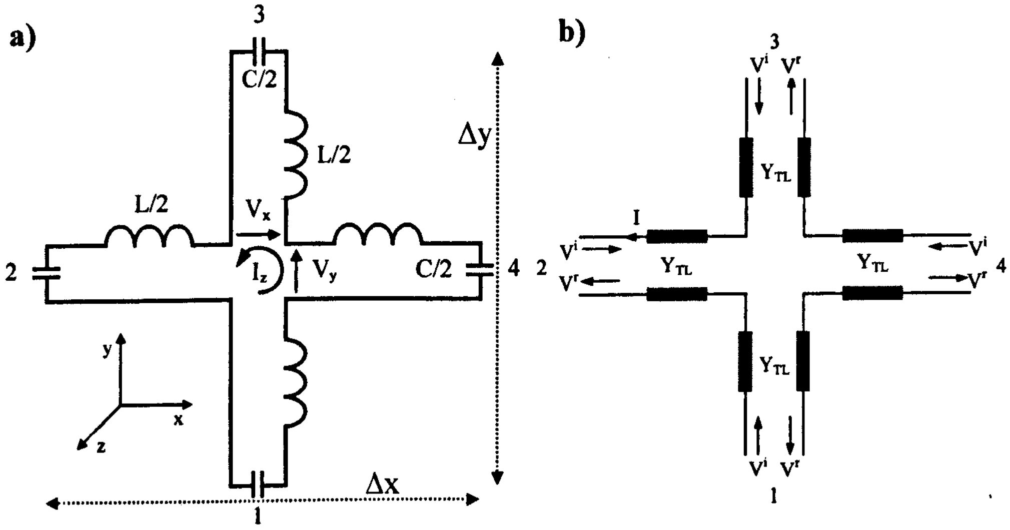

Figure 2.5. TLM series node (a) and its transmission line equivalent (b)

Computations in a series node are performed by employing the transmission line equivalent shown in Figure 2.5(b) and using similar scattering and connection paradigm as for a shunt node with the only difference lying in the scattering matrix representation, which now is:

$$\underline{\underline{S}} = 0.5 \cdot \begin{bmatrix} 1 & 1 & 1 & -1 \\ 1 & 1 & -1 & 1 \\ 1 & -1 & 1 & 1 \\ -1 & 1 & 1 & 1 \end{bmatrix}$$

The explicit algorithm has been formulated for both shunt and series node that calculates the EM field at each point of the mesh at an incremental time step Δt starting from time t_0 at which all the initial conditions are set. The boundary conditions at the edges of the computational window are implemented in the connection phase at the appropriate port(s) for the boundary points. Typical examples of boundaries are illustrated in the next sub-section.

2.6.1.3. Boundary Conditions

Due to finite computational resources the extent of the computational domain is restricted in simulations by introducing numerical or physical boundaries. Furthermore, either symmetry or material boundaries need to be accounted for. Typical examples of boundary conditions are presented in Figure 2.6; so called short circuit (s/c), open circuit (o/c) and matched boundary condition.

It is noticeable that the boundaries are modelled by introducing the impulse reflection coefficient Γ in the TLM network. For s/c $\Gamma = -1$ and the o/c boundary sets $\Gamma = 1$. Such boundaries are perfect reflecting walls of either zero or infinite impedance. For the matched boundary condition of Figure 2.6(c), which is used to model open boundaries at the interface with an infinite region or free space, the reflection coefficient is defined as $\Gamma = (Y_{TL} - Y)/(Y_{TL} + Y)$. Matching the admittance Y to the one of simulated media allows the outward propagating radiation to be absorbed and hence truncate the problem in space. This creates an illusion of an infinite space for unbounded field simulations, which otherwise would require an unlimited data storage.

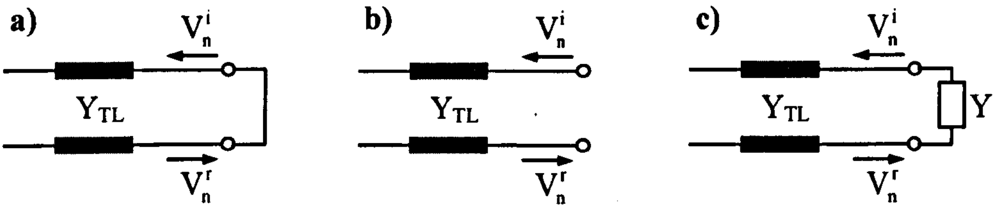

$${}_{k+1}V_n^i = -{}_kV_n^r \qquad {}_{k+1}V_n^i = {}_kV_n^r \qquad {}_{k+1}V_n^i = \frac{(Y_{TL}^n - Y)}{(Y_{TL}^n + Y)}\,{}_kV_n^r$$

Figure 2.6. Boundary conditions: short-circuit (a), open-circuit (b) and matched (c)

It should be pointed out that for 2D TLM the discretisation error called dispersion, which is manifested by phase velocity error for high frequencies, requires the cell size to be set approximately one-tenth of the smallest simulated wavelength [2.8], for either of the node configurations illustrated above. It is also noteworthy that shunt and series representations are perfectly dual. According to the Babinet's principle, one case can be transformed into the other by simply replacing voltages V with currents I, ε with μ, and admittances Y with impedances Z, [2.10]. This implies that both TM and TE case can be modelled with only one of the node type shown above. However, as will be shown later, both shunt and series nodes are applied in this work.

2.6.2. Time Step Criteria and Stability

In this section the time step requirements and the stability of the 2D TLM model will be briefly discussed. Consider a medium of (ε, μ) modelled by a shunt node presented in Figure 2.7(a). If the time step of the calculation is chosen to be Δt, the propagation time on each line presented in Figure 2.7(c) is $\Delta t/2$. It is now intended to identify transmission line parameters for such a node.

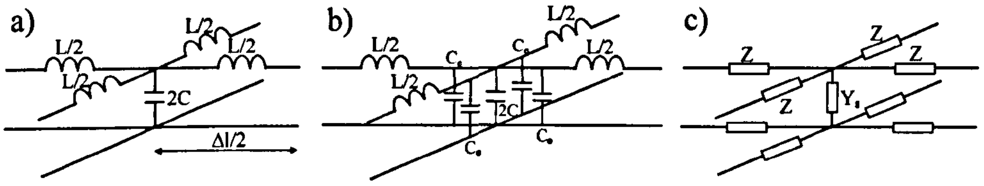

Figure 2.7. Shunt node and its transmission line implementation

The values of inductor and capacitor as discussed previously are $L = Z\Delta t = \mu\Delta l$ and $C = \Delta t/Z = \varepsilon\Delta l/2$ respectively. The link line impedance of the equivalent transmission line presented in Figure 2.7(c) is now chosen to be $Z = \mu\Delta l/\Delta t$. Each of the link inductor models is associated with a capacitance C_e given in Equation (2.74). Hence, the effective capacitance to be modelled is now $C_{eff} = 2C - 4C_e = 2C - 4(\Delta t/2)^2/L/2$. Therefore, the required value of stub admittance Y_s is : $Y_s = \frac{C_{eff}}{\Delta t} = \left(\varepsilon\Delta l - \frac{2\Delta t^2}{\mu\Delta l}\right)/\Delta t$.

It is well known that the TLM model is stable provided that all components of transmission lines have non-negative values [2.8], thus $Y_s \geq 0$. This places a constraint on the time step that has to be selected according to formula: $\Delta t \leq \frac{\varepsilon\mu\,\Delta l}{\sqrt{2}}$. For empty space this equals $\Delta t \leq \frac{\varepsilon_0\mu_0\,\Delta}{\sqrt{2}} \leq \frac{\Delta l}{\sqrt{2}c}$ and the transmission line velocity $u = \frac{\Delta l}{\Delta t} \leq \sqrt{2}c$ where c is speed of light.

The last statement indicates that the wave on the transmission line cannot travel faster than the speed of light. It is also pointed out that in the TLM simulation it is required to keep the time step constant for the whole network, therefore, the only parameter that can be manipulated is the impedance of the line. Thus, by identifying the required capacitance and inductance the transmission line model can be designed and implemented using appropriate link and stub values

2.6.3. 3D TLM

Most of the problems encountered in engineering applications are three dimensional and cannot be meaningfully simplified to two-dimensional systems, therefore 3D, full-vector models are of great demand. It is intuitive that whereas shunt and series nodes model TM and TE modes, each consist of three field components, the combination of these two variations should give a full description, six vectors of the field, i.e. three magnetic and three electric field elements. The appropriate topology of a 3D unit cell called Symmetrical Condensed Node (SCN) is shown in Figure 2.8.

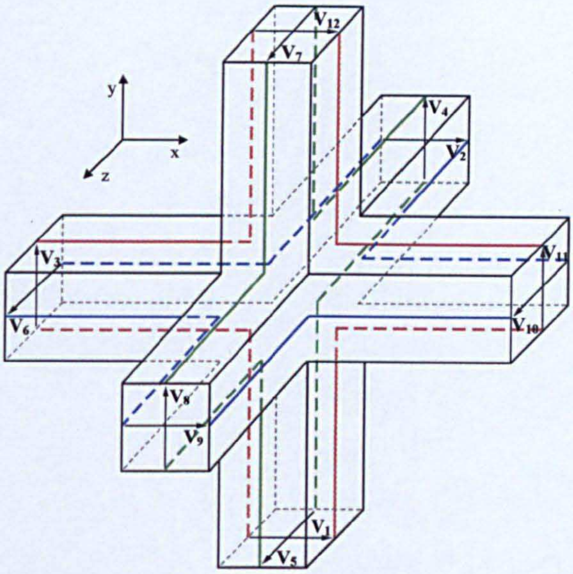

Figure 2.8. Three-dimensional Symmetrical Condensed Node (SCN)

The 3D node consists of 12 ports representing 2 polarisations in each coordinate direction. The voltages corresponding to those two configurations are carried on transmission line pairs highlighted in Figure 2.8 by the lines of different colours. Following the same approach as for the 2D nodes the equivalence between fields and circuit parameters is established in the form [2.8]:

$$\begin{aligned} E_x &\equiv V_x, \qquad & H_x &\equiv I_x \\ E_y &\equiv V_y, \qquad & H_y &\equiv I_y \\ E_z &\equiv V_z, \qquad & H_z &\equiv I_z \end{aligned} \tag{2.92}$$

Computations in 3D case follow similarly to the procedure obtained for a mesh of transmission lines in 2D. The calculation starts by imposing initial conditions and excitation. The pulses propagate along transmission lines and are scattered according to the transmission line theory. For empty space simulation the scattering matrix is derived as [2.8]:

$$\underline{\underline{S}} = 0.5\begin{bmatrix} 0 & 1 & 1 & 0 & 0 & 0 & 0 & 0 & 1 & 0 & -1 & 0 \\ 1 & 0 & 0 & 0 & 0 & 1 & 0 & 0 & 0 & -1 & 0 & 1 \\ 1 & 0 & 0 & 1 & 0 & 0 & 0 & 1 & 0 & 0 & 0 & -1 \\ 0 & 0 & 1 & 0 & 1 & 0 & -1 & 0 & 0 & 0 & 1 & 0 \\ 0 & 0 & 0 & 1 & 0 & 1 & 0 & -1 & 0 & 1 & 0 & 0 \\ 0 & 1 & 0 & 0 & 1 & 0 & 1 & 0 & -1 & 0 & 0 & 0 \\ 0 & 0 & 0 & -1 & 0 & 1 & 0 & 1 & 0 & 1 & 0 & 0 \\ 0 & 0 & 1 & 0 & -1 & 0 & 1 & 0 & 0 & 0 & 1 & 0 \\ 1 & 0 & 0 & 0 & 0 & -1 & 0 & 0 & 0 & 1 & 0 & 1 \\ 0 & -1 & 0 & 0 & 1 & 0 & 1 & 0 & 1 & 0 & 0 & 0 \\ -1 & 0 & 0 & 1 & 0 & 0 & 0 & 1 & 0 & 0 & 0 & 1 \\ 0 & 1 & -1 & 0 & 0 & 0 & 0 & 0 & 1 & 0 & 1 & 0 \end{bmatrix}$$

The scattering matrix refers to the Figure 2.8 where the port voltages are numbered from 1 to 12. The connection algorithm for the empty space simulation is similar to the 2D approach and is expressed by simple exchanging of voltages between neighbouring nodes.

2.7. Closing Remarks

In this chapter the principles of electromagnetic field theory have been presented. The main focus has been placed on cylindrical waves scattered from the circular-shaped cylinders as this problem is widely studied in this thesis for different practical configurations. Therefore, the wave equation was derived from Maxwell's equations and its solution was discussed from the modal point of view. The necessary background theory of the Transmission Line Modelling (TLM) method was also given. Two nodal configurations, namely the shunt and series nodes were shown as these are frequently used throughout this project. The basic unit of a 3D network, the so called Symmetrical Condensed Node was also demonstrated. Finally, the concept of link and stub components is described as these elements form fundamental building blocks of TLM networks.

2.8. References

[2.1] Collin, R.E., *"Field Theory of Guided Waves"*, IEEE Press, second edition, New York, 1991

[2.2] Balanis, C. A., *"Advanced Engineering Electromagnetics"*, John Wiley and Sons, New York, 1989

[2.3] Ramo, S., Whinnery, J.R., Van Duzer, T., *"Fields and Waves in Communication Electronics"*, John Wiley & Sons, Inc, third edition, New York, 1994

[2.4] Morse, P.M., Feshbach, H., *"Methods of Theoretical Physics"*, Part 1, McGraw-Hill Book Company, Inc, New York, 1953

[2.5] Taflove, A. Hagness, S.S, , *"Computational Electrodynamics: The Finite Difference Time-Domain Method"*, second edition, Norwell, MA: Artech House, 2000,

[2.6] Russer, P., *"The Transmission Line Matrix Method"*, Part IV in "*Applied Computational Electromagnetics State of the Art and Future Trends*", edited by Uzunoglu, N.K., Nikita, K.S., Kaklamani, D.I., Nato ASI Series F: Computer and Systems Sciences, Vol. 171, Springer, 2000

[2.7] Smith, G.D., *"Numerical solution of Partial Differential Equations – Finite Difference Methods*", Clarendon Press, Oxford, 1985

[2.8] Christopoulos, C., "*The Transmission-Line Modeling Method: TLM"*, Piscataway, New Jersey: IEEE Press, 1995

[2.9] Hoefer, W.J.R., So, P.P.M., "*The Electromagnetic Wave Simulator*", John Wiley & Sons, Chichester, 1991

[2.10] Paul, J., Christopoulos, C., Thomas, D.W.P., "*Generalized material models in TLM – part I: materials with frequency-dependent properties*", IEEE Trans. Antennas and Propagation, Vol. 47, No. 10, pp. 1528-1534, 1999

[2.11] Paul, J., Christopoulos, C., Thomas, D.W.P., "*Generalized material models in TLM – part II: materials with anisotropic properties*", IEEE Trans. Antennas and Propagation, Vol. 47, No. 10, pp. 1535-1542, 1999

[2.12] Paul, J., Christopoulos, C., Thomas, D.W.P., "*Generalized material models in TLM – part III: materials with nonlinear properties*", IEEE Trans. Antennas and Propagation, Vol. 50, No. 7, pp. 997-1004, 2002

[2.13] Lindenmeier, S., Pierantoni, L., Russer, P., "*Hybrid space discretizing integral equation methods for numerical modeling of transient interference*", IEEE Trans. Electromag. Compat., Vol. 41, pp 425-430, 1999

Chapter 3

A General Approach to Embedding Sub-Wavelength Objects into TLM

In this chapter the approach used in this thesis that enables arbitrarily shaped sub-wavelength structures to be embedded into a single 3D TLM cell will be presented. A *special node* will be derived that encloses fine objects and mimics the behaviour of such features under the exposure to electromagnetic fields. Solutions for electromagnetic fields in the presence of the small objects under consideration will be given in the first part of this chapter, followed by a description of the process of linking these solutions with the adjacent cells of a time-domain numerical network. A scattering algorithm for the special node developed will be presented at the final stage of this section.

3.1. General Concepts

The philosophy of the approach is to identify a suitable set of local frequency domain solutions to Maxwell's equations within the vicinity of the enclosed object and, by sampling the fields on the boundary of the TLM cell, to interface these with the numerical algorithm. The idea, whilst straightforward in principle, must yield an overall algorithm that is computationally stable and, as will be shown below, this requires that the local field solutions must be sampled in a physically consistent manner. It is underlined that identifying the required local field solutions is a pre-processing activity of the proposed scheme and furthermore there is no requirement placed upon how these are obtained, only on how they are interfaced with the rest of the numerical algorithm. As will be demonstrated further in this thesis, in some cases it is possible to obtain a suitable set of local solutions by completely analytic means. However, it is equally permissible to use purely numerical or experimental techniques to obtain the required set for those structures where an analytical solution is hard to formulate or is unavailable. This important observation emphasizes the flexibility of this work and the generic nature of the special node with fine features embedded to be described.

3.2. Theoretical Formulations

Consider a small object bounded by a cuboidal surface, a 3D TLM cell, as shown in Figure 3.1. To clarify the terminology used in this work, a volume of empty space in the presence of EM fields is referred to as a *cell* and an equivalent electrical circuit model used in the TLM method to mimic the behaviour of the fields in that cell as a *node*. It is intended to map the tangential electric and magnetic field on each face of the cube to a voltage and current in an equivalent electrical network. As all passive electrical networks are reciprocal this places a constraint upon the relationship between the fields and the network quantities. However as the cubical surface, which contains a scattering object, completely encloses the volume of space, the tangential fields on the faces of the cube also satisfy a well known reciprocity relationship, a fact that underpins the viability of finding a suitable mapping from fields to voltages and currents. In practice, this mapping must involve discretely sampling the continuous fields and if this is not performed correctly, the reciprocity exhibited by the fields will not carry over to the electrical network as required. For instance, simply directly sampling the tangential electric and magnetic fields at the centre of each face, numbered from 1 to 6 in Figure 3.1, does not, in general, maintain reciprocity.

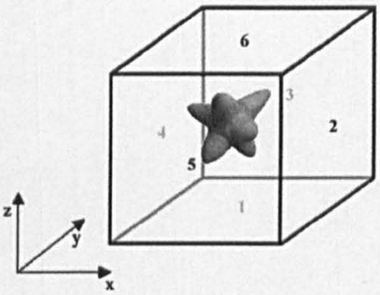

Figure 3.1. An example of a fine feature enclosed by a 3D TLM cell

The fields inside the cube are represented as a superposition of local vector field solutions, $\mathbf{e}_n$ and $\mathbf{h}_n$ weighted by expansion coefficients X_n. Each local solution is required to satisfy the boundary conditions on the enclosed object.

$$\mathbf{E} = \sum_n \mathbf{e}_n X_n = \underline{\mathbf{e}}^T \underline{X} \quad \text{and} \quad \mathbf{H} = \sum_n \mathbf{h}_n X_n = \underline{\mathbf{h}}^T \underline{X} \tag{3.1}$$

Here and throughout, (double) underlined quantities denote (matrices) column vectors and full field vectors are denoted in bold.

It will be shown that it is possible to identify such a representation that is complete with respect to the tangential fields on the surfaces of the cubic cell.

A set of ports is defined as spatially non-overlapping regions of the surface enclosing the volume of the computational cell, in this case the faces of the cube. Each port corresponds to a surface denoted by S_p where $p = 1,2,...,6$. Port voltages can be now defined so that the tangential electric field on S_p is represented in the form:

$$\mathbf{E}_{tp} = \sum_m \mathbf{f}_{pm} V_{pm} \tag{3.2}$$

where the port voltages are expressed by

$$V_{pm} = \iint_{S_p} \mathbf{f}^*_{pm} \cdot \mathbf{E}_t dS \tag{3.3}$$

and $\mathbf{f}_p$ is a set of orthonormal vector basis functions defined for port *p*. In addition the normalisation of $\iint_{S_p} \mathbf{f}^*_{pm} \cdot \mathbf{f}_{pn} dS = \delta_{mn}$ has also been assumed; where subscripts n, m denote a pair of basis functions.

Often in practice only two terms of $\underline{\mathbf{f}}_p$ will be used in Equation (3.2), each representing one of the orthogonal polarisations of the tangential electric field on each face as is the case for the conventional TLM node. This is consistent with the TLM cell being small compared to the smallest wavelength available in simulation (although modification may be needed if enclosed object is close to the face). For instance, when considering the Cartesian coordinate system and the surface $p = 1$ of the cubical cell illustrated in Figure 3.1, two basis functions can be chosen $f_{11} = \hat{x}$ and $f_{12} = \hat{y}$. It is noted that choosing these two terms to be the two unit vectors in the plane of the face allows straightforward interfacing with adjacent conventional TLM nodes. Nevertheless, more complex basis functions could be used to allow higher order schemes to be derived, if desired or if deemed necessary, to correctly capture the physical processes involved. For example, when considering an object that passes through the surface S_p it might be necessary to increase the number of basis functions to remain consistent with the boundary conditions existing at that face. This scenario will be discussed later in this thesis based on the example of tilted wire passing through the cell. Further detailed consideration of these cases is omitted at this stage, as the emphasis of this chapter is the development of the overall framework of the model.

Substituting Equation (3.1), the electric field formulation, into Equation (3.3) leads to a definition of a general voltage vector defined as:

$$\underline{V} = \iint_S \underline{\mathbf{f}} \cdot \underline{\mathbf{e}}^T dS\,\underline{X} = \underline{\underline{u}}\,\underline{X} \tag{3.4}$$

The vector of expansion coefficients $\underline{X}$ in Equation (3.1) can be now determined from the port voltages as:

$$\underline{X} = \underline{\underline{u}}^{-1}\underline{V} = \underline{\underline{w}}\,\underline{V} \tag{3.5}$$

and hence the general tangential field solutions will be expressed in the form:

$$\mathbf{E} = \underline{\mathbf{e}}^T \underline{\underline{w}}\,\underline{V} \quad \text{and} \quad \mathbf{H} = \underline{\mathbf{h}}^T \underline{\underline{w}}\,\underline{V} \tag{3.6}$$

It should be pointed out that Equation (3.5) indicates that matrix $\underline{\underline{u}}$ must be non-singular and invertible-square, which in effect requires that the number of basis fields in Equation (3.1) is the same as the number of port voltages. It will be shown later in this thesis that this is not necessarily the case and consequently matrix $\underline{\underline{w}}$ should be interpreted as the general inverse of $\underline{\underline{u}}$, as discussed in [3.1].

Having defined the relationship between the tangential electric fields and the port voltages, port currents are now defined in a similar manner, i.e.

$$\mathbf{H}_{tm} \times \hat{\mathbf{S}}_p = \sum_m \mathbf{f}_{pm} I_{pm} \tag{3.7}$$

where $\hat{S}_p$ is the unit vector normal to the surface S_p.

Thus

$$\iint_{S_p} \mathbf{E}^* \times \mathbf{H} \cdot d\mathbf{S} = \int_{S_p} dS \sum_n \mathbf{f}^*_{pn} V^*_{pn} \cdot \sum_m \mathbf{f}_{pm} I_{pm} = \sum_m V^*_{pm} I_{pm} \tag{3.8}$$

When mapping the fields to passive network quantities the power must be conserved, i.e.

$$\iint_{S_p} \mathbf{E}^* \times \mathbf{H} \cdot d\mathbf{S} = \underline{V}^H \underline{I} \tag{3.9}$$

where the superscript H denotes Hermitian, i.e. conjugate transpose. Combining Equations (3.6) and (3.9) the following can be derived:

$$\underline{V}^H \underline{\underline{w}}^H \left[\iint_S \underline{e}^* \times \underline{h}^T \cdot dS \right] \underline{\underline{w}}\,\underline{V} = \underline{V}^H \underline{I} \tag{3.10}$$

This condition leads to a reciprocal admittance relationship between the discrete sets of port currents and voltages which completely characterise the response of the special node:

$$\underline{I} = \underline{\underline{w}}^H \left[\iint_S \underline{e}^* \times \underline{h}^T \cdot dS \right] \underline{\underline{w}}\,\underline{V} \tag{3.11}$$

or in a general form:

$$\underline{I} = \underline{\underline{Y}}\,\underline{V} \tag{3.12}$$

It should be clear that the reciprocity relationship satisfied by the local field solutions e_n and h_n, which are used to represent the total electric and magnetic fields, i.e.

$$-j\iint_S \underline{e}_p^* \times \underline{h}_q^T \cdot dS = \left(-j\iint_S \underline{e}_q^* \times \underline{h}_p^T \cdot dS\right)^* \qquad (3.13)$$

is embedded within Equation (3.11) in such a manner so as to ensure a corresponding reciprocal relationship between the port voltages and port currents. Equation (3.11) also holds a recipe to proceed from physical fields into an equivalent transmission line network.

An alternative approach working from the magnetic field solutions leads to the derivation of an impedance matrix in a similar fashion.

As mentioned previously, in the cases where local analytical solutions are not available for the local field solutions, e_n and h_n, these can be obtained by a pre-processing numerical simulation on a fine mesh, or any other method such as Method of Moments (MoM) [3.1], and the integrations in Equations (3.4) and (3.9) are performed numerically. Having obtained the admittance relationship presented in Equation (3.11), the implementation into a real time-domain numerical network will now be addressed.

3.3. Implementation into a TLM Scheme

In many engineering problems the solutions to Maxwell's equation (e_n and h_n) are available via the frequency domain, especially when analytical description is considered. Therefore, attention will now be focused upon the implementation of these frequency-domain tangential field solutions into a time-domain numerical technique such as TLM. In order to do so the equivalent circuit elements will be now extracted from Equation (3.11) and the corresponding network topology designed.

The TLM algorithm is derived by making an analogy between the behaviour of the electric and magnetic fields in a small region of space and the voltages and currents in an equivalent electrical network. Once the mapping between field and network quantities has been identified, the individual networks representing the different regions of space are interconnected, recognizing that continuity of the fields is ensured by enforcing the appropriate continuity of voltages and currents between adjacent nodes. A simulation then proceeds by simply solving the overall electrical network problem by any suitable means. As described in Chapter 2 in the case of a TLM method the simulations are performed in an explicit manner by scattering and propagating voltage impulses along short lengths of commensurate transmission lines. One particular attraction of developing TLM algorithms is that stability and energy conservation can be easily assured by inspection; if the equivalent electrical network only contains inductive and capacitive elements with positive component values, then the scheme will conserve and be stable, [3.3].

It is emphasised that for acceptable accuracy the size of the cubes corresponding to each TLM node are small, typically one tenth of the smallest wavelength of interest. Consequently, each element of the admittance matrix, $\underline{\underline{Y}}$, in Equation

(3.12) is approximated to a second order accuracy by a sum of two terms, one proportional to frequency, and the other inversely proportional to frequency. It is therefore simple to identify the corresponding series of inductor-capacitor combinations required in the equivalent circuit. However, in this work a slightly different approach will be presented that is believed to be more flexible and efficient for practical implementation.

Decomposing the admittance matrix $\underline{\underline{Y}}$ from Equation (3.12) into its eigensolutions defined by:

$$\underline{\underline{Y}}\,\underline{T}_{\gamma} = \gamma\,\underline{T}_{\gamma} \tag{3.14}$$

the admittance relationship can be re-expressed as follows:

$$\underline{I} = \underline{\underline{T}}\,\underline{\underline{\gamma}}\,\underline{\underline{T}}^{H}\,\underline{V} \tag{3.15}$$

where $\underline{\underline{T}}$ is a matrix whose columns consist of the eigenvectors of $\underline{\underline{Y}}$ and $\underline{\underline{\gamma}}$ is a diagonal matrix of elements containing its eigenvalues.

Given that $\underline{\underline{T}}^{H}\underline{\underline{T}}$ is the identity matrix, the above equation can be equivalently written in the following manner:

$$\underline{\underline{T}}^{H}\,\underline{I} = \underline{\underline{\gamma}}\,\underline{\underline{T}}^{H}\,\underline{V} \tag{3.16}$$

Physically the eigensolutions of $\underline{\underline{Y}}, \gamma$, correspond to the field solutions where electric and magnetic field samples are proportional to each other and the eigenvalues are proportional to the input admittance at the particular frequency. Those eigensolutions can be considered as modal solutions of Maxwell's equations.

It is noted that $\underline{\underline{Y}}$ is reciprocal and its eigenvalues , γ, are all purely imaginary which physically means that the system is lossless. Furthermore, for the range of frequencies over which TLM is regarded as acceptably accurate, the eigenvectors are almost purely real and frequency independent, with the corresponding eigenvalue either proportional or inversely proportional to the frequency as has been pinpointed before, i.e.

$$\underline{V}_n = j\omega L_n \underline{I}_n, \quad \text{or} \quad \underline{I}_n = j\omega C_n \underline{V}_n \tag{3.17}$$

In this regime the electrical network presented in Figure 3.2 can be constructed to embody Equation (3.11) in which the N-port transformer is defined so that:

$$\underline{x} = \underline{\underline{T}}^H \underline{V} \quad \text{and} \quad \underline{V} = \underline{\underline{T}}\,\underline{x} \tag{3.18}$$

N represents the number of ports i.e. 12 for three-dimensional and 4 for two-dimensional TLM and $\underline{x}$ is a vector of modal solutions with the element x_n being an amplitude of the selected n-th mode that the total field consists of.

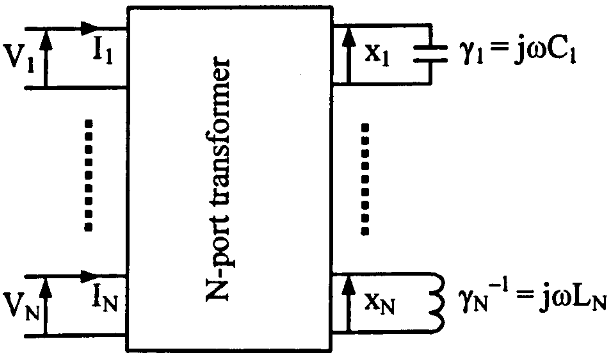

Figure 3.2. A general equivalent circuit for the TLM node in the frequency domain

The circuit of Figure 3.2 follows from the derivation of Equation (3.16) and has been identified in the frequency domain. An explicit time domain model is recovered if the lumped capacitors and inductors are implemented using short commensurate lengths of open or short-circuit transmission lines and this is illustrated in the next section.

3.3.1. A Modal View of TLM

In order to recover the time domain algorithm, closer focus has to be placed upon what happens when the pulse from neighbouring nodes is incident upon the special node under consideration. As is known, TLM represents fields as voltages travelling along transmission lines. On all transmission lines, the relationship between the total voltage and current and the travelling wave amplitudes is given by

$$V_p(t) = V_p^i(t) + V_p^r(t) \quad \text{and} \quad I_p(t) = y_L\left(V_p^i(t) - V_p^r(t)\right) \tag{3.19}$$

as shown in Figure 3.3 where superscripts i and r denote incident and reflected voltages respectively and y_L is the characteristic impedance of the transmission line.

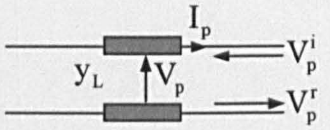

Figure 3.3. Total voltage and current on the transmission line

Combining Equation (3.19) with the general admittance relationship given by Equation (3.12) and rearranging gives:

$$(y_L\underline{\underline{I}} + \underline{\underline{Y}})\underline{V}^r = (y_L\underline{\underline{I}} - \underline{\underline{Y}})\underline{V}^i \tag{3.20}$$

where $\underline{\underline{I}}$ is the identity matrix.

Using the definition of the N-port transformer from Equation (3.18) in Equation (3.20) leads to a scattering relationship for the modal amplitudes travelling on each individual line of Figure 3.2:

$$x_n^r = \frac{y_L - \gamma_n}{y_L + \gamma_n} x_n^i \tag{3.21}$$

when *n* denotes the n^{th} line and $n = 1,\ldots,N$

It can be easily shown that the modal scattering, Equation (3.21), can be approximated to second order accuracy as a time delay on the individual transmission lines:

$$x_n^r = \pm e^{-j\sigma_n} x_n^i \tag{3.22}$$

The sign depends on the termination; (+) for open and (–) for short-circuit. By comparison of Equations (3.21) and (3.22) it can be also demonstrated that $\sigma_n = -j\frac{2\gamma_n}{y_L}$ for an open and $\sigma_n = -j\frac{2y_L}{\gamma_n}$ for a short-circuit termination.

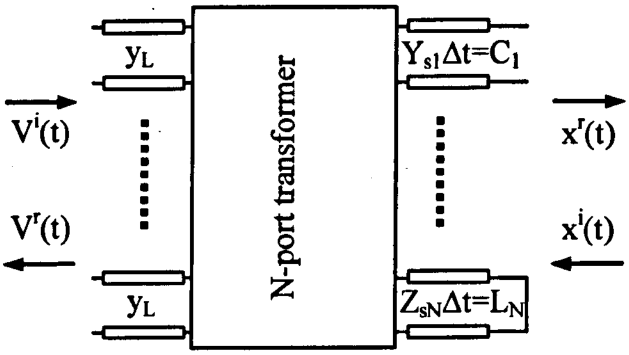

Figure 3.4. A transmission line implementation of a general equivalent circuit model for the special node

Hence, an explicit time-domain model of the circuit presented in Figure 3.2 can be obtained when the lumped components, capacitors and inductors are implemented using short-circuited or open-circuited stubs respectively, as shown in Figure 3.4. The eigenvalues of $\underline{\underline{Y}}$, γ_n, correspond to the input admittance looking into a short-circuited or open-circuited stub, as shown in Figure 3.5(a) and (b) respectively.

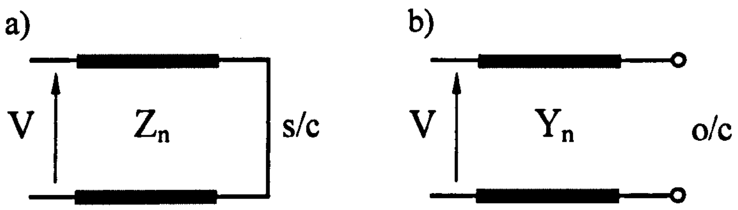

Figure 3.5. A Short-circuited (a) and an open-circuited termination (b)

Thus, using transmission line properties presented in Chapter 2, the input impedance looking into the stub can be calculated as [3.1]:

$$\gamma_n^{-1} = jZ_n \tan(\omega\Delta t/2) \quad \text{and} \quad \gamma_n = jY_n \tan(\omega\Delta t/2) \tag{3.23}$$

for a short-circuit and open-circuit termination respectively. The appropriate values of circuit components can be then found as $L_n = Z_n\Delta t$ for a short-circuited and $C_n = Y_n\Delta t$ for open-circuited stub, where Δt is a round trip transit time of the pulses propagating along each of the transmission line. Such stubs are well established within the TLM algorithm and were already discussed in Chapter 2. For more detailed information the reader is referred to [3.1].

For a better understanding of the general implementation shown in Figure 3.4 an additional diagram is presented in Figure 3.6. An example of a two-dimensional

TLM network with the special node embedded is illustrated showing the manner in which the link-lines from neighbouring nodes are connected to the modal transformer.

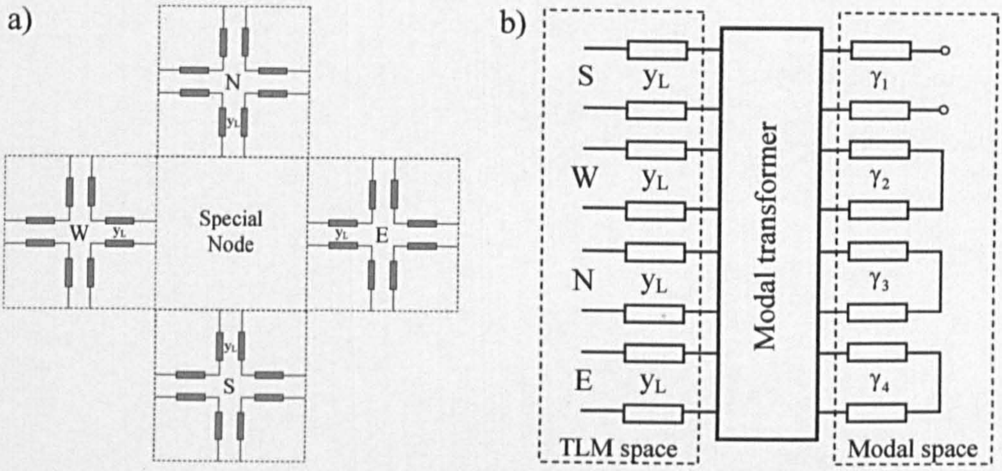

Figure 3.6. 2D TLM network with a special node (SN) (a) and the connection to the neighbouring nodes (b)

The model presented in Figure 3.4 is a general nodal network for the TLM method and the inclusion of different objects simply changes the values of the passive components. These values are defined by the solutions of Equation (3.11), the set of local field solutions $\underline{\mathbf{e}}$, $\underline{\mathbf{h}}$ being either analytically or numerically determined by any means. Examples of calculations for $\underline{\mathbf{e}}$ and $\underline{\mathbf{h}}$ using both approaches will be presented further in this thesis.

In practice, the TLM technique presented here is implemented in the time domain as an explicit algorithm using the scatter-connect paradigm of the conventional SCN node [3.4]. The overall scattering process in the special node can be summarised as:

- transform the real space port voltages into modal space amplitudes using the transformer matrix $\underline{\underline{T}}^H$
- scatter each mode individually
- convert modal reflected amplitudes back to port voltages using matrix $\underline{\underline{T}}$

The scattering operation of the special node enclosing the small object(s) is then explicitly implemented as:

$$x_n^r(t) = \pm x_n^i(t-\Delta t) \tag{3.24}$$

where the + and – signs are used for the open and short-circuited stubs respectively. The action of the N-port transformer in the node is described by the following equations:

$$\begin{aligned} x_n(t) &= \frac{2y_L \sum_p T_{np} V_p^i(t) + 2Y_{sn} x_n^i(t)}{y_L + Y_{sn}}, \\ x_n^r(t) &= x_n(t) - x_n^i(t), \\ V_p^r(t) &= \sum_n T_{pn} x_n^i(t) - V_p^i(t) \end{aligned} \tag{3.25}$$

where Y_{sn} is the characteristic admittance of the n^{th} stub, n denoting an eigensolution.

Applying this scheme to the problem of fields scattered from objects positioned in air gives more flexibility as only the special nodes in the network contains stubs that in TLM algorithm contribute to the dispersion error [3.1]. As it will be demonstrated further in this thesis for some examples, especially for symmetrical structures placed centrally in the cell, it is possible to eliminate the N-port transformer and construct an equivalent circuit model for a special node without explicit conversion from real-space voltages to modal amplitudes.

3.4. Closing Remarks

In this chapter the basic theoretical framework has been presented to allow fine-features to be embedded into a single cell of a TLM method. A set of local field solutions to Maxwell's equations has been derived in a manner that provides a robust and stable algorithm. Linking these field solutions with a real time-domain network has also been illustrated. This approach allows features of different geometries to be arbitrarily located within a cell. The objects can be wholly enclosed by a single cell or pass across several cells. It accounts for multiple bodies of various characteristics to be modelled within a single cell provided that the tangential field solutions at the surfaces of the mesh cell can be identified. It is highlighted that the algorithm has been developed based upon implementation with the TLM method, however it can also be readily applied to other time-domain techniques.

3.5. References

[3.1] Press, W.H., Teukolsky, A.A., Vettering W.T. and Flannery P.B., *"Numerical recipes in C: The art of Scientific Computing"*, 2nd Edition, Cambridge University Press, 1992

[3.2] Itoh, T., "Numerical Techniques for Microwave and Millimeter-Wave Passive Structures", John Wiley & Sons, NY, 1989

[3.3] Christopoulos, C., *"The Transmission-Line Modeling Method: TLM"*, Piscataway, NJ: IEEE Press, 1995.

[3.4] Johns, P.B., *"A symmetrical condensed node for TLM method"*, IEEE Trans on Microwave Theory and Tech, Vol. 35, No. 4, pp. 370-377, 1987

Chapter 4

Embedding Conducting Wires into a Single Cell of 2D TLM model

In this chapter, the general methodology presented in the previous chapter will be applied to develop a special node, referred to in this work as a *multi-feature node*, that enables various scatterers to be embedded in a single cell of a two-dimensional TLM model. Particular focus will be placed upon the inclusion of conducting wires that play a vital role in the EMC simulations. In the pre-processing stage prior to a TLM run, the total electromagnetic fields around wires will be evaluated theoretically, in terms of local field solutions expressed as a series of cylindrical harmonics. As will be shown, the infinite number of harmonics (modes) must be truncated and discretised in a consistent manner to provide a suitable set of solutions that can be linked with the adjacent nodes of a time-domain numerical mesh, as has already been discussed in Chapter 3. Finally, the flexibility of the algorithm, its robustness and the ease of its application to various practical configurations will be demonstrated. This will be based on an example of field scattering from conducting wires clustered in a single cell of 2D TLM. All results will be verified against the known analytical solutions for this problem.

4.1. Introduction

In this part of the thesis the general approach to embedding small objects into a 3D TLM cell will be applied to two-dimensional simulations of waves propagating in the presence of conducting wires. In order to derive the reciprocal admittance relationship between the electric and magnetic fields, or correspondingly the relationship between the port voltages and port currents in the equivalent circuit model for a special node, the local field solutions will be formulated analytically. The behaviour of such fields is expressed as infinite series of cylindrical harmonics, which are in turn represented by the Bessel functions of the first and second kind. However the infinite number of modes that contribute to the total field needs to be truncated in order to maintain consistency with the 2D numerical network; to form a reciprocal set of solutions applicable for a mapping process presented in Chapter 3. The results of our multi-feature node will be first validated for the case of a single wire placed at the centre of the cell against analytical solution and the previously reputed macro-node designed for this scenario [4.1]. Next, the ability of the approach to mimic the behaviour of a cluster of wires (enclosed within a single cell) and excited by an EM field, will be demonstrated and the results verified against the known solution. To begin with, the analytical solution for a cluster of metal wires will be formulated in the next paragraph.

4.2. Fields Around Wires – Analytical Formulations

The analytical formulations of field scattering from metal wires clustered in a close proximity will be derived in this section for two electromagnetic field polarisations, namely Transverse Electric (TE) with the electric field polarised perpendicular and Transverse Magnetic (TM) mode with the electric field polarised parallel to the axis of a cylinder. Therefore, consideration is now placed upon an arbitrary number of infinitely long z-directed wires in a close proximity so that they all lie within the scope of a single TLM cell as shown in Figure 4.1. In order to estimate the near field interactions between the wires and derive all the necessary formulations that govern the scattering phenomenon, it is convenient and most clear to focus upon the behaviour of only two wires and then to generalise the expressions obtained to the case of an arbitrary number of cylindrical wires clustered in a single TLM cell.

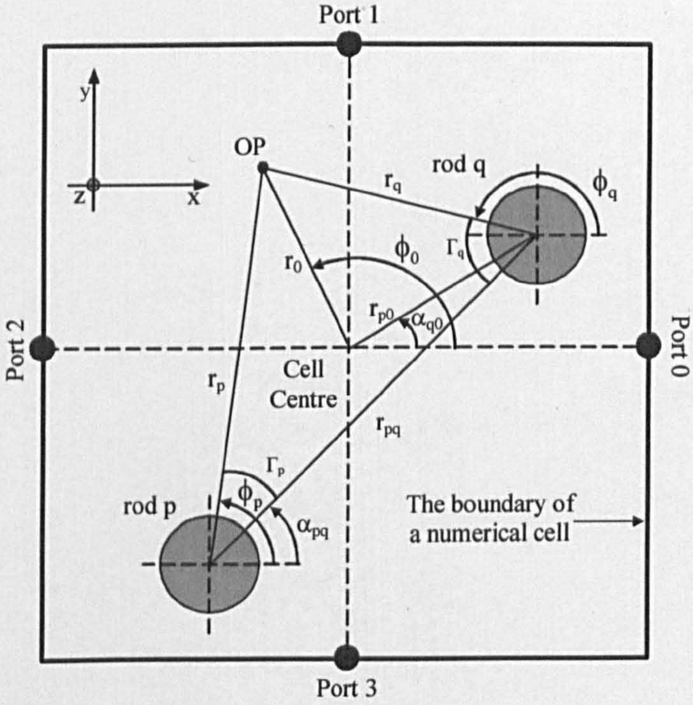

Figure 4.1. A representation of a TLM cell with wires enclosed within

Figure 4.1 shows the notation used to describe the pair of wires where the centre of the cell is the origin of a polar coordinate system (r_0, ϕ_0) and OP indicates an observation point at a distance r_0 from the cell centre. Similarly the wires' coordinate systems are denoted by radii and angles: (r_p,ϕ_p) and (r_q,ϕ_q) for wire *p* and wire *q* respectively. The distance between the wires is labelled $r_{pq}=r_{qp}$ and the angle of rotation between the *p* and *q* coordinate systems $\alpha_{pq}=\alpha_{qp}-\pi$.

As has already demonstrated in section 2.5 of Chapter 2, the total field in the presence of any scatterers can be expressed as follows:

$$F_t = F_i + F_s \tag{4.1}$$

where the subscripts *t, i* and *s* denote the total, incident and scattered fields respectively and F represents either the electric field in the case of TM $(E_z \neq 0 \text{ and } H_z = 0)$ polarisation being considered or the magnetic field for TE $(H_z \neq 0 \text{ and } E_z = 0)$ polarisation. In the case of cylindrical scatterers each of the two components of the total field are expressed in terms of Bessel and Hankel functions, as discussed in Chapter 2. The incident field (F_i) is expanded in terms of cylindrical harmonics centred on the cell coordinate system, whereas the scattered field (F_s) is obtained as a sum of fields reflected from each scatterer. Each element of the sum is calculated using a series of outgoing Hankel functions originating at the centre of each of the scatterers. In the next two sections, these contributors to the total field will be examined in more detail, starting with the scattered field formulations.

4.2.1. Total Field Formulae

Based on the approach outlined in section 2.5 of Chapter 2, the scattered electric and magnetic fields due to the presence of the q^{th} wire can be defined as a series of Hankel functions centred on the q^{th} wire in the form:

$$\begin{aligned} \text{TM:} \quad & E_{Zsq}(r,\phi) = \sum_{n=-\infty}^{\infty} e^{-jn\phi_q} H_n^{(2)}(kr_q) X_{qn} = \sum_{n=-\infty}^{\infty} f_{qn} X_{qn} = \underline{f}_q^T \underline{X}_q, \\ \text{TE:} \quad & H_{Zsq}(r,\phi) = \sum_{n=-\infty}^{\infty} e^{-jn\phi_q} H_n^{(2)}(kr_q) X_{qn} = \sum_{n=-\infty}^{\infty} f_{qn} X_{qn} = \underline{f}_q^T \underline{X}_q, \end{aligned} \tag{4.2}$$

where

$$f_{qn} = e^{-jn\phi_q} H_n^{(2)}(kr_q) \tag{4.3}$$

and $\underline{X}$ is a vector of the yet unknown scattering coefficients, k being the wavenumber of the medium under consideration, in this case empty space $k = k_0$. The total scattered field at wire *p* can be obtained as a sum of the fields reflected from each of the wires:

$$F_s = \underline{f}_p^T \underline{X}_p + \sum_{q \neq p} \underline{f}_q^T \underline{X}_q \tag{4.4}$$

The incident field F_i is given in terms of harmonics centred on the TLM node:

$$F_i = \underline{g}_0^T \underline{X}_0 \tag{4.5}$$

where

$$g_{pn} = e^{-jn\phi_p} J_n(kr_p) \tag{4.6}$$

and vector $\underline{X}_0$ contains a set of as yet unknown incident coefficients.

Thus, the total field in the presence of a number of wires can be calculated according to Equation (4.1) as:

$$F_t = \underline{g}_0^T \underline{X}_0 + \underline{f}_p^T \underline{X}_p + \sum_{q \neq p} \underline{f}_q^T \underline{X}_q \tag{4.7}$$

In order to calculate scattering coefficients $\underline{X}_p$ given incident wave coefficients $\underline{X}_0$, the physical boundary conditions at the surface of each wire needs to be imposed. However, it is observed that different coordinate systems have been utilised in the formulation of the total field which is inconvenient for this purpose. Therefore, Equation (4.7) must be re-expressed in the coordinate system of the particular cylindrical wire at which the boundary condition is to be imposed. Using the Bessel summation theorem presented in [4.2] and utilising the properties of the Bessel functions, Equation (B.1) in Appendix B, the components of the scattered field can be rearranged as follows:

$$\begin{aligned} e^{-jn\phi_q} H_n^{(2)}(kr_q) &= e^{-jn(\alpha_{qp}-\Gamma_q)} H_n^{(2)}(kr_q) = e^{-jn\alpha_{qp}} e^{jn\Gamma_q} H_n^{(2)}(kr_q) \\ &= e^{-jn\alpha_{qp}} \sum_{m=-\infty}^{\infty} J_m(kr_p) H_{m+n}(kr_{qp}) e^{jm\Gamma_p} \\ &= e^{-jn\alpha_{qp}} \sum_{m=-\infty}^{\infty} (-1)^m J_m(kr_p) H_{n-m}(kr_{qp}) e^{-jm\Gamma_p} \\ &= e^{-jn\alpha_{qp}} \sum_{m=-\infty}^{\infty} (-1)^m J_m(kr_p) H_{n-m}(kr_{qp}) e^{-jm(\phi_p-\alpha_{qp}+\pi)} \\ &= \sum_{m=-\infty}^{\infty} e^{-j(n-m)\alpha_{qp}} J_m(kr_p) H_{n-m}(kr_{qp}) e^{-jm\phi_p} \end{aligned} \tag{4.8}$$

where Γ_p, Γ_q are the angles between r_p, r_q and r_{pq} respectively shown in Figure 4.1. Hence, it is observed that the scattered field from one cylinder can be re-expressed in the coordinate system centred on another cylinder. Thus, in general, the components of the field scattered from wire are:

$$e^{-jn\phi_q} H_n^{(2)}(kr_q) = \sum_{m=-\infty}^{\infty} e^{-jm\phi_p} J_m(kr_p) \left[T_{qp}\right]_{nm} \tag{4.9}$$

where $\left[T_{qp}\right]_{nm}$ is the *n,m* element of a matrix $\underline{\underline{T}}_{qp}$, specifically

$$\left[T_{qp}\right]_{nm} = e^{-j(n-m)\alpha_{qp}} H_{n-m}(kr_{qp}) \tag{4.10}$$

Taking advantage of the definition presented in Equation (4.6), the following can be concluded.

$$f_{qn} = \underline{g}_p^T T_{qpn} \text{ and } \underline{f}_q^T = \underline{g}_p^T \underline{\underline{T}}_{qp} \tag{4.11}$$

Finally, the total scattered field is formulated entirely in the p^{th} wire's coordinate system as:

$$F_s = \underline{f}_p^T \underline{X}_p + \sum_{q \neq p} \underline{g}_p^T \underline{\underline{T}}_{qp} \underline{X}_q \tag{4.12}$$

Similarly, the incident field can be evaluated in the coordinate system centred on the p^{th} wire using a matrix $\underline{\underline{U}}$, derived in a similar manner to matrix $\underline{\underline{T}}$ in Equation (4.8).

$$e^{-jn\phi_q} J_n(kr_q) = \sum_{m=-\infty}^{\infty} e^{-jm\phi_p} J_m(kr_p) \left[U_{qp}\right]_{nm} \tag{4.13}$$

where $\left[U_{qp}\right]_{nm}$ is the *n,m* element of a matrix $\underline{\underline{U}}_{qp}$, i.e.

$$\left[U_{qp}\right]_{nm} = e^{-j(n-m)\alpha_{qp}} J_{n-m}(kr_{qp}) \tag{4.14}$$

Applying Equations (4.13) and (4.14) into (4.5) and identifying that $\underline{g}_q^T = \underline{g}_p^T \underline{\underline{U}}_{qp}$ yields:

$$F_i = \underline{g}_p^T \underline{\underline{U}}_{0p} \underline{X}_0 \tag{4.15}$$

The total field introduced initially in Equation (4.1) can now be expressed in p^{th} wire coordinate system only:

$$F_t = \underline{g}_p^T \underline{\underline{U}}_{0p} \underline{X}_0 + \underline{f}_p^T \underline{X}_p + \sum_{q \neq p} \underline{g}_p^T \underline{\underline{T}}_{qp} \underline{X}_q \tag{4.16}$$

It should be clear that this formula accounts for all the interactions that occur between the wires bounded by the TLM cell. Thus, it is now possible to apply the boundary condition at the surface of the p^{th} wire.

4.2.1.1. Boundary Conditions at the Surface of Wires

So far no physical requirements have been imposed on the surface of the cylindrical wires. Assuming that they are perfect conductors, the total electric field is wholly reflected from the surface of the wire, which means that the Dirichlet or Neumann boundary condition [4.3] for perfect electric (TM) or perfect magnetic (TE) scattering needs to be satisfied at the surface of the *p*th wire. Thus: .

$$\begin{aligned} \text{TM:}\quad & E_z(r,\phi)=0 \\ \text{TE:}\quad & E_\phi(r,\phi)=-\frac{1}{j\omega\varepsilon}\frac{\partial H_z}{\partial r}=0 \end{aligned} \tag{4.17}$$

Combining Equation (4.17) with (4.16) given that $r_p=a_p$, where a_p is the radius of the p^{th} wire leads to:

$$\begin{aligned} \text{TM:}\quad & \underline{g}_p^T\underline{\underline{U}}_{0p}\underline{X}_0+\underline{f}_p^T\underline{X}_p+\sum_{q\neq p}\underline{g}_p^T\underline{\underline{T}}_{qp}\underline{X}_q\bigg|_{r_p=a_p}=0 \\ \text{TE:}\quad & \frac{\partial}{\partial r}\left(\underline{g}_p^T\underline{\underline{U}}_{0p}\underline{X}_0+\underline{f}_p^T\underline{X}_p+\sum_{q\neq p}\underline{g}_p^T\underline{\underline{T}}_{qp}\underline{X}_q\right)\Bigg|_{r_p=a_p}=0 \end{aligned} \tag{4.18}$$

For convenience, Equation (4.18) can be reorganised into the form:

$$\underline{\underline{U}}_{0p}\underline{X}_0+\underline{\underline{A}}_p\underline{X}_p+\sum_{q\neq p}\underline{\underline{T}}_{qp}\underline{X}_q=0 \tag{4.19}$$

where the elements of the diagonal matrix $\underline{\underline{A}}_p$ are defined as follows:

$$A_{p\,n,n}=\begin{cases} H_n^{(2)}(ka_p)/J_n(ka_p) & \text{for TM mode} \\ \dfrac{\partial}{\partial r}H_n^{(2)}(kr_p)/\dfrac{\partial}{\partial r}J_n(kr_p)\bigg|_{r_p=a_p} & \text{for TE mode} \end{cases} \tag{4.20}$$

The boundary condition is consecutively applied at the surface of every single wire bounded by a TLM cell which results in a set of linear equations as detailed below, with the wires numbered from 1:

$$\begin{pmatrix} \underline{\underline{A}}_1 & \underline{\underline{T}}_{12} & \underline{\underline{T}}_{13} & .. \\ \underline{\underline{T}}_{21} & \underline{\underline{A}}_2 & \underline{\underline{T}}_{23} & .. \\ \underline{\underline{T}}_{31} & \underline{\underline{T}}_{32} & \underline{\underline{A}}_3 & .. \\ .. & .. & .. & .. \end{pmatrix} \begin{pmatrix} \underline{X}_1 \\ \underline{X}_2 \\ \underline{X}_3 \\ \cdots \end{pmatrix} = - \begin{pmatrix} \underline{\underline{U}}_{01} \underline{X}_0 \\ \underline{\underline{U}}_{02} \underline{X}_0 \\ \underline{\underline{U}}_{03} \underline{X}_0 \\ \cdots \end{pmatrix} = - \begin{pmatrix} \underline{\underline{U}}_{01} \\ \underline{\underline{U}}_{02} \\ \underline{\underline{U}}_{03} \\ \cdots \end{pmatrix} \underline{X}_0 \qquad (4.21)$$

or in general form:

$$\underline{\underline{M}}\,\underline{X} = -\underline{\underline{U}}_0\,\underline{X}_0 \qquad (4.22)$$

Vector $\underline{X}^T = \begin{bmatrix} \underline{X}_1 & \underline{X}_2 & \underline{X}_3 & \ldots \end{bmatrix}^T$ represents the scattered field coefficients.

In principle, Equation (4.21) can be solved for the scattered coefficients $\underline{X}$ given the excitation coefficients $\underline{X}_0$, which provides the reference results used to validate the accuracy of the multi-feature node. However, in order to implement the solution of Equation (4.21) into a TLM algorithm it is necessary for the incident and reflected waves to be expressed in terms of the coordinate system centred at the numerical cell and not at the centres of the wires, as Equation (4.21) indicates. Thus, it is necessary to seek a solution of the scattered field in the following form:

$$F_s = \sum_{n=-\infty}^{\infty} H_n^{(2)}(kr_0)\, e^{-jn\phi_0} X_{sn} = \underline{f}_0^T \underline{X}_s \qquad (4.23)$$

where $\underline{X}_s$ is a vector of coefficients for the scattered field expressed in the coordinates centred on the numerical cell.

4.3. Mapping the Analytical Solution into Numerical Network

In order to discretise the analytical solution and to carry out the procedure of linking it with a numerical network, the scattered coefficients $\underline{X}_s$ from Equation (4.23) have to be determined. Therefore the solution of Equation (4.21) needs to be transformed back from the coordinate systems of the individual scatterers to the cell-centred one. This is done by means of Green's functions. The process is illustrated below, the cases of TM and TE mode being considered separately.

4.3.1. Scattering Coefficients for a TM Polarisation

In the presence of a current along the wire J_z, the electric field E_z due to electric current source is given by [4.3]

$$E_z = -j\omega\mu \iiint\limits_{\text{source}} dx'dy'dz' G_{EJ}(x,y,z;x',y',z')J_z(x',y',z') \tag{4.24}$$

where μ is a permeability of the space modelled and ω is the angular frequency. Here, primed quantities denote source points, unprimed observation points unless stated otherwise.

In 2D the Green's function G_{EJ} is given by:

$$G_{EJ} = \begin{cases} \dfrac{j}{4}\sum\limits_{v=-\infty}^{\infty} J_v(kr_0)H_v^{(2)}(kr_0')\, e^{-jv(\phi_0-\phi_0')} & r_0 < r_0' \\ \dfrac{j}{4}\sum\limits_{v=-\infty}^{\infty} J_v(kr_0')H_v^{(2)}(kr_0)\, e^{-jv(\phi_0-\phi_0')} & r_0' < r_0 \end{cases} \tag{4.25}$$

The current on the surface of the perfect metal wire is $J_z = -H_\phi$, and from Maxwell's equations for TM polarised wave one obtains the relationship:

$$j\omega\mu H_\phi = -\frac{\partial E_z}{\partial r} \tag{4.26}$$

The electric field has already been derived in Equation (4.16) and is

$$E_z = \underline{g}_p^T \underline{\underline{U}}_{0p} \underline{X}_0 + \underline{f}_p^T \underline{X}_p + \sum_{q\neq p} \underline{g}_p^T \underline{\underline{T}}_{qp} \underline{X}_q \tag{4.27}$$

Updating the expression for the electric field from Equation (4.27) into (4.26) yields the formulation of the "total" wire currents:

$$J_z = -\frac{1}{j\omega\mu}\sum_p \delta(r'_p - a_p)\frac{\partial}{\partial r'_p}\left[\underline{g}'^T_p\underline{\underline{U}}_{0p}\underline{X}_0 + \underline{f}^T_p\underline{X}_p + \sum_{q\neq p}\underline{g}'^T_p\underline{\underline{T}}_{qp}\underline{X}_q\right]_{r'_p=a_p} \tag{4.28}$$

Therefore, the scattered field E_z is represented as:

$$\begin{aligned} E_z = &\iiint_{source} dx'dy'dz'\frac{j}{4}\sum_{v=-\infty}^{\infty} J_v(kr_0')H_v^{(2)}(kr_0)\, e^{-jv(\phi_0-\phi_0')}\,\cdot \\ &\cdot\sum_p \delta(r_p'-a_p)\frac{\partial}{\partial r'_p}\left[\underline{g}'^T_p\underline{\underline{U}}_{0p}\underline{X}_0 + \underline{f}^T_p\underline{X}_p + \sum_{q\neq p}\underline{g}'^T_p\underline{\underline{T}}_{qp}\underline{X}_q\right] \end{aligned} \tag{4.29}$$

Rearranging,

$$\begin{aligned} E_z = &\sum_{v=-\infty}^{\infty} H_v^{(2)}(kr_0)\, e^{-jv\phi_0}\iiint_{source} dx'dy'dz'\frac{j}{4}J_v(kr_0')\, e^{jv\phi_0'}\,\cdot \\ &\cdot\sum_p \delta(r_p'-a_p)\frac{\partial}{\partial r'_p}\left[\underline{g}'^T_p\underline{\underline{U}}_{0p}\underline{X}_0 + \underline{f}^T_p\underline{X}_p + \sum_{q\neq p}\underline{g}'^T_p\underline{\underline{T}}_{qp}\underline{X}_q\right] \end{aligned} \tag{4.30}$$

which by inspection with the required solution from Equation (4.23) identifies $\underline{X}_s$ as:

$$\underline{X}_s = \frac{j}{4}\iiint_{source} dx'dy'dz'\sum_p \underline{g}_0^*\delta(r_p'-a_p)\frac{\partial}{\partial r'_p}\left[\underline{g}'^T_p\underline{\underline{U}}_{0p}\underline{X}_0 + \underline{f}^T_p\underline{X}_p + \sum_{q\neq p}\underline{g}'^T_p\underline{\underline{T}}_{pq}\underline{X}_q\right]$$

It should be noted that $\underline{g}_0^* = \underline{\underline{U}}^H_{p0}\underline{g}_p^*$ by the definition of matrix $\underline{\underline{U}}$ in Equation (4.14), so that:

$$\begin{aligned} \underline{X}_s = &\frac{j}{4}\sum_p\iiint_{source} r_p'dr_p'd\phi_p'\,\underline{\underline{U}}^H_{0p}\underline{g}_p^*\delta(r_p'-a_p) \\ &\cdot\frac{\partial}{\partial r'_p}\left[\underline{g}'^T_p\underline{\underline{U}}_{0p}\underline{X}_0 + \underline{f}^T_p\underline{X}_p + \sum_{q\neq p}\underline{g}'^T_p\underline{\underline{T}}_{qp}\underline{X}_q\right] \end{aligned} \tag{4.31}$$

Applying identities (4.32) and (4.33) to Equation (4.31):

$$\begin{aligned} \int_0^{2\pi} d\phi'_p\,\underline{g}_p^*\frac{\partial}{\partial r'_p}\underline{g}_p'^T &= \int_0^{2\pi}\left(e^{+jv\phi_p}J_v(kr'_p)\right)\left(e^{-jn\phi'_p}\frac{\partial}{\partial r'_p}J_n(kr'_p)\right)d\phi'_p \\ &= 2\pi\left(\delta_{vn}J_v(kr'_p)\frac{\partial}{\partial r'_p}J_n(kr'_p)\right) \end{aligned} \tag{4.32}$$

$$\begin{aligned}\int_0^{2\pi} d\phi'_p \, \underline{g}'^{*}_p \frac{\partial}{\partial r'_p} \underline{f}^T_p &= \int_0^{2\pi} \left(e^{+jv\phi_p} J_v(kr'_p) \right) \left(e^{-jn\phi'_p} \frac{\partial}{\partial r'_p} H^{(2)}_n(kr'_p) \right) d\phi'_p \\ &= 2\pi \left(\delta_{vn} J_v(kr'_p) \frac{\partial}{\partial r'_p} H^{(2)}_n(kr'_p) \right)\end{aligned} \tag{4.33}$$

leads to:

$$\underline{X}_s = \frac{jk\pi}{2} \sum_p a_p \underline{\underline{U}}^H_{0p} \left[\underline{\underline{J}}_p \underline{\underline{J}}'_p \underline{\underline{U}}_{p0} \underline{X}_0 + \underline{\underline{J}}_p \underline{\underline{H}}'_p \underline{X}_p + \underline{\underline{J}}_p \underline{\underline{J}}'_p \sum_{q \neq p} \underline{\underline{T}}_{qp} \underline{X}_q \right] \tag{4.34}$$

In Equations (4.34), the prime on Bessel and Hankel functions now denotes $J'_v(kr) = \frac{\partial}{\partial r} J_v(kr)\big|_{r=a}$ and $H^{(2)}_v{}'(kr) = \frac{\partial}{\partial r} H^{(2)}_v(kr)\big|_{r=a}$ respectively. Overall $\underline{\underline{J}}_p$ and $\underline{\underline{J}}'_p$ are diagonal matrices of elements $J_v(ka_p)$ and $J'_v(ka_p)$, and $\underline{\underline{H}}_p$ and $\underline{\underline{H}}'_p$ are diagonal matrices of elements $H^{(2)}_v(ka_p)$ and $H^{(2)}_v{}'(ka_p)$.

From Equation (4.18) for TM mode boundary condition, the following can be concluded: $\underline{\underline{J}}_p \underline{\underline{U}}_{0p} \underline{X}_0 + \underline{\underline{J}}_p \sum_{q \neq p} \underline{\underline{T}}_{qp} \underline{X}_q = -\underline{\underline{H}}_p \underline{X}_p$, Therefore, Equation (4.34) is rearranged into a form:

$$\underline{X}_s = \frac{jk\pi}{2} \sum_p a_p \underline{\underline{U}}^H_{0p} \left[\underline{\underline{J}}_p \underline{\underline{H}}'_p - \underline{\underline{J}}'_p \underline{\underline{H}}_p \right] \underline{X}_p \tag{4.35}$$

Using the Bessel Wronskian Equation (B.2), shown in Appendix B, gives $\underline{\underline{J}}_p \underline{\underline{H}}'_p - \underline{\underline{J}}'_p \underline{\underline{H}}_p = -\frac{j2}{\pi k a_p}$. Hence, the vector of scattered coefficients for the field of Equation (4.23) is finally derived as:

$$\underline{X}_s = \sum_p \underline{\underline{U}}^H_{0p} \underline{X}_p \tag{4.36}$$

It is observed that the vector of scattered field coefficients for a TM mode is now expressed in a coordinate system centred at the TLM cell.

Having obtained both incident and reflected fields in the coordinate system centred at the cell, the total field can be calculated. It can then be discretised and the mapping process carried out. This will be presented later in this chapter. Prior to this, the focus of the next subsection is to evaluate scattering coefficients for the TE polarisation using a similar procedure to that presented above.

4.3.2. Scattering Coefficients for a TE Polarisation

In the presence of a current around the wire J_ϕ, the magnetic field H_Z due to magnetic current source is given by:

$$H_z = \iiint_{\text{source}} dx'dy'dz' G_{HJ}(x,y,z;x',y',z') J_\phi(x',y',z') \tag{4.37}$$

where the Green's function G_{HJ} is defined by:

$$G_{HM} = \begin{cases} \dfrac{j}{4}\sum\limits_{v=-\infty}^{\infty} J_v(kr_0)\dfrac{\partial}{\partial r'}H_v^{(2)}(kr_0')\, e^{-jv(\phi_0-\phi_0')} & r_0 < r_0' \\ \dfrac{j}{4}\sum\limits_{v=-\infty}^{\infty} \dfrac{\partial}{\partial r'}J_v(kr_0')H_v^{(2)}(kr_0)\, e^{-jv(\phi_0-\phi_0')} & r_0' < r_0 \end{cases} \tag{4.38}$$

Again, the primed quantities here denote source points and unprimed observation points as in previous section, unless stated otherwise.

The currents that flow around the wire due to applied magnetic field are $J_\phi = H_z$, where $H_z = \underline{g}_p^T \underline{\underline{U}}_{0p} \underline{X}_0 + \underline{f}_p^T \underline{X}_p + \sum_{q \neq p} \underline{g}_p^T \underline{\underline{T}}_{qp} \underline{X}_q$ by the definition presented in Equation (4.16). Hence the wire currents are:

$$J_{\phi} = \sum_{p} \delta(r'_{p} - a_{p}) \left[\underline{g}'^{T}_{p} \underline{\underline{U}}_{0p} \underline{X}_{0} + \underline{f}^{T}_{p} \underline{X}_{p} + \sum_{q \neq p} \underline{g}'^{T}_{p} \underline{\underline{T}}_{qp} \underline{X}_{q} \right]_{r_p = a_p} \tag{4.39}$$

Using the Green's function G_{HM} given in Equation (4.38), the scattered field H_z is determined as:

$$\begin{aligned} H_{z} = & \iiint_{\text{source}} dx'dy'dz' \frac{j}{4} \sum_{i=-\infty}^{\infty} \frac{\partial}{\partial r'_{p}} J_{v}(kr_{0}') H_{v}^{(2)}(kr_{0}) e^{-jv(\phi_{0} - \phi_{0}')} \\ & \cdot \sum_{p} \delta(r_{p}' - a_{p}) \left[\underline{g}'^{T}_{p} \underline{\underline{U}}_{0p} \underline{X}_{0} + \underline{f}^{T}_{p} \underline{X}_{p} + \sum_{q \neq p} \underline{g}'^{T}_{p} \underline{\underline{T}}_{qp} \underline{X}_{q} \right] \end{aligned} \tag{4.40}$$

Regrouping:

$$\begin{aligned} H_{z} = & \sum_{v=-\infty}^{\infty} H_{v}^{(2)}(kr_{0}) e^{-jv\phi_{0}} \iiint_{\text{source}} dx'dy'dz' \frac{j}{4} \frac{\partial}{\partial r'_{p}} J_{v}(kr_{0}') e^{jv\phi_{0}'} \\ & \cdot \sum_{p} \delta(r_{p}' - a_{p}) \left[\underline{g}'^{T}_{p} \underline{\underline{U}}_{0p} \underline{X}_{0} + \underline{f}^{T}_{p} \underline{X}_{p} + \sum_{q \neq p} \underline{g}'^{T}_{p} \underline{\underline{T}}_{qp} \underline{X}_{q} \right] \end{aligned} \tag{4.41}$$

which comparing to desired form of scattered field presented in Equation (4.23) identifies $\underline{X}_s$ as:

$$\underline{X}_{s} = \frac{j}{4} \iiint_{\text{source}} dx'dy'dz' \sum_{p} \frac{\partial}{\partial r'_{p}} \underline{g}_{0}^{*} \delta(r_{p}' - a_{p}) \left[\underline{g}'^{T}_{p} \underline{\underline{U}}_{0p} \underline{X}_{0} + \underline{f}'^{T}_{p} \underline{X}_{p} + \sum_{q \neq p} \underline{g}'^{T}_{p} \underline{\underline{T}}_{qp} \underline{X}_{q} \right] \tag{4.42}$$

By the definition of matrix $\underline{\underline{U}}$ specified in Equation (4.14) the following can be assumed: $\frac{\partial}{\partial r} \underline{g}_{0}^{*} = \underline{\underline{U}}_{0p}^{H} \frac{\partial}{\partial r} \underline{g}_{p}^{*}$, so that

$$\begin{aligned} \underline{X}_{s} = & \frac{j}{4} \sum_{p} \iiint_{\text{source}} r_{p}' dr_{p}' d\phi_{p}' \underline{\underline{U}}_{0p}^{H} \\ & \cdot \frac{\partial}{\partial r'_{p}} \underline{g}_{p}^{*} \delta(r_{p}' - a_{p}) \left[\underline{g}'^{T}_{p} \underline{\underline{U}}_{0p} \underline{X}_{0} + \underline{f}^{T}_{p} \underline{X}_{p} + \sum_{q \neq p} \underline{g}'^{T}_{p} \underline{\underline{T}}_{qp} \underline{X}_{q} \right] \end{aligned} \tag{4.43}$$

Similarly, employing the identities from Equations (4.32) and (4.33) gives:

$$\underline{X}_{s} = \frac{jk\pi}{2} \sum_{p} a_{p} \underline{\underline{U}}_{0p}^{H} \left[\underline{\underline{J}}_{p} \underline{\underline{J}}'_{p} \underline{\underline{U}}_{0p} \underline{X}_{0} + \underline{\underline{J}}_{p} \underline{\underline{H}}'_{p} \underline{X}_{p} + \underline{\underline{J}}_{p} \underline{\underline{J}}'_{p} \sum_{q \neq p} \underline{\underline{T}}_{qp} \underline{X}_{q} \right] \tag{4.44}$$

Analogously to Equations (4.34), the prime on Bessel and Hankel functions now denotes the derivative of those functions with respect to *r* when $r = a_p$ Utilising Equation (4.18) for a TE mode boundary condition that brings the equality of $\underline{\underline{J}}'_p \underline{\underline{U}}_{0p} \underline{X}_0 + \underline{\underline{J}}'_p \sum_{q \neq p} \underline{\underline{T}}_{qp} \underline{X}_q = -\underline{\underline{H}}'_p \underline{X}_p$ into Equation (4.44), the final vector of scattering field coefficients for TE polarisation can be formulated in a coordinate system centred at the TLM cell

$$\underline{X}_s = \frac{jk\pi}{2} \sum_p a_p \underline{\underline{U}}^H_{0p} \left[\underline{\underline{J}}'_p \underline{\underline{H}}_p - \underline{\underline{J}}_p \underline{\underline{H}}'_p \right] \underline{X}_p = \sum_p \underline{\underline{U}}^H_{0p} \underline{X}_p \tag{4.45}$$

As has been shown for the TM mode, the incident and scattered field for a TE mode are now expressed in a coordinate system centred at the TLM cell. This formula can be substituted back into Equation (4.21), to form a complete analytical solution for a wave propagating in the presence of a cluster of conducting wires bounded by a single TLM cell. The total field formulation that is suitable for mapping into a TLM method is:

$$F_t = \underline{g}_0^T \underline{X}_0 + \underline{f}_0^T \underline{X}_s \tag{4.46}$$

where F_t denotes the total electric field in the case of a TM and total magnetic field in the case of a TE polarised wave.

4.3.3. Formulating the Admittance Relationship

In order to implement the total fields derived in the previous two sub-sections into the TLM algorithm, the technique presented in Chapter 3 is now applied. As has been demonstrated, the backbone for the mapping process is to identify the tangential fields at the edges of the numerical node and to obtain the admittance relationship in the form: $\underline{\underline{E}} = \underline{Y}\underline{\underline{H}}$. Therefore, the observation point (OP) is now placed at the points where the information between two two-dimensional TLM cells is interchanged, i.e. ports 0,1,2 or 3 as illustrated in Figure 4.1. The values of electric field E_z (for TM mode) and magnetic fields H_z (for TE mode) at those four ports, where $r_0 = \Delta$ and Δ is the radius of the node, are evaluated from the total fields derived above, Equation (4.46). The remaining fields components, i.e. magnetic field H_ϕ (for TM) and electric field E_ϕ (for TE polarisation) are determined from Maxwell's equations. Therefore, for TM fields:

$$\begin{aligned} E_i + E_s &= \sum_{n=-\infty}^{\infty} J_n(k\Delta) e^{-jn\phi_0} X_{0n} + \sum_{n=-\infty}^{\infty} H_n^{(2)}(k\Delta) e^{-jn\phi_0} X_{sn} \\ &= \underline{g}_0^T(k\Delta)\underline{X}_0 + \underline{f}_0^T(k\Delta)\underline{X}_s \end{aligned} \tag{4.47}$$

$$\begin{aligned} j\omega\mu(H_i + H_s) &= \sum_{n=-\infty}^{\infty} \frac{dJ_n(k\Delta)}{d\Delta} e^{-jn\phi_0} X_{0n} + \sum_{n=-\infty}^{\infty} \frac{dH_n^{(2)}(k\Delta)}{d\Delta} e^{-jn\phi_0} X_{sn} \\ &= \frac{d\underline{g}_0^T(k\Delta)}{d\Delta}\underline{X}_0 + \frac{d\underline{f}_0^T(k\Delta)}{d\Delta}\underline{X}_s \end{aligned} \tag{4.48}$$

and for TE fields:

$$\begin{aligned} H_i + H_s &= \sum_{n=-\infty}^{\infty} J_n(k\Delta) e^{-jn\phi_0} X_{0n} + \sum_{n=-\infty}^{\infty} H_n^{(2)}(k\Delta) e^{-jn\phi_0} X_{sn} \\ &= \underline{g}_0^T(k\Delta)\underline{X}_0 + \underline{f}_0^T(k\Delta)\underline{X}_s \end{aligned} \tag{4.49}$$

$$\begin{aligned} -j\omega\varepsilon(E_i + E_s) &= \sum_{n=-\infty}^{\infty} \frac{dJ_n(k\Delta)}{d\Delta} e^{-jn\phi_0} X_{0n} + \sum_{n=-\infty}^{\infty} \frac{dH_n^{(2)}(k\Delta)}{d\Delta} e^{-jn\phi_0} X_{sn} \\ &= \frac{d\underline{g}_0^T(k\Delta)}{d\Delta}\underline{X}_0 + \frac{d\underline{f}_0^T(k\Delta)}{d\Delta}\underline{X}_s \end{aligned} \tag{4.50}$$

where the functions $f(k\Delta)$, $g(k\Delta)$, are defined in Equations (4.3) and (4.6) respectively and are evaluated at the node radius Δ.

It should be noticed at this point that ϕ_0 in Equation (4.47) - (4.50) can take only discrete values of $\phi_0 = \left\{0, \frac{\pi}{2}, \pi, \frac{3}{2}\pi\right\}$ corresponding to the four ports of the 2D TLM node. Thus the cylindrical harmonics $\left(e^{jn\phi_0}\right)$ will be represented by a combination of the trigonometric functions $\cos(n\phi_0)$ and $\sin(n\phi_0)$. Furthermore, to obtain compatibility with the four ports of the 2D TLM node, the infinite number of solutions need to be truncated and only the lowest order harmonics are used to calculate the fields at the link points of the node. The lowest order harmonics in the analytical series are those for $n = -1, 0, 1, 2$. The superposition of these harmonics will produce all possible combinations of discrete voltages incident into the node. The approximation of analytical solution to only four harmonics is fully justified as the series of Bessel and Hankel functions converge very rapidly and is consistent with second order accuracy with respect to Δ. The convergence of these series will be shown later in this chapter for particular practical problems.

Attention will now be focused upon the manner the eigenvalue problem is imposed in practice. In order to discretise the fields the vector of scattered field coefficients $\underline{X}_s$ needs to be determined. This, according to the formula given in Equation (4.36) and (4.45) requires obtaining the solution of $\underline{X}$ from Equation (4.21) which is completely determined by the vector of incident harmonics $\underline{X}_0$. This would necessitate calculating the inverse of matrix $\underline{\underline{M}}$ given in

Equation (4.22) which numerically might be difficult. Instead a sequence of linear equations is solved as described below.

Assume $\underline{e}_n$ to be a vector of the same size as $\underline{X}_0$, large enough for the summation theorem to converge, with all elements equals 0 except for the *nth* which is equal 1. If the *"incident"* field $\underline{X}_0 = \underline{e}_n$ which means that there is only one *incident* harmonic, then the Equation (4.21) is solved for the scattered field coefficients $\underline{X}$ and this solution is labelled as $\underline{Y}_{sn}$. For any general vector of incident modes $\underline{X}_0 = \sum_{n=1}^{4} \underline{e}_n X_{0n}$ the scattered field coefficients will be formulated as $\underline{X} = \sum_{n=1}^{4} \underline{Y}_{sn} X_{0n}$, or in the matrix form as $\underline{X} = \left[\underline{Y}_{s1} \quad \underline{Y}_{s2} \quad \underline{Y}_{s3} \quad \underline{Y}_{s4}\right] \underline{X}_0 = \underline{\underline{Y}}_s \underline{X}_0$.

Hence, the vector of coefficients representing scattered field in coordinate system centred at the cell is calculated as $\underline{X}_s = \sum_p \underline{\underline{U}}_{0p}^H \underline{X}_p = \underline{\underline{U}}_0 \underline{\underline{Y}}_s \underline{X}_0$.

Thus, the fields at the ports, shown initially in Equation (4.47) to (4.50) are:

for TM fields:

$$E_i + E_s = \left(\underline{g}_0^T(k\Delta) + \underline{f}_0^T(k\Delta) \underline{\underline{U}}_0 \underline{\underline{Y}}_s\right) \underline{X}_0 \tag{4.51}$$

$$j\omega\mu(H_i + H_s) = \left(\frac{d\underline{g}_0^T(k\Delta)}{d\Delta} + \frac{d\underline{f}_0^T(k\Delta)}{d\Delta} \underline{\underline{U}}_0 \underline{\underline{Y}}_s\right) \underline{X}_0 \tag{4.52}$$

and for TE fields:

$$H_i + H_s = \left(\underline{g}_0^T(k\Delta) + \underline{f}_0^T(k\Delta) \underline{\underline{U}}_0 \underline{\underline{Y}}_s\right) \underline{X}_0 \tag{4.53}$$

$$-j\omega\varepsilon(E_i + E_s) = \left(\frac{d\underline{g}_0^T(k\Delta)}{d\Delta} + \frac{d\underline{f}_0^T(k\Delta)}{d\Delta} \underline{\underline{U}}_0 \underline{\underline{Y}}_s\right) \underline{X}_0 \tag{4.54}$$

Formulating the eigenvalue problem, i.e. enforcing the total electric field at the node edge to be proportional to the total magnetic field at the edge of the node, leads to the admittance relationship:

$$\left(\frac{d\underline{g}_0^T(k\Delta)}{d\Delta} + \frac{d\underline{f}_0^T(k\Delta)}{d\Delta} \underline{\underline{U}}_0 \underline{\underline{Y}}_s \right) \underline{X}_0 = \underline{\gamma} \left(\underline{g}_0^T(k\Delta) + \underline{f}_0^T(k\Delta) \underline{\underline{U}}_0 \underline{\underline{Y}}_s \right) \underline{X}_0 \qquad (4.55)$$

The eigenvalues γ_n represents the value of the admittance looking into the cell centre for TM polarisation and value of the impedance in case of TE polarisation. In addition, the eigenvalues will be purely imaginary and scaled by the intrinsic admittance or impedance of the medium, in this case empty space for which the intrinsic impedance equals $Z_0 = \sqrt{\mu_0 / \varepsilon_0} \approx 120\pi\ \Omega \approx 377\,\Omega$. The implementation of the eigensolutions into a time-domain numerical network using a short or open-circuited stubs and voltage-to-mode port-transformer, $\underline{\underline{T}}$, has been already presented in Chapter 3 and will not be repeated here. Instead, in the next section the formulations presented above will be applied to the case of field scattering from a single wire placed in the centre of a TLM cell. Due to the particular symmetry of this problem it is also possible to design an equivalent circuit that mimics the behaviour of the node containing a single, centrally positioned wire without the use of the port-transformer. Although it is just a special case of proceeding multi-wire analysis, it is instructive to determine the approach for this simple scenario. The results of this wire node will be verified against analytical solutions.

4.4. A Validation for a Single Wire

In order to verify the accuracy and demonstrate the results of our approach, consideration will now be focused upon a single wire centred in the TLM node. This example has been already widely studied in literature [4.1, 4.4, 4.5], therefore is an excellent benchmark for comparison. For the scenario described above it is possible to develop a simple equivalent electrical circuit that mimics the behaviour of the multi-feature node. The equivalent circuit for a TM polarised fields was already introduced in [4.1], however the necessary derivations will also be presented here with extension to TE field, as they help to better understand the overall framework of 2D multi-feature model.

4.4.1. Electrical Equivalent Circuit for a Single Wire

In a case of electromagnetic fields in the presence of a single conducting wire, two different polarisations ought to be considered, namely the TM and TE fields. Intuitively, to model TM polarised fields a shunt node of two-dimensional TLM network is used and the series node for a TE configuration. Each of those nodes has been presented in Chapter 2. It is underlined that due to the duality of the network models either shunt or series node are sufficient to simulate both field polarisations [4.6]. However, for a single wire case, the accuracy of both models will be addressed below for comparison with our multi-feature approach.

Consider a single cylindrical conductor placed at the centre of the TLM cell representing homogeneous and source free region of empty space. The total field can be obtain using the formula given in Equation (4.46). However, recognising the fact that now the wire coordinate system and the node coordinate system overlap each other i.e. $(r_p,\phi_p)\equiv(r_0,\phi_0)$ the total field formulae can be obtained directly as discussed in Chapter 2:

for TM fields

$$E_z(r\ge a,\phi)=\sum_{n=-\infty}^{\infty}e^{-jn\phi_0}X_{0n}\left[J_n(k_0r)+H_n^{(2)}(k_0r)\hat{X}_{sn}\right] \tag{4.56}$$

$$H_\theta(r\ge a,\phi)=\frac{k_0}{j\omega\mu_0}\sum_{n=-\infty}^{\infty}e^{-jn\phi_0}X_{0n}\left[J'_n(k_0r)+H'^{(2)}_n(k_0r)\hat{X}_{sn}\right] \tag{4.57}$$

and for TE fields

$$H_z(r\ge a,\phi)=\sum_{n=-\infty}^{\infty}e^{-jn\phi_0}X_{0n}\left[J_n(k_0r)+H_n^{(2)}(k_0r)\hat{X}_{sn}\right] \tag{4.58}$$

$$E_\theta(r\ge a,\phi)=\frac{k_0}{j\omega\varepsilon_0}\sum_{n=-\infty}^{\infty}e^{-jn\phi_0}X_{0n}\left[J'_n(k_0r)+H'^{(2)}_n(k_0r)\hat{X}_{sn}\right] \tag{4.59}$$

By applying the boundary conditions, i.e. enforcing the total electric field at the surface of the wire to zero, the scattering coefficients are explicitly determined:

$$\hat{X}_{sn}=-\frac{J_n(k_0a)}{H_n^{(2)}(k_0a)}\quad\text{for TM mode} \tag{4.60}$$

$$\hat{X}_{sn}=-\frac{J'_n(k_0a)}{H'^{(2)}_n(k_0a)}\quad\text{for TE mode} \tag{4.61}$$

In order to map the field solutions to 2D numerical network the admittance relationship in a form of $\underline{\underline{H}}=\underline{Y}\cdot\underline{\underline{E}}$ can be now constructed:

for TM fields:

$$\underline{Y}=\frac{\underline{\underline{H}}}{\underline{\underline{E}}}=\frac{k}{j\omega\mu}\frac{\sum_{n=-\infty}^{\infty}e^{-jn\phi_0}X_{0n}\left[J'_n(k_0r)-\frac{J_n(k_0a)}{H_n^{(2)}(k_0a)}H'^{(2)}_n(k_0r)\right]}{\sum_{n=-\infty}^{\infty}e^{-jn\phi_0}X_{0n}\left[J_n(k_0r)-\frac{J_n(k_0a)}{H_n^{(2)}(k_0a)}H_n^{(2)}(k_0r)\right]} \tag{4.62}$$

for TE fields:

$$\underline{Y}=\frac{\underline{\underline{H}}}{\underline{\underline{E}}}=\frac{j\omega\varepsilon}{k}\frac{\sum\limits_{n=-\infty}^{\infty}e^{-jn\phi_0}X_{0n}\left[J_n(k_0r)-\frac{J'_n(k_0a)}{H'^{(2)}_n(k_0a)}H^{(2)}_n(k_0r)\right]}{\sum\limits_{n=-\infty}^{\infty}e^{-jn\phi_0}X_{0n}\left[J'_n(k_0r)-\frac{J'_n(k_0a)}{H'^{(2)}_n(k_0a)}H'^{(2)}_n(k_0r)\right]} \tag{4.63}$$

It is clear that the admittance operator $\underline{Y}$ is frequency dependent and contains information about the properties and geometry of the object inserted into the node. To maintain consistency of field solutions to Maxwell's equations with 2D TLM network, the admittance relationship is now evaluated at the four positions corresponding to four ports of 2D TLM node. As discussed in the previous section, the series solution is also calculated for the four lowest order harmonics. The 4-port transformer, $\underline{T}$, that decomposes the modal field solutions to port voltages can be easily identified as:

$$\underline{T}=\begin{bmatrix}\cos 0 & \cos\phi_1 & \sin\phi_1 & \cos 2\phi_1\\ \cos 0 & \cos\phi_2 & \sin\phi_2 & \cos 2\phi_2\\ \cos 0 & \cos\phi_3 & \sin\phi_3 & \cos 2\phi_3\\ \cos 0 & \cos\phi_4 & \sin\phi_4 & \cos 2\phi_4\end{bmatrix}\xrightarrow{\underline{T}^H\underline{T}=\underline{I}}\begin{bmatrix}1/2 & 1/\sqrt{2} & 0 & 1/2\\ 1/2 & 0 & 1/\sqrt{2} & -1/2\\ 1/2 & -1/\sqrt{2} & 0 & 1/2\\ 1/2 & 0 & -1/\sqrt{2} & -1/2\end{bmatrix} \tag{4.64}$$

where $\underline{I}$ is the identity matrix and the angles ϕ_i are $0,\frac{\pi}{2},\pi,\frac{3\pi}{2}$.

The combination of port voltages that produces the appropriate modal field solution is presented in Table 4.1 and also illustrated symbolically in Figure 4.2.

n	V_1	V_2	V_3	V_4
0	1	1	1	1
1	1	0	-1	0
-1	0	1	0	-1
2	1	-1	1	-1

Table 4.1. Modal field solutions in terms of port voltages entering the 2D TLM node

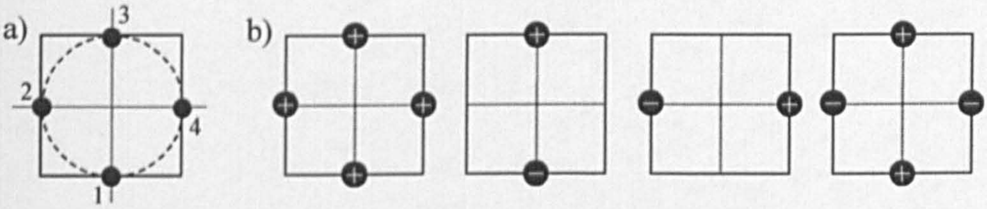

Figure 4.2. Symbolic representation of 2D TLM node (a) and its modal patterns (b)

Attention will now be focused on the simplification of the mode admittances from Equation (4.62) and (4.63). Replacing the Bessel functions with their small argument approximations (shown in Equation (B.3) in Appendix B) is consistent with the scale of the object and the frequency range of interest. As TLM is restricted by its dispersion behaviour to 10% of the maximum frequency modelled, i.e. ten spatial samples per wavelength [4.7], the modal admittances can be reduced as follows,

for TM modes:

$$Y_{n=0} = \frac{H}{E} \approx \frac{1}{j\omega\mu} \frac{1}{\Delta \ln(\Delta / a)} \qquad \text{for } n = 0$$

$$Y_{n\neq 0} = \frac{H}{E} \approx \frac{1}{j\omega\mu} \frac{|n|}{\Delta} \frac{(\Delta^{2|n|} + a^{2|n|})}{(\Delta^{2|n|} - a^{2|n|})} \qquad \text{for } n \neq 0 \tag{4.65}$$

for TE modes:

$$Y_{n=0} = \frac{H}{E} \approx \frac{1}{j\omega\mu} \frac{2\Delta}{(\Delta^2 - a^2)} \qquad \text{for } n = 0$$

$$Y_{n\neq 0} = \frac{H}{E} \approx j\omega\varepsilon \frac{\Delta}{|n|} \frac{(\Delta^{2|n|} + a^{2|n|})}{(\Delta^{2|n|} - a^{2|n|})} \qquad \text{for } n \neq 0 \tag{4.66}$$

A detailed derivation is given in section 4 of Appendix B.

It is seen that admittances are either proportional or inversely proportional to frequency. Therefore, a short-circuited or an open-circuited line can be used to provide these frequency dependent admittances in a time-domain method. According to transmission line theory [4.8], the impedance of a short or open-circuit termination is given by:

$$jZ_n \tan(\omega\Delta t/2) = \gamma_n^{-1} \qquad \text{for a short-circuited termination}$$

$$-jZ_n \operatorname{ctan}(\omega\Delta t/2) = \gamma_n^{-1} \qquad \text{for an open-circuited termination} \tag{4.67}$$

where $\omega\Delta t/2$ is a phase delay on each transmission line, [4.7].

It can easily be shown that the phase delay for 2D TLM equals $k_0\Delta/\sqrt{2}$. By inspection, comparing the expressions given in Equation (4.67) with Equations (4.65) and (4.66) it is concluded that a short-circuit stub is required for all the modes representing TM polarised fields and for the $n = 0$ harmonic of TE polarised fields. For the remaining modes corresponding to $n \neq 0$ for TE polarisation an open-circuit stub needs to be used.

As the admittances and impedances are reciprocal quantities, only impedances will be employed for convenience in further analysis.

By assuming that for small arguments $x \ll 1 \Rightarrow \tan(x) \approx x$ and taking into account the fact that for an empty space shunt node and a series node the link-line impedance of the numerical network Z_L equals $Z_L = \sqrt{2} Z_0$ and $Z_L = Z_0 / \sqrt{2}$ respectively, the input impedances looking into the stubs can be calculated as:

for a TM mode and a shunt node:

$$Z_n = Z_L \ln(\Delta / a) \qquad \text{for } n = 0$$
$$Z_n = \frac{Z_L}{|n|} \frac{(\Delta^{2|n|} - a^{2|n|})}{(\Delta^{2|n|} + a^{2|n|})} \qquad \text{for } n \neq 0 \tag{4.68}$$

and for a TE mode and a series node

$$Z_n = Z_L \frac{\Delta^2 - a^2}{\Delta^2} \qquad \text{for } n = 0$$
$$Z_n = Z_L |n| \frac{(\Delta^{2|n|} - a^{2|n|})}{(\Delta^{2|n|} + a^{2|n|})} \qquad \text{for } n \neq 0 \tag{4.69}$$

Having calculated the impedances looking into the stubs, the time-domain network presented in Figure 4.3 for (a) TM and (b) TE modes can be designed.

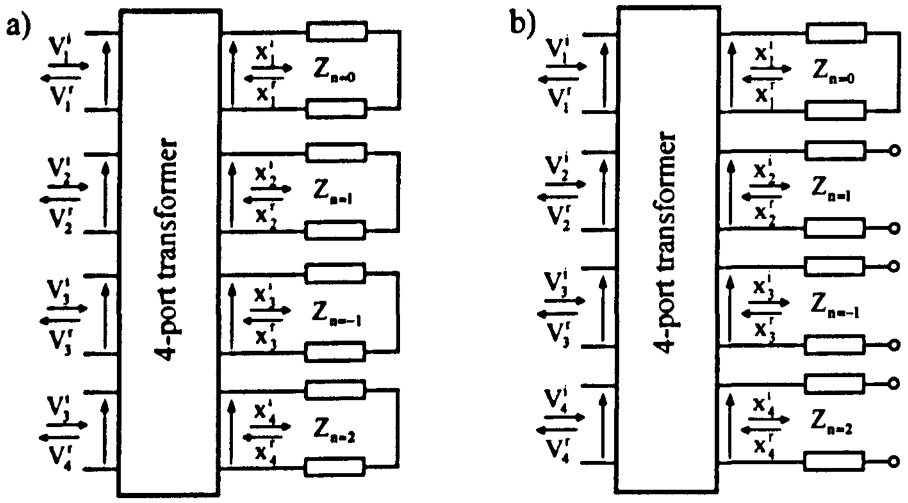

Figure 4.3. Time-domain network model that mimics behaviour of

TM (a) and TE (b) polarised wire

It is noted that in both models the impedances related to harmonics $n = 1$ and $n = -1$ are equal. Furthermore, for any wire radius $0 < a < \Delta$ the stub impedances are related as: $Z_{n=0} > Z_{n=1} > Z_{n=2}$ for TM polarisation, and $Z_{n=2} > Z_{n=0} > Z_{n=1}$ for TE polarisation respectively.

The impedances $Z_{n=0}$ and $Z_{n=1}$ are the dominant terms for TM polarisation. The TM model can therefore be further simplified without significant loss in accuracy if the impedance corresponding to $n = 2$ is approximated to that of $n = \pm 1$. This provides an advantage when developing an equivalent circuit for the TM case. To achieve this, first the circuit link line impedance, Z, is set to that of the line impedance for the mode $n = \pm 1$, i.e. $Z = Z_{n=\pm 1}$. A standard time delay can then be implemented for all the modal link lines and a short circuit stub is used to model a deficit in impedance for the mode $n = 0$, as shown in Figure 4.4(a). It can be seen that according to transmission line theory the stub impedance of Figure 4.4(a) $Z_S = Z_0 - Z$. A similar approach can be adopted for the TE case. First the admittance corresponding to $n = 2$ is approximated to $Z_{n=\pm 1}$. This value is used as a link line impedance, Z, for the node and the impedance deficit for the mode $n = 0$ is compensated by the stub $Z_S = Z_0 - Z$, as shown in Figure 4.4(b).

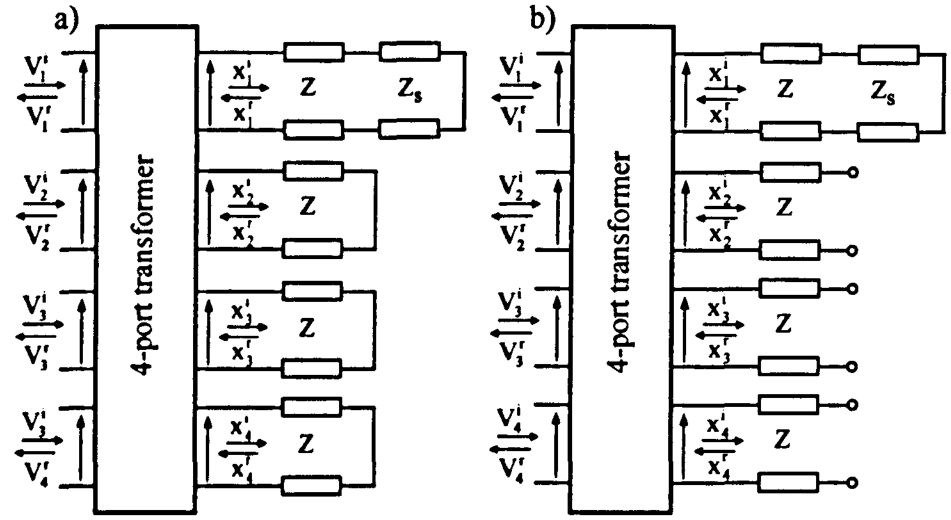

Figure 4.4. Standardised modal network for a conducting wire in a shunt node (a) and series node (b)

Extracting a common link line impedance, Z, for all the modes in both of the models permits moving them before the 4-port transformer as depicted in Figure 4.5.

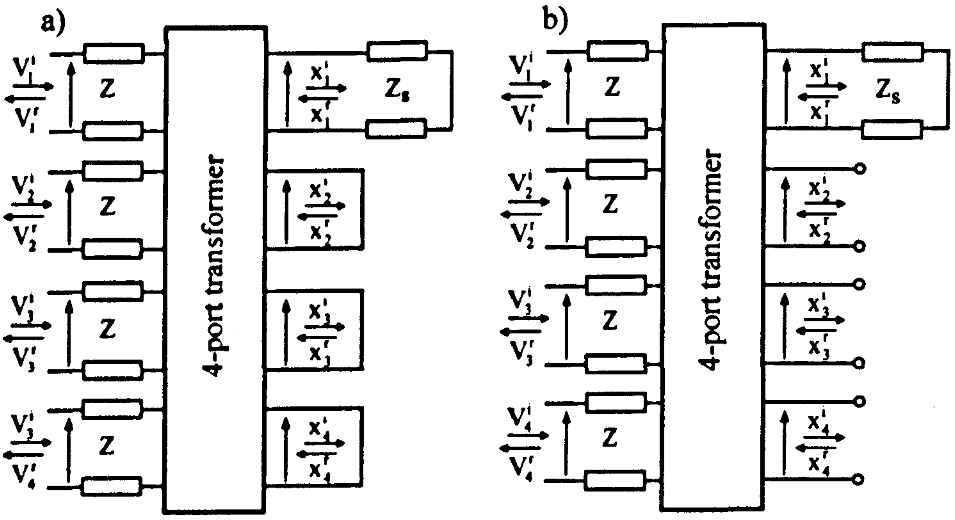

Figure 4.5. A standardised network model for a single wire in a shunt node (a) and series node (b)

Due to symmetry of the problem and by taking into account the properties of the shunt and series node, the standardised model presented above can be simplified further into the equivalent circuits presented in Figure 4.6(a) and (b).

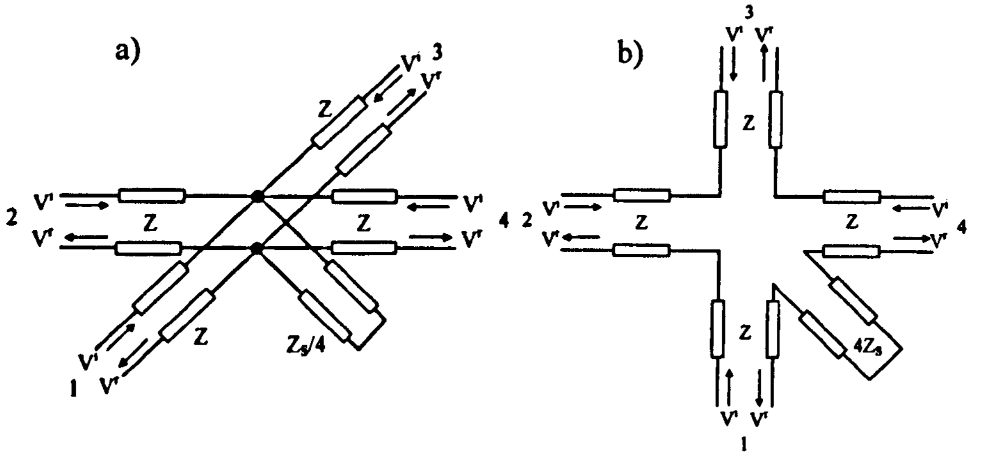

Figure 4.6. An equivalent circuit model for a centrally placed single wire in shunt node (a) and series node (b)

The short circuit stub of line 1 presented in Figure 4.5(a) has been placed at the centre of the node, as shown in Figure 4.6(a). This is consistent with the mode distributions presented in Figure 4.2 as only the $n = 0$ modal amplitudes couple with the short-circuited stub. For the remaining modes, the voltage at the centre of the node is zero therefore those modes do not couple with the short-circuited stub. In addition, the stub value has been divided by four due to the parallel combination of the four link lines present for the $n = 0$ mode. An equivalent circuit for TE fields is shown in Figure 4.6(b). Similarly, only the current of the $n = 0$ mode will flow through the stub.

It should be pointed out that the proposed approach is not the only way to develop an equivalent circuit. The expanded model can be designed by extracting a different common value of the link line impedance, Z, and the deficit in modal impedances can be modelled using stubs on all four modal lines. The only constraint in manipulating the stub impedances is that the stub value is required to be positive to ensure that the circuit components, i.e. lumped capacitors and inductor, are positive. This condition also guarantees the stability of the approach presented, as already discussed in Chapter 2.

4.4.2. Two-Dimensional Numerical Experiment

Before the numerical validations are presented, the experimental set-up will briefly be explained, as the majority of 2D simulations presented in this thesis are based on the same geometric configuration.

Figure 4.7 shows a computational window for two-dimensional simulations that is centred at point (0,0). The multi-feature node (MN) with the feature(s) embedded in it is placed at the centre of the window. The position of the enclosed feature(s) in a cell, e.g. wires, is described by (r,ϕ) where r is the distance between the centre of the node, position (0,0), and the centre of the object and ϕ is the angle between the positive x-axis and the radius r.

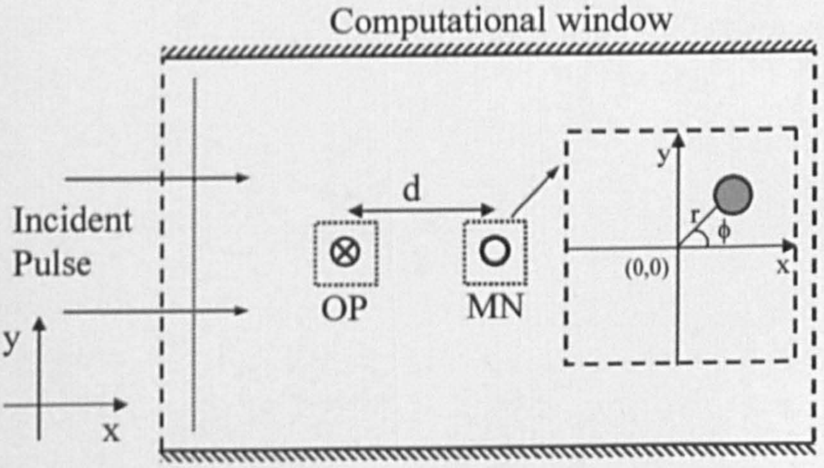

Figure 4.7. Numerical configuration for 2D simulations

The problem is excited by an incident pulsed plane wave as indicated in Figure 4.7 and the fields are recorded at observation point (OP) at a distance d from the multi-feature node. The distance, d, will be usually expressed in terms of number of cells. For example, (-2,0) indicates that OP is positioned two nodes from the MN on the negative x-axis; (2,0) OP is positioned two nodes from the MN on the positive x-axis etc. The fields will be recorded and verified for two zones, namely the near-field zone, defined 2 nodes distant and the far-field zone at 8 nodes distant from the MN. A matched boundary condition has been imposed on the edges of the computational window parallel to x-axis (half-shaded lines) and an open-circuit boundary condition on the edges perpendicular to the x-axis (dashed lines) unless stated otherwise.

4.4.3. Convergence of the Analytical Solution

The aim of this section is to demonstrate the convergence of the analytical solution represented in terms of Bessel functions and therefore to justify approximating the infinite series to only four harmonics, made when mapping the fields into a numerical network.

The convergence of total fields for TM and TE polarisation are shown in Figure 4.8 at the point corresponding to one of the ports of TLM cell, ($r = \Delta = 0.5\,\text{m}$, $\phi = \pi$) over the frequency range that would normally be applied for TLM simulations. The frequency is scaled to the maximum frequency in a 2D TLM simulation, i.e. $f_{max} = (2\Delta t)^{-1}$ with the time-step $\Delta t = \dfrac{2\Delta}{c\sqrt{2}} = \dfrac{\Delta\sqrt{2}}{c}$ where c is the speed of light in vacuo.

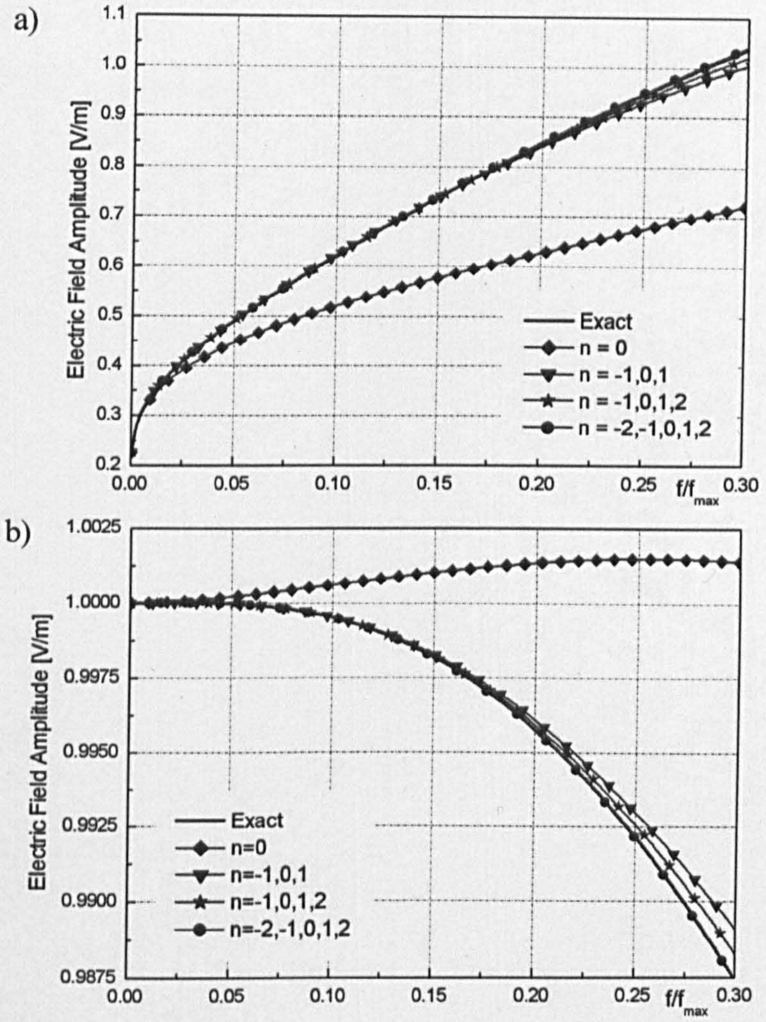

Figure 4.8. A convergence of analytical solution for a single wire for TM (a) and TE (b) polarisation

The analytical solution for a single wire of radius $a = 0.125\Delta$ is illustrated in Figure 4.8 for different truncation of the series in Equations (4.56) and (4.59). [The Hankel and Bessel functions that the total field is represented by have been calculated using routines from Numerical Algorithms Group (NAG) Fortran Library].

It is noted that number of terms that must be retained increases with distance from the scatterer. Here, with $r \leq \Delta$, 30 harmonic terms are sufficient for good convergence which is the case labelled "Exact" in Figure 4.8. Over the frequency range that TLM is valid (10 samples per wavelength) which corresponds to $f/f_{max} = 0.1$ in both graphs, the lowest order harmonics play the dominant role and very good agreement is seen between the exact solution and the use of just four lowest order modes. This justifies the approximation of using only four harmonics when mapping analytically derived fields into the time-domain numerical network.

4.4.4. Numerical Validations for a Single Wire

Although the multi-feature node has been developed to mimic EM field behaviour in the presence of an arbitrary number of wires clustered in a single numerical cell, it is appropriate to verify its accuracy for a single wire centrally positioned within the cell, as this problem has been widely studied in literature [4.1, 4.4, 4.5]. Therefore the aim of this section is to validate the theory of multi-feature node and its equivalent circuit developed above against the analytical solution for this configuration. It is emphasised that two TLM nodes have been presented: (i) the full multi-feature node implemented in Figure 4.3 and (ii) its approximation referred to as an "equivalent circuit" shown in Figure 4.6.

Consider the configuration presented in Figure 4.7, where the multi-feature node contains a single conducting wire placed at the centre of the TLM cell. The problem is excited by a Gaussian pulse of RMS width 2.5 time steps. For the simulations presented in this section, a computational window of 1000 by 1000 cells is used and 2048 time-step iterations are taken to ensure sufficient frequency domain granularity, when the Fast Fourier Transform (FFT) routine is conducted to convert the time-domain field data. Figure 4.9 shows the total electric field amplitude at OPs placed in the near-field zone (2 nodes away from the MN) and the far-field zone (8 nodes away from the MN) in front, behind and to the sides of the node with a single wire. The wire radius equals $a = 0.25\Delta$ and $\Delta = 0.025\,\mathrm{m}$, where Δ is the radius of the TLM node. The results are presented versus normalised frequency.

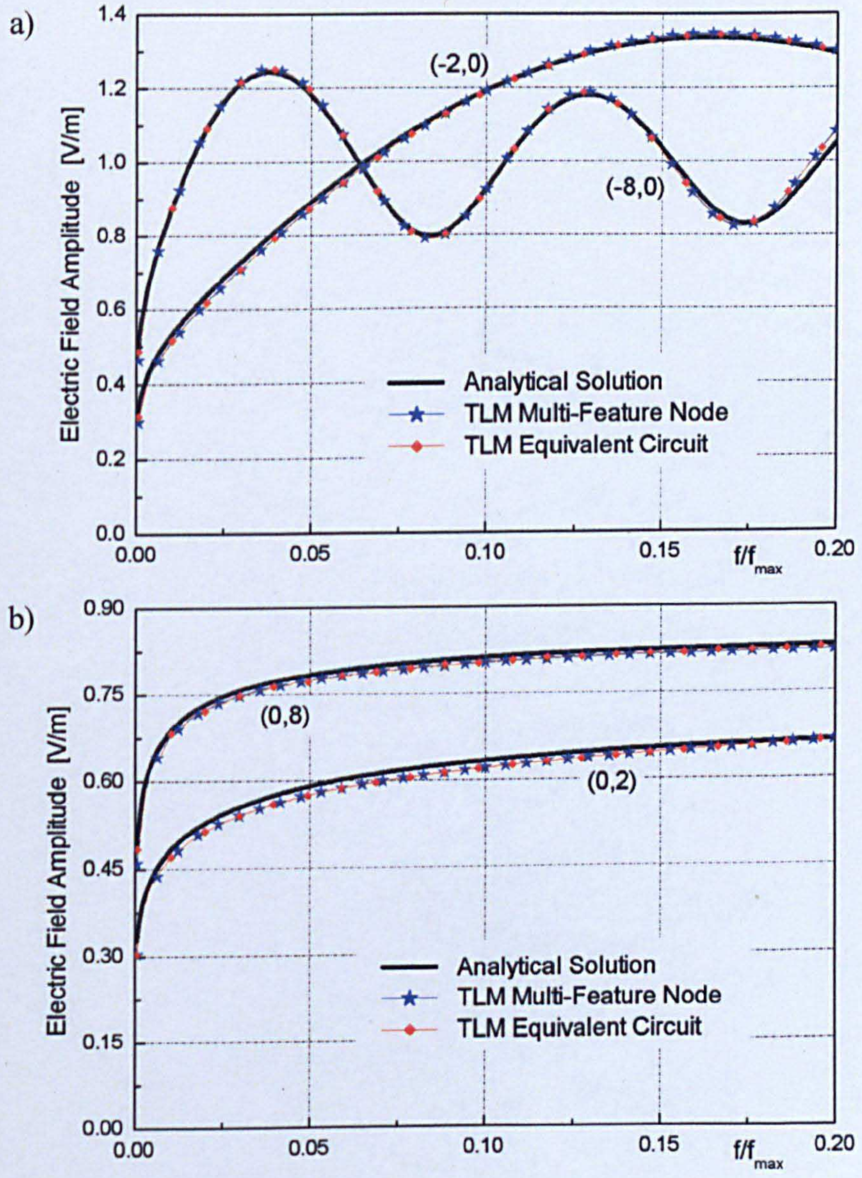

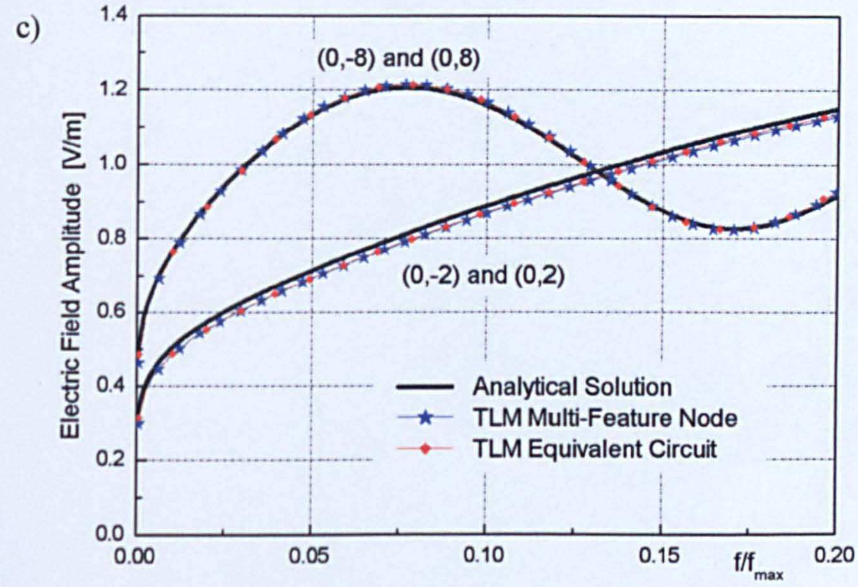

Figure 4.9. Amplitude of the total electric field measured in the near and far-field zone in front (a) behind (b) and to both sides (c) of the single TM polarised wire

It can be seen clearly that very good agreement is achieved between the multi-feature node, its equivalent circuit and the exact solution. The results for the TE polarised case are illustrated in Figure 4.10. The simulation parameters are the same as for the TM case.

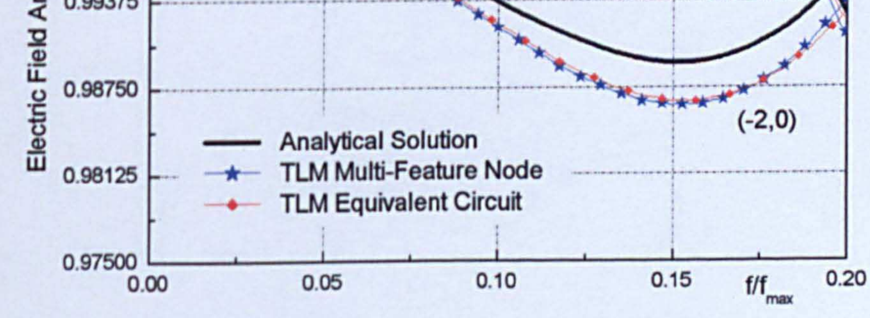

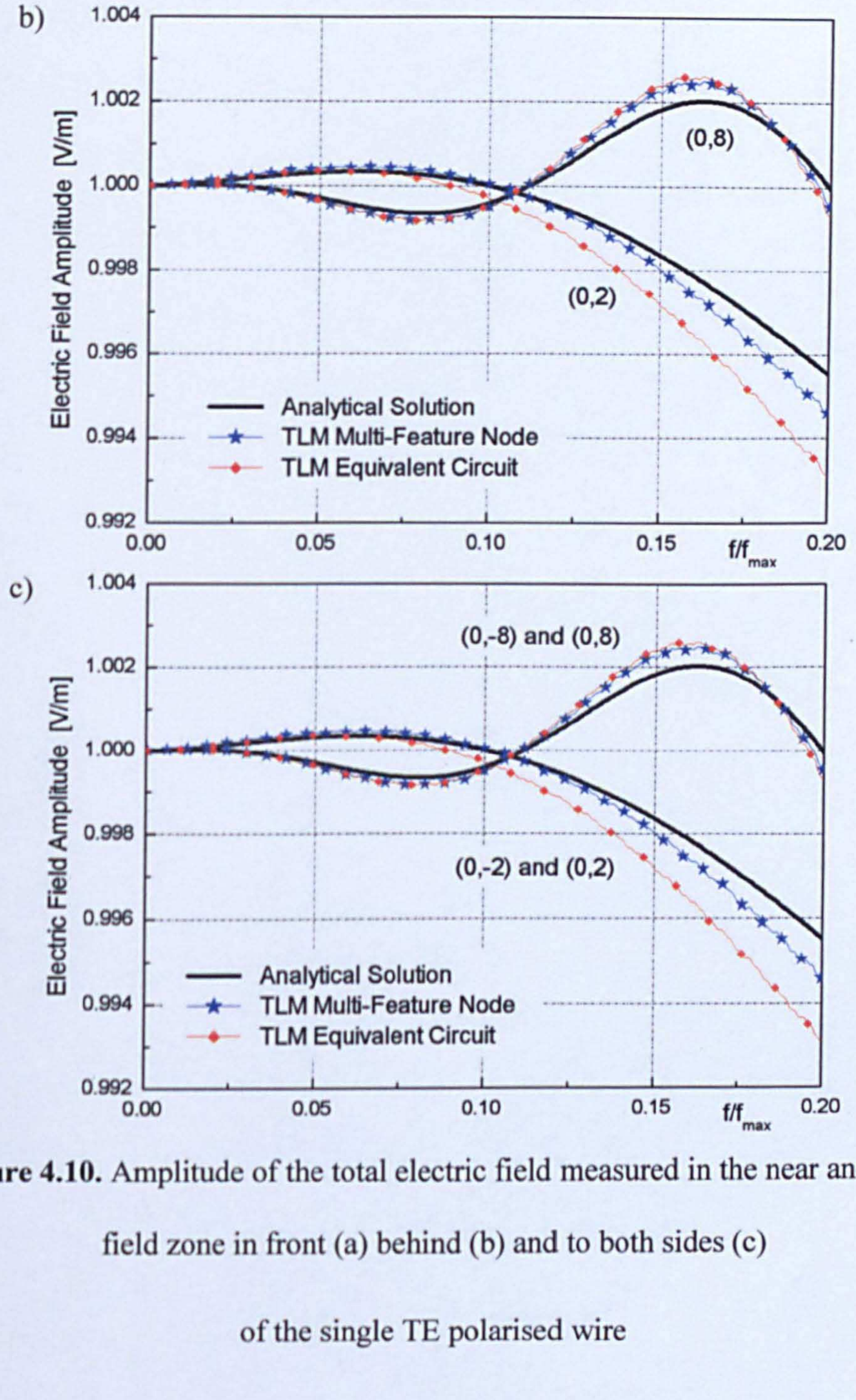

Figure 4.10. Amplitude of the total electric field measured in the near and far-field zone in front (a) behind (b) and to both sides (c) of the single TE polarised wire

Figure 4.10 presents the total electric field amplitude for OPs in near and far-field zones. The TE fields are captured in front, behind and to both sides of the node containing a single wire. As expected, the TE polarised case exhibits much weaker scattering compared to the TM polarised scattering.

Despite the small field variation for TE polarisation, the results using the multi-feature node and its equivalent circuit are in very good agreement with the exact solution up to 10% of the maximum frequency. A slight discrepancy can be observed beyond the cut-off point due to the dispersion that occurs in the TLM mesh and this is much more visible for such a weak scattering. The results for the equivalent circuit show a marginally larger error then those for the multi-feature node itself, especially with the near-field zone. It is believed that the error is due to the impedance approximation for the mode $n = 2$ to that of the mode $n = \pm 1$. For such a weak field disturbance, the contribution of the second harmonic becomes of greater significance than was observed for a wave in the TM configuration.

In the next two graphs, the impact of the wire radius will be demonstrated for both polarisations. Again, the simulation parameters remain unchanged with the numerical mesh size being $2\Delta = 0.05\,\text{m}$.

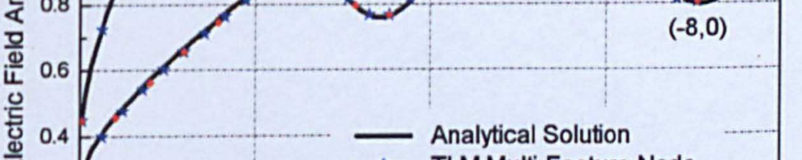

Figure 4.11. Amplitude of the total electric field for a TM polarised wire of radius $a = 0.5\Delta$

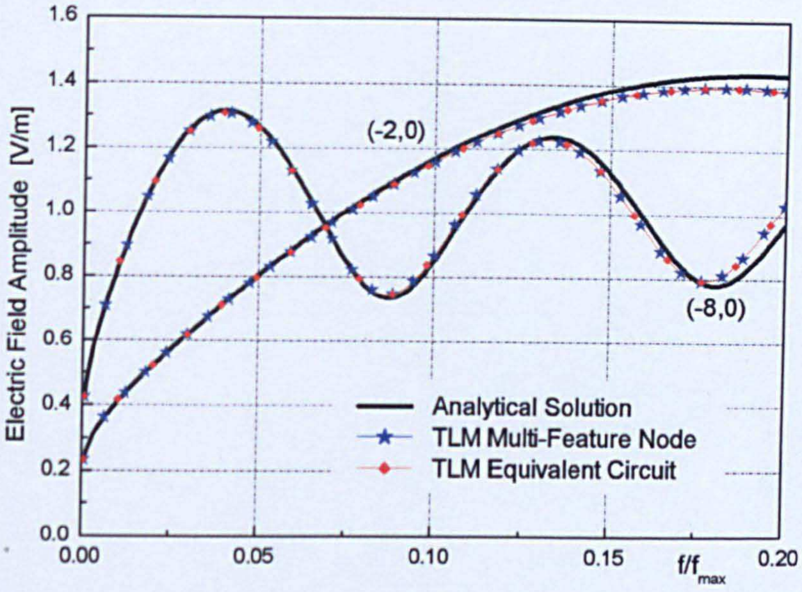

Figure 4.12. Amplitude of the total electric field for a TM polarised wire of radius a = 0.75Δ

It is observed in Figure 4.11 and Figure 4.12, for TM fields that the match between the numerical and the analytical results is extremely close and independent of the wire radius.

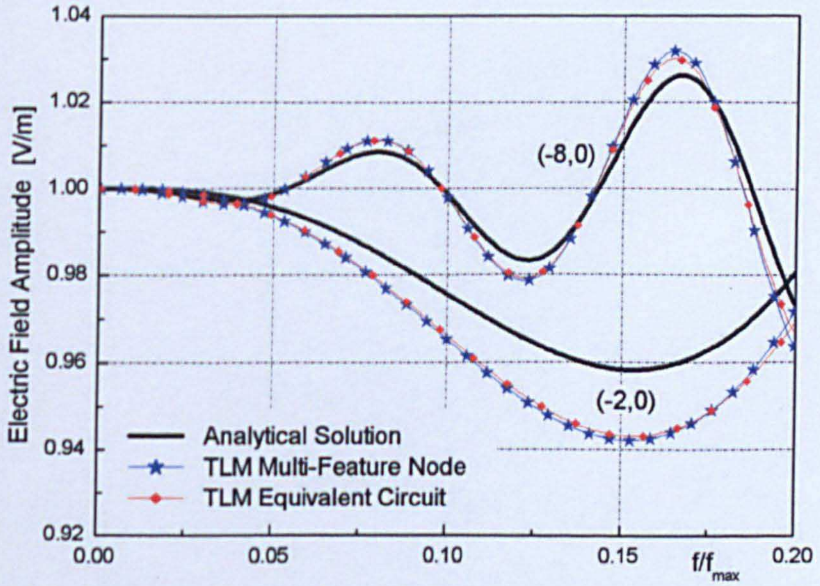

Figure 4.13. Amplitude of the total electric field for a TE polarised wire of radius a = 0.5Δ

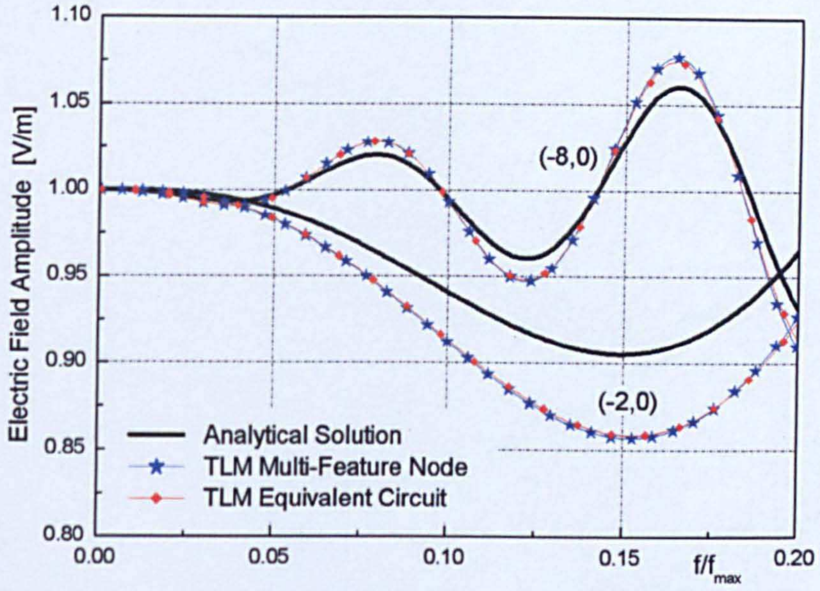

Figure 4.14. Amplitude of the total electric field for a TE polarised

wire of radius $a = 0.75\Delta$

A slight dependency upon radius is observed for TE polarised scattering as illustrated in Figure 4.13 and Figure 4.14, where the results exhibits more error with increasing wire radius. The results for the near-field zone exhibit this error much more than those in the far-field zone. The maximum absolute error in that zone, at the $f/f_{max} = 0.1$ is approximately 3-4%. It should be pointed out that the approach has been developed for EMC applications and such an error is typically acceptable. The present approach accounts for the wire geometry as is also confirmed by the time-domain numerical simulations presented in Figure 4.15.

The time-domain electric fields scattered from a single wire for both polarisations are presented in Figure 4.15. The field is observed in the far-field region, 8 nodes in front of the multi-feature node for a wire radius of 0.1Δ to 0.9Δ. It is clear that the information about the geometry of the object is correctly embedded within the multi-feature node, as larger field is reflected back from the wires of larger radii.

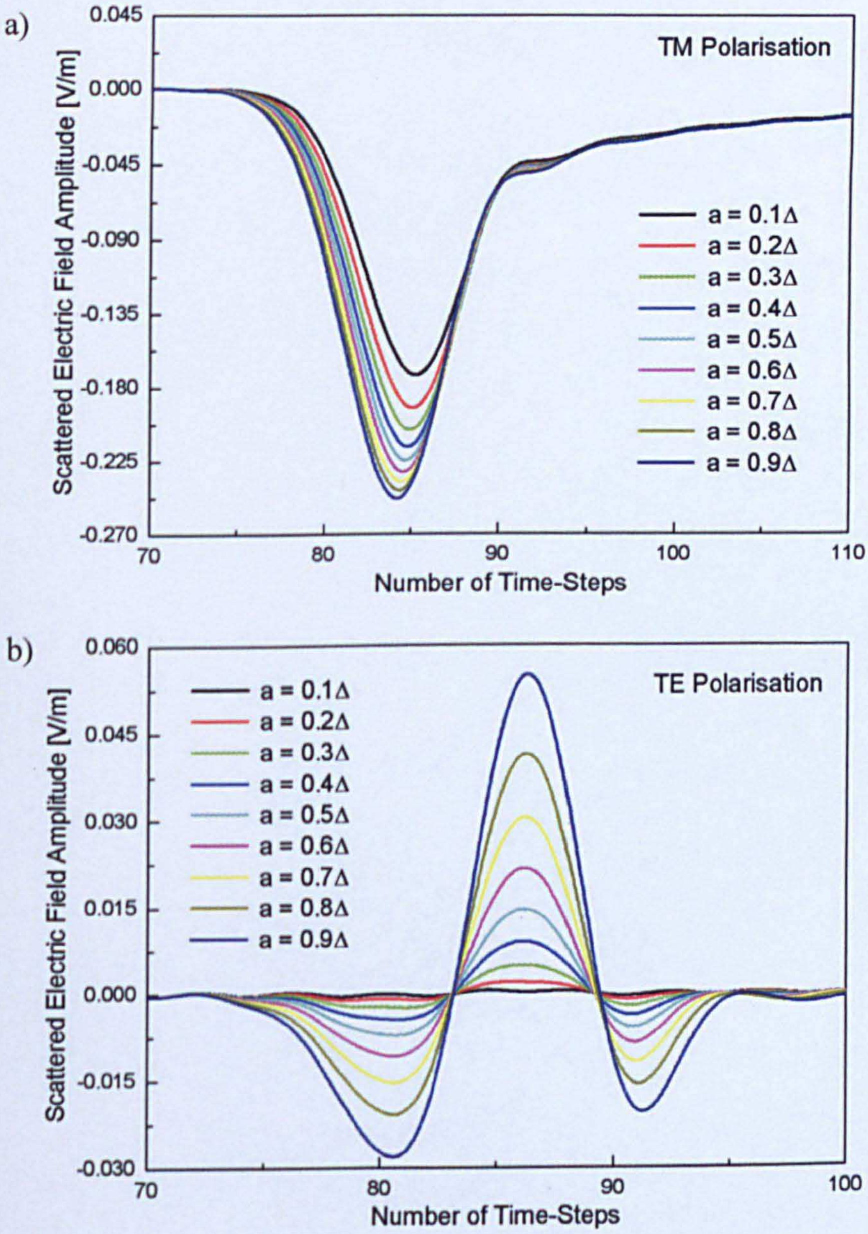

Figure 4.15. Fields scattered from a single wire for TM polarisation (a) and TE polarisation (b)

In electromagnetic field simulations it is very often required to adequately model not only the amplitude of the signal, but also its phase. Therefore, in Figure 4.16 the accuracy of our approach in modelling the electric field phase based on the example of the field scattered from a single wire of radius $a = 0.25\Delta$ is demonstrated.

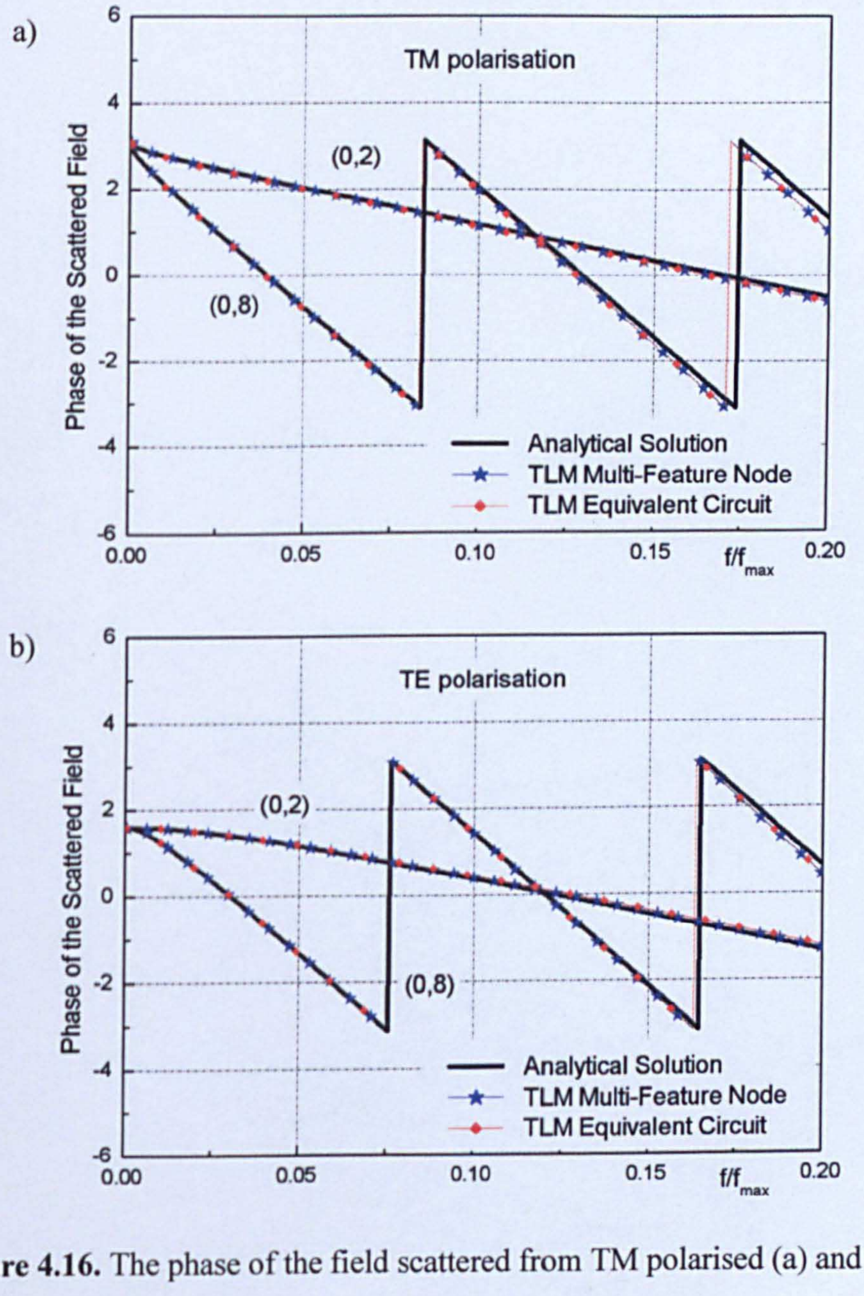

Figure 4.16. The phase of the field scattered from TM polarised (a) and TE polarised (b) single wire of radius $a = 0.25\Delta$

It can be seen in Figure 4.16 that the comparison between the numerical and analytical solution is exact over the frequency range of interest for both polarisations.

In order to further examine the accuracy of the proposed approach the coupling through the near fields of two wires in different cells will be shown in the next experiment.

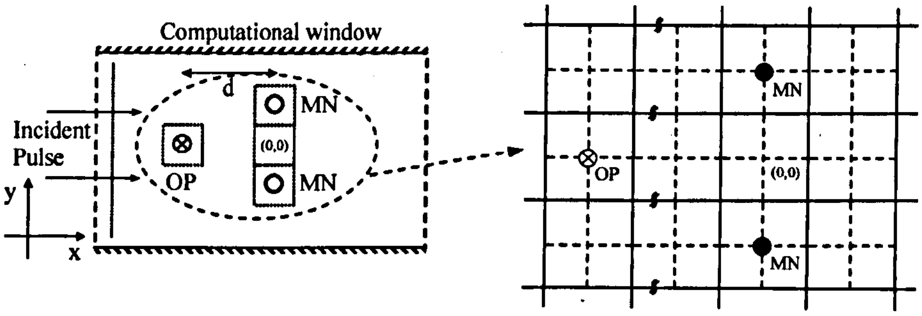

Figure 4.17. Numerical experiment for two multi-feature nodes in close proximity

Figure 4.17 shows the configuration for the next simulation. Two multi-feature nodes each containing a single wire have been placed in close proximity in such a manner that there is a single empty node in-between them. The radii of both wires embedded in the cells are $a = 0.5\Delta$ where $\Delta = 0.025\,\mathrm{m}$. The fields are shown in Figure 4.18 and are observed at the point in line with the empty node positioned between the multi-feature nodes in a far and near-field zone on the negative x-axis.

Again, the analytical and numerical solutions are in good agreement for TM fields. The error for TE polarisation is similar to that exhibited by a single node with a wire embedded inside. Therefore, placing two multi-feature nodes in close proximity does not introduce any additional errors other than that associated with the accuracy of the multi-feature approach and the dispersion of TLM method.

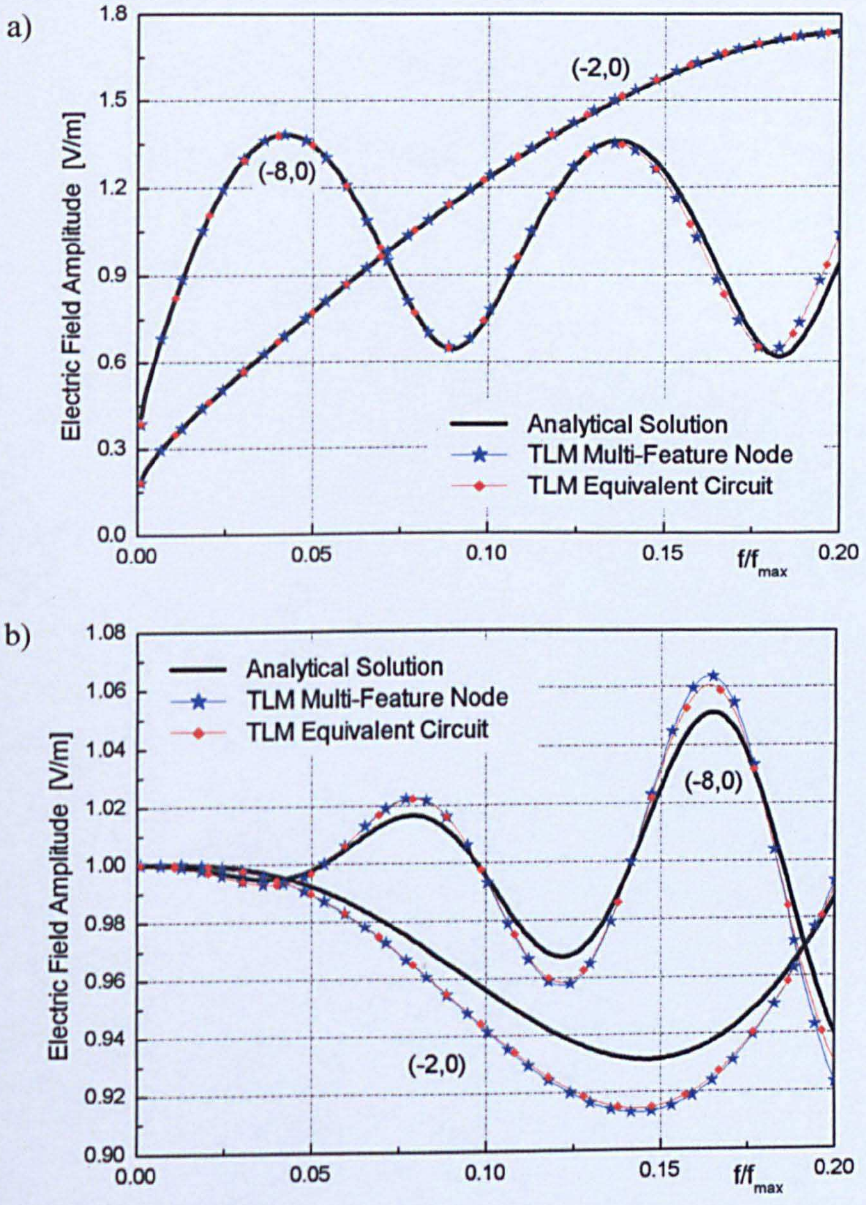

Figure 4.18. Electric field amplitude 2 and 8 nodes in front of two multi-feature nodes placed in close proximity for TM (a) and TE (b) polarisation

In many practical configurations it might be very difficult to employ a uniform coarse mesh distribution that ensures that single wires are located at the centre of a cell. Additional problematic examples involve modelling wire cables, looms and bundles. However, such problems can easily be resolved with the multi-feature approach as it allows embedding of many features inside a single TLM cell. The results of these scenarios are the subject of the next section.

4.5. A Single TLM Node with Multiple Wires

In the section above, the multi-feature node has been proven to provide a good accuracy for the simulation of the fields scattered from a single wire embedded in a coarse cell of TLM mesh. This section validates the more complex problems for which the multi-feature node has been designed, i.e. embedding multiple objects into a single TLM cell. Consideration will now be given to inserting an arbitrary number of conducting wires within a single cell, with arbitrary placement within the cell. It should be clear that it is not expected to be able to develop a universal equivalent circuit analogous to that in Figure 4.6 that mimics the behaviour of such a cell containing many conducting wires. Therefore, only the approach utilising multi-feature node can be employed to describe in sufficient detail the complexity of the problem.

From the derivation presented in this chapter it should be clear that there is no restriction on the positions or radii of the wires, provided that they all lie within the scope of a TLM cell and they do not overlap one another. This method is applicable to a wide range of EMC problems, including a scattering from a single wire placed centrally, as shown in section 4.4.4 of this chapter, scattering from a single wire which is offset from the centre of the cell, through wave propagation in the presence of cluster of wires, to simulation of the fields scattered from wire shields, metal cables and bundles, linear antenna arrays and so on. In this section, the validation of the approach will be presented for the case of fields scattered from a cluster of conducting wires.

Consider the multi-feature node that is positioned at the point (0,0), at the centre of the computational window presented in Figure 4.7. The MN encapsulates six metal wires of arbitrary placement within the node and various radii, as presented in Figure 4.19. Details on the parameters of the wires, their positions and radii are specified in Table 4.2.

No	Radius	Distance r	Angle ϕ
1	0.25Δ	0.00Δ	0°
2	0.40Δ	0.67Δ	40°
3	0.12Δ	0.50Δ	130°
4	0.10Δ	0.62Δ	160°
5	0.35Δ	0.65Δ	225°
6	0.30Δ	0.60Δ	320°

Table 4.2. Parameters of the wires embedded in a single TLM cell.

In Table 4.2, the position of each of the wires is given by (r,ϕ), where r denotes the distance between the wire centre and the centre of the node and ϕ is the angle between the node's positive x-axis and the radius r. The simulation is excited by a Gaussian Pulse of RMS width 2.5 time-steps and the fields are measured in a near and far-field region, assigned 2 and 8 nodes respectively in line with the MN and in front of it, looking from the direction of wave propagation. A computational window of 1000 by 1000 nodes is used. The TLM nodes of radius $\Delta = 0.025\,\mathrm{m}$ are used and the time-domain procedure iterates for 2048 time-steps.

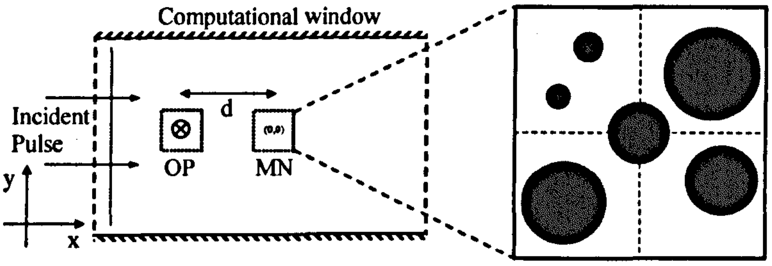

Figure 4.19. A numerical configuration for a simulation of a TLM cell containing multiple wires

Before the complete numerical results are presented, justification of the approximation to the analytical solution for this problem to only four harmonics will be given in a similar fashion to that for the single wire case.

The exact solution illustrated in Figure 4.20 was calculated using $n = 20$ harmonics. It is observed that over the frequency range for which the TLM method is regarded as accurate, i.e. $f/f_{max} = 0.1$, the four lowest order harmonics closely match the exact solution.

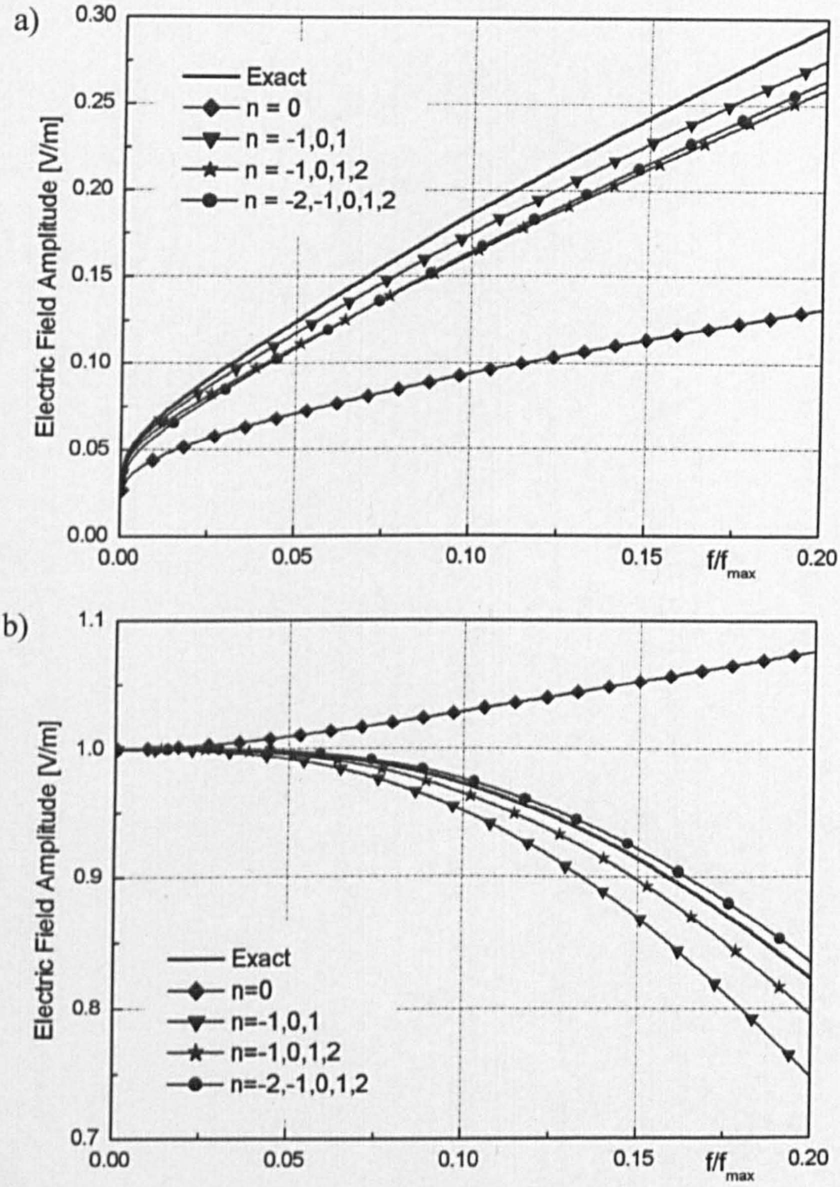

Figure 4.20. A Convergence of analytical solution for a cluster of wires for TM (a) and TE (b) polarisation

The results of the numerical simulations are presented in Figure 4.21 for the TM polarisation and Figure 4.22 for the TE polarisations.

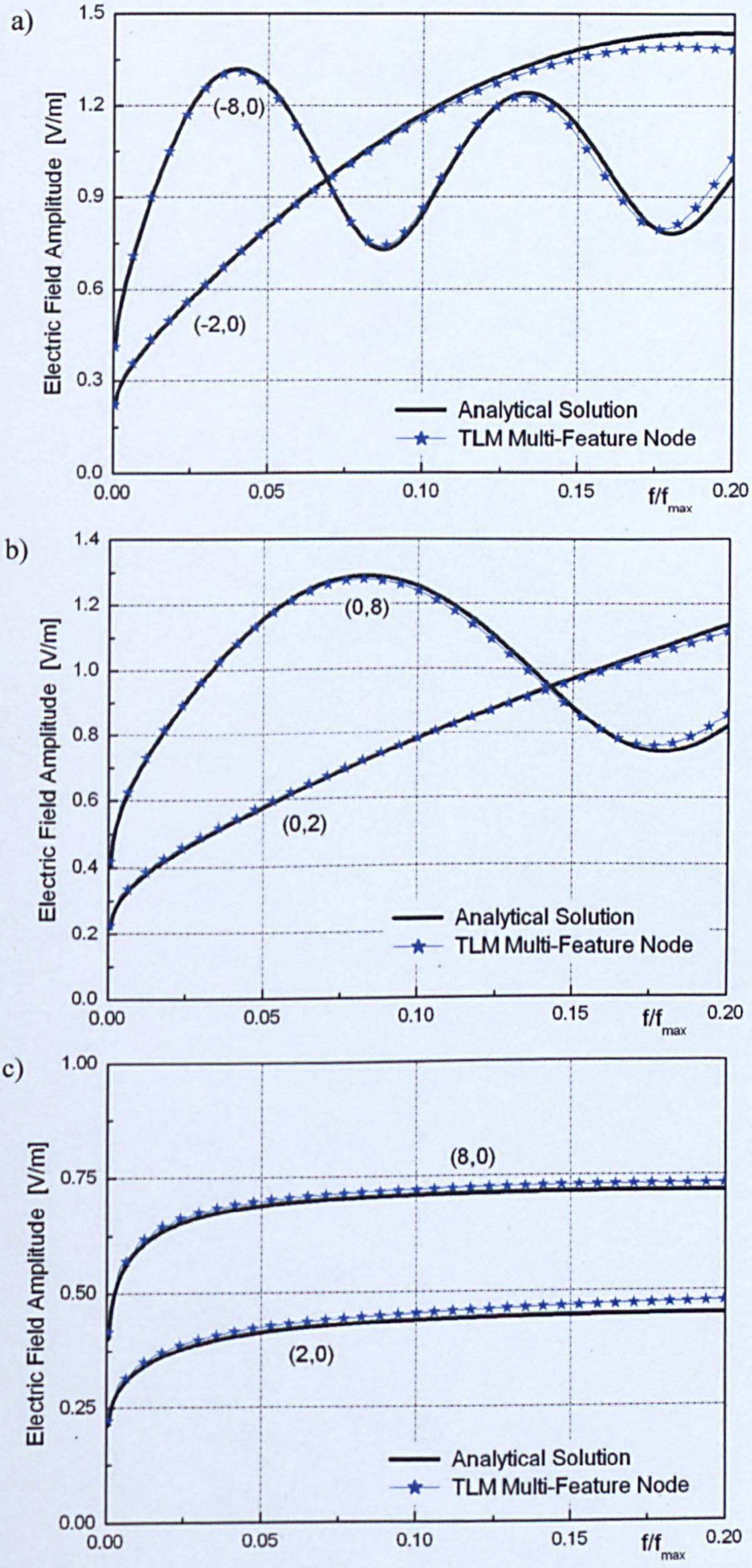
a)
Electric Field Amplitude [V/m]
1.5
1.2
0.9
0.6
0.3
0.0
0.00
0.05
0.10
0.15
0.20
f/f$_{max}$
(-8,0)
(-2,0)
Analytical Solution
TLM Multi-Feature Node
b)
Electric Field Amplitude [V/m]
1.4
1.2
1.0
0.8
0.6
0.4
0.2
0.0
0.00
0.05
0.10
0.15
0.20
f/f$_{max}$
(0,8)
(0,2)
Analytical Solution
TLM Multi-Feature Node
c)
Electric Field Amplitude [V/m]
1.00
0.75
0.50
0.25
0.00
0.00
0.05
0.10
0.15
0.20
f/f$_{max}$
(8,0)
(2,0)
Analytical Solution
TLM Multi-Feature Node

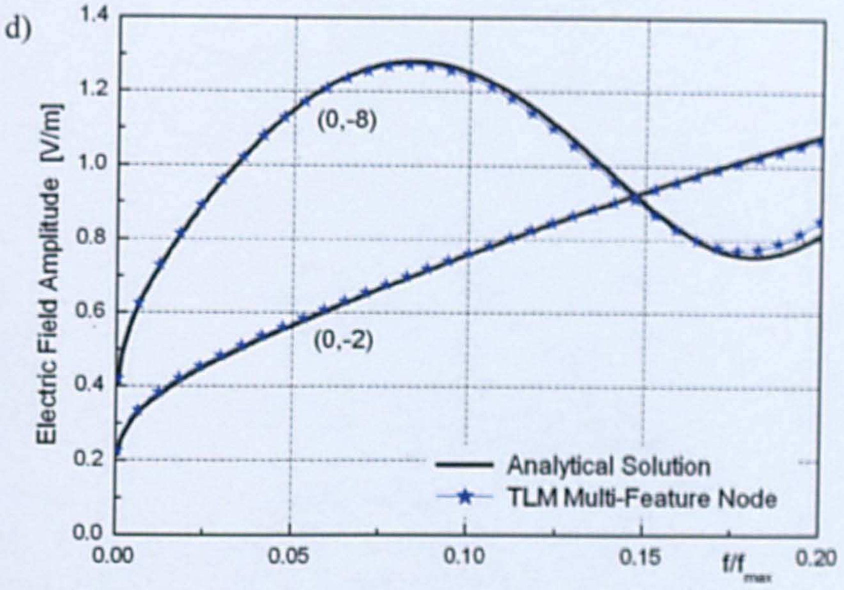

Figure 4.21. Amplitude of the TM polarised total electric field in the near and far-field zone in front (a) behind (b), and to both sides (c) and (d) of the MN

Figure 4.21 presents the amplitude of the total electric field scattered from the multi-feature node with six wires embedded within in both the near and far-field zones. The fields are observed in front, behind and to both sides of the multi-feature node. As can be seen, the numerical results for the TM polarisation are in excellent agreement with the analytical solution for both the near and far-field regions, even for frequencies well beyond the dispersion-less operating range of the TLM method.

Figure 4.22 presents the TE polarised total electric field amplitude for the case of the multi-feature node containing six wires.

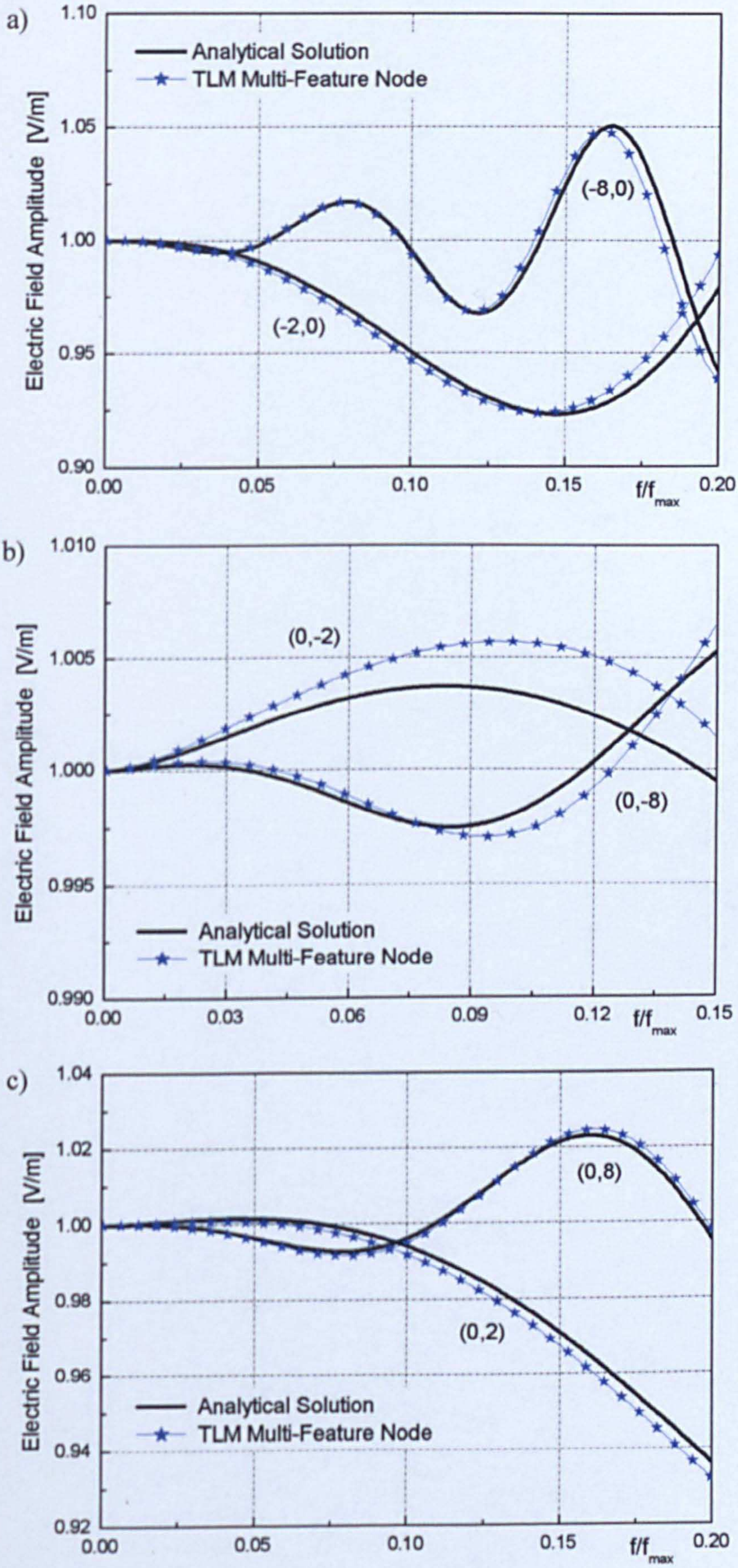
a)
Analytical Solution
TLM Multi-Feature Node
Electric Field Amplitude [V/m]
1.10
1.05
1.00
0.95
0.90
0.00
0.05
0.10
0.15
0.20
f/f$_{max}$
(-8,0)
(-2,0)
b)
1.010
1.005
1.000
0.995
0.990
0.00
0.03
0.06
0.09
0.12
0.15
f/f$_{max}$
(0,-2)
(0,-8)
Electric Field Amplitude [V/m]
Analytical Solution
TLM Multi-Feature Node
c)
1.04
1.02
1.00
0.98
0.96
0.94
0.92
0.00
0.05
0.10
0.15
0.20
f/f$_{max}$
(0,8)
(0,2)
Electric Field Amplitude [V/m]
Analytical Solution
TLM Multi-Feature Node

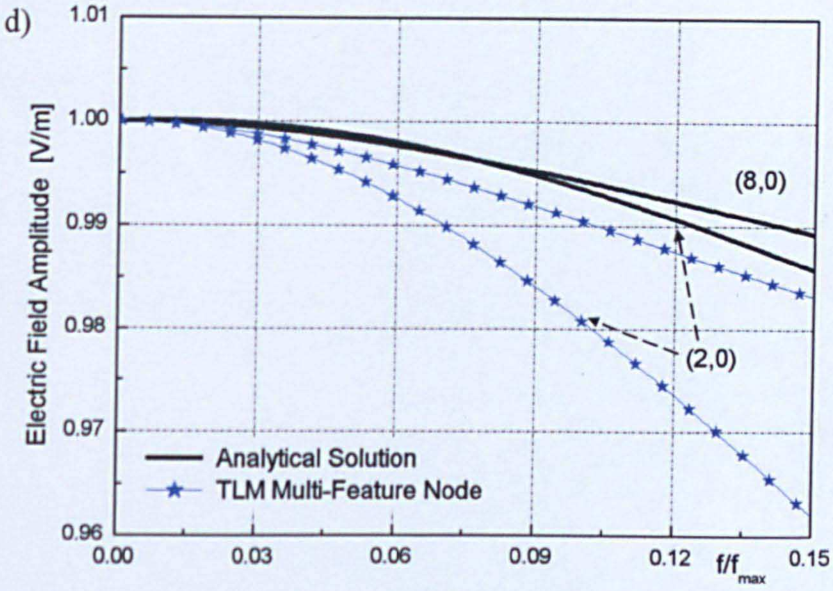

Figure 4.22. Amplitude of the TE polarised total electric field in the near and far-field zone in front (a) behind (b) and to both sides (c) and (d) of the MN

It is again observed that very good agreement between the results using multi-feature node and from the analytical solution for TE polarisation is achieved. Almost exact matching is seen for fields in front and both of the sides of the node containing six wires. Even the weak scattering is quite well estimated. A slightly larger error is observed when the OP is positioned in the shadow of the multi-feature node, i.e. behind the MN. The near field for that scenario is more in error when compared to the fields measured at the remaining OPs. However, the distribution follows the trend of changes exhibited by analytical solution. Despite the visible deviation the absolute error for the near field is only 1.3% for $f/f_{max} = 0.1$

The ability of a multi-feature node with multiple embedded wires to correctly predict the phase of the signal is demonstrated in Figure 4.23. Both, TM and TE polarisations are considered. The phase of the scattered signal is captured at 2 and 8 nodes in front of the multi-feature node. It is observed in Figure 4.23 that the multi-node is capable, not only of accurately modelling the amplitudes of the fields, but also their phases. For both polarisations, the analytical solution is well rendered by the results of the numerical simulations.

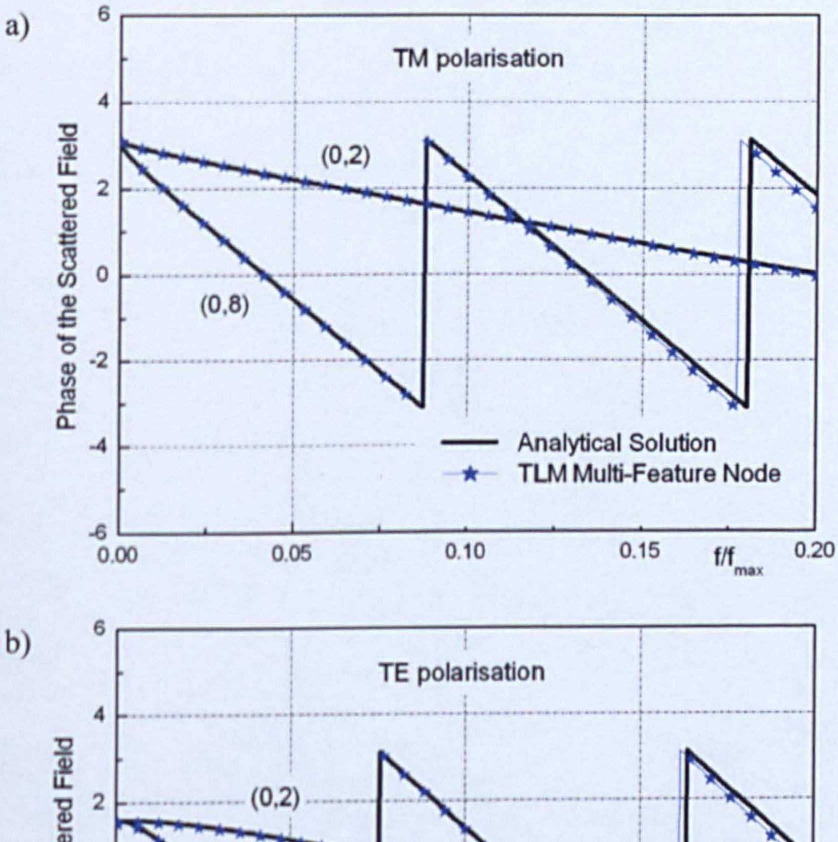

Figure 4.23. The phase of the field scattered from TM polarised (a) and TE polarised (b) node with multiple wires

4.6. Closing Remarks

In this chapter, the multi-feature node has been developed that enables multiple conducting wires to be embedded with second order accuracy into a single TLM cell. The approach utilises an analytical derivation to account for mutual interactions between the wires in close proximity. This analytical solution is appropriately sampled at the edges of the 2D TLM node and linked with the time-domain algorithm, using the mode decomposition and short length transmission lines with short or open-circuit terminations.

The results of the approach was first validated for the case of a single wire, positioned centrally within the node before the technique was applied to cells enclosing multiple wires. In both scenarios the approach was proven to be accurate even for frequencies beyond which the TLM is regarded as dispersionless. Both the amplitude of the field and its phase were modelled well and the results were shown for two different polarisations, namely TM and TE. No numerical instabilities were found when employing the multi-feature approach to a range of engineering problems. It is underlined that the TM polarisation features stronger scattering which increases the level of mutual interactions and interference between the elements of the system, placing a greater demand for high EMI immunity of the body under EMC tests. Nevertheless, the results for TE polarisation were demonstrated to illustrate that even when a weak electromagnetic field variation is concerned, the proposed approach is capable of modelling those small deviations with the accuracy required for EMC applications.

4.7. References

[4.1] Choong, Y.K., Sewell, P., Christopoulos, C., "*New thin wire formulation for Time-Domain differential-equation models*", Intern. Journal of Numerical Modelling, vol. 15, pp. 489–501, 2002

[4.2] Gradshteyn, I.S., Ryzhik I.M., Jeffrey Alan (Editor), "*Table of Integrals, Series, and Products*", Academic Press, San Diego, CA, pp. 879, 1993

[4.3] Morse, P.M., Freshbach, H., "Methods of Theoretical Physics, McGraw-Hill Book Company", Inc., New York, 1953

[4.4] Choong, Y.K., Sewell, P., Christopoulos, C., "*Hybrid node for description of thin wires based on analytical field representation in EMC problems*", IEEE 2002 International Symposium on Electromagnetic Compatibility, Minneapolis, Minnesota USA, August 19-23, 2002

[4.5] Naylor, P., and Christopoulos, C., "*A new wire node for modeling thin wires in electromagnetic field problems solved by transmission line modeling*", IEEE Trans. on Microwave Theory and Techniques, Vol. 38, No. 3, pp 328-330, 1990

[4.6] Hoefer, W.J.R., So, P.P.M., "*The Electromagnetic Wave Simulator*", John Wiley & Sons, Chichester, 1991

[4.7] Christopoulos, C., "*The Transmission-Line Modeling Method: TLM*", Piscataway, NJ: IEEE Press, 1995

[4.8] Staelin, D.H., Morgenthaler, A.W., Kong, J.A., "*Electromagnetic Waves*", Prentice-Hall International, Inc., New Jersey, 1994

Chapter 5

Modelling Dielectric Fine Features in a Coarse Mesh

In this chapter, the theoretical formulations for the problem of a wave scattered from a cluster of cylinders of different characteristics, rather than perfect conductors, will be presented. This includes scattering from dielectric rods, dielectric coated wires and wires shielded with an arbitrary number of dielectric layers. Initially, the necessary conditions that have to be satisfied at the surface of dielectric rods to maintain field continuity will be considered. Similarly to the case of conducting wires embedded in a single numerical cell presented in Chapter 4, the admittance relationship between the field quantities $\underline{\underline{H}} = \underline{Y} \cdot \underline{\underline{E}}$ will be evaluated at the edges of the cell containing the objects. The derivations will be delivered for both field polarisations, namely TE and TM. Validation of the theory given will be demonstrated for a number of practical examples.

5.1. Formulation of Dielectric Cylindrical Boundary

In this section, the analytical formulations for a field scattered from a cluster of dielectric cylinders will be given. The derivations will be based upon the case of conducting wires enclosed in a single TLM cell demonstrated in Chapter 4, and will deal with the two field polarisations separately.

5.1.1. TM Polarised Wave

This paragraph presents the field formulae for the case of dielectric rods embedded in a single TLM cell, with reference to Figure 4.1 from Chapter 4 where now the cylindrical scatterers are dielectric rods rather than conducting wires. In the case of electromagnetic wave incident from free space and scattered from dielectric surface, two regions of interest are distinguished:

(i) free space region of intrinsic admittance $\gamma = \gamma_0 = \sqrt{\varepsilon_0 / \mu_0}$ and the wavenumber $k = k_0 = \omega\sqrt{\mu_0 \varepsilon_0}$, and

(ii) dielectric region of parameters $\gamma_D = \sqrt{\varepsilon_0 \varepsilon_D / \mu_0 \mu_D} = \gamma_0 n_D$ and $k_D = \omega\sqrt{\mu_0 \mu_D \varepsilon_0 \varepsilon_D} = k_0 n_D$, where $n_D = \sqrt{\varepsilon_D}$ is a refractive index of the dielectric.

Both areas consist of non-magnetic materials, therefore the permeability $\mu_D = 1$.

In the presence of homogeneous dielectric posts the total electric and magnetic field for TM polarised fields in the region (ε_0, μ_0) can be described in a polar coordinate system centred on the p^{th} cylinder, as derived in Chapter 4:

$$E_z(r \ge a_p, \phi) = \underline{g}_p^T \underline{\underline{U}}_{0p} \underline{X}_0 + \underline{f}_p^T \underline{X}_p + \sum_{q \ne p} \underline{g}_p^T \underline{\underline{T}}_{qp} \underline{X}_q \tag{5.1}$$

$$\begin{aligned} H_\theta(r \ge a_p, \phi) &= \frac{1}{j\omega\mu_0} \frac{\partial E_z}{\partial r} = \frac{k_0}{j\omega\mu_0} \left(\underline{g}_p'^T \underline{\underline{U}}_{0p} \underline{X}_0 + \underline{f}_p'^T \underline{X}_p + \sum_{q \ne p} \underline{g}_p'^T \underline{\underline{T}}_{qp} \underline{X}_q \right) \\ &= -j\gamma_0 \left(\underline{g}_p'^T \underline{\underline{U}}_{0p} \underline{X}_0 + \underline{f}_p'^T \underline{X}_p + \sum_{q \ne p} \underline{g}_p'^T \underline{\underline{T}}_{qp} \underline{X}_q \right) \end{aligned} \tag{5.2}$$

The elements $f_{pn}, f'_{pn}, g_{pn}, g'_{pn}$ are specified by:

$$\begin{aligned} f_{pn} &= e^{-jn\phi_p} H_n^{(2)}(kr_p) \quad \text{and} \quad f'_{pn} = e^{-jn\phi_p} H'^{(2)}_n(kr_p) \\ g_{pn} &= e^{-jn\phi_p} J_n(kr_p) \quad \text{and} \quad g'_{pn} = e^{-jn\phi_p} J'_n(kr_p) \end{aligned} \tag{5.3}$$

where $J'_n(kr_p) = \dfrac{dJ'_n(kr_p)}{d(kr_p)}$ and $H'^{(2)}_n(kr_p) = \dfrac{dH'^{(2)}_n(kr_p)}{d(kr_p)}$,

The boundary condition requires continuity of the tangential field components at the interface $r_p = a_p$ where a_p is the radius of the p^{th} cylinder, thus:

$$\begin{aligned} (\underline{E}^0 - \underline{E}^D) \times \hat{\mathbf{r}} &= 0 \\ (\underline{H}^0 - \underline{H}^D) \times \hat{\mathbf{r}} &= 0 \end{aligned} \tag{5.4}$$

where the superscript *D* denotes fields in the dielectric region and *0* fields in empty space. Hence, the boundary condition can be formulated in the form:

$$\begin{aligned} &\left(\underline{g}_p^0\right)^T \underline{\underline{U}}_{0p}^0 \underline{X}_0^0 + \left(\underline{f}_p^0\right)^T \underline{X}_p^0 + \sum_{q \neq p} \left(\underline{g}_p^0\right)^T \underline{\underline{T}}_{qp}^0 \underline{X}_q^0 \\ &\qquad = \left(\underline{g}_p^D\right)^T \underline{\underline{U}}_{0p}^D \underline{X}_0^D + \left(\underline{f}_p^D\right)^T \underline{X}_p^D + \sum_{q \neq p} \left(\underline{g}_p^D\right)^T \underline{\underline{T}}_{qp}^D \underline{X}_q^D \end{aligned} \tag{5.5}$$

$$\begin{aligned} &\gamma_0 \left(\left(\underline{g}_p'^0\right)^T \underline{\underline{U}}_{0p}^0 \underline{X}_0^0 + \left(\underline{f}_p'^0\right)^T \underline{X}_p^0 + \sum_{q \neq p} \left(\underline{g}_p'^0\right)^T \underline{\underline{T}}_{qp}^0 \underline{X}_q^0 \right) \\ &\qquad = \gamma_D \left(\left(\underline{g}_p'^D\right)^T \underline{\underline{U}}_{0p}^D \underline{X}_0^D + \left(\underline{f}_p'^D\right)^T \underline{X}_p^D + \sum_{q \neq p} \left(\underline{g}_p'^D\right)^T \underline{\underline{T}}_{qp}^D \underline{X}_q^D \right) \end{aligned} \tag{5.6}$$

At the origin $r_p = 0$, the Bessel functions of the second kind are infinite for any order and for that reason are not included in the final field solutions on the rods, hence $\underline{X}_p^D = 0$. Assuming linear, homogenous and isotropic media the boundary conditions are finally expressed as:

$$\left(\underline{g}_p^0\right)^T \underline{\underline{U}}_{0p}^0 \underline{X}_0^0 + \left(\underline{f}_p^0\right)^T \underline{X}_p^0 + \sum_{q \neq p} \left(\underline{g}_p^0\right)^T \underline{\underline{T}}_{qp}^0 \underline{X}_q^0 = \left(\underline{g}_p^D\right)^T \underline{\underline{U}}_{0p}^D \underline{X}_0^D \tag{5.7}$$

$$\left(\underline{g}'^{0}_{p}\right)^{T}\underline{\underline{U}}^{0}_{0p}\underline{X}^{0}_{0}+\left(\underline{f}'^{0}_{p}\right)^{T}\underline{X}^{0}_{p}+\sum_{q\neq p}\left(\underline{g}'^{0}_{p}\right)^{T}\underline{\underline{T}}^{0}_{qp}\underline{X}^{0}_{q}=\gamma_{0}^{-1}\gamma_{D}\left(\underline{g}'^{D}_{p}\right)^{T}\underline{\underline{U}}^{D}_{0p}\underline{X}^{D}_{0} \tag{5.8}$$

It should be pointed out that having only two sets of equations for each wire it is impossible to obtain an explicit solution for the three unknown vectors of coefficients; namely $\underline{X}^{D}_{0}$, $\underline{X}^{0}_{0}$, $\underline{X}^{0}_{p(q)}$. One way to resolve that problem is to construct the admittance relationship at the interface between the regions of different permittivity in the form of $\underline{\underline{H}}=\underline{Y}\cdot\underline{\underline{E}}$. Substituting the expression for the E and H-field given by Equations (5.1) and (5.2) yields:

$$\begin{aligned}&\left(\underline{g}'^{0}_{p}\right)^{T}\underline{\underline{U}}^{0}_{0p}\underline{X}^{0}_{0}+\left(\underline{f}'^{0}_{p}\right)^{T}\underline{X}^{0}_{p}+\sum_{q\neq p}\left(\underline{g}'^{0}_{p}\right)^{T}\underline{\underline{T}}^{0}_{qp}\underline{X}^{0}_{q}\\&\quad=j\frac{\underline{Y}}{\gamma_{0}}\left(\left(\underline{g}^{0}_{p}\right)^{T}\underline{\underline{U}}^{0}_{0p}\underline{X}^{0}_{0}+\left(\underline{f}^{0}_{p}\right)^{T}\underline{X}^{0}_{p}+\sum_{q\neq p}\left(\underline{g}^{0}_{p}\right)^{T}\underline{\underline{T}}^{0}_{qp}\underline{X}^{0}_{q}\right)\end{aligned} \tag{5.9}$$

where the functions f_p, g_p and their derivatives are evaluated for the argument $kr_p = k_0a_p$. Utilising the right-hand side of Equation (5.7) and (5.8) into (5.9) leads to:

$$\frac{\gamma_{D}}{\gamma_{0}}\left(\underline{g}'^{D}_{p}\right)^{T}\underline{\underline{U}}^{D}_{0p}\underline{X}^{D}_{0}=j\frac{\underline{Y}}{\gamma_{0}}\left(\underline{g}^{D}_{p}\right)^{T}\underline{\underline{U}}^{D}_{0p}\underline{X}^{D}_{0} \tag{5.10}$$

Rearranging gives:

$$j\frac{\underline{Y}}{\gamma_{0}}=\frac{\gamma_{D}}{\gamma_{0}}\frac{\left(\underline{g}'^{D}_{p}\right)^{T}}{\left(\underline{g}^{D}_{p}\right)^{T}}=\frac{\gamma_{D}}{\gamma_{0}}\frac{\left(\underline{J}'^{D}\right)^{T}}{\left(\underline{J}^{D}\right)^{T}}=\underline{K} \tag{5.11}$$

where the vectors $\underline{J}^{D}$ and $\underline{J}'^{D}$ consist of elements $J_n(k_Da_p)$ and $J'_n(k_Da_p)$ respectively. Substituting Equation (5.11) into the boundary admittance relationship defined in Equation (5.9) results in:

$$\begin{aligned}&\left(\underline{g}'^{0}_{p}\right)^{T}\underline{\underline{U}}^{0}_{0p}\underline{X}^{0}_{0}+\left(\underline{f}'^{0}_{p}\right)^{T}\underline{X}^{0}_{p}+\sum_{q\neq p}\left(\underline{g}'^{0}_{p}\right)^{T}\underline{\underline{T}}^{0}_{qp}\underline{X}^{0}_{q}\\&\qquad=\frac{\gamma_{D}}{\gamma_{0}}\frac{\underline{J}'^{D}}{\underline{J}^{D}}\left(\left(\underline{g}^{0}_{p}\right)^{T}\underline{\underline{U}}^{0}_{0p}\underline{X}^{0}_{0}+\left(\underline{f}^{0}_{p}\right)^{T}\underline{X}^{0}_{p}+\sum_{q\neq p}\left(\underline{g}^{0}_{p}\right)^{T}\underline{\underline{T}}^{0}_{qp}\underline{X}^{0}_{q}\right)\end{aligned}\tag{5.12}$$

After some mathematical arrangements one obtains:

$$\underline{\underline{U}}^{0}_{0p}\underline{X}^{0}_{0}+\frac{\left(\underline{f}'^{0}_{p}\right)^{T}-\underline{\kappa}\left(\underline{f}^{0}_{p}\right)^{T}}{\left(\underline{g}'^{0}_{p}\right)^{T}-\underline{\kappa}\left(\underline{g}^{0}_{p}\right)^{T}}\underline{X}^{0}_{p}+\sum_{q\neq p}\underline{\underline{T}}^{0}_{qp}\underline{X}^{0}_{q}=0\tag{5.13}$$

where $\underline{\kappa}$ is determined in Equation (5.11).

Analogously to the scheme adopted in Chapter 4, the procedure described by Equations (5.1) to (5.13) needs to be carried out for every single dielectric rod enclosed in the TLM cell and the boundary condition applied at the surface of each. This process will result in a set of linear equations of the form:

$$\begin{pmatrix}\underline{\underline{A}}_{1} & \underline{\underline{T}}_{12} & \underline{\underline{T}}_{13} & \cdot\cdot\\ \underline{\underline{T}}_{21} & \underline{\underline{A}}_{2} & \underline{\underline{T}}_{23} & \cdot\cdot\\ \underline{\underline{T}}_{31} & \underline{\underline{T}}_{32} & \underline{\underline{A}}_{3} & \cdot\cdot\\ \cdot\cdot & \cdot\cdot & \cdot\cdot & \cdot\cdot\end{pmatrix}\begin{pmatrix}\underline{X}^{0}_{1}\\ \underline{X}^{0}_{2}\\ \underline{X}^{0}_{3}\\ \cdots\end{pmatrix}=-\begin{pmatrix}\underline{\underline{U}}_{01}\underline{X}^{0}_{0}\\ \underline{\underline{U}}_{02}\underline{X}^{0}_{0}\\ \underline{\underline{U}}_{03}\underline{X}^{0}_{0}\\ \cdots\end{pmatrix}=-\begin{pmatrix}\underline{\underline{U}}_{01}\\ \underline{\underline{U}}_{02}\\ \underline{\underline{U}}_{03}\\ \cdots\end{pmatrix}\underline{X}^{0}_{0}\tag{5.14}$$

where the dielectric posts are numbered from 1.

This is a similar expression to that presented in Equation (4.21) in Chapter 4, with the only difference lying in the components $\underline{\underline{A}}_{p}$ constructed as:

$$\underline{\underline{A}}_{p}=\frac{\left(\underline{f}'^{0}_{p}\right)^{T}-\underline{\kappa}\left(\underline{f}^{0}_{p}\right)^{T}}{\left(\underline{g}'^{0}_{p}\right)^{T}-\underline{\kappa}\left(\underline{g}^{0}_{p}\right)^{T}}\tag{5.15}$$

Thus the *nth* element of the diagonal matrix $\underline{\underline{A}}$ is defined by:

$$A_{np}=\frac{\gamma_{0}H'^{(2)}_{n}(k_{0}a_{p})J_{n}(k_{D}a_{p})-\gamma_{D}J'_{n}(k_{D}a_{p})H^{(2)}_{n}(k_{0}a_{p})}{\gamma_{0}J'_{n}(k_{0}a_{p})J_{n}(k_{D}a_{p})-\gamma_{D}J'_{n}(k_{D}a_{p})J_{n}(k_{0}a_{p})}\tag{5.16}$$

It is clear from the foregoing derivation that each cylindrical object embedded in the cell can possess a different geometry and material properties.

In order to use the solution of Equation (5.14) in the numerical scheme, the vector of scattered field coefficients $\underline{X}_s^T = [\underline{X}_1 \quad \underline{X}_2 \quad \underline{X}_3 \quad \dots]^T$ has to be now re-expressed in a polar coordinate system centred at the TLM cell. This is done by means of Green's functions. This procedure has already been demonstrated in Chapter 4, for the case of conducting wires encased in a TLM cell, and for brevity will not be repeated here. Also the algorithm to impose the eigenvalue problem, necessary to link the field solutions with the adjacent nodes of the TLM grid, has been illustrated in the Chapter 4 and is therefore omitted from this section. Instead in the next section, the field derivations for a cluster of dielectric posts excited by a TE polarised plane wave will be presented.

5.1.2. TE Polarised Wave

Here, the solution for the electromagnetic field behaviour in the presence of dielectric rods inserted in a single empty space cell of TLM model and excited by a plane wave with its electric field polarised perpendicular to the cylinder axis is derived. In the region (ε_0, μ_0), the fields are described by Maxwell's equations and can be expressed in a polar coordinate system centred on the cylinder p^{th} as:

$$H_z(r \geq a_p, \phi) = j\gamma \left(\underline{g}_p^T \underline{\underline{U}}_{0p} \underline{X}_0 + \underline{f}_p^T \underline{X}_p + \sum_{q \neq p} \underline{g}_p^T \underline{\underline{T}}_{qp} \underline{X}_q \right) \tag{5.17}$$

$$\begin{aligned} E_\theta(r \geq a_p, \phi) &= \frac{1}{j\omega\varepsilon}\frac{\partial H_z}{\partial r} = \frac{jk}{j\omega\varepsilon\gamma}\left(\underline{g}'^{T}_{p}\,\underline{\underline{U}}_{0p}\,\underline{X}_0 + \underline{f}'^{T}_{p}\,\underline{X}_p + \sum_{q\neq p}\underline{g}'^{T}_{p}\,\underline{\underline{T}}_{qp}\,\underline{X}_q \right) \\ &= \underline{g}'^{T}_{p}\,\underline{\underline{U}}_{0p}\,\underline{X}_0 + \underline{f}'^{T}_{p}\,\underline{X}_p + \sum_{q\neq p}\underline{g}'^{T}_{p}\,\underline{\underline{T}}_{qp}\,\underline{X}_q \end{aligned} \tag{5.18}$$

where $\gamma_0 = \sqrt{\varepsilon_0/\mu_0}$ is the intrinsic admittance of the medium, k_0 is the empty space wavenumber and $f_{pn}, f'_{pn}, g_{pn}, g'_{pn}$ have been defined in Equation (5.3). To ensure that the fields are continuous at the interface between empty space and the dielectric material, the boundary conditions formulated in Equation (5.4) have to be satisfied.

Thus, for the magnetic field continuity one obtains:

$$\begin{aligned} &\gamma_0\left(\left(\underline{g}^{0}_{p}\right)^{T}\underline{\underline{U}}^{0}_{0p}\,\underline{X}^{0}_{0} + \left(\underline{f}^{0}_{p}\right)^{T}\underline{X}^{0}_{p} + \sum_{q\neq p}\left(\underline{g}^{0}_{p}\right)^{T}\underline{\underline{T}}^{0}_{qp}\,\underline{X}^{0}_{q} \right) \\ &\qquad = \gamma_D\left(\left(\underline{g}^{D}_{p}\right)^{T}\underline{\underline{U}}^{D}_{0p}\,\underline{X}^{D}_{0} + \left(\underline{f}^{D}_{p}\right)^{T}\underline{X}^{D}_{p} + \sum_{q\neq p}\left(\underline{g}^{D}_{p}\right)^{T}\underline{\underline{T}}^{D}_{qp}\,\underline{X}^{D}_{q} \right) \end{aligned} \tag{5.19}$$

and for electric field continuity:

$$\begin{aligned} &\left(\underline{g}'^{0}_{p}\right)^{T}\underline{\underline{U}}^{0}_{0p}\,\underline{X}^{0}_{0} + \left(\underline{f}'^{0}_{p}\right)^{T}\underline{X}^{0}_{p} + \sum_{q\neq p}\left(\underline{g}'^{0}_{p}\right)^{T}\underline{\underline{T}}^{0}_{qp}\,\underline{X}^{0}_{q} \\ &\qquad = \left(\underline{g}'^{D}_{p}\right)^{T}\underline{\underline{U}}^{D}_{0p}\,\underline{X}^{D}_{0} + \left(\underline{f}'^{D}_{p}\right)^{T}\underline{X}^{D}_{p} + \sum_{q\neq p}\left(\underline{g}'^{D}_{p}\right)^{T}\underline{\underline{T}}^{D}_{qp}\,\underline{X}^{D}_{q} \end{aligned} \tag{5.20}$$

The admittance relationship in the form of $\underline{\underline{H}} = \underline{Y}\cdot\underline{\underline{E}}$ is now constructed for a TE mode from Maxwell's equations at the surface of the p^{th} rod leading to:

$$\begin{aligned} &\left(\underline{g}^{0}_{p}\right)^{T}\underline{\underline{U}}^{0}_{0p}\,\underline{X}^{0}_{0} + \left(\underline{f}^{0}_{p}\right)^{T}\underline{X}^{0}_{p} + \sum_{q\neq p}\left(\underline{g}^{0}_{p}\right)^{T}\underline{\underline{T}}^{0}_{qp}\,\underline{X}^{0}_{q} \\ &\qquad = \frac{\underline{Y}}{j\gamma_0}\left(\left(\underline{g}'^{0}_{p}\right)^{T}\underline{\underline{U}}^{0}_{0p}\,\underline{X}^{0}_{0} + \left(\underline{f}'^{0}_{p}\right)^{T}\underline{X}^{0}_{p} + \sum_{q\neq p}\left(\underline{g}'^{0}_{p}\right)^{T}\underline{\underline{T}}^{0}_{qp}\,\underline{X}^{0}_{q} \right) \end{aligned} \tag{5.21}$$

Assuming finite fields, the terms containing Hankel functions in the region where $r = 0$ are removed from Equations (5.19) and (5.20), and these two equations are substituted into Equation (5.21), resulting in:

$$\frac{\gamma_D}{\gamma_0}\left(\underline{g}_p^D\right)^T \underline{\underline{U}}_{0p}^D \underline{X}_0^D = \frac{Y}{j\gamma_0}\left(\underline{g}'^D_p\right)^T \underline{\underline{U}}_{0p}^D \underline{X}_0^D \tag{5.22}$$

Rearranging yields:

$$\frac{Y}{j\gamma_0} = \frac{\gamma_D}{\gamma_0}\frac{\left(\underline{g}_p^D\right)^T}{\left(\underline{g}'^D_p\right)^T} = \frac{\gamma_D}{\gamma_0}\frac{\left(\underline{J}^D\right)^T}{\left(\underline{J}'^D\right)^T} = \underline{\kappa} \tag{5.23}$$

where the vectors $\underline{J}^D$ and $\underline{J}'^D$ consist of elements $J_n(k_D a_p)$ and $J'_n(k_D a_p)$ respectively. Substituting Equation (5.23) into the boundary admittance relationship given by Equation (5.21) leads to:

$$\begin{aligned}&\left(\underline{g}_p^0\right)^T \underline{\underline{U}}_{0p}^0 \underline{X}_0^0 + \left(\underline{f}_p^0\right)^T \underline{X}_p^0 + \sum_{q\neq p}\left(\underline{g}_p^0\right)^T \underline{\underline{T}}_{qp}^0 \underline{X}_q^0 \\ &\qquad = \frac{\gamma_D}{\gamma_0}\frac{\underline{J}^D}{\underline{J}'^D}\left(\left(\underline{g}'^0_p\right)^T \underline{\underline{U}}_{0p}^0 \underline{X}_0^0 + \left(\underline{f}'^0_p\right)^T \underline{X}_p^0 + \sum_{q\neq p}\left(\underline{g}'^0_p\right)^T \underline{\underline{T}}_{qp}^0 \underline{X}_q^0\right)\end{aligned} \tag{5.24}$$

After some rearrangement,

$$\underline{\underline{U}}_{0p}^0 \underline{X}_0^0 + \frac{\left(\underline{f}_p^0\right)^T - \underline{\kappa}\left(\underline{f}'^0_p\right)^T}{\left(\underline{g}_p^0\right)^T - \underline{\kappa}\left(\underline{g}'^0_p\right)^T}\underline{X}_p^0 + \sum_{q\neq p}\underline{\underline{T}}_{qp}^0 \underline{X}_q^0 = 0 \tag{5.25}$$

where $\underline{\kappa}$ is defined in Equation (5.23).

Applying the procedure described by Equation (5.19) to (5.25) for every single dielectric rod enclosed by a single TLM cell, the set of linear equations already presented in Equation (5.14) is obtained, except that the elements of diagonal matrix $\underline{\underline{A}}_p$ are now identified as:

$$\underline{\underline{A}}_p = \frac{\left(\underline{f}_p^0\right)^T - \underline{\kappa}\left(\underline{f}'^0_p\right)^T}{\left(\underline{g}_p^0\right)^T - \underline{\kappa}\left(\underline{g}'^0_p\right)^T} \quad . \tag{5.26}$$

Thus the n^{th} element of a matrix $\underline{\underline{A}}$ is given by:

$$A_{np} = \frac{\gamma_0 H_n^{(2)}(k_0 a_p) J'_n(k_D a_p) - \gamma_D J_n(k_D a_p) H'^{(2)}_n(k_0 a_p)}{\gamma_0 J_n(k_0 a_p) J'_n(k_D a_p) - \gamma_D J_n(k_D a_p) J'_n(k_0 a_p)} \tag{5.27}$$

The algorithm for solving for the scattered field coefficients as well as the mapping process has already been demonstrated in Chapter 4 for the case of TE polarised perfectly conducting cylinders and for brevity will not be repeated here.

5.2. Wires with a Single and Multi-Layered Dielectric Coating

An extension of the work discussed in the previous two sub-sections is now presented that allows the incorporation of an arbitrary number of conducting wires (or dielectric rods) with dielectric coatings within a multi-feature node. A derivation of TM polarised electromagnetic field in the presence of dielectric coated conducting wires will be given. The algorithm will be then generalised to the case of wires with coatings that consist of many dielectric layers of different permittivity ε_r. Although the algorithm is demonstrated based on TM polarised excitation, the essential aspects of TE mode are indicated when necessary. Results will be shown for both TM and TE polarisations.

5.2.1. Dielectric Coated Perfect Conducting Wires

Scattering from wires with dielectric coatings can be carried out using the same approach as scattering from simple dielectric rods. The general EM field formulations need to be re-expressed in terms of a polar coordinate system based on one of wires, e.g. the p^{th} wire. For a TM polarized plane wave the fields can be assigned as:

$$E_z(r > d_p, \phi) = \underline{g}_p^T \underline{\underline{U}}_{0p} \underline{X}_0^0 + \underline{f}_p^T \underline{X}_p^0 + \sum_{q \neq p} \underline{g}_p^T \underline{\underline{T}}_{qp} \underline{X}_q^0 \tag{5.28}$$

$$H_\theta(r > d_p, \phi) = -j\gamma_0 \left(\underline{g}'^T_p \underline{\underline{U}}_{0p} \underline{X}_0^0 + \underline{f}'^T_p \underline{X}_p^0 + \sum_{q \neq p} \underline{g}'^T_p \underline{\underline{T}}_{qp} \underline{X}_q^0 \right) \tag{5.29}$$

The outstanding task is to determine the scattered field coefficients $\underline{X}_p^0$ given the excitation coefficients $\underline{X}_0^0$. In order to achieve this, two boundary conditions have to be taken into account, i.e. at the conductor/dielectric interface where $r = a_p$ and at the dielectric/empty space interface where $r = d_p$, and d_p is the radius of a dielectric coating measured from the centre of the cylinder, as shown in Figure 5.1.

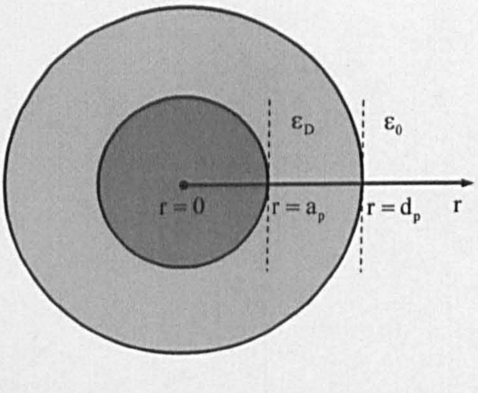

Figure 5.1. An example of dielectric coated wire with marked interfaces between the regions of different permittivity ε

At the first interface $r = a_p$ the total electric field is given by a similar formula to that presented in Equation (5.28)

$$E_z(r=a_p,\phi)=\underline{g}_p^T\underline{\underline{U}}_{0p}\underline{X}_0^a+\underline{f}_p^T\underline{X}_p^a+\sum_{q\neq p}\underline{g}_p^T\underline{\underline{T}}_{qp}\underline{X}_q^a=0 \tag{5.30}$$

It is underlined that the excitation coefficients and scattered coefficients now have superscript *a*, compared to those for fields outside the scatterer in empty space denoted by *0*, as in Equations (5.28) and (5.29). Recognising the fact that the electric field on the surface of each metal wire is zero, a set of linear equations will be formed, with the cylinders numbered from 1:

$$\begin{pmatrix} \underline{\underline{A}}_1 & \underline{\underline{T}}_{12} & \underline{\underline{T}}_{13} & .. \\ \underline{\underline{T}}_{21} & \underline{\underline{A}}_2 & \underline{\underline{T}}_{23} & .. \\ \underline{\underline{T}}_{31} & \underline{\underline{T}}_{32} & \underline{\underline{A}}_3 & .. \\ .. & .. & .. & .. \end{pmatrix}\begin{pmatrix} \hat{\underline{X}}_1^a \\ \hat{\underline{X}}_2^a \\ \hat{\underline{X}}_3^a \\ ... \end{pmatrix}=-\begin{pmatrix} \underline{\underline{U}}_{01} \\ \underline{\underline{U}}_{02} \\ \underline{\underline{U}}_{03} \\ ... \end{pmatrix} \tag{5.31}$$

where the scattered field coefficients have been normalised by the incident wave coefficients i.e. $\hat{\underline{X}}_p=\underline{X}_p/\underline{X}_0$, and elements of diagonal matrices $\underline{\underline{A}}_p$ are evaluated in the form:

for a TM mode: $$A_{np} = H_n^{(2)}(ka_p)/J_n(ka_p) \tag{5.32}$$

and for a TE mode $$A_{np} = H'^{(2)}_n(ka_p)/J'_n(ka_p) \tag{5.33}$$

It should be clear that given the excitation coefficients the vector of coefficients weighting the scattered field $\hat{\underline{X}}_p$ can be explicitly calculated from Equation (5.31).

At the second interface $r=d_p$, the continuity of the electric and magnetic field needs to be preserved. Hence, the following equalities have to be accounted for, as defined in Equation (5.5) and (5.6):

$$\begin{aligned}\left(\underline{g}_p^0\right)^T \underline{\underline{U}}_{0p}^0+\left(\underline{f}_p^0\right)^T \underline{\hat{X}}_p^0+\sum_{q\neq p}\left(\underline{g}_p^0\right)^T \underline{\underline{T}}_{qp}^0 \underline{\hat{X}}_q^0 \\ =\left(\underline{g}_p^D\right)^T \underline{\underline{U}}_{0p}^D+\left(\underline{f}_p^D\right)^T \underline{\hat{X}}_p^a+\sum_{q\neq p}\left(\underline{g}_p^D\right)^T \underline{\underline{T}}_{qp}^D \underline{\hat{X}}_q^a\end{aligned} \tag{5.34}$$

and

$$\begin{aligned}\gamma_0\left(\left(\underline{g}_p^{\prime 0}\right)^T \underline{\underline{U}}_{0p}^0+\left(\underline{f}_p^{\prime 0}\right)^T \underline{\hat{X}}_p^0+\sum_{q\neq p}\left(\underline{g}_p^{\prime 0}\right)^T \underline{\underline{T}}_{qp}^0 \underline{\hat{X}}_q^0\right) \\ =\gamma_D\left(\left(\underline{g}_p^{\prime D}\right)^T \underline{\underline{U}}_{0p}^D+\left(\underline{f}_p^{\prime D}\right)^T \underline{\hat{X}}_p^a+\sum_{q\neq p}\left(\underline{g}_p^{\prime D}\right)^T \underline{\underline{T}}_{qp}^D \underline{\hat{X}}_q^a\right)\end{aligned} \tag{5.35}$$

Contrary to the case of dielectric rods, the Hankel functions cannot be ignored, here they do not represent fields at the origin $r=0$. Expanding the admittance relationship $\underline{\underline{H}}=\underline{Y}\cdot\underline{\underline{E}}$ formulated at the boundary, $r=d_p$ with the expressions for the electric and magnetic fields given in Equation (5.28) and (5.29) yields:

$$\begin{aligned}\left(\underline{g}_p^{\prime 0}\right)^T \underline{\underline{U}}_{0p}^0+\left(\underline{f}_p^{\prime 0}\right)^T \underline{\hat{X}}_p^0+\sum_{q\neq p}\left(\underline{g}_p^{\prime 0}\right)^T \underline{\underline{T}}_{qp}^0 \underline{\hat{X}}_q^0 \\ =j\frac{\underline{Y}}{\gamma_0}\left(\left(\underline{g}_p^0\right)^T \underline{\underline{U}}_{0p}^0+\left(\underline{f}_p^0\right)^T \underline{\hat{X}}_p^0+\sum_{q\neq p}\left(\underline{g}_p^0\right)^T \underline{\underline{T}}_{qp}^0 \underline{\hat{X}}_q^0\right)\end{aligned} \tag{5.36}$$

The left and right-hand side of Equation (5.36) can be substituted from Equations (5.34) and (5.35) respectively, which leads to the following:

TM fields: $$j\frac{\underline{Y}}{\gamma_0}=\frac{\gamma_D}{\gamma_0}\frac{\left(\underline{g}_p^{\prime D}\right)^T \underline{\underline{U}}_{0p}^D+\left(\underline{f}_p^{\prime D}\right)^T \underline{\hat{X}}_p^a+\sum_{q\neq p}\left(\underline{g}_p^{\prime D}\right)^T \underline{\underline{T}}_{qp}^D \underline{\hat{X}}_q^a}{\left(\underline{g}_p^D\right)^T \underline{\underline{U}}_{0p}^D+\left(\underline{f}_p^D\right)^T \underline{\hat{X}}_p^a+\sum_{q\neq p}\left(\underline{g}_p^D\right)^T \underline{\underline{T}}_{qp}^D \underline{\hat{X}}_q^a}=\underline{\kappa} \tag{5.37}$$

TE fields: $$j\frac{\underline{Y}}{\gamma_0}=\frac{\gamma_D}{\gamma_0}\frac{\left(\underline{g}_p^D\right)^T \underline{\underline{U}}_{0p}^D+\left(\underline{f}_p^D\right)^T \underline{\hat{X}}_p^a+\sum_{q\neq p}\left(\underline{g}_p^D\right)^T \underline{\underline{T}}_{qp}^D \underline{\hat{X}}_q^a}{\left(\underline{g}_p^{\prime D}\right)^T \underline{\underline{U}}_{0p}^D+\left(\underline{f}_p^{\prime D}\right)^T \underline{\hat{X}}_p^a+\sum_{q\neq p}\left(\underline{g}_p^{\prime D}\right)^T \underline{\underline{T}}_{qp}^D \underline{\hat{X}}_q^a}=\underline{\kappa} \tag{5.38}$$

Updating and rearranging Equation (5.36) gives:

$$\frac{\left(\underline{f}'^{0}_{p}\right)^{T}-\underline{\kappa}\left(\underline{f}^{0}_{p}\right)^{T}}{\left(\underline{g}'^{0}_{p}\right)^{T}-\underline{\kappa}\left(\underline{g}^{0}_{p}\right)^{T}}\hat{\underline{X}}^{0}_{p}+\sum_{q\neq p}\underline{\underline{T}}^{0}_{qp}\hat{\underline{X}}^{0}_{q}=-\underline{\underline{U}}^{0}_{0p} \tag{5.39}$$

As before, a set of linear equations is derived as follows:

$$\begin{pmatrix} \underline{\underline{A}}_{1} & \underline{\underline{T}}_{12} & \underline{\underline{T}}_{13} & \cdot\cdot \\ \underline{\underline{T}}_{21} & \underline{\underline{A}}_{2} & \underline{\underline{T}}_{23} & \cdot\cdot \\ \underline{\underline{T}}_{31} & \underline{\underline{T}}_{32} & \underline{\underline{A}}_{3} & \cdot\cdot \\ \cdot\cdot & \cdot\cdot & \cdot\cdot & \cdot\cdot \end{pmatrix}\begin{pmatrix} \hat{\underline{X}}^{0}_{1} \\ \hat{\underline{X}}^{0}_{2} \\ \hat{\underline{X}}^{0}_{3} \\ \cdots \end{pmatrix}=-\begin{pmatrix} \underline{\underline{U}}_{01} \\ \underline{\underline{U}}_{02} \\ \underline{\underline{U}}_{03} \\ \cdots \end{pmatrix} \tag{5.40}$$

where for TM fields:

$$\underline{\underline{A}}_{p}=\frac{\left(\underline{f}'^{0}_{p}\right)^{T}-\underline{\kappa}\left(\underline{f}^{0}_{p}\right)^{T}}{\left(\underline{g}'^{0}_{p}\right)^{T}-\underline{\kappa}\left(\underline{g}^{0}_{p}\right)^{T}} \tag{5.41}$$

and for TE fields:

$$\underline{\underline{A}}_{p}=\frac{\left(\underline{f}^{0}_{p}\right)^{T}-\underline{\kappa}\left(\underline{f}'^{0}_{p}\right)^{T}}{\left(\underline{g}^{0}_{p}\right)^{T}-\underline{\kappa}\left(\underline{g}'^{0}_{p}\right)^{T}} \tag{5.42}$$

and $\underline{\kappa}$ has been defined in Equation (5.37) and (5.38) for TM and TE polarisation respectively. In order to solve Equation (5.40) a set of linear equations from Equation (5.31) needs to be calculated for the scattered coefficients $\hat{\underline{X}}^{s}_{p}$ and the vector $\underline{\kappa}$ obtained. As was shown in Chapter 4, the scattered coefficients can be then redefined in a coordinate system centred at the TLM cell by means of the Green's function and the final fields for the TM fields formulated as:

$$E_{z}(r,\phi)=\underline{g}^{T}_{0}\underline{X}^{0}_{0}+\underline{f}^{T}_{0}\hat{\underline{X}}^{0}_{s}\underline{X}^{0}_{0} \tag{5.43}$$

$$H_{\theta}(r,\phi)=-j\gamma\left(\underline{g}^{T}_{0}\underline{X}^{0}_{0}+\underline{f}^{T}_{0}\hat{\underline{X}}^{0}_{s}\underline{X}^{0}_{0}\right) \tag{5.44}$$

These solutions can be used to construct the admittance relationship between the electric and magnetic field at the edge of the node, which is essential for the process of integrating the multi-feature node with the time-domain TLM algorithm.

5.2.2. Wires with Multiple Dielectric Coatings

The extension to problems of scattering from cluster of wires or dielectric rods with *m* dielectric coating layers of radii $d_1, d_2, ..., d_m$ is now very straightforward. The algorithm starts at the interface $r = a_p$ between the inner conducting wire (or dielectric rod) of radius a_p and the first dielectric coating layer of radius d_1. At this interface, the vector of scattering coefficients $\underline{\hat{X}}_p^a$ is obtained directly by solving the set of linear equations discussed in the previous section. Then the algorithm proceeds in the same fashion for consecutive interfaces $r = d_i$ where $i = 1, 2, ..., m-1$:

1. Apply the appropriate boundary conditions at the interface $r = d_i$ which preserves continuity of the fields at the i^{th} dielectric interface
2. Construct the admittance relationship $\overline{H} = Y \cdot \overline{E}$ at the interface $r = d_i$
3. Calculate the vector of normalised scattered coefficients $\underline{\hat{X}}_p^{d_i}$ taking into account the vector of scattered coefficients obtained in the previous step, i.e. for $\underline{\hat{X}}_p^a$ for $i = 1$, and $\underline{\hat{X}}_p^{d_i}$ for $i > 1$
4. Follow points 1-3 until the interface $r = d_m$ between the last dielectric layer and the free space is reached

The condition at interface $r = d_m$ enables the last vector of normalised scattering coefficients $\underline{\widehat{X}}_p^0$ to be calculated in the same manner as for the case of a wire with a single dielectric coating.

Clearly, the algorithm accounts for the boundary conditions separately at the surface of every single scatterer enclosed within a TLM cell. Therefore, it is possible to change the material properties or geometries of a scatterer without redefining the whole procedure. Thus, the approach allows embedding scatterers of various radii and properties in one TLM cell without restriction to a particular class of objects, e.g. a cell with only conducting wires or with only dielectric rods, which can be very beneficial in simulations of waves scattered from cable looms and cable bundles.

5.3. Numerical Validation for a Cell with Multiple Dielectric Rods

In this section the numerical validation of the theory given above will be presented. As for the case of metal wires embedded in a single TLM cell, an illustration that practically justifies the truncation of analytical solution to four incident harmonics will first be provided for each simulation.

Consider the single square TLM cell containing four dielectric rods of material permittivity $\varepsilon_r = 10$, shown in Figure 5.2. The positions of the cylinders within the cell and their geometries are randomly chosen assuring that all of them lie completely within the cell and that they do not overlap one another; details are listed in Table 5.1. For the time-domain numerical simulation the node radius was selected to be $\Delta = 0.025\,\text{m}$, the computational window 1000 by 1000 nodes and the number of iterations is 2048. The multi-feature node (MN) enclosing the dielectric cylinders is illuminated with a plane wave Gaussian pulse of RMS width 2.5 time-steps. The fields are captured in both near and far-field regions and the accuracy is verified with the exact solution.

No	Radius	Distance r	Angle ϕ
1	0.40Δ	0.5Δ	45°
2	0.30Δ	0.4Δ	300°
3	0.20Δ	0.5Δ	130°
4	0.25Δ	0.5Δ	190°

Table 5.1. Position and geometry of dielectric rods clustered in a TLM cell

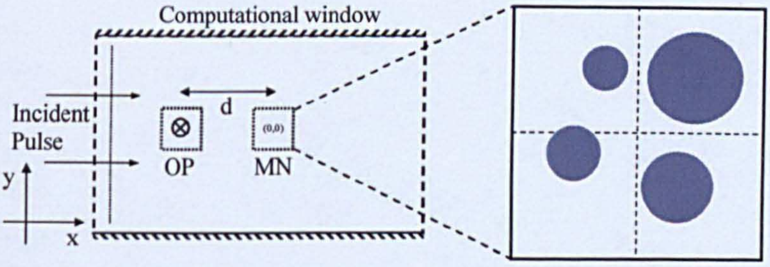

Figure 5.2. The numerical set-up for a simulation of a TLM cell with multiple dielectric rods

For the scenario described above an explicit justification of the truncation of the cylindrical harmonic series within the TLM node is presented in Figure 5.3. Here, the total electric field is observed at the boundary of the node containing the rods (point $(-\Delta, 0)$ corresponding to port 2 of Figure 4.1 in Chapter 4) for different degrees of truncation. It is clear that four terms give a very good approximation to the exact solution over the normalised frequency range $(f/f_{\max} < 0.1)$.

It is noted that to ensure convergence of the analytic result at larger distances from the scatterer, 40 harmonic terms have been selected for that purpose and is labelled in Figure 5.3 as “Exact”.

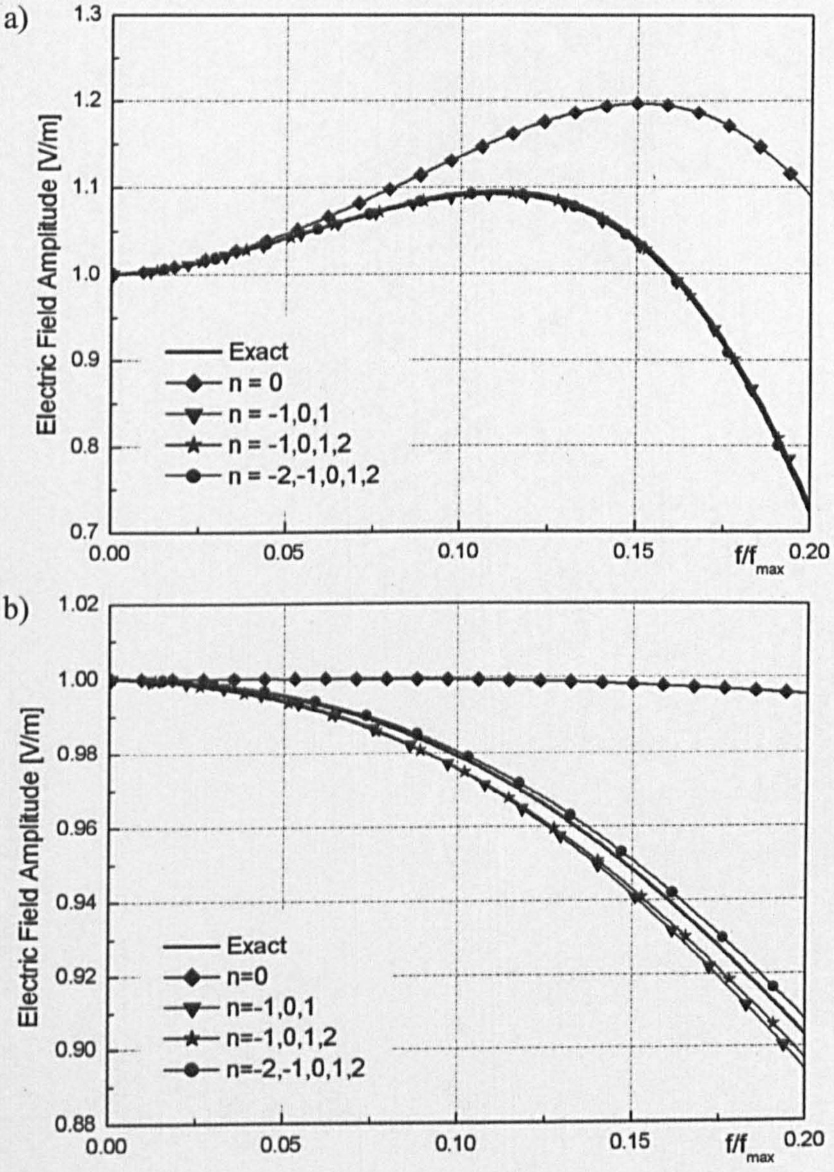

Figure 5.3. Convergence of analytical solution for a cluster of dielectric rods for TM (a) and TE (b) polarisation

a)

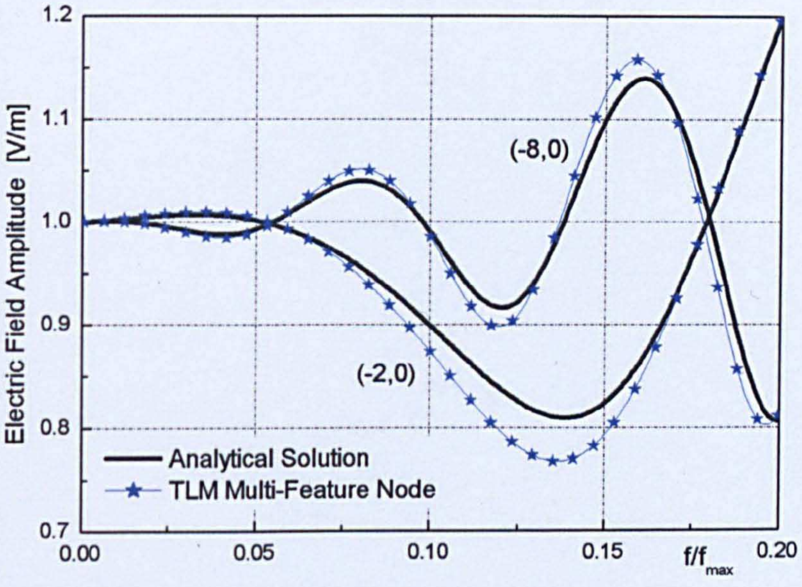
Electric Field Amplitude [V/m]
1.2
1.1
1.0
0.9
0.8
0.7
0.00
0.05
0.10
0.15
0.20
f/f$_{max}$
(-8,0)
(-2,0)
Analytical Solution
TLM Multi-Feature Node

b)

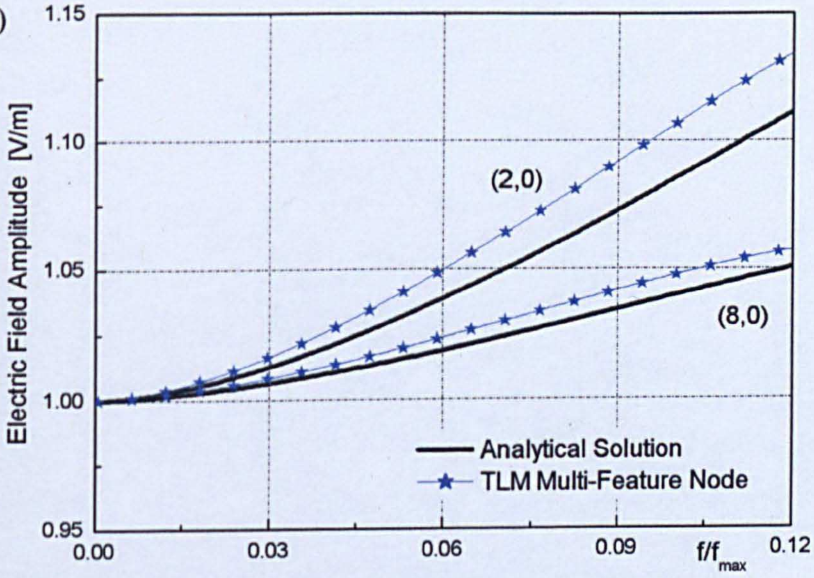
Electric Field Amplitude [V/m]
1.15
1.10
1.05
1.00
0.95
0.00
0.03
0.06
0.09
0.12
f/f$_{max}$
(2,0)
(8,0)
Analytical Solution
TLM Multi-Feature Node

c)

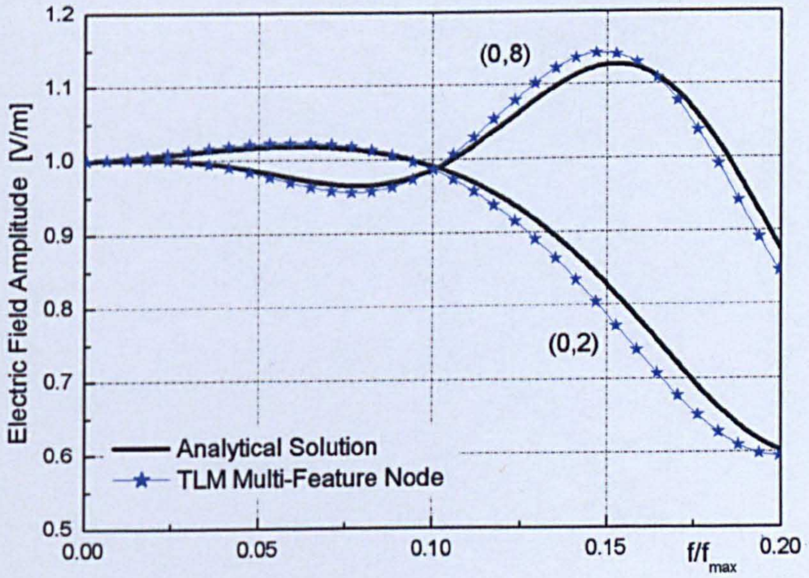
Electric Field Amplitude [V/m]
1.2
1.1
1.0
0.9
0.8
0.7
0.6
0.5
0.00
0.05
0.10
0.15
0.20
f/f$_{max}$
(0,8)
(0,2)
Analytical Solution
TLM Multi-Feature Node

d)

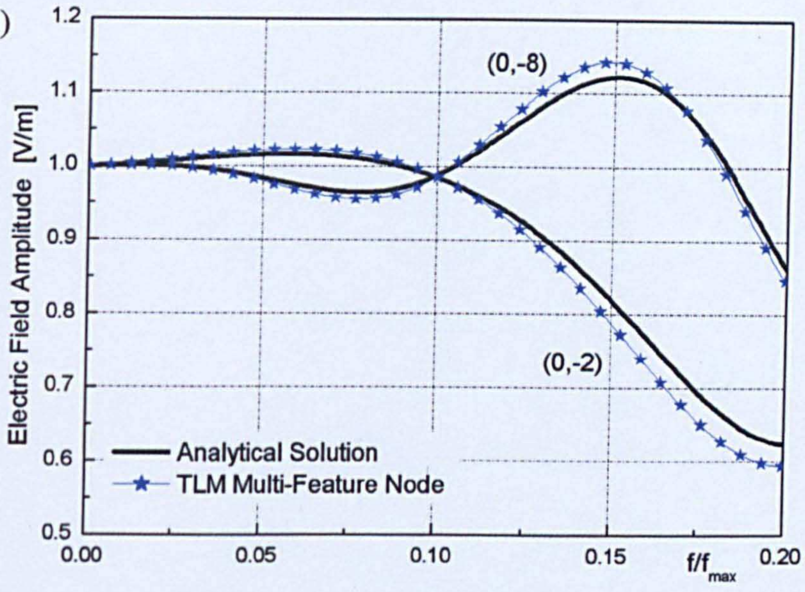

Figure 5.4. Amplitude of the total electric field measured in near and far-field zones in front (a), behind (b) and to both sides (c), (d) of TM polarised MN

The comparison presented in Figure 5.4 between the analytical and numerical solution for a cluster of dielectric cylinders illuminated by a TM polarised plane wave shows excellent agreement for observation points placed in front of, behind and to both sides of the multi-feature node in the near and far-field zones. Moreover, the good agreement is observed well beyond $f/f_{max} = 0.1$.

Figure 5.5 shows a similar comparison for a TE polarised case. As observed, the analytical and numerical results for scattering from a cluster of dielectric cylinders correspond very closely notwithstanding the relatively weak scattering that occurs in this case. Again, the agreement extends beyond $f/f_{max} = 0.1$.

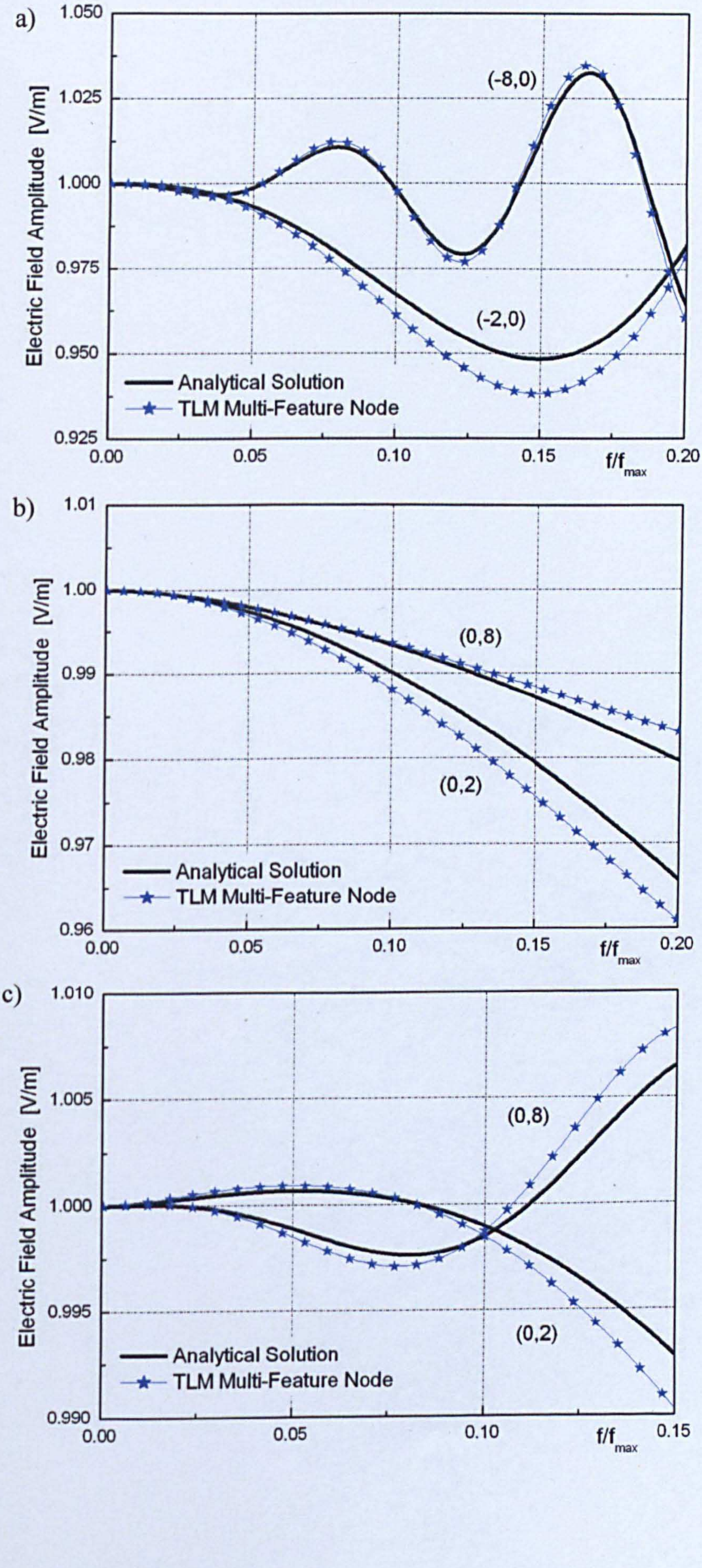
a)
1.050
1.025
1.000
0.975
0.950
0.925
Electric Field Amplitude [V/m]
(-8,0)
(-2,0)
Analytical Solution
TLM Multi-Feature Node
0.00
0.05
0.10
0.15
f/f_max
0.20
b)
1.01
1.00
0.99
0.98
0.97
0.96
Electric Field Amplitude [V/m]
(0,8)
(0,2)
Analytical Solution
TLM Multi-Feature Node
0.00
0.05
0.10
0.15
f/f_max
0.20
c)
1.010
1.005
1.000
0.995
0.990
Electric Field Amplitude [V/m]
(0,8)
(0,2)
Analytical Solution
TLM Multi-Feature Node
0.00
0.05
0.10
f/f_max
0.15

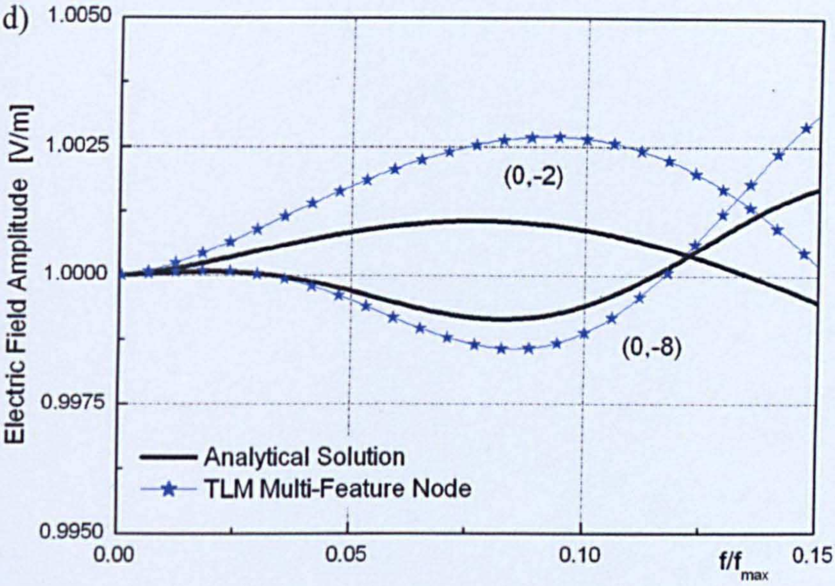

Figure 5.5. Amplitude of the total electric field measured in near and far-field zones in front (a), behind (b) and to both sides (c), (d) of TE polarised MN

In order to further investigate the behaviour of the node with dielectric cylinders embedded within, the influence of dielectric constant will be studied for the same cluster of posts and both field polarisations.

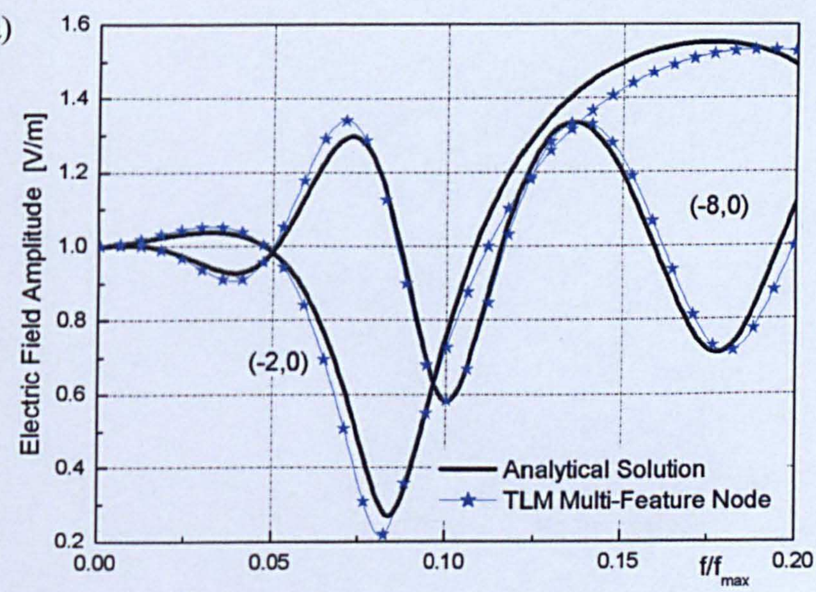

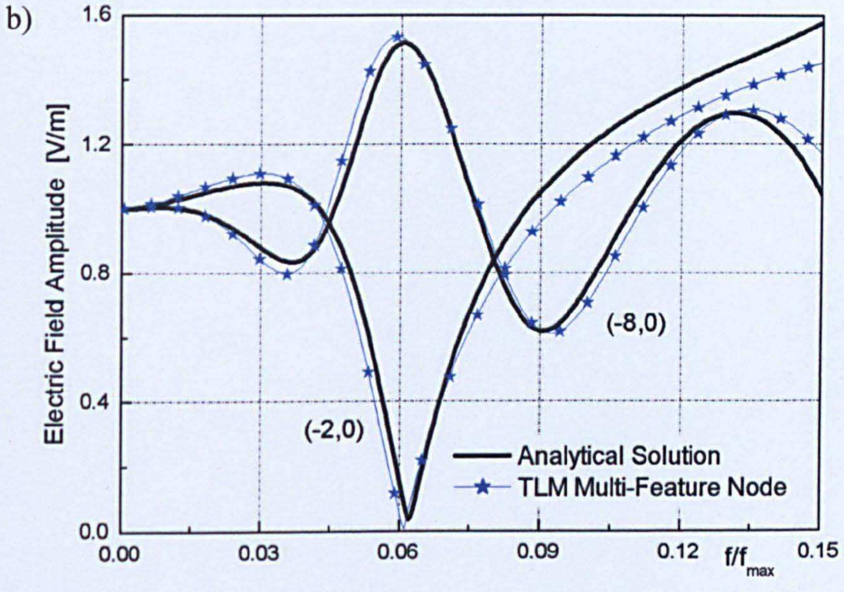

Figure 5.6. Amplitude of electric field 2 and 8 nodes in front of the MN containing TM polarised dielectric rods of permittivity:

$\varepsilon_r = 50$ (a) and $\varepsilon_r = 100$ (b)

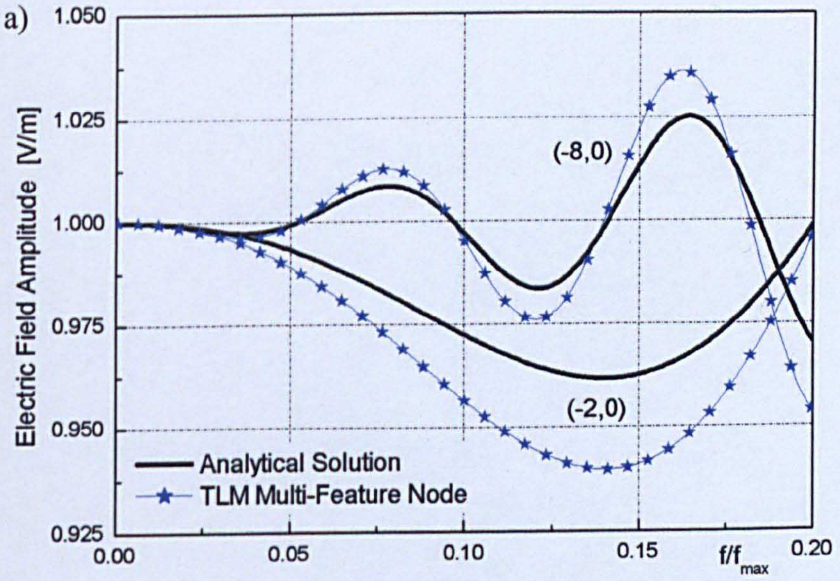

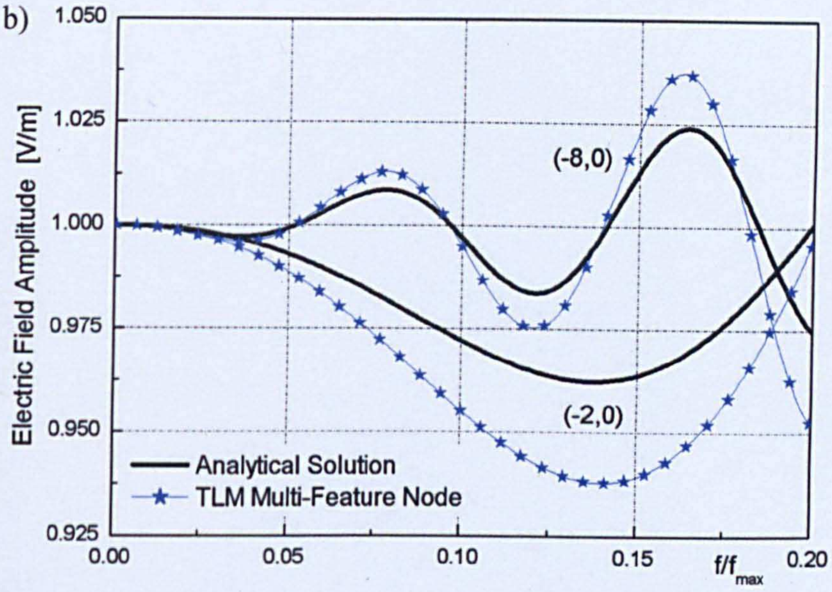

Figure 5.7. Amplitude of electric field 2 and 8 nodes in front of the MN containing TE polarised dielectric rods of permittivity $\varepsilon_r = 50$ (a) and $\varepsilon_r = 100$ (b)

Figure 5.6 and Figure 5.7 demonstrate the capability of the approach to model dielectric cylindrical rods of different material properties. The increase in the value of permittivity does not incur additional errors for TM polarisation and good agreement is achieved between the exact solution and the numerical approximation. An increase in a value of permittivity for a TE case leads to a slight overestimation in the numerical prediction, especially visible in the near-field region. The near-field errors in both cases can be explained by the limited number of sample points available when observing field in the near-field, since the field around the object, although modelled accurately by the analytical expansion, is sparsely sampled by the small number of TLM nodes in close vicinity to the objects.

Finally, it is shown that in the case of dielectric rods enclosed by a single TLM cell, the approach discussed in this work is capable of accurately identifying the phase of the signal under investigation for both field polarisations. Excellent matching is observed for a wide range of frequencies in the near and far-field regions as seen in Figure 5.8.

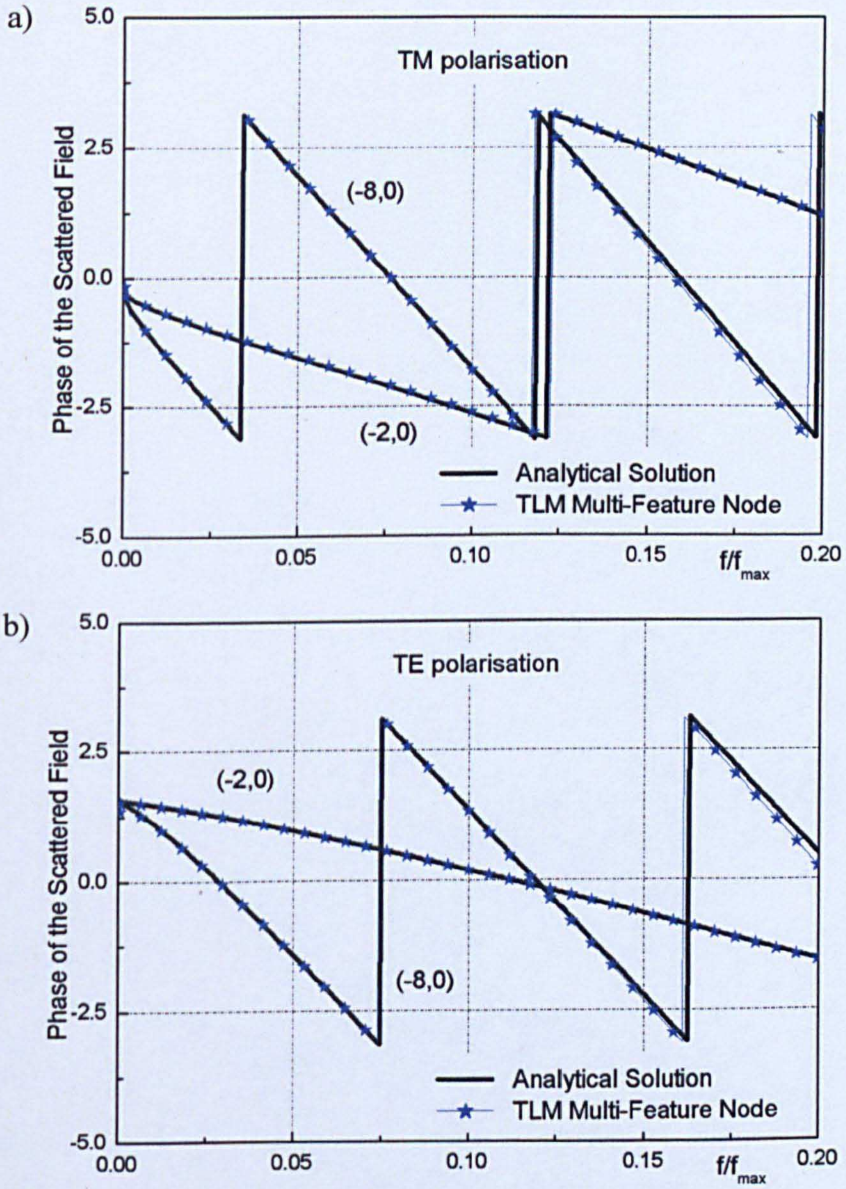

Figure 5.8. The phase of the field scattered from TM (a) and TE (b) TE polarised cluster of dielectric rods of permittivity $\varepsilon_r = 10$ captured 2 and 8 nodes in front of MN

5.4. Numerical Validation for a Cell with Dielectric Coated Wires

In this section, the multi-feature node is applied to modelling dielectric coated wires. In order to explore the flexibility of the approach in simulating such objects, three coated wires of different material properties and geometries embedded within a single TLM cell are investigated, as demonstrated in Figure 5.9(a).

	a_w	a_c	ε_r	r	ϕ
1	0.30Δ	0.35Δ	10	0.70Δ	45°
2	0.15Δ	0.45Δ	35	0.45Δ	315°
3	0.20Δ	0.30Δ	75	0.50Δ	175°

Table 5.2. Parameters of the wires embedded in a single TLM cell

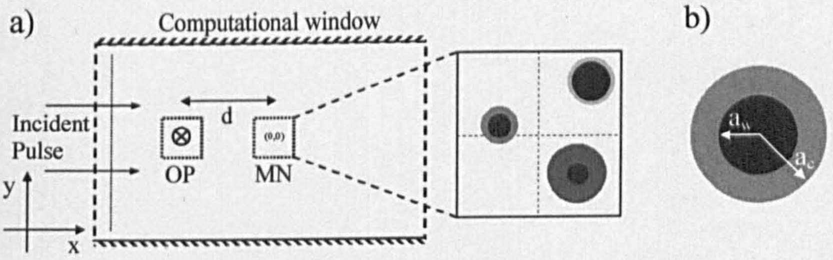

Figure 5.9. Numerical set-up for a simulation of a TLM cell containing multiple dielectric coated wires (a), illustration of wires parameters (b)

The characteristics of the coated wires are listed in Table 5.2, where (r,ϕ) denotes the position of the wires within the MN, a_w being the radius of the conductor, a_c and ε_r are radius and dielectric permittivity of the coating layers respectively.

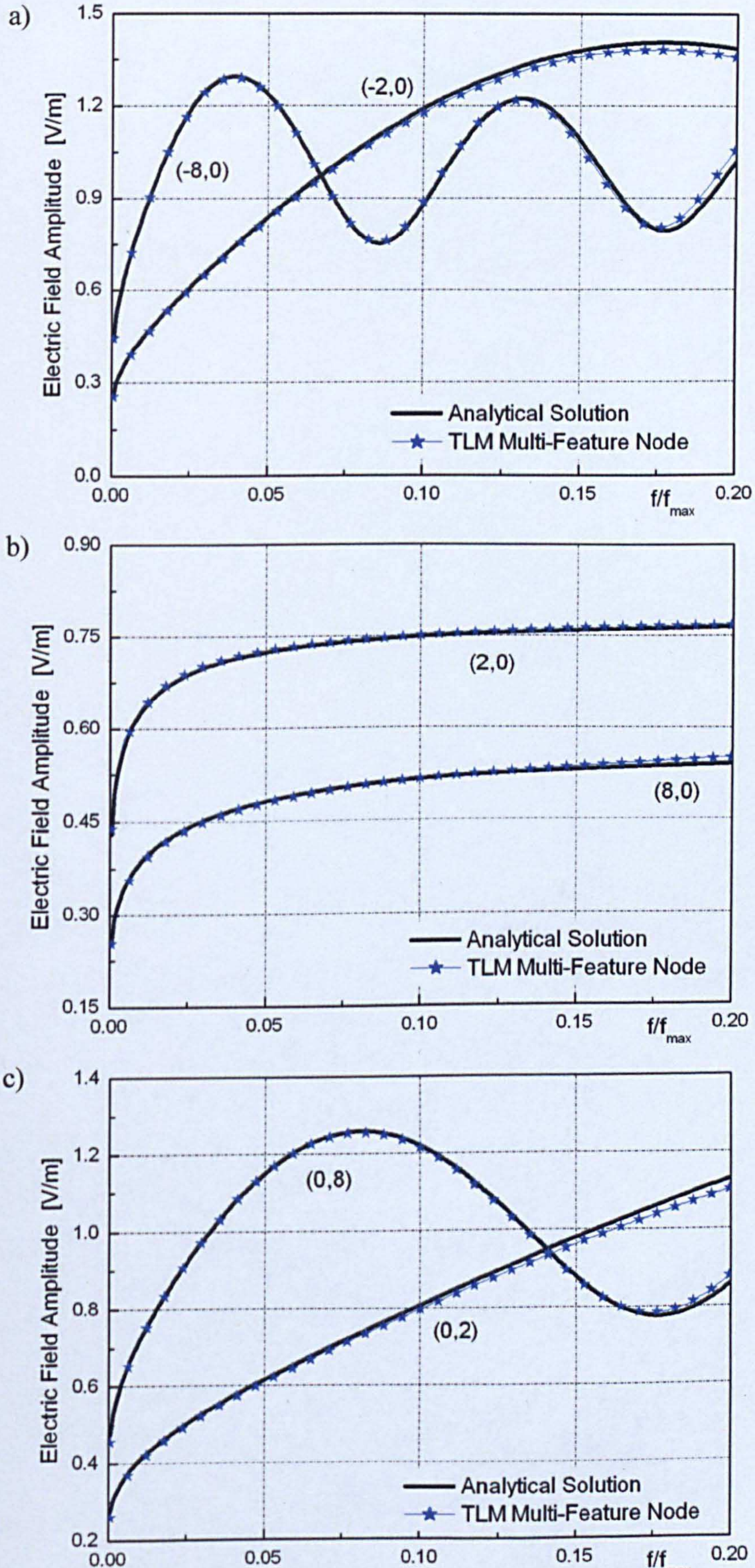
a)
Electric Field Amplitude [V/m]
1.5
1.2
0.9
0.6
0.3
0.0
(-2,0)
(-8,0)
Analytical Solution
TLM Multi-Feature Node
0.00
0.05
0.10
0.15
f/f_max
0.20
b)
Electric Field Amplitude [V/m]
0.90
0.75
0.60
0.45
0.30
0.15
(2,0)
(8,0)
Analytical Solution
TLM Multi-Feature Node
0.00
0.05
0.10
0.15
f/f_max
0.20
c)
Electric Field Amplitude [V/m]
1.4
1.2
1.0
0.8
0.6
0.4
0.2
(0,8)
(0,2)
Analytical Solution
TLM Multi-Feature Node
0.00
0.05
0.10
0.15
f/f_max
0.20

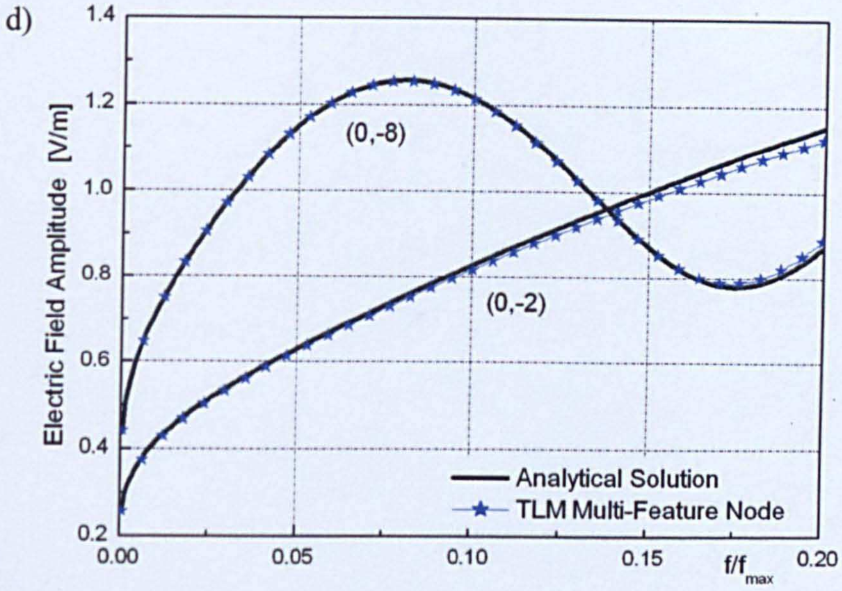

Figure 5.10. Amplitude of electric field 2 and 8 nodes in front (a), behind (b) and to both sides (c), (d) of the MN containing TM polarised dielectric coated wires

For TM fields the comparison between the analytical solution and the numerical prediction for a cluster of multiple wires with dielectric coatings is presented in Figure 5.10 and is excellent for a wide range of frequencies. As expected, the influence of the dielectric layers is minor; as the field hits the dielectric boundary only a small part is reflected from the surface of dielectric, the majority of the field penetrating inside is totally scattered from the surface of the perfect conductor. Thus one expects that for a wave propagating in a presence of coated wires the scattered field should resemble that for perfect conductors.

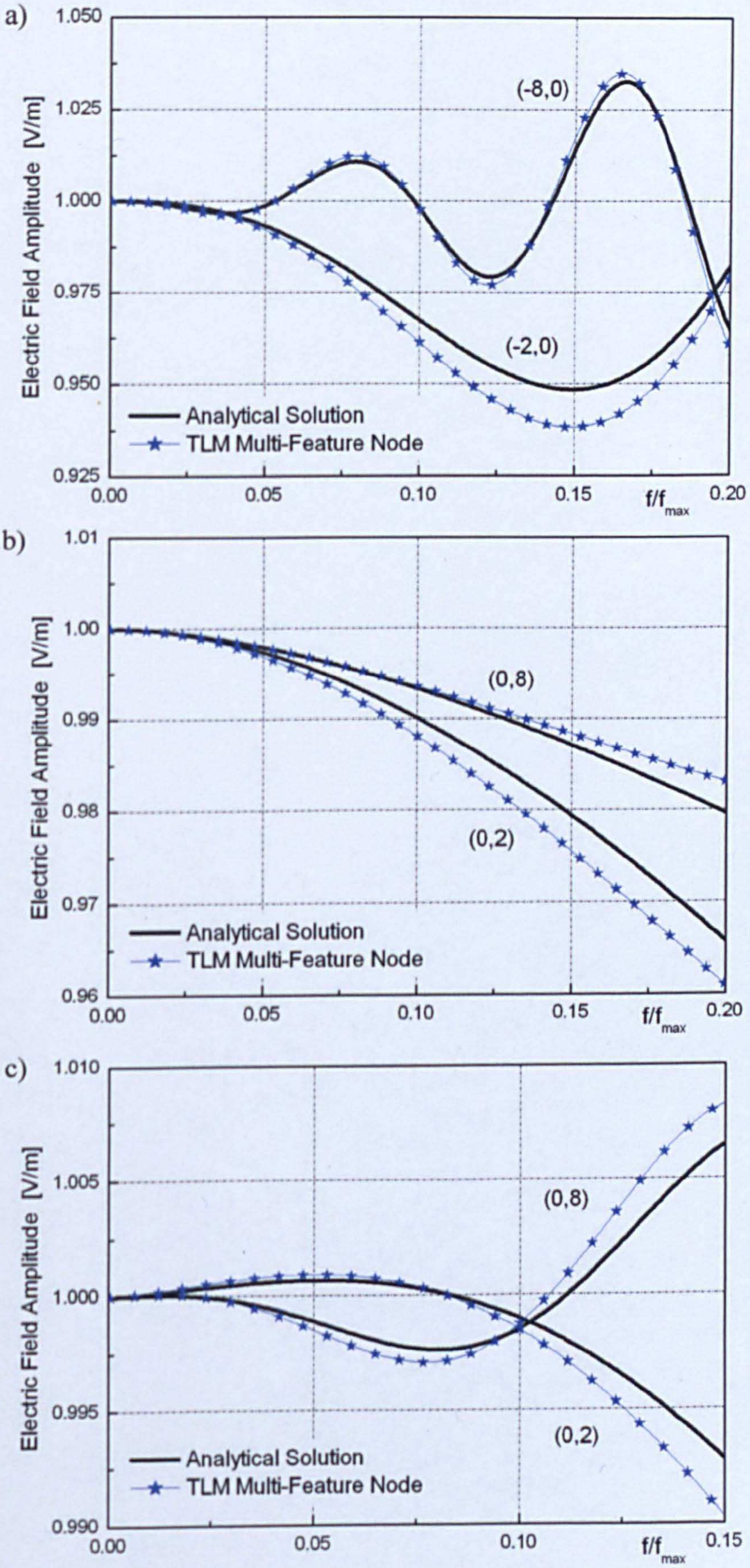
a)
1.050
1.025
1.000
0.975
0.950
0.925
Electric Field Amplitude [V/m]
(-8,0)
(-2,0)
Analytical Solution
TLM Multi-Feature Node
0.00
0.05
0.10
0.15
0.20
f/f_max
b)
1.01
1.00
0.99
0.98
0.97
0.96
Electric Field Amplitude [V/m]
(0,8)
(0,2)
Analytical Solution
TLM Multi-Feature Node
0.00
0.05
0.10
0.15
0.20
f/f_max
c)
1.010
1.005
1.000
0.995
0.990
Electric Field Amplitude [V/m]
(0,8)
(0,2)
Analytical Solution
TLM Multi-Feature Node
0.00
0.05
0.10
0.15
f/f_max

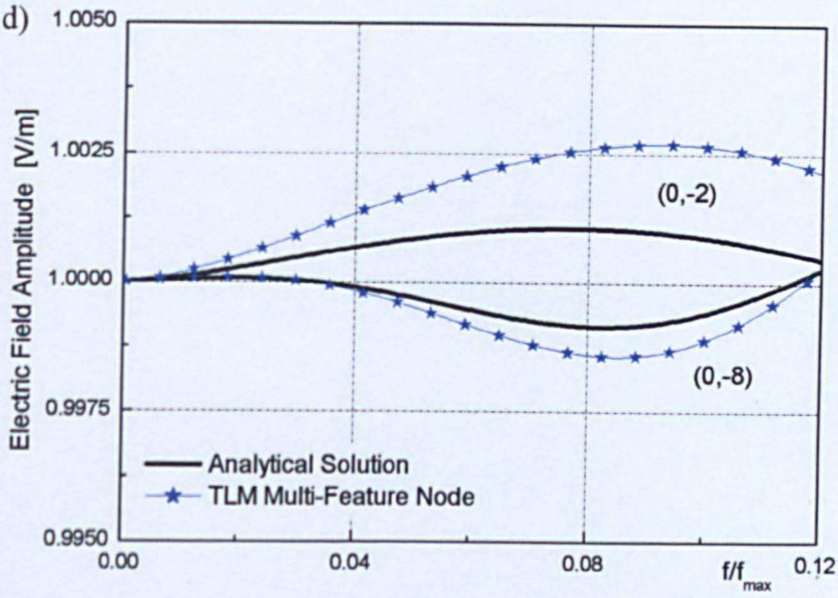

Figure 5.11. Amplitude of electric field 2 and 8 nodes in front (a), behind (b) and to both sides (c), (d) front of the MN containing TE polarised dielectric coated wires

As observed in Figure 5.11 for a cell with multiple dielectric coated wires illuminated by a TE polarised wave, the results in the far-field zone are in good agreement with the analytical solution up to 10% of maximum frequency of the TLM simulation. Beyond that point the dispersion of numerical method causes greater deviation between those two solutions especially when such weak scattering is considered. Numerical estimation for the near-field becomes more erroneous compared to the far-field zone due to the number of available sampling points in close vicinity of the multi-feature node. As the distance from the scatterers increases, the TLM grid provides better numerical resolution of the reflected wavefronts which leads to a more accurate field description.

Validation for phase is illustrated in Figure 5.12 for both field illuminations. Again, excellent matching is observed for a wide range of frequencies for observation points placed in both the near and far-field regions.

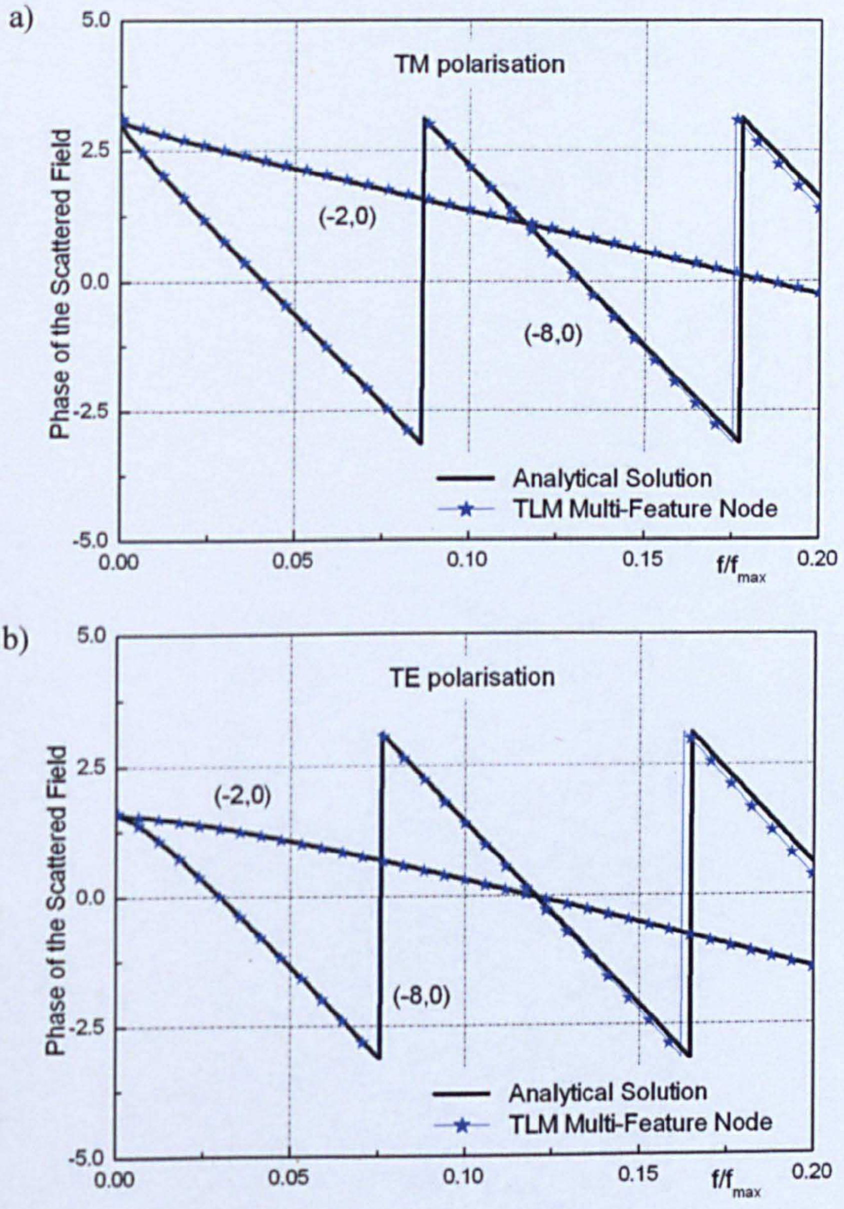

Figure 5.12. The phase of the field scattered from TM (a) and TE (b) polarised cluster of coated wires captured 2 and 8 nodes in front of MN

5.5. Closing Remarks

In this chapter the approach for embedding small objects into a time-domain numerical algorithm has been presented based on the example of dielectric cylinders and dielectric coated conducting wires. The results were verified against exact solutions and show excellent agreement even for frequencies beyond the conventional operating range of TLM. Having presented the approach for a variety of EMC application, the next chapter explores possible application in other areas.

Chapter 6

Generalised Multi-Feature Node

In this chapter attention will be focused upon the implementation of the multi-feature node in simulations of various practical configurations. This will be carried out by dividing the examples into two categories. The first section explores further opportunities for employing the proposed scheme in EMC analysis, such as predictions of fields scattered from lossy wires. The second part focuses mainly on photonic applications and presents a description of the macroscopic behaviour of photonic systems.

6.1. Wires with Losses

Consideration has so far been focused on waves propagating in lossless media and incident upon lossless cylindrical structures. Therefore, it was assumed that the cylinder was either a perfect conductor whose conductivity $\sigma \to \infty$ or else a lossless (perfect) dielectric in which case $\sigma = 0$. Here, the application of the approach for embedding cylindrical wires that exhibit losses will be demonstrated. General lossy round dielectric structures are now studied from which special cases such as lossy wires can be derived. It should be noted that a lossy dielectric can be alternatively regarded as a partially conducting medium (imperfect dielectric or imperfect conductor) in which an EM wave loses power as it propagates due to a finite conductivity $\sigma \neq 0$.

6.1.1. Theoretical Formulation

To incorporate losses within the system one needs to start with Maxwell's equations. Consider a linear, isotropic, homogeneous, lossy dielectric medium that is charge-neutral. Suppressing the time factor $e^{j\omega t}$, Maxwell's equations become:

$$\nabla \cdot \mathbf{D} = 0 \tag{6.1}$$

$$\nabla \cdot \mathbf{B} = 0 \tag{6.2}$$

$$\nabla \times \mathbf{E} = -j\omega\mu\mathbf{H} \tag{6.3}$$

$$\nabla \times \mathbf{H} = j\omega\varepsilon\mathbf{E} + \mathbf{J} \tag{6.4}$$

where $\varepsilon = \varepsilon_0\varepsilon_r$ and $\mu = \mu_0\mu_r$ are real values where ε_0, μ_0 and ε_r, μ_r characterise the permittivity and permeability of empty space and the material respectively. Comparison with Maxwell's equations in Chapter 2 reveals that there is an additional element in the form of conduction current density $\mathbf{J}$ $(\mathrm{A/m^2})$ present in Equation (6.4). This current occurs due to the drift of charge carriers when an electric field is applied to conductor, which in the low velocity case is modelled by:

$$\mathbf{J} = \sigma\mathbf{E} \tag{6.5}$$

where σ is the conductivity of the material expressed in Siemens per metre. Substituting Equation (6.5) into (6.4) leads to:

$$\nabla \times \mathbf{H} = (j\omega\varepsilon + \sigma)\mathbf{E} \tag{6.6}$$

This equation can be rearranged to the form:

$$\nabla \times \mathbf{H} = j\omega\left(\varepsilon - j\frac{\sigma}{\omega}\right)\mathbf{E} = j\omega\varepsilon\left(1 - j\frac{\sigma}{\omega\varepsilon}\right)\mathbf{E} = j\omega\varepsilon_{eff}\mathbf{E} \tag{6.7}$$

where an effective permittivity is identified as:

$$\varepsilon_{eff} = \varepsilon\left(1 - j\frac{\sigma}{\omega\varepsilon}\right) \tag{6.8}$$

Finally, Equation (6.4) is formulated as:

$$\nabla \times \mathbf{H} = j\omega\varepsilon_{eff}\mathbf{E} \tag{6.9}$$

From Equation (6.9) it is clear that embedding lossy dielectric(s) into the proposed multi-feature node should not significantly differ from the implementation of perfect dielectric(s) case. However, the fact that the effective dielectric constant appears in Equation (6.8) is now complex needs to be addressed; this effective permittivity equals:

$$\varepsilon_{eff} = \varepsilon_0\left(1 - j\frac{\sigma}{\omega\varepsilon_0}\right) = \varepsilon_0\left(1 - j\frac{\sigma}{ck_0\varepsilon_0}\right) = \varepsilon_0\varepsilon_r \tag{6.10}$$

where c is the speed of light in vacuo and k_0 is the empty space wavenumber. Having obtained this complex relative permittivity the scheme for embedding lossy scatterers is similar to the approach presented in Chapter 5. A brief description will now be given for the case of a TM polarised wave incident upon round lossy conductors clustered within a single TLM cell.

6.1.2. TLM Implementation

In the presence of homogeneous dielectric posts the behaviour of the total electric and magnetic can be described in a polar coordinate system centred on the p^{th} cylinder as shown in Chapter 5:

$$E_z(r \ge a_p,\phi) = \underline{g}_p^T \underline{\underline{U}}_{0p} \underline{X}_0 + \underline{f}_p^T \underline{X}_p + \sum_{q \ne p} \underline{g}_p^T \underline{\underline{T}}_{qp} \underline{X}_q \qquad (6.11)$$

$$H_\theta(r \ge a_p,\phi) = -j\gamma_0 \left(\underline{g}'^T_p \underline{\underline{U}}_{0p} \underline{X}_0 + \underline{f}'^T_p \underline{X}_p + \sum_{q \ne p} \underline{g}'^T_p \underline{\underline{T}}_{qp} \underline{X}_q \right) \qquad (6.12)$$

where $\gamma_0 = \sqrt{\varepsilon_0 / \mu_0}$ is the intrinsic admittance of the medium and k_0 is the wavenumber. The elements $f_{pn}, f'_{pn}, g_{pn}, g'_{pn}$ are specified by:

$$\begin{aligned} f_{pn} &= e^{-jn\phi_p} H_n^{(2)}(kr_p) \quad \text{and} \quad f'_{pn} = e^{-jn\phi_p} H'^{(2)}_n(kr_p) \\ g_{pn} &= e^{-jn\phi_p} J_n(kr_p) \quad \text{and} \quad g'_{pn} = e^{-jn\phi_p} J'_n(kr_p) \end{aligned} \qquad (6.13)$$

where $J'_n(kr_p) = \dfrac{dJ'_n(kr_p)}{d(kr_p)}$ and $H'^{(2)}_n(kr_p) = \dfrac{dH'^{(2)}_n(kr_p)}{d(kr_p)}$, and the matrices $\underline{\underline{U}}_{0p}$ and $\underline{\underline{T}}_{qp}$ have been already introduced in Chapter 4.

The boundary condition at the interface between the dielectric post and the surrounding homogeneous medium has to be taken into account. In the lossy dielectric the intrinsic admittance γ_D and wavenumber k_D now are both complex quantities.

Continuity of tangential field components at the interface $r_p = a_p$, where a_p is the radius of the *p* cylinder, requires that:

$$\begin{aligned} (\underline{E}^0 - \underline{E}^D) \times \hat{r} &= 0 \\ (\underline{H}^0 - \underline{H}^D) \times \hat{r} &= 0 \end{aligned} \qquad (6.14)$$

where the superscript *D* denotes fields in the lossy dielectric region and *0* fields in the homogeneous space. Explicitly, the boundary condition can be formulated as in Chapter 5 as:

$$\left(\underline{g}_p^0\right)^T \underline{\underline{U}}_{0p}^0 \underline{X}_0^0 + \left(\underline{f}_p^0\right)^T \underline{X}_p^0 + \sum_{q \ne p} \left(\underline{g}_p^0\right)^T \underline{\underline{T}}_{qp}^0 \underline{X}_q^0 = \left(\underline{g}_p^D\right)^T \underline{\underline{U}}_{0p}^D \underline{X}_0^D \qquad (6.15)$$

$$\left(\underline{g}'^{0}_{p}\right)^{T}\underline{\underline{U}}^{0}_{0p}\underline{X}^{0}_{0}+\left(\underline{f}'^{0}_{p}\right)^{T}\underline{X}^{0}_{p}+\sum_{q\neq p}\left(\underline{g}'^{0}_{p}\right)^{T}\underline{\underline{T}}^{0}_{qp}\underline{X}^{0}_{q}=\gamma_0^{-1}\gamma_D\left(\underline{g}'^{D}_{p}\right)^{T}\underline{\underline{U}}^{D}_{0p}\underline{X}^{D}_{0} \tag{6.16}$$

As before the concept of the admittance relationship at the interface between the regions of different permittivity in the form of $\underline{\underline{H}}=\underline{Y}\cdot\underline{\underline{E}}$ is now investigated. Substituting the expression for the E and H-fields given by Equations (6.11) and (6.12) into the admittance relationship yields:

$$\begin{aligned}&\left(\underline{g}'^{0}_{p}\right)^{T}\underline{\underline{U}}^{0}_{0p}\underline{X}^{0}_{0}+\left(\underline{f}'^{0}_{p}\right)^{T}\underline{X}^{0}_{p}+\sum_{q\neq p}\left(\underline{g}'^{0}_{p}\right)^{T}\underline{\underline{T}}^{0}_{qp}\underline{X}^{0}_{q}\\&=j\frac{\underline{\underline{Y}}}{\gamma_0}\left(\left(\underline{g}^{0}_{p}\right)^{T}\underline{\underline{U}}^{0}_{0p}\underline{X}^{0}_{0}+\left(\underline{f}^{0}_{p}\right)^{T}\underline{X}^{0}_{p}+\sum_{q\neq p}\left(\underline{g}^{0}_{p}\right)^{T}\underline{\underline{T}}^{0}_{qp}\underline{X}^{0}_{q}\right)\end{aligned} \tag{6.17}$$

where the functions f_p, g_p and their derivatives are evaluated for the argument $kr_p = k_0 a_p$. Utilising the right-hand side of Equation (6.15) and (6.16) in (6.17) leads to:

$$\frac{\gamma_D}{\gamma_0}\left(\underline{g}'^{D}_{p}\right)^{T}\underline{\underline{U}}^{D}_{0p}\underline{X}^{D}_{0}=j\frac{\underline{\underline{Y}}}{\gamma_0}\left(\underline{g}^{D}_{p}\right)^{T}\underline{\underline{U}}^{D}_{0p}\underline{X}^{D}_{0} \tag{6.18}$$

Rearranging yields

$$j\frac{\underline{\underline{Y}}}{\gamma_0}=\frac{\gamma_D}{\gamma_0}\frac{\left(\underline{g}'^{D}_{p}\right)^{T}}{\left(\underline{g}^{D}_{p}\right)^{T}}=\frac{\gamma_D}{\gamma_0}\frac{\left(\underline{J}'^{D}\right)^{T}}{\left(\underline{J}^{D}\right)^{T}}=\underline{K} \tag{6.19}$$

where the vectors $\underline{J}^{D}$ and $\underline{J}'^{D}$ consist of elements $J_n(k_D a_p)$ and $J'_n(k_D a_p)$ respectively. Substituting Equation (6.19) into the boundary admittance relationship defined in Equation (6.17) results in:

$$\begin{aligned}&\left(\underline{g}'^{0}_{p}\right)^{T}\underline{\underline{U}}^{0}_{0p}\underline{X}^{0}_{0}+\left(\underline{f}'^{0}_{p}\right)^{T}\underline{X}^{0}_{p}+\sum_{q\neq p}\left(\underline{g}'^{0}_{p}\right)^{T}\underline{\underline{T}}^{0}_{qp}\underline{X}^{0}_{q}\\&=\frac{\gamma_D}{\gamma_0}\frac{\underline{J}'^{D}}{\underline{J}^{D}}\left(\left(\underline{g}^{0}_{p}\right)^{T}\underline{\underline{U}}^{0}_{0p}\underline{X}^{0}_{0}+\left(\underline{f}^{0}_{p}\right)^{T}\underline{X}^{0}_{p}+\sum_{q\neq p}\left(\underline{g}^{0}_{p}\right)^{T}\underline{\underline{T}}^{0}_{qp}\underline{X}^{0}_{q}\right)\end{aligned} \tag{6.20}$$

After some mathematical arrangements one obtains:

$$\underline{\underline{U}}^0_{0p}\underline{X}^0_0 + \frac{\left(\underline{f}'^0_p\right)^T - \underline{\kappa}\left(\underline{f}^0_p\right)^T}{\left(\underline{g}'^0_p\right)^T - \underline{\kappa}\left(\underline{g}^0_p\right)^T}\underline{X}^0_p + \sum_{q\neq p}\underline{\underline{T}}^0_{qp}\underline{X}^0_q = 0 \tag{6.21}$$

where $\underline{\kappa}$ is determined in Equation (6.19).

As studied in Chapter 4 and 5, the boundary conditions need to be applied at the surface of every lossy cylinder enclosed in a TLM cell and the procedure described by Equations (6.11) to (6.21) carried out for each of them. As a result, a set of linear equations is formed:

$$\begin{pmatrix} \underline{\underline{A}}_1 & \underline{\underline{T}}_{12} & \underline{\underline{T}}_{13} & .. \\ \underline{\underline{T}}_{21} & \underline{\underline{A}}_2 & \underline{\underline{T}}_{23} & .. \\ \underline{\underline{T}}_{31} & \underline{\underline{T}}_{32} & \underline{\underline{A}}_3 & .. \\ .. & .. & .. & .. \end{pmatrix} \begin{pmatrix} \underline{X}^0_1 \\ \underline{X}^0_2 \\ \underline{X}^0_3 \\ ... \end{pmatrix} = - \begin{pmatrix} \underline{\underline{U}}_{01}\underline{X}^0_0 \\ \underline{\underline{U}}_{02}\underline{X}^0_0 \\ \underline{\underline{U}}_{03}\underline{X}^0_0 \\ ... \end{pmatrix} = - \begin{pmatrix} \underline{\underline{U}}_{01} \\ \underline{\underline{U}}_{02} \\ \underline{\underline{U}}_{03} \\ ... \end{pmatrix} \underline{X}^0_0 \tag{6.22}$$

where the lossy cylinders are numbered from 1. The components $\underline{\underline{A}}_p$ are constructed in the same way as in Equation (5.15) and (5.16) presented in Chapter 5.

Similarly to the procedure presented in previous two chapters, the vector of scattered field coefficients $\underline{X}^T_s = \left[\underline{X}_1 \quad \underline{X}_2 \quad \underline{X}_3 \quad ...\right]^T$ from Equation (6.22) is now calculated and the fields are re-expressed back from the wire coordinate systems to the node coordinates by the means of Green's functions. Also the algorithm to impose the eigenvalue problem, necessary to link the field solutions with the adjacent nodes of TLM grid, has already been given in Chapter 4 and for brevity is not repeated here.

However, an important point needs to be highlighted when implementing the local field solutions into a TLM model. Solving the eigenvalue problem $\underline{\underline{H}}\underline{X}_0 = \gamma\underline{\underline{E}}\underline{X}_0$

(Equation (4.54) in Chapter 4) at the edges of the node will this time result in complex eigenvalues. As discussed in Chapter 3 and 4, the vector of eigenvalues, $\underline{\gamma}$, represents input impedances looking into the multi-feature node. In addition to components that are proportional or inversely proportional to frequency, the eigenvalues, i.e. modal admittances also possess a frequency-independent element. Thus, the circuit model reflecting the character of these admittances is formulated as $\gamma_i^{-1} = j\omega L_i + R_i$ or $\gamma_i = j\omega C_i + G_i$, where R_i and G_i denote resistance and conductance on the i^{th} line respectively. In previous chapters circuit models were implemented in the time-domain model using open or short-circuited transmission lines. Modifications to that model are now devised to account for this extra, frequency-independent behaviour and are shown in Figure 6.1. Therefore, additional components in the form of conductances that represent the losses the wave encounters while propagating on the transmission line are now included in the line model.

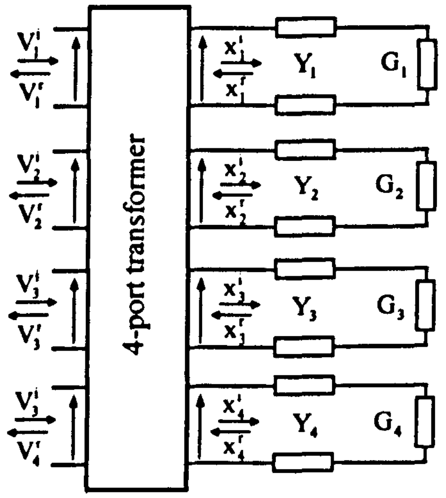

Figure 6.1. General transmission line implementation of non-standard node for embedding lossy scatterers

The value of each conductance can be calculated using transmission line theory. The input admittance for a transmission line of characteristic admittance Y terminated by a conductance G equals:

$$Y_{in} = Y_i \frac{G_i + jY_i \tan(k\Delta)}{Y_i + jG_i \tan(k\Delta)} \tag{6.23}$$

where k is the wavenumber in the transmission line of length Δ.

After some mathematical rearrangements shown in Appendix C this admittance can be expressed for low frequencies as:

$$Y_{in} = G_i + jk\Delta G_i \left(\frac{Y_i}{G_i} - \frac{G_i}{Y_i} \right) \tag{6.24}$$

On the other hand the complex admittance calculated from the eigenvalue problem can be written in the form:

$$\gamma_i = \gamma'_i + j\omega\mu\gamma''_i \tag{6.25}$$

By direct inspection of the two above equations, the values of network elements are evaluated:

$$G_i = \gamma'_i \tag{6.26}$$

$$\frac{\gamma''_i}{\gamma_0\Delta} = G_i \left(\frac{Y_i}{G_i} - \frac{G_i}{Y_i} \right) = Y_i - \frac{(\gamma'_i)^2}{Y_i} \tag{6.27}$$

Equation (6.27) is a quadratic equation of

$$Y_i^2 - \frac{\gamma'_i}{\Delta\gamma_0} Y_i - (\gamma'_i)^2 = 0 \tag{6.28}$$

which is solved for the value of Y_i.

$$Y_i = \frac{-\gamma''_i}{2\Delta\gamma_0} \pm \frac{1}{2}\sqrt{\left(\frac{\gamma''_i}{\gamma_0\Delta} \right)^2 + 4\gamma'_i} \tag{6.29}$$

Only the positive value of the two solutions presented in Equation (6.29) is used.

Having calculated the values of Y_i and G_i for all the $i = 1,2,3,4$ lines, the network model presented in Figure 6.1 is considered, where Y_i is a link line admittance terminated by conductance G_i. The computations in the multi-feature node will differ slightly from those presented in Chapter 3. The connection process remains unchanged and is described by Equation (3.25), however the scattering in the node is now expressed by:

$$x_i^{ref}(t) = \Gamma_i x_i^{inc}(t - \Delta t) \tag{6.30}$$

where Γ_i is a reflection coefficient:

$$\Gamma_i = \frac{Y_i - G_i}{Y_i + G_i} \tag{6.31}$$

6.1.3. Numerical Validations

In this section numerical results will be validated against the analytical solutions presented in Equations (6.11) and (6.12) where the scattered coefficients were obtained by solving the boundary condition formulated in Equation (6.22). The numerical set-up is shown in Figure 6.2. The multi-feature node (MN) contains a single lossy wire positioned at the centre of the node. The set-up is excited by a plane wave with the electric field polarised in the z-direction, i.e. parallel to the cylinder's axis. The field is observed 2 and 8 nodes in front and in line with the wire embedded in the node on the negative x-axis. The remaining simulation parameters are: the computational window $60\text{m} \times 60\text{m}$, TLM node size $2\Delta = 0.05\text{m}$ and the radius of the wire $a = 0.5\Delta$. Three different values of conductivity are considered as presented in Figure 6.3, i.e. $\sigma = 1$, $\sigma = 50$ and $\sigma = 100$ S/m.

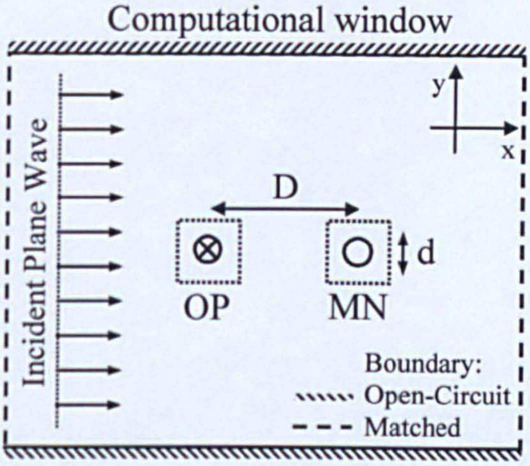

Figure 6.2. Experimental set-up for the analysis of lossy wires

It is clear that very good agreement between the analytical and numerical solutions is achieved. The excellent match extends over the full frequency range over which TLM dispersion is negligible, that is $f / f_{max} < 0.1$ or in other words to 10 samples per wavelength.

a)

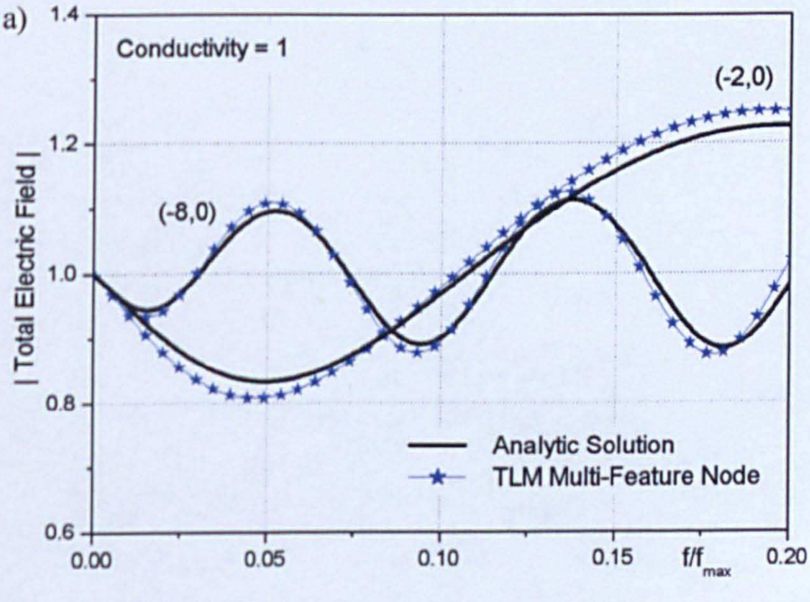

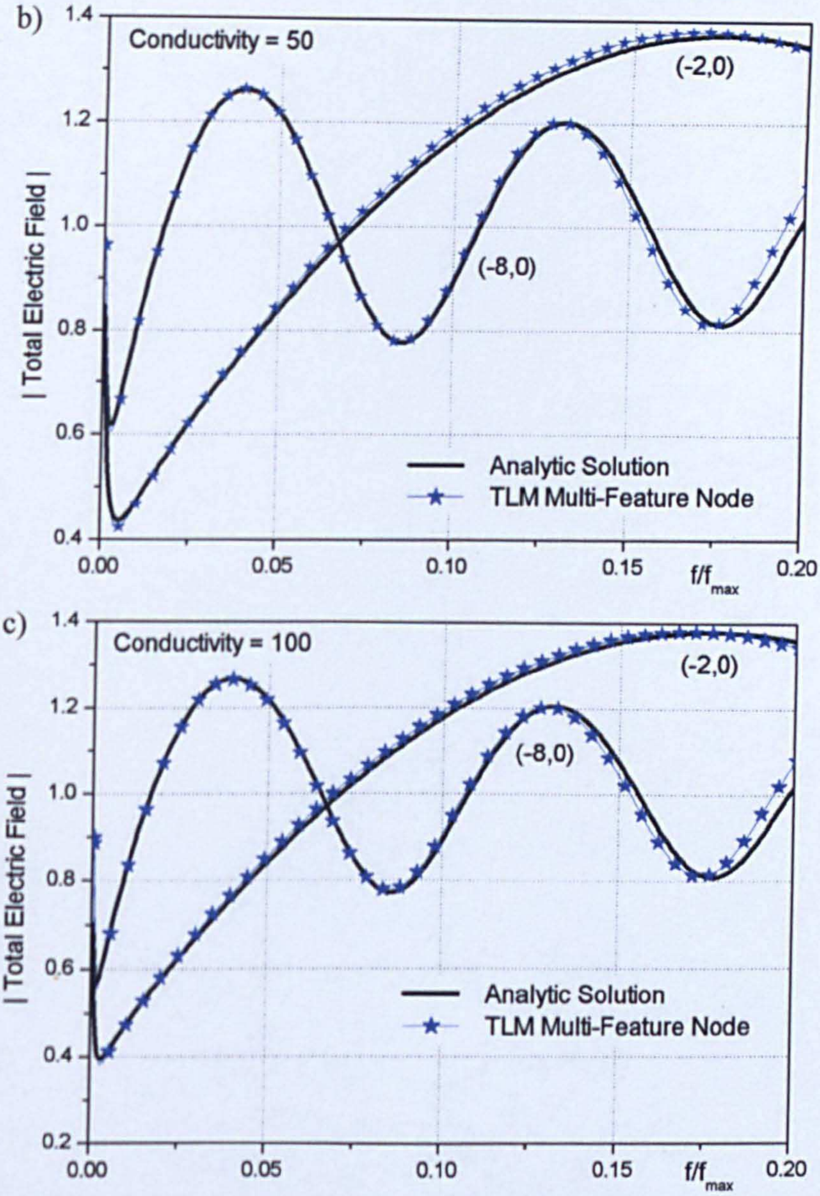

Figure 6.3. Total electric field amplitude observed 2 and 8 nodes in front on the multi-feature node containing a lossy wire for different values of wire conductivity: (a) $\sigma = 1$, (b) $\sigma = 50$, (c) $\sigma = 100$

It is noted that for a conductivity larger than 100 S/m results tend to the solutions obtained for a perfect conducting wire and only a small difference in the low frequency range distinguishes between imperfect and perfect conductors. To verify accuracy in this range the solutions from Figure 6.3 are also presented in Figure 6.4.

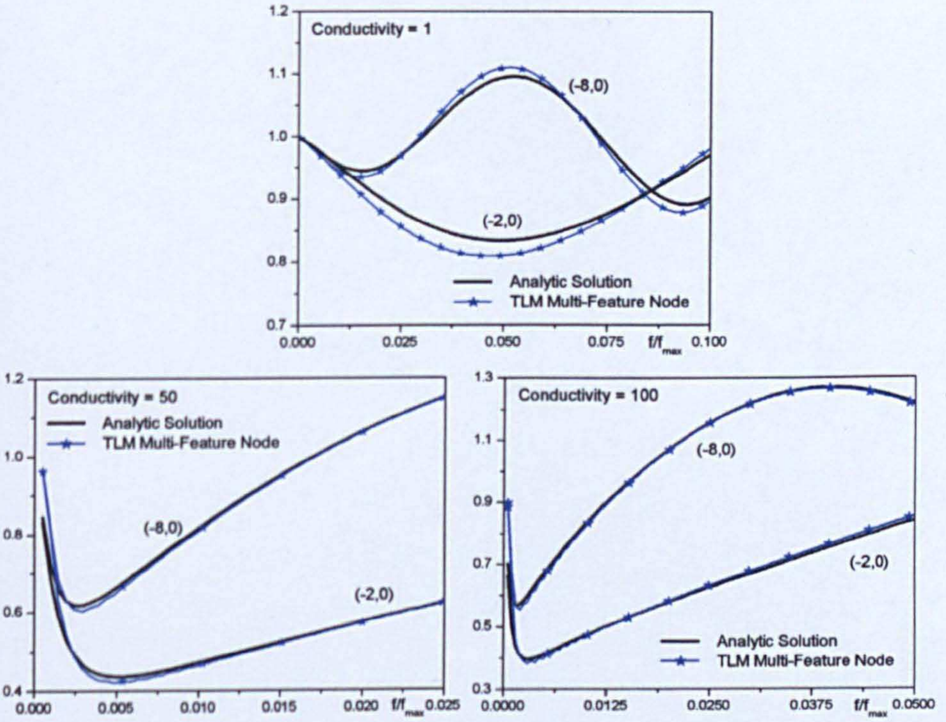

Figure 6.4. Total electric fields from Figure 6.3 presented in a low frequency range

It is observed that in this range the numerical approximation strictly adheres to the exact analytical solution and furthermore, more accurate results are obtained for increasing value of conductivity.

In the next section the possibility of employing the multi-feature node for simulations in other areas rather than EMC modelling will be examined.

6.2. Photonic Band-Gap Structures

In this section the possibility of implementing the 2D multi-feature node for simulations of photonic systems will be explored. Of significant interest is the ability to predict the performance of photonic band-gap materials that have already attracted a lot of attention over the last decade [6.1-6.5]. These kind of structures are often constructed from a lattice of dielectric rods or air holes etched into a substrate and possess frequency stop-bands in which the propagation of energy through the material is forbidden [6.1, 6.2]. The conventional approach to numerical modelling of PBG lattice utilises direct discretisation with fine meshes, notably smaller than the size of the individual rods or holes. This guarantees correct representation of the scatterer geometry and provides high accuracy. However this approach results in very long computational run-times and huge memory consumption. Therefore, such direct numerical approaches to PBG characterisation are only suited to the analysis of single unit cells or for benchmarking. In practice, the computational overheads significantly increase when one deals with an array of cells or when modelling the global response of a large number of devices integrated on a single substrate. For this reason many simulations of PBG structures are so intensive as to render the possibility of their application for modelling sub-system performance impossible. Hence, the objective here is to produce simulations of the macroscopic behaviour of PBG devices, recovering the essential features of their characteristics, albeit without providing resolution of all the fine detail.

For this purpose the 2D multi-feature node approach seems to be very suitable as it employs meshes much larger than the geometry of individual scatterer. In the previous chapters it proved to be a very powerful tool for predicting the performance of sub-system models for EMC applications. In the following sections the algorithm will be scaled to micro-wavelength operation and its use in simulations of photonic devices will be demonstrated.

6.2.1. Photonic Crystal Devices

Consider a periodic structure consisting of dielectric rods distributed within a region of empty space with periodicity *a*, as presented in Figure 6.5(a).

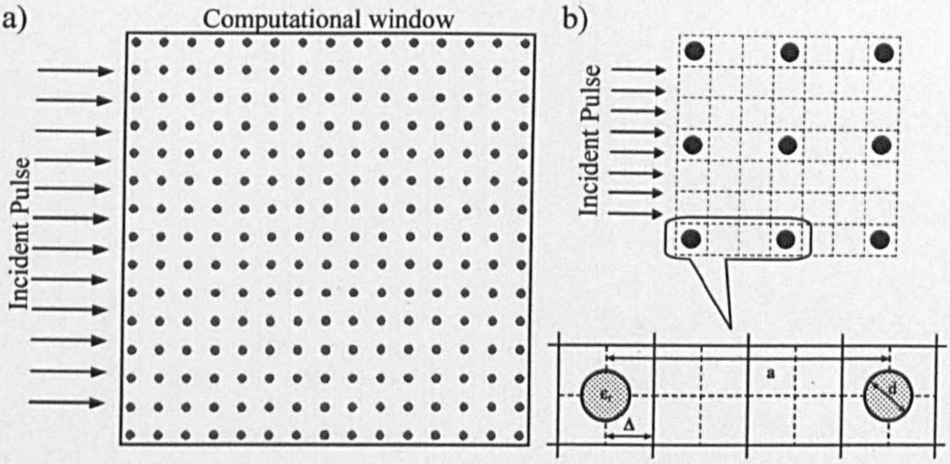

Figure 6.5. Numerical set-up: Lattice of 15×15 dielectric rods (a) and a segment of lattice presenting mesh fitting and lattice parameters (b)

It has been found that when the refractive index contrast between the dielectric material and the surrounding space is high enough, a range of wavelengths exists for which propagation is forbidden in all directions [6.1]. A straightforward method for determining the band-gap is to calculate the transmission of a broad-band electromagnetic signal through the structure in all dimensions for the reduced Brillouin Zone (BZ). To achieve this, a TLM method with multi-feature nodes is utilised. The square lattice of 15×15 dielectric rods in Figure 6.5(a) is discretised so that there are two empty TLM nodes in between multi-feature nodes each containing a centrally placed dielectric cylinder, as shown in Figure 6.5(b). The lattice parameters are chosen after [6.3] and with reference to Figure 6.5(b) these are: $a = 0.6\mu m$, $d = 0.15\mu m$, refractive index $n = \sqrt{\varepsilon_r} = 3.4$ and the TLM mesh radius is $\Delta = 0.1\mu m$.

Prior to the TLM simulation, the band-gap for the structure described above is first calculated using a planewave-based block-iterative algorithm [6.5] available commercially in [6.6] as a benchmark.

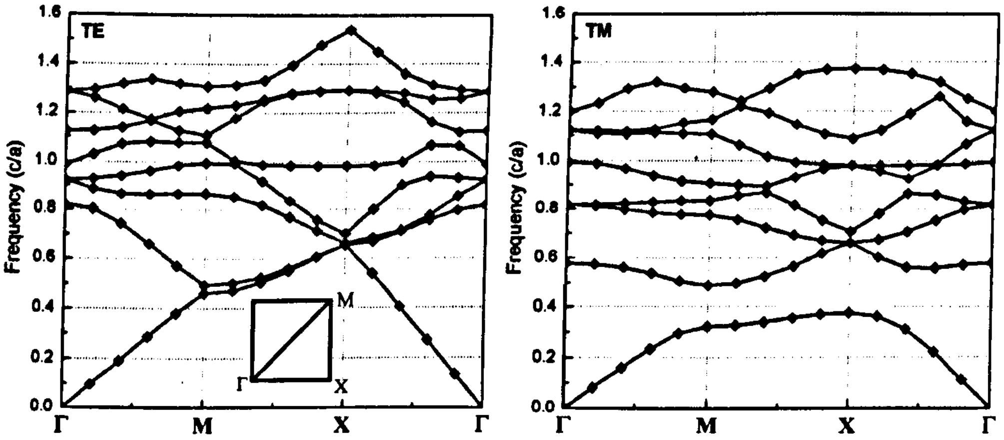

Figure 6.6. Diagrams of photonic band structure from Figure 6.5 for TE and TM polarisation.

Figure 6.6 shows the diagram of the band structure presented in Figure 6.5 for TE and TM illumination calculated by the MIT Photonic Band package [6.6]. In these diagrams the dispersion is calculated along the high-symmetry line Γ-X-M-Γ, where $\Gamma = (0,0)$, $X = (\pi/a, 0)$ and $M = (\pi/a, \pi/a)$ are the high-symmetric points in the first BZ. It can be observed that the lattice from Figure 6.5 exhibits a forbidden frequency band only for TM polarised waves. This band-gap is estimated to lie in the frequency range from 0.375 to 0.485 (c/a), where *c* is the speed of light in vacuum and *a* is the periodicity of the lattice.

Similar results are obtained using the TLM method. A TM polarised, pulse of RMS width 1.5 time-steps, short enough so that the resulting electromagnetic wave contains a wide range of wavelengths, is injected into bottom corner of the left-hand side of the structure, position Γ in the diagram in Figure 6.7. The Fast Fourier transform is performed for the transmitted fields recorded at the right-hand side of the lattice for a range of propagation angles, between 0 and 45° that covers the reduced BZ of the square lattice.

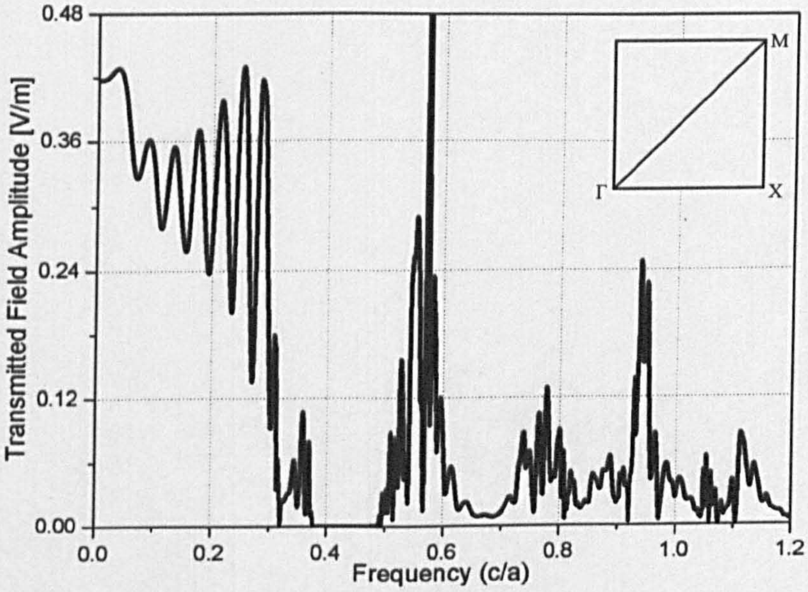

Figure 6.7. Frequency spectrum for a TM illuminated square lattice of $d = 0.15a$ output at point M of band diagram.

Plotting out the frequency responses in the first BZ allows the band-gap to be evaluated. This band-stop is confirmed and clearly visible in Figure 6.7, where the frequency response for a lattice from Figure 6.5(a) is observed at point M of the first BZ.

By creating a defect in a lattice which consequently breaks its periodicity, photonic devices in various configurations can be designed [6.3]. As an example, a waveguide can be formed by simply eliminating a row of rods from the lattice. Modulating the input signal with the frequency from the band-gap the light is confined within the waveguide. Similarly, other configurations can be created; some of them are illustrated in Figure 6.8. These include: a straight waveguide, a sharp-bend waveguide, a beam splitter and a coupler shown in Figure 6.8(a), (b), (c) and (d) respectively. In each of the designs presented in Figure 6.8, the TLM mesh was illuminated with a TM polarised Gaussian Pulse modulated with a frequency of 0.4 (c/a) and the time-domain electric field was plotted out after 300 time-steps. An impedance absorbing boundary condition was assumed at the edges of the computational window enclosing the lattice.

It should be pointed out that light with a frequency outside the stop-band does not provide light confinement within the waveguide. In such a scenario conventional scattering phenomenon occurs; the wave is scattered from particular dielectric rods throughout the whole lattice.

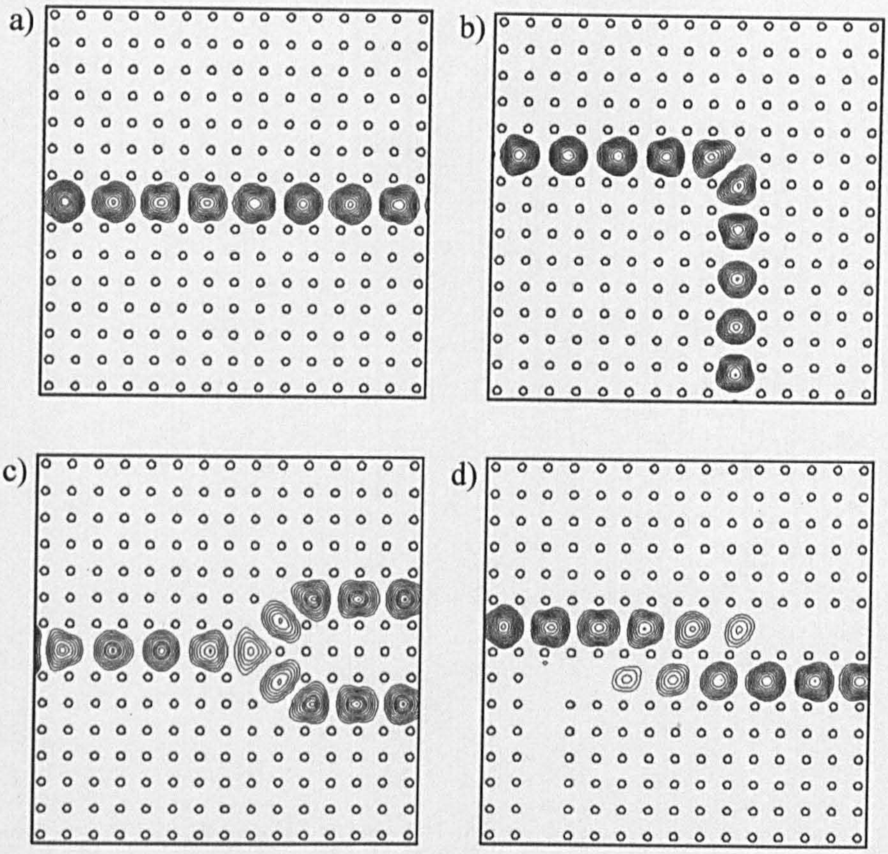

Figure 6.8. Photonic devices based on a lattice of dielectric rods: straight waveguide (a), sharp-bend waveguide (b), beam splitter (c) and coupler (d)

The results presented above indicate that the multi-feature node is highly applicable for the simulation of photonic band-gap devices. As the number of mesh nodes is significantly reduced compared to a fine mesh discretisation, the performance of the photonic component can be obtained within a short period of computational time. Furthermore, embedding dielectric rods within a TLM model incurs only slight additional overheads compared to the conventional TLM cells.

The extra quantities that have to be stored in the node are typically stub impedances and stub voltages, as pointed out in Chapter 3.

Although only canonical examples have been presented above it should be underlined that the multi-feature scheme is very attractive for the simulation of practical systems. The fact that it allows objects of different characteristics to be arbitrarily placed within the numerical cells is very advantageous for models where the periodicity of the lattice does not coincide with that of the numerical grid.

In summary, the approach provides a rapid assessment of photonic crystal devices in the context of larger sub-systems and circuits. The ability to assess the global performance of many elements integrated on a single chip is illustrated in Figure 6.9.

In terms of the design and optimisation process, it is very desirable to simulate a system consisting of many elements integrated on a single chip. This gives an opportunity to verify whether or not the system responds as predicted based on a single device, account for factors such as mutual interference caused by high-levels of integration and generally to improve the model. An example of such an integrated system is presented in Figure 6.9 which shows a 1×16 beam splitter designed on a lattice of 81×51 dielectric rods with lattice parameters as specified in the previous examples. It is clear that simulation of such a system with a mesh of a fine granularity would be very expensive in terms of computational resources.

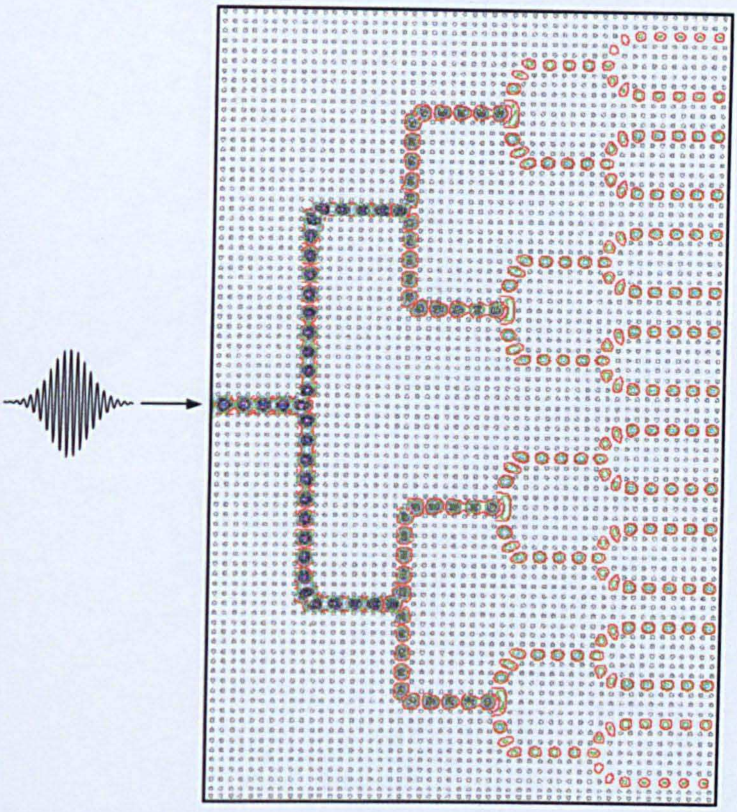

Figure 6.9. 1×16 beam splitter based on a lattice of dielectric posts

In the next example presented in Figure 6.10, the multi-feature node is used to simulate another computationally demanding configuration, the Mach-Zehnder interferometer. The Mach-Zehnder interferometer is a simple device which is used for many purposes in integrated optics. A light beam is first split into two parts by a beam splitter and then recombined by a second beam splitter (not shown in Figure 6.10). Depending on the relative phase acquired by the beam along the two paths the output from second beam splitter will lie between 0 and 100% of the input power. In a design of this seemingly simple device, many parameters have to be taken into account, amongst which the following can be included: the necessary length of the arms so that the phase shift can be applied to one of them; angle of alignment and the minimum distance between the arms that guarantees transmission of the two signals propagating down the arms with the lowest possible interference. In order to estimate those optimal working characteristics, it is required to model a slightly over-designed configuration, at least at the early stage. Hence, a lattice of large dimensions can be used for such purpose, as presented in Figure 6.10 where the interferometer is incorporated in a periodic material built from 101×45 dielectric cylinders.

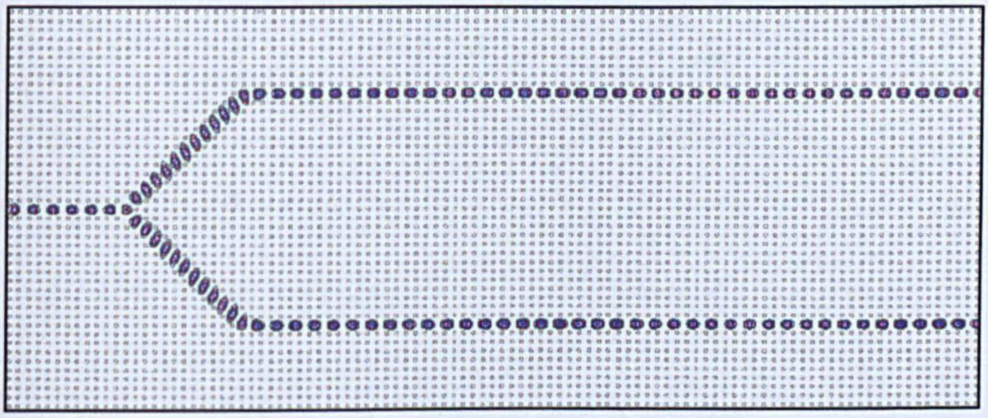

Figure 6.10. Mach-Zehnder interferometer design on a lattice of dielectric rods

It is clear that with growing complexity of the systems, simulations involving techniques based on a direct meshing can be hard, if at all feasible, to implement for such large problems. Therefore there is a great demand for approaches such as the one presented above to deal with complex structures utilising best the available resources to provide a quick and yet accurately enough assessment.

More information about the implementation of the 2D multi-feature node in photonic applications including different practical examples can be found in the author's paper [6.7].

6.3. Closing remarks

In this chapter the multi-feature node has been extended to simulate an important group of problems as scattering from a lossy wires and lossy dielectric rods. It was shown that the multi-feature node is very suitable for application to such practical configurations. By changing slightly the derivation in order to account for a new boundary-value problem, a lossy wire was embedded in a single TLM cell and the numerical results demonstrate excellent agreement with the known solution. It was also demonstrated that EMC problems are not the only ones that can be solved using this technique. As shown, it was successfully employed in photonics where the macroscopic behaviour of microstructures like photonic band-gap materials can be easily estimated without the need to characterise in detail every single feature.

6.4. References

[6.1] Joannopoulos, J.D., Meade, R.D. and Winn, J.N., *"Photonic crystals: Molding the Flow of Light"*, Princeton University Press, Princeton, New Jersey, 1995

[6.2] Johnson, S.G., Joannopoulos, J.D., *"Photonic crystals : the road from theory to practice"*, Kluwer Academic, Boston, 2002

[6.3] Stoffer, R., Hoekstra, H.J.W.M., De Ridder, R.M., Van Groesen E., and Van Beckum, F. P. H., *"Numerical studies of 2D photonic crystals: Waveguides, coupling between waveguide and filters"*, Optical and Quantum Electronics, Vol. 32, pp. 947-961, 2000

[6.4] Johnson, S.G., Fan, S., Villeneuve, P.R., Joannopoulos J.D., and Kolodziejski L.A., *"Guided modes in photonic crystal slabs"*, Physical Review B, Vol. 60, No. 8, pp. 5752-5758, 1999

[6.5] Johnson, S.G., and Joannopoulos, J.D., "Block-iterative frequency-domain methods for Maxwell's equations in a plane wave basis," Optics Express 8, No. 3, pp.173-190, 2001

[6.6] URL: http://ab-initio.mit.edu/mpb/

[6.7] Biwojno K., Sewell, P., Liu Y., Christopoulos C., *"Electromagnetic Modelling of Fine Features in Photonic Applications"*, Optical and Quantum Electronics, Special Issue on Waveguide Theory and Numerical Modelling, Vol. 38, No. 1-3, pp. 187-201, 2006

Chapter 7

A Special Node Containing a Strip or Slot

The aim of the work discussed in this chapter is to demonstrate the applicability of the general approach presented in Chapter 3 in combination with an elliptical coordinate system which can characterise non circular objects embedded in a TLM model. The set of local field solutions to Maxwell's equations that forms the key component of our technique will be obtained by analytical means. The problem of an electromagnetic wave incident upon homogeneous elliptic cylinders will be derived in terms of Mathieu functions. The analytical solutions for wave scattered from a small conducting strip or penetrating through a narrow slot will be presented. Finally, numerical results will be shown for both a strip and a slot embedded in a single cell of a coarse TLM mesh.

7.1. Introduction

The flexibility of the approach introduced in Chapter 3 will now be demonstrated in its application to various scattering objects described mathematically by different coordinate systems. Particular attention will be focused on the elliptical coordinate system. The fundamental reason for selecting this system lies in geometrical considerations. Owing to the fact that elliptic cross-sections can be modified by changing the axes ratio, elliptical cylinders can be effectively used to approximate a variety of important geometrical shapes. Indeed, the example scattering problems illustrated in this chapter will not be restricted to canonical diffraction from elliptic cylinders but also encompass thin metallic strips, which are often encountered as tracks on Printed Circuit Boards (PCB) and narrow slots in metal planes that form ground plane slotlines or enclosure apertures for cooling. Both of these models are very useful in their own right and also pave the way for the future development of accurate 3D modelling of multi-track and multi-layer PCBs. The technique starts with a formulation of the wave equation in elliptical coordinates systems and identifies its solutions by the separation of variables. Appropriate boundary conditions are imposed at the surface of the small feature under consideration and the infinite number of elliptical harmonics is approximated to form a set of solutions that is suitable for linking the multi-feature node with the adjacent nodes of the TLM model ensuring continuity of the fields and conservation of the power in the network.

7.2. Wave Equation in the Elliptical Coordinate System

In this section, the elliptical coordinate system will be introduced and analytical solutions for the fields in the presence of an elliptical cylinder will be obtained. For brevity, only the necessary theory will be demonstrated here and for more details the reader is referred to the literature [7.1-7.7]. The elliptical coordinate system in the (x,y) plane is presented in Figure 7.1. The surfaces $u = constant$ represent a family of elliptic cylinders having the same foci at $x = \pm d$ on the x-axis and $v = constant$ represent a family of confocal hyperbolic cylinders. The transformation from the elliptic to the Cartesian (x,y,z) coordinate system is given by:

$$\begin{aligned} x &= \frac{d}{2}\cosh u \cos v \\ y &= \frac{d}{2}\sinh u \sin v \\ z &= z \end{aligned} \qquad (7.1)$$

where d is the distance between foci of the ellipse as shown in Figure 7.1.

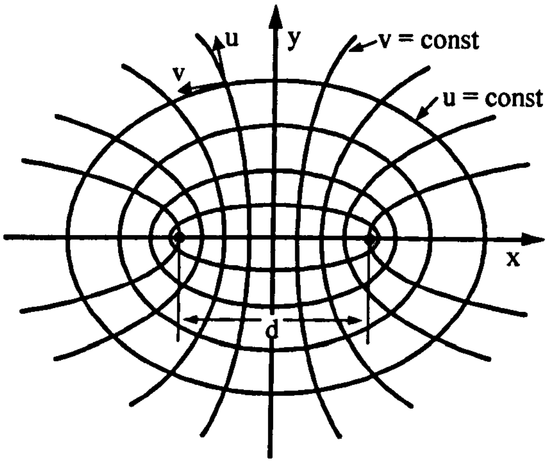

Figure 7.1. Elliptic cylinder coordinate

In order to facilitate the derivation additional variables are introduced:

$$\xi = \cosh u \qquad (7.2)$$

$$\eta = \cos v \qquad (7.3)$$

The inverse transformation from Cartesian to elliptic coordinates is given by [7.1]:

$$\xi = \sqrt{\frac{4(x^2+y^2)+d^2+\sqrt{16(x^2+y^2)^2+d^4-8d^2(x^2-y^2)}}{2d^2}}, \text{ and } \eta = \frac{2x}{d\xi} \qquad (7.4)$$

Time-harmonic fields are considered and the time-dependence $e^{j\omega t}$ is suppressed for clarity. Two illuminations will be discussed, i.e. (i) a uniform plane wave of transverse magnetic type with the electric field vector polarised along z-axis; and (ii) a uniform plane wave of transverse electric with magnetic field vector orientated along z-axis. It is assumed that the elliptical object is surrounded by a volume of empty space (ε_0, μ_0).

In all coordinate systems, the field solutions obey the Helmholz equation:

$$\nabla^2 F_z + k^2 F_z = 0 \tag{7.5}$$

where F_z denotes E_z for TM and H_z for TE polarisation.

In elliptical coordinates, this equation is expressed in the form [7.4]:

$$\frac{\partial^2 F_z}{\partial u^2} + \frac{\partial^2 F_z}{\partial v^2} + d^2(\cosh^2 u - \cos^2 v)\left[\frac{\partial^2}{\partial z^2} + k^2\right]F_z = 0 \tag{7.6}$$

Equation (7.6) can be solved by separation of the variables:

$$F_z = U(u)V(v)Z(z) \tag{7.7}$$

Substituting Equation (7.7) into Equation (7.6) leads to:

$$\frac{U''}{U} + \frac{V''}{V} + d^2(\cosh^2 u - \cos^2 v)\left[\frac{Z''}{Z} + k^2\right] = 0 \tag{7.8}$$

Defining the separation constant C so that:

$$\frac{Z''}{Z} + C = 0 \tag{7.9}$$

then U and V must satisfy:

$$U'' - (a - 1/2c^2 \cosh 2u)U = 0 \tag{7.10}$$

$$V'' + (a + 1/2c^2 \cos 2v)V = 0 \tag{7.11}$$

where $c = \sqrt{k^2 + C}\, d/2$, [7.4], and k is the wavenumber, $k = k_0$. In exploiting Equation (7.10) and (7.11) it will be assumed that there is no z-dependence and therefore in Equation (7.9) $C \to 0$. Equation (7.10) is known as Mathieu equation and Equation (7.11) as the modified Mathieu equation. Equation (7.11) is a linear second-order differential equation that has two families of independent solutions, namely the even and odd angular Mathieu functions (AMF):

$$V_m = \begin{cases} Ce_m(c,\eta) & m = 0,1,2,..., \\ Se_m(c,\eta) & m = 1,2,3,..., \end{cases} \tag{7.12}$$

The cosine-elliptic $Ce(c,\eta)$ and sine-elliptic $Se(c,\eta)$ functions are analogous to trigonometric cosine and sine functions and with vanishing c they become trigonometric functions. The symmetry and periodicity of these functions is the same as for their trigonometric counterparts; the corresponding expansions fall into four classes: even solution of period of π: $Ce_{2r}(c,\eta)$, even solution of period of 2π: $Ce_{2r+1}(c,\eta)$, odd solution of period of π: $Se_{2r}(c,\eta)$ and finally odd solution of period of 2π: $Se_{2r+1}(c,\eta)$, where $r = 0,1,2,...,$. In addition, any even AMF is orthogonal to any odd AMF on the interval of $(0,2\pi)$, thus,

$$\int_0^{2\pi} Ce_r(c,\eta)Se_m(c,\eta)dv = 0 \tag{7.13}$$

The solution to Equation (7.10), is expressed in the form of even $Mc_m^{(i)}(c,\xi)$ and odd $Ms_m^{(i)}(c,\xi)$ radial Mathieu functions (RMF), where *i* denotes the kind and *m* the order of the RMF. In elliptic coordinates the RMF play a similar role to the Bessel functions in circular cylindrical coordinates. Analogously to the Bessel functions, the family of radial Mathieu functions splits into four independent solutions, odd and even RMF of the first and the second kind. Further analysis of Mathieu functions is out of the scope of this work and the reader is referred to [7.5] where a visualisation of those functions is given and [7.6] where a full study is carried out.

7.3. Scattering from the Strip

Here, the expansion of a plane wave in the form of elliptic-cylinder harmonics will be considered and applied to the problem of a wave scattered from a thin conducting strip. In elliptic cylindrical coordinates the strip is defined by $u = 0$ and the strip width is denoted as d. Both TM and TE illuminations will be analysed simultaneously.

7.3.1. Analytical Description

The z-directed, electric and magnetic, field incident at an angle ϕ_0 from the positive x-axis, in terms of elliptical harmonics is expressed as a rapidly converging series of Mathieu functions [7.7]:

$$\text{TM:} \qquad E_z^{inc} = \sum_{m=0}^{\infty} a_m^{inc} Mc_m^{(1)}(c,\xi) Ce_m(c,\eta) + \sum_{m=1}^{\infty} b_m^{inc} Ms_m^{(1)}(c,\xi) Se_m(c,\eta) \qquad (7.14)$$

$$\text{TE:} \qquad H_z^{inc} = \sum_{m=0}^{\infty} a_m^{inc} Mc_m^{(1)}(c,\xi) Ce_m(c,\eta) + \sum_{m=1}^{\infty} b_m^{inc} Ms_m^{(1)}(c,\xi) Se_m(c,\eta) \qquad (7.15)$$

where

$$\begin{aligned} a_m^{inc} &= \sqrt{8\pi}\frac{(-j)^m}{N_m^{(e)}} Ce(c,\cos\phi_0) \\ b_m^{inc} &= \sqrt{8\pi}\frac{(-j)^m}{N_m^{(o)}} Se(c,\cos\phi_0) \end{aligned} \qquad (7.16)$$

and $N_m^{(e)}$ and $N_m^{(o)}$ are functions of *c* defined as:

$$N_r^{(o)} = \int_0^{2\pi} Se_r^2(c,\eta) dv \qquad (7.17)$$

$$N_r^{(e)} = \int_0^{2\pi} Ce_r^2(c,\eta) dv \qquad (7.18)$$

These two functions are usually presented as a Fourier series of *c* and the recurrence formula for calculating them is given in [7.6].

The scattered field can be expressed in terms of Mathieu functions of the fourth kind, $Mc_m^{(4)}$ and $Ms_m^{(4)}$, which represent outgoing waves similar to the Hankel functions for the circular case discussed in Chapter 2. As for Hankel functions these fourth kind functions are linear combinations of the corresponding RMF of the first and second kinds, i.e. $Mc_m^{(4)} = Mc_m^{(1)} - jMc_m^{(2)}$ and $Ms_m^{(4)} = Ms_m^{(1)} - jMs_m^{(2)}$. Thus, the scattered field is written in the form:

TM: $$E_z^{scat} = \sum_{m=0}^{\infty} a_m^{scat} Mc_m^{(4)}(c,\xi) Ce_m(c,\eta) + \sum_{m=1}^{\infty} b_m^{scat} Ms_m^{(4)}(c,\xi) Se_m(c,\eta) \qquad (7.19)$$

TE: $$H_z^{scat} = \sum_{m=0}^{\infty} a_m^{scat} Mc_m^{(4)}(c,\xi) Ce_m(c,\eta) + \sum_{m=1}^{\infty} b_m^{scat} Ms_m^{(4)}(c,\xi) Se_m(c,\eta) \qquad (7.20)$$

where the scattering coefficients a_m^{scat} and b_m^{scat} are yet to be determined.

The total fields are now:

TM: $$\begin{aligned} E_z^{tot} &= \sum_{m=0}^{\infty} Ce_m(c,\eta)\left[a_m^{inc} Mc_m^{(1)}(c,\xi) + a_m^{scat} Mc_m^{(4)}(c,\xi)\right] \\ &+ \sum_{m=1}^{\infty} Se_m(c,\eta)\left[b_m^{inc} Ms_m^{(1)}(c,\xi) + b_m^{scat} Ms_m^{(4)}(c,\xi)\right] \end{aligned} \qquad (7.21)$$

TE: $$\begin{aligned} H_z^{tot} &= \sum_{m=0}^{\infty} Ce_m(c,\eta)\left[a_m^{inc} Mc_m^{(1)}(c,\xi) + a_m^{scat} Mc_m^{(4)}(c,\xi)\right] \\ &+ \sum_{m=1}^{\infty} Se_m(c,\eta)\left[b_m^{inc} Ms_m^{(1)}(c,\xi) + b_m^{scat} Ms_m^{(4)}(c,\xi)\right] \end{aligned} \qquad (7.22)$$

The total magnetic and electric fields follow from Maxwell's equations [7.1]:

TM: $$H^{tot} = \frac{1}{j\omega\mu_0 h}\left(\bar{u}\frac{\partial E_z^{tot}}{\partial u} + \bar{v}\frac{\partial E_z^{tot}}{\partial v}\right) \qquad (7.23)$$

TE: $$E^{tot} = \frac{-1}{j\omega\varepsilon_0 h}\left(\bar{u}\frac{\partial H_z^{tot}}{\partial u} - \bar{v}\frac{\partial H_z^{tot}}{\partial v}\right) \qquad (7.24)$$

where $h = \frac{d}{2}\sqrt{\cosh^2 u - \cos^2 v}$.

Accounting for the fact that the electric field is entirely reflected from the surface of a conducting strip ($E^{tot} = 0$) and comparing terms in the tangential electric field expansion, the scattered field coefficients are:

TM: $$a_m^{scat} = -a_m^{inc}\frac{Mc_m^{(1)}(c,\xi_a)}{Mc_m^{(4)}(c,\xi_a)} \text{ and } b_m^{scat} = -b_m^{inc}\frac{Ms_m^{(1)}(c,\xi_a)}{Ms_m^{(4)}(c,\xi_a)} \qquad (7.25)$$

TE: $$a_m^{scat} = -a_m^{inc}\frac{Mc_m^{(1)\prime}(c,\xi_a)}{Mc_m^{(4)\prime}(c,\xi_a)} \text{ and } b_m^{scat} = -b_m^{inc}\frac{Ms_m^{(1)\prime}(c,\xi_a)}{Ms_m^{(4)\prime}(c,\xi_a)} \qquad (7.26)$$

where $\xi_a = 1$ and the derivative given in $Mc_m^{(1,4)\prime}(c,\xi_a)$ is calculated with respect to u, i.e.

$$Mc(s)_m^{(1,4)\prime}(c,\xi_a) = \frac{\partial Mc(s)_m^{(1,4)\prime}(c,\xi)}{\partial\xi}\frac{\partial\xi}{\partial u}\bigg|_{\xi=\xi_a} \qquad (7.27)$$

Thus, the fields in the final form are expressed as:

TM: $$E_z^{tot} = \sum_{m=0}^{\infty} a_m^{inc}\, Ce_m(c,\eta)\, fc_m(c,\xi) + \sum_{m=1}^{\infty} b_m^{inc}\, Se_m(c,\eta)\, fs_m(c,\xi) \qquad (7.28)$$

TE: $$H_z^{tot} = \sum_{m=0}^{\infty} a_m^{inc}\, Ce_m(c,\eta)\, gc_m(c,\xi) + \sum_{m=1}^{\infty} b_m^{inc}\, Se_m(c,\eta)\, gs_m(c,\xi) \qquad (7.29)$$

where

$$fc_m(c,\xi) = Mc_m^{(1)}(c,\xi) - \frac{Mc_m^{(1)}(c,\xi_a)}{Mc_m^{(4)}(c,\xi_a)} Mc_m^{(4)}(c,\xi) \qquad (7.30)$$

$$fs_m(c,\xi) = Ms_m^{(1)}(c,\xi) - \frac{Ms_m^{(1)}(c,\xi_a)}{Ms_m^{(4)}(c,\xi_a)} Ms_m^{(4)}(c,\xi) \qquad (7.31)$$

$$gc_m(c,\xi) = Mc_m^{(1)}(c,\xi) - \frac{Mc_m^{(1)\prime}(c,\xi_a)}{Mc_m^{(4)\prime}(c,\xi_a)} Mc_m^{(4)}(c,\xi) \qquad (7.32)$$

$$\mathrm{gs_m}(c,\xi)=\mathrm{Ms_m^{(1)}}(c,\xi)-\frac{\mathrm{Ms_m^{(1)\prime}}(c,\xi_a)}{\mathrm{Ms_m^{(4)\prime}}(c,\xi_a)}\mathrm{Ms_m^{(4)}}(c,\xi) \tag{7.33}$$

It is noted that each term of the field series intrinsically exhibits the known singular field behaviour at the metal edges so that even a single term of the correct symmetry is a good representation of the fields near to the feature. Having obtained the general analytical description of electromagnetic waves in the presence of the conducting strip, the procedure of linking these solutions with real time-domain network will be now discussed.

7.3.2. Embedding into TLM model

The process of embedding the analytical solutions into a time-domain numerical technique was first introduced in Chapter 3 and described in detail whilst considering a conducting wire placed centrally in the node in Chapter 4. The study of the latter revealed that the key component of the mapping process lies in constructing the admittance relationship between the port voltages and port currents, or equivalently between the electric and magnetic fields, by selecting a suitable set of tangential field solutions at the edges of the node. The node containing the strip in the TM configuration is presented in Figure 7.2(a) showing also the sampling points at the edges of the 2D TLM cell.

The outstanding task is to evaluate the tangential field components (H_x, H_y) and (E_x, E_y) for TM and TE illumination respectively. To achieve this the infinite expansion of fields is approximated to the four lowest order symmetrical harmonics only $m=-1,0,1,2$, as discussed in Chapter 4.

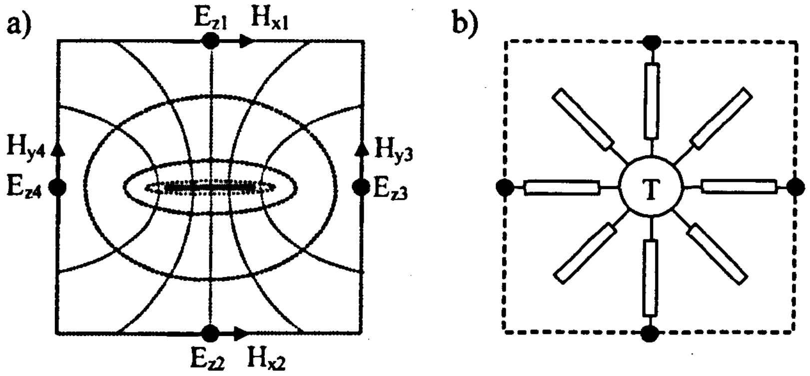

Figure 7.2. Thin strip geometry and field sampling points at the edges of the node (a). The equivalent electrical circuit of the non-standard TLM node (b)

Thus truncating the series in fields from Equations (7.28) and (7.29) results in:

TM:
$$\underline{E}_z = \begin{Bmatrix} fc_0(c,\xi)\,Ce_0(c,\eta), \\ fc_1(c,\xi)\,Ce_1(c,\eta), \\ fs_1(c,\xi)\,Se_1(c,\eta), \\ fc_2(c,\xi)\,Ce_2(c,\eta) \end{Bmatrix} \tag{7.34}$$

TE:
$$\underline{H}_z = \begin{Bmatrix} gc_0(c,\xi)\,Ce_0(c,\eta), \\ gc_1(c,\xi)\,Ce_1(c,\eta), \\ gs_1(c,\xi)\,Se_1(c,\eta), \\ gc_2(c,\xi)\,Ce_2(c,\eta) \end{Bmatrix} \tag{7.35}$$

The remaining tangential field components can be derived from Maxwell's equations, for TM:

$$-j\omega\mu H_x = \frac{\partial E_z}{\partial y} = \frac{\partial E_z}{\partial u}\frac{\partial u}{\partial y} + \frac{\partial E_z}{\partial v}\frac{\partial v}{\partial y} \tag{7.36}$$

$$j\omega\mu H_y = \frac{\partial E_z}{\partial x} = \frac{\partial E_z}{\partial u}\frac{\partial u}{\partial x} + \frac{\partial E_z}{\partial v}\frac{\partial v}{\partial x} \tag{7.37}$$

and for TE:

$$j\omega\varepsilon E_x = \frac{\partial H_z}{\partial y} = \frac{\partial H_z}{\partial u}\frac{\partial u}{\partial y} + \frac{\partial H_z}{\partial v}\frac{\partial v}{\partial y} \tag{7.38}$$

$$-j\omega\varepsilon E_y = \frac{\partial H_z}{\partial x} = \frac{\partial H_z}{\partial u}\frac{\partial u}{\partial x} + \frac{\partial H_z}{\partial v}\frac{\partial v}{\partial x} \tag{7.39}$$

Restricting Equation (7.36), (7.37), (7.38) and (7.39) to the permissible harmonics only yields:

$$-j\omega\mu H_x = \begin{pmatrix} \frac{\partial u}{\partial y} fc'_0(q,u)Ce_0(q,v) + \frac{\partial v}{\partial y} fc_0(q,u)Ce'_0(q,v), \\ \frac{\partial u}{\partial y} fc'_1(q,u)\,Ce_1(q,v) + \frac{\partial v}{\partial y} fc_1(q,u)Ce'_1(q,v), \\ \frac{\partial u}{\partial y} fs'_1(q,u)\,Se_1(q,v) + \frac{\partial v}{\partial y} fs_1(q,u)Se'_1(q,v), \\ \frac{\partial u}{\partial y} fc'_2(q,u)Ce_2(q,v) + \frac{\partial v}{\partial y} fc_2(q,u)Ce'_2(q,v), \end{pmatrix} \tag{7.40}$$

$$j\omega\mu H_y = \begin{pmatrix} \frac{\partial u}{\partial x} fc'_0(q,u)Ce_0(q,v) + \frac{\partial v}{\partial x} fc_0(q,u)Ce'_0(q,v), \\ \frac{\partial u}{\partial x} fc'_1(q,u)Ce_1(q,v) + \frac{\partial v}{\partial x} fc_1(q,u)\,Ce'_1(q,v), \\ \frac{\partial u}{\partial x} fs'_1(q,u)\,Se_1(q,v) + \frac{\partial v}{\partial x} fs_1(q,u)\,Se'_1(q,v), \\ \frac{\partial u}{\partial x} fc'_2(q,u)Ce_2(q,v) + \frac{\partial v}{\partial x} fc_2(q,u)Ce'_2(q,v), \end{pmatrix} \tag{7.41}$$

$$-j\omega\varepsilon E_x = \begin{pmatrix} \frac{\partial u}{\partial y} gc'_0(q,u)Ce_0(q,v) + \frac{\partial v}{\partial y} gc_0(q,u)Ce'_0(q,v), \\ \frac{\partial u}{\partial y} gc'_1(q,u)\,Ce_1(q,v) + \frac{\partial v}{\partial y} gc_1(q,u)\,Ce'_1(q,v), \\ \frac{\partial u}{\partial y} gs'_1(q,u)\,Se_1(q,v) + \frac{\partial v}{\partial y} gs_1(q,u)\,Se'_1(q,v), \\ \frac{\partial u}{\partial y} gc'_2(q,u)Ce_2(q,v) + \frac{\partial v}{\partial y} gc_2(q,u)Ce'_2(q,v), \end{pmatrix} \tag{7.42}$$

and

$$j\omega\varepsilon E_y = \left(\begin{array}{l} \frac{\partial u}{\partial x} gc'_0(q,u)Ce_0(q,v) + \frac{\partial v}{\partial x} gc_0(q,u)Ce'_0(q,v), \\ \frac{\partial u}{\partial x} gc'_1(q,u)Ce_1(q,v) + \frac{\partial v}{\partial x} gc_1(q,u)Ce'_1(q,v), \\ \frac{\partial u}{\partial x} gs'_1(q,u)Se_1(q,v) + \frac{\partial v}{\partial x} gs_1(q,u)Se'_1(q,v), \\ \frac{\partial u}{\partial x} gc'_2(q,u)Ce_2(q,v) + \frac{\partial v}{\partial x} gc_2(q,u)Ce'_2(q,v), \end{array}\right) \qquad (7.43)$$

where the derivatives $\frac{\partial u}{\partial x}, \frac{\partial u}{\partial y}, \frac{\partial v}{\partial x}$ and $\frac{\partial v}{\partial y}$ are derived in Appendix D.

The use of the lowest order cosine-elliptic and sine-elliptic functions results in a 4-port transformer which is identical to that presented in Chapter 4 for a single wire embedded at the centre of the node.

The tangential field components can be identified using Equations (7.34), (7.35) and (7.40), (7.41), (7.42), (7.43) depending on the port at which they are evaluated, as indicated in Figure 7.2. The general admittance relationship

$$\underline{\underline{E}} = \underline{\underline{Y}}\,\underline{\underline{H}} \qquad (7.44)$$

is constructed as before. The eigenvalue analysis yields a purely inductive or a capacitive relationship between the tangential electric and magnetic fields at the sample points in the limiting case of large wavelengths with respect to the node size for each of the elliptic harmonics. In the equivalent circuit shown in Figure 7.2(b) the voltage on each of the stub transmission lines corresponds to the amplitude of one of the eigensolutions and the stub is either open or short circuited respectively to produce the required capacitive or inductive behaviour. The transformer T simply maps the sampled field values onto the eigensolution amplitudes. It is noted that stability is ensured as the new node corresponds to a passive electrical network with non-negative component values and that the simulation time step remains the same as for the conventional TLM node.

The approach of embedding the tangential field solution into a time-domain model was discussed in detail in Chapter 3 and repeated in Chapter 4 for the case of a single conducting wire placed in the node. Therefore, for brevity is omitted at this point. Instead, numerical results will be presented to validate the model discussed above.

7.3.3. Numerical Validations

In this section, numerical results are presented to support the theory of wave scattering from a small conductive strip presented above. The results for that section were prepared in cooperation with Dr Y. Liu of the GGIEMR at The University of Nottingham.

The numerical set-up for this experiment is shown in Figure 7.3. In this case, the total mesh area is 60m by 60m, with the TLM node size of 0.05m and the width of the strip is 0.04m. The problem is illuminated by a TM polarised plane wave travelling in the +x direction. The total field is observed at a distance 0.3m in line and in front of the strip node.

The AMF and RMF necessary to obtain the field solutions were calculated using FORTRAN routines for computation of special functions [7.8].

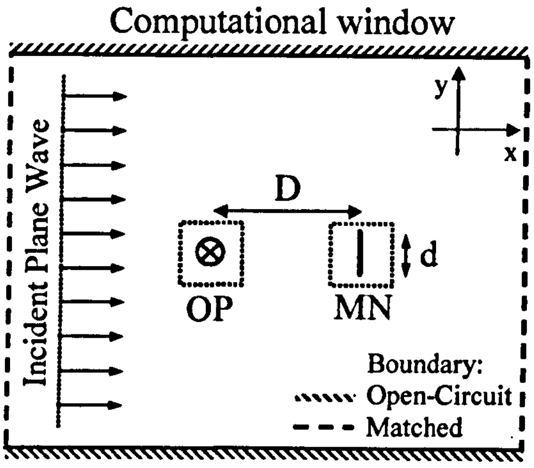

Figure 7.3. This strip simulation configuration

In Figure 7.4, the amplitude of the total field observed in front of the conducting strip is plotted against frequency normalised to the maximum frequency in the simulation ($f_{max} = (2\Delta t)^{-1}$, Δt being the simulation time step). The results of the multi-feature node with strip embedded inside are compared to both the analytic solution as well as the simulation of a round cross section wire inserted into a single TLM node presented in Chapter 4, where the diameter of the round wire equals the width of the metal strip.

It is clear that the accuracy obtained with the TLM simulation of the strip model is excellent over a wide range of frequencies. Furthermore, it is noted that the large scale consequences of the different nature of the fields close to the wire and strip are clearly apparent at even moderate frequencies. Attention is particularly drawn to the fact that at higher frequencies the small difference in the phase of the reflected field due to the fact that the front of the wire is slightly closer to the observation point is detected, even though this distance is smaller than the node size.

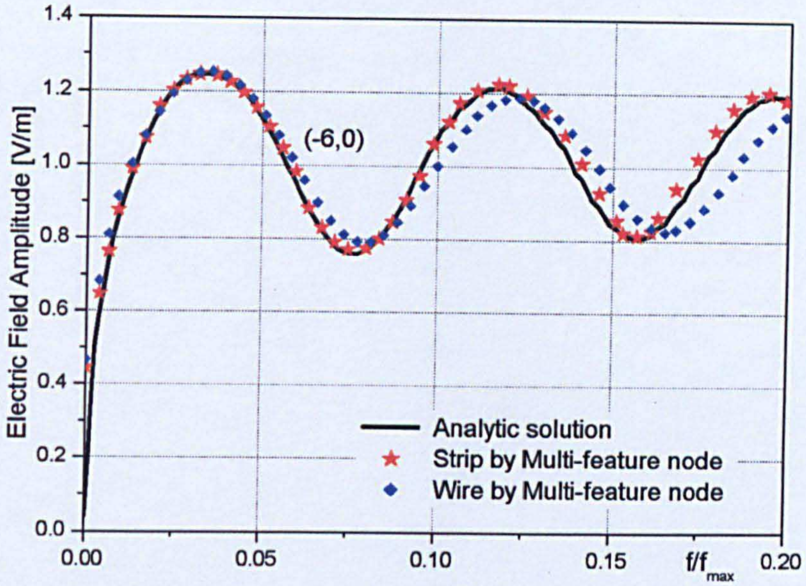

Figure 7.4. Results of the thin strip simulations for the set-up from Figure 7.3

7.4. Fields Penetrating Through a Narrow Slot

In this section the elliptical coordinate system is used to describe the fields penetrating through a slot in a zero thickness conductor. Similar to the analysis of the strip presented above the analytical solution will be first derived, followed by the results of numerical simulations.

7.4.1. Analytical Description

The study of the fields penetrating through a narrow slot is performed based on the field derivation carried out for a conducting strip presented in the previous section. The only difference in the description accounts for a new boundary condition that requires the total electric field to be zero at the edges of the slot. Thus, the total fields are described by Equation (7.28) and (7.29) for TM and TE polarisations respectively, where the functions $f_m(c,\xi)$ and $g_m(c,\xi)$ are now defined with respect to the new boundary condition as:

$$\mathrm{fc_m}(c,\xi)=\mathrm{Mc_m^{(1)}}(c,\xi)-\frac{\lim\limits_{\xi_a\to\infty}\mathrm{Mc_m^{(1)}}(c,\xi_a)}{\lim\limits_{\xi_a\to\infty}\mathrm{Mc_m^{(4)}}(c,\xi_a)}\mathrm{Mc_m^{(4)}}(c,\xi) \tag{7.45}$$

$$\mathrm{fs_m}(c,\xi)=\mathrm{Ms_m^{(1)}}(c,\xi)-\frac{\lim\limits_{\xi_a\to\infty}\mathrm{Ms_m^{(1)}}(c,\xi_a)}{\lim\limits_{\xi_a\to\infty}\mathrm{Ms_m^{(4)}}(c,\xi_a)}\mathrm{Ms_m^{(4)}}(c,\xi) \tag{7.46}$$

$$\mathrm{gc_m}(c,\xi)=\mathrm{Mc_m^{(1)}}(c,\xi)-\frac{\lim\limits_{\xi_a\to\infty}\mathrm{Mc_m^{(1)}}'(c,\xi_a)}{\lim\limits_{\xi_a\to\infty}\mathrm{Mc_m^{(4)}}'(c,\xi_a)}\mathrm{Mc_m^{(4)}}(c,\xi) \tag{7.47}$$

$$\mathrm{gs_m}(c,\xi)=\mathrm{Ms_m^{(1)}}(c,\xi)-\frac{\lim\limits_{\xi_a\to\infty}\mathrm{Ms_m^{(1)}}'(c,\xi_a)}{\lim\limits_{\xi_a\to\infty}\mathrm{Ms_m^{(4)}}'(c,\xi_a)}\mathrm{Ms_m^{(4)}}(c,\xi) \tag{7.48}$$

and the derivatives of RMF $\mathrm{Mc(s)_m^{(1,4)}}'(c,\xi_a)$ are defined in Equation (7.27).

7.4.2. Mapping into TLM model

The TLM slot node is illustrated in Figure 7.5 with the field sampling points shown. It is observed that compared to the conducting strip, only two of the field sample points of the TLM slot node are not on the conducting surfaces. Hence, only a pair of Mathieu functions, the lowest order functions of each symmetry, is used to interpolate the tangential field values at these points. Therefore, at points corresponding to $\eta=0$ and $\eta=\pi$ the tangential fields are zero. Taking into account the form of the functions $f_m(c,\xi)$ and $g_m(c,\xi)$ defined in Equations (7.45) and (7.48), the remaining field components necessary to construct the admittance relationship are obtained from Equations (7.36)-(7.43) by analogy to the conducting strip case presented above.

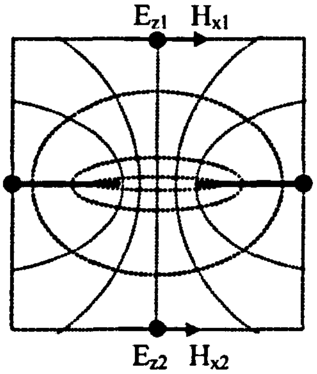

Figure 7.5. Thin slot geometry and field sampling points at the edges of the node.

7.4.3. Numerical Validations

A simple test is now conducted to verify the model of waves penetrating through a narrow slot given in the previous two sections. The numerical set-up for this experiment is presented in Figure 7.6.

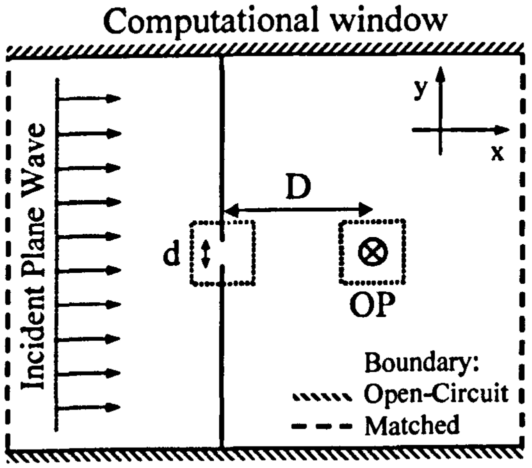

Figure 7.6. This slot simulation configuration.

The simulation parameters used in this example are a total mesh area of 60m by 60m, where the TLM node size is 0.05m. The problem is excited by a plane wave travelling in the +x direction and the fields are observed in line with and behind the slot at observation points 0.5m distant from the slot. The tests are carried out for two slot widths, 0.04m and 0.01m.

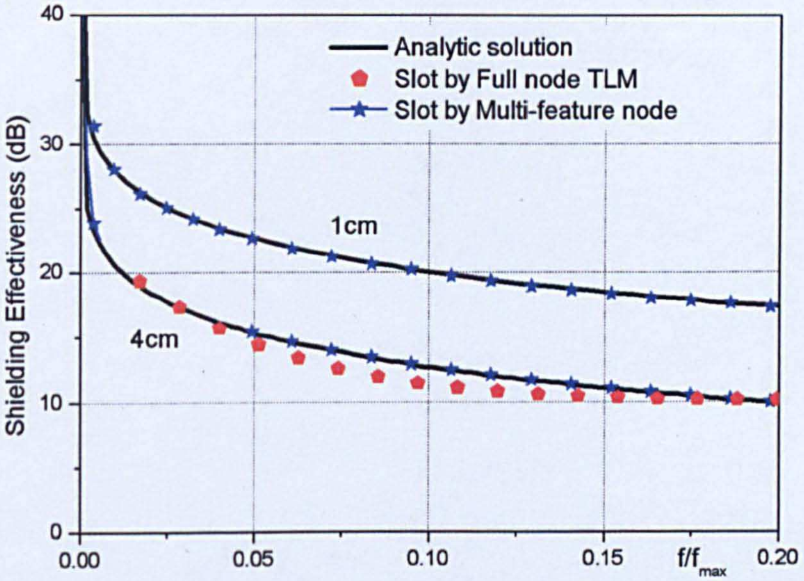

Figure 7.7. Results of the narrow slot simulations for the set-up from Figure 7.6

In Figure 7.7 the electric field that penetrates through a narrow slot is plotted against normalised frequency expressed in the form of the shielding effectiveness. The shielding effectiveness is defined as $-20\log|E|$, where E is the observed field for unit amplitude excitation. To demonstrate how accurate the approach is, results are also shown for the case where the slot is modelled without the special slot node, simply by just using one full width conventional TLM node to model the slot. It is seen that even for the 4cm wide slot (80% of the node width) the special node model clearly provides more accurate results than when the slot is quantised to a full node width. This effect is far more dramatic for the case of a 1cm wide slot (20% of the node width). For that case the multi-feature node model still demonstrates extremely good agreement with the analytical results and now the full node width approximation is 8dB in error.

7.5. Closing Remarks

In this chapter, the general approach for embedding small features in a single cell of numerical method has been applied to objects described by an elliptical coordinate system. Verification of the model for thin conducting flat strips and narrow slots in conducting planes with analytical results proved the approach to be extremely accurate. Very good matching is observed for frequencies even beyond the range of TLM dispersionless operation (10 samples per wavelength). The significance of this technique is that it allows substantial savings in both run time and memory to be achieved over simulations that directly resolve these features by fine meshing. This is of particular importance in the realm of EMC where a wide range of physical scales is a common occurrence.

7.6. References

[7.1] Morse, P., and Feshbach, H.,: *"Methods of Theoretical Physics"*. McGraw Hill, 1953

[7.2] Bowman, J.J., Senior , T.B.A., Uslenghi, P.L.E., *"Electromagnetic and acoustic scattering by simple shapes"*, North-Holland Publishing Company, Amsterdam, 1969

[7.3] Erricolo, D., Uslenghi, P.L.E., *"Exact Radiation and Scattering for an Elliptic Metal Cylinder at the Interface Between Isorefractive Half-*

Spaces", IEEE Transactions on Antennas and Propagations, Vol. 52, No 9, pp. 2214-2225, 2004

[7.4] Holland, R., Cable V.P., *"Mathieu Functions and Their Applications to Scattering by a Coated Strip"*, IEEE Transactions on Electromagnetic Compatibility, Vol. 34, No 1, pp. 9-16, 1992

[7.5] Gutierrez-Vega, J.C., Rodriguez-Dagnino, R.M., Meneses-Nava, M.A. and Chavez-Cerda, S., *"Mathieu functions, a visual approach"*, American Journal of Physics, Vol. 71, No 3, pp 233-242, 2003

[7.6] McLachlan, N.W., *"Theory and Application of Mathieu Functions"*, Oxford University Press, 1947

[7.7] Caorsi, S., Pastorino, M., Raffetto, M., "Electromagnetic Scattering by Multilayer Elliptic Cylinder Under Transverse-Magnetic Illumination: Series Solution in Terms of Mathieu Functions", IEEE Transactions on Antennas and Propagation, Vol. 45, No 6, pp. 926-935, 1997

[7.8] http://jin.ece.uiuc.edu/routines/routines.html

Chapter 8

3D Simulations of Small Objects

In this chapter further modelling of the behaviour of small objects exposed to electromagnetic fields is presented based upon the approach introduced in Chapter 3. The simulations here are dedicated to three-dimensional models seeking to utilise a uniform coarse mesh throughout the problem space with a small number of non-standard nodes containing the scatterers. As demonstrated in Chapter 3 the backbone of the proposed technique is to identify a suitable set of local field solutions and interface them with a numerical network that represent the empty space. It has been underlined that the set of local field solutions to Maxwell's equations can be obtained by any means; the key possibilities being: (i) analytical formulations of the local problem or (ii) numerical approximation to the local fields. Both representations will be explored in this chapter. Initially, the analytical approach is illustrated for the example of tilted conducting wires and rings, each built from small linear segments of thin cylindrical wire. Numerical analysis of the local fields is investigated for the canonical problem of a small conducting cubic box embedded within a 3D TLM cell. In the final section, the potential to apply the spherical coordinate system with our approach is studied and validations are presented for the fields scattered from small conducting and dielectric spheres.

8.1. Analytical Approximation to Local Field Solutions

In this section, the analytical approach is adopted to derive an appropriate set of local field solutions to Maxwell's equations within a 3D cubic cell containing an arbitrarily routed conducting wire. The analytical description of the wire embedded in 3D TLM was previously proposed [8.1], although there the method was restricted to only a single, centrally placed infinitely long z-directed wire. Here, a significant extension will be given to enable simulation of a wire passing arbitrarily through the cell. This goal is achieved by applying a piecewise linear segmentation of the wire in each cell of the 3D mesh. The canonical node required to model such a piecewise linear approximation of the arbitrarily routed wire is illustrated in Figure 8.1.

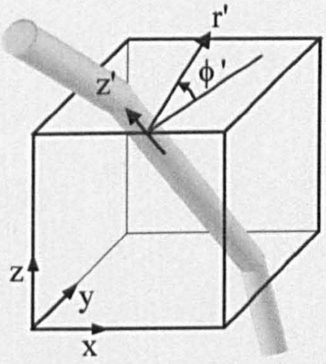

Figure 8.1. A piecewise linear wire segment within a single 3D TLM cell

Each non-standard node contains only a segment of straight wire which is arbitrarily oriented with respect to the node and passes through two of the bounding surfaces, as demonstrated in Figure 8.2.

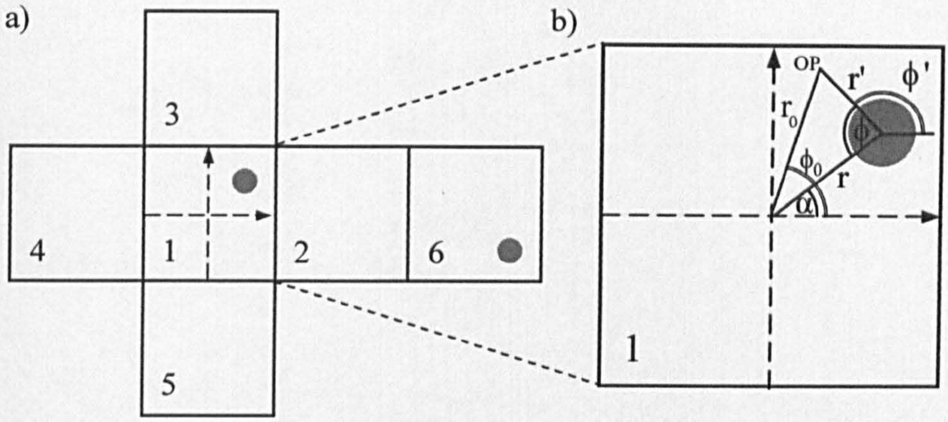

Figure 8.2. Unfolded cubic node with the wires passing through two faces (a), face 1 with the wire description (b)

Similarly to the case of the centred, straight wire in [8.1], four different types of modes have been utilised in the analytical solutions to represent the fields in the vicinity of the wire segment

a) Transverse Magnetic, TM, with $E_{z'} \neq 0$, $H_{z'} = 0$ and no variation in the z' direction.

b) Transverse Electric, TE, with $H_{z'} \neq 0$, $E_{z'} = 0$ and no variation in the z' direction.

c) Transverse Electromagnetic, TEM, with $E_{z'} = 0$, $H_{z'} = 0$ and even symmetry along z'-axis.

d) Transverse Electromagnetic, TEM, with $E_{z'} = 0$, $H_{z'} = 0$ and odd symmetry along z'-axis.

The modes listed above have already been discussed in Chapter 2, however a brief summary is given below for the case of a single conducting wire.

The total electric and magnetic field around the wire is described in wire coordinate system (r',ϕ',z') as presented in Figure 8.1 and 8.2(b), and as derived in Chapter 2 and also studied in Chapter 4 in section 4.1 these are:

for TM fields: $$E_z^{tot} = \sum_{n=-\infty}^{\infty} X_{0n}\left(J_n(k_0r') - \frac{J_n(k_0a)}{H_n^{(2)}(k_0a)}H_n^{(2)}(k_0r')\right)e^{-jn\phi'} \quad (8.1)$$

for TE fields: $$H_z^{tot} = -j\gamma_0 \sum_{n=-\infty}^{\infty} X_{0n}\left(J_n(k_0r') - \frac{J'_n(k_0a)}{H'^{(2)}_n(k_0a)}H_n^{(2)}(k_0r')\right)e^{-jn\phi'} \quad (8.2)$$

where k_0 and a is the wavenumber in free space and the radius of the wire respectively. Assuming

$$f_n(r') = J_n(k_0r') - \frac{J_n(k_0a)}{H_n^{(2)}(k_0a)}H_n^{(2)}(k_0r') \quad (8.3)$$

and

$$g_n(r') = J_n(k_0r') - \frac{J'_n(k_0a)}{H'^{(2)}_n(k_0a)}H_n^{(2)}(k_0r') \quad (8.4)$$

these fields take the form of:

for TM fields: $$E_z^{tot} = \sum_{n=-\infty}^{\infty} X_{0n}\, f_n(r')e^{-jn\phi'} \quad (8.5)$$

for TE fields: $$H_z^{tot} = -j\gamma_0 \sum_{n=-\infty}^{\infty} X_{0n}\, g_n(r')e^{-jn\phi'} \quad (8.6)$$

The remaining field components can be calculated from Maxwell's equations given in Appendix A in Equation (A.14) taking into account the properties of the modes discussed in section 2.4 in Chapter 2:

$$
\begin{array}{ll}
\text{for TM mode:} & \text{for TE mode:} \\
E_r = 0 & H_r = 0 \\
E_\phi = 0 & H_\phi = 0 \\
H_z = 0 & E_z = 0 \\
H_r = -\dfrac{1}{j\omega\mu_0}\dfrac{1}{r}\dfrac{\partial E_z}{\partial \phi} & E_r = \dfrac{1}{j\omega\varepsilon_0}\dfrac{1}{r}\dfrac{\partial H_z}{\partial \phi} \\
H_\phi = \dfrac{1}{j\omega\mu_0}\dfrac{\partial E_z}{\partial r} & E_\phi = -\dfrac{1}{j\omega\varepsilon_0}\dfrac{\partial H_z}{\partial r}
\end{array}
\tag{8.7}
$$

For TEM fields, introduced in section 2.4.3 in Chapter 2 the Maxwell's Equations can be written as follows:

$$
\begin{array}{ll}
j\omega\mu_0 H_r = \dfrac{\partial E_\phi}{\partial z} & j\omega\varepsilon_0 E_r = -\dfrac{\partial H_\phi}{\partial z} \\
j\omega\mu_0 H_\phi = -\dfrac{\partial E_r}{\partial z} & j\omega\varepsilon_0 H_\phi = \dfrac{\partial H_r}{\partial z} \\
\dfrac{\partial (rE_\phi)}{\partial r} = \dfrac{\partial E_r}{\partial \phi} & \dfrac{\partial (rH_\phi)}{\partial r} = \dfrac{\partial H_r}{\partial \phi}
\end{array}
\tag{8.8}
$$

The TEM mode is a solution for transverse static fields and can be determined by introducing a vector potential which is evaluated in the form of cylindrical harmonics as:

$$
A_z(F_z) = (r^n + X_n^s r^{-n}) \substack{\cos \\ \sin}(n\phi) \substack{\cos \\ \sin}(k_0 z) \tag{8.9}
$$

The coefficient X_n^s is explicitly determined by the boundary condition that requires tangential electric field be zero at the surface of the wire, i.e. $E_\phi(r = a, \phi, z) = 0$.

Utilising Equation (2.51) shown in Chapter 2 in section 2.4.3 and Maxwell's equations for the TEM mode defined in Equation (8.8) the field components can be identified. Those solutions are evaluated for the low order modes, i.e. $n=-2,-1,0,1,2$ as listed in Tables 8.1 and 8.2.

From the discussion given in section 2.4 of Chapter 2 it is clear that the TM and TE mode are selected under the condition that there is no variation of the field along the z'-direction. As shown in the same section, the TEM mode provides a link to the three-dimensional case where the z'-directed variation is considered with the transverse wavenumber approaching zero. Such a solution describes the static transverse fields on the surface of the wire.

Both, the even and odd solutions with respect to z'-direction are selected for the TEM configuration. Compared to the modes derived for the two-dimensional wire case presented in Chapter 4 an additional harmonic appears in the form of $\sin 2\phi$. This is because the wire is not placed at the centre of the cell and therefore this solution is not zero at the sampling points as in the centred wire case. Overall, a set of 20 modes is selected that provides a physically realistic, second order accurate description of the fields around the wire offset from the centre of the cell.

MODE	E_z	E_θ	E_r
TM_0	$f_0(r')$	0	0
$TM_{1(c)}$	$f_1(r')\cos\theta'$	0	0
$TM_{1(s)}$	$f_1(r')\sin\theta'$	0	0
$TM_{2(c)}$	$f_2(r')\cos 2\theta'$	0	0
$TM_{2(s)}$	$f_2(r')\sin 2\theta'$	0	0
TE_0	0	$g_0(r')$	0
$TE_{1(c)}$	0	$g_1(r')\cos\theta'$	$\frac{g_1(r')}{r'}\sin\theta'$
$TE_{1(s)}$	0	$g_1(r')\sin\theta'$	$-\frac{g_1(r')}{r'}\cos\theta'$
$TE_{2(c)}$	0	$g_2(r')\cos 2\theta'$	$2\frac{g_2(r')}{r'}\sin 2\theta'$
$TE_{2(s)}$	0	$g_2(r')\sin 2\theta'$	$-2\frac{g_2(r')}{r'}\cos 2\theta'$
$TEM_0^{(e)}$	0	0	$\frac{a}{r'}\cos(k_0z')$
$TEM_{1(c)}^{(e)}$	0	$-\frac{a}{2r'}\left(\frac{a}{r'}-\frac{r'}{a}\right)\sin\theta'\cos(k_0z')$	$\frac{a}{2r'}\left(\frac{a}{r'}+\frac{r'}{a}\right)\cos\theta'\cos(k_0z')$
$TEM_{1(s)}^{(e)}$	0	$\frac{a}{2r'}\left(\frac{a}{r'}-\frac{r'}{a}\right)\cos\theta'\cos(k_0z')$	$\frac{a}{2r'}\left(\frac{a}{r'}+\frac{r'}{a}\right)\sin\theta'\cos(k_0z')$
$TEM_{2(c)}^{(e)}$	0	$-\frac{a}{2r'}\left(\left(\frac{a}{r'}\right)^2-\left(\frac{r'}{a}\right)^2\right)\sin 2\theta'\cos(k_0z')$	$\frac{a}{2r'}\left(\left(\frac{a}{r'}\right)^2+\left(\frac{r'}{a}\right)^2\right)\cos 2\theta'\cos(k_0z')$
$TEM_{2(s)}^{(e)}$	0	$\frac{a}{2r'}\left(\left(\frac{a}{r'}\right)^2-\left(\frac{r'}{a}\right)^2\right)\cos 2\theta'\cos(k_0z')$	$\frac{a}{2r'}\left(\left(\frac{a}{r'}\right)^2+\left(\frac{r'}{a}\right)^2\right)\sin 2\theta'\cos(k_0z')$
$TEM_0^{(o)}$	0	0	$\frac{a}{r'}\sin(k_0z')$
$TEM_{1(c)}^{(o)}$	0	$-\frac{a}{2r'}\left(\frac{a}{r'}-\frac{r'}{a}\right)\sin\theta'\sin(k_0z')$	$\frac{a}{2r'}\left(\frac{a}{r'}+\frac{r'}{a}\right)\cos\theta'\sin(k_0z')$
$TEM_{1(s)}^{(o)}$	0	$\frac{a}{2r'}\left(\frac{a}{r'}-\frac{r'}{a}\right)\cos\theta'\sin(k_0z')$	$\frac{a}{2r'}\left(\frac{a}{r'}+\frac{r'}{a}\right)\sin\theta'\sin(k_0z')$
$TEM_{2(c)}^{(o)}$	0	$-\frac{a}{2r'}\left(\left(\frac{a}{r'}\right)^2-\left(\frac{r'}{a}\right)^2\right)\sin 2\theta'\sin(k_0z')$	$\frac{a}{2r'}\left(\left(\frac{a}{r'}\right)^2+\left(\frac{r'}{a}\right)^2\right)\cos 2\theta'\sin(k_0z')$
$TEM_{2(s)}^{(o)}$	0	$\frac{a}{2r'}\left(\left(\frac{a}{r'}\right)^2-\left(\frac{r'}{a}\right)^2\right)\cos 2\theta'\sin(k_0z')$	$\frac{a}{2r'}\left(\left(\frac{a}{r'}\right)^2+\left(\frac{r'}{a}\right)^2\right)\sin 2\theta'\sin(k_0z')$

Table 8.1. A set TM, TE and TEM modes of electric field. The subscript *s* and *c* denote sine and cosine function for angular dependence. For the TEM modes *(e)* and *(o)* denote even and odd solution with respect to z.

MODE	$j\omega\mu_0 H_z$	$j\omega\mu_0 H_\theta$	$j\omega\mu_0 H_r$
TM_0	0	$f'_0(r')$	0
$TM_{1(c)}$	0	$f'_1(r')\cos\theta'$	$\frac{f_1(r')}{r'}\sin\theta'$
$TM_{1(s)}$	0	$f'_1(r')\sin\theta'$	$-\frac{f_1(r')}{r'}\cos\theta'$
$TM_{2(c)}$	0	$f'_2(r')\cos 2\theta'$	$2\frac{f_2(r')}{r'}\sin 2\theta'$
$TM_{2(s)}$	0	$f'_2(r')\sin 2\theta'$	$-2\frac{f_2(r')}{r'}\cos 2\theta'$
TE_0	$k_0^2 g_0(r')$	0	0
$TE_{1(c)}$	$k_0^2 g_1(r')\cos\theta'$	0	0
$TE_{1(s)}$	$k_0^2 g_1(r')\sin\theta'$	0	0
$TE_{2(c)}$	$k_0^2 g_2(r')\cos 2\theta'$	0	0
$TE_{2(s)}$	$k_0^2 g_2(r')\sin 2\theta'$	0	0
$TEM_0^{(e)}$	0	$-k_0\frac{a}{r'}\sin(k_0 z')$	0
$TEM_{1(c)}^{(e)}$	0	$-k_0\frac{a}{2r'}\left(\frac{a}{r'}+\frac{r'}{a}\right)\cos\theta'\sin(k_0 z')$	$k_0\frac{a}{2r'}\left(\frac{a}{r'}-\frac{r'}{a}\right)\sin\theta'\sin(k_0 z')$
$TEM_{1(s)}^{(e)}$	0	$-k_0\frac{a}{2r'}\left(\frac{a}{r'}+\frac{r'}{a}\right)\sin\theta'\sin(k_0 z')$	$-k_0\frac{a}{2r'}\left(\frac{a}{r'}-\frac{r'}{a}\right)\cos\theta'\sin(k_0 z')$
$TEM_{2(c)}^{(e)}$	0	$-k_0\frac{a}{2r'}\left(\left(\frac{a}{r'}\right)^2+\left(\frac{r'}{a}\right)^2\right)\cos 2\theta'\sin(k_0 z')$	$k_0\frac{a}{2r'}\left(\left(\frac{a}{r'}\right)^2-\left(\frac{r'}{a}\right)^2\right)\sin 2\theta'\sin(k_0 z')$
$TEM_{2(s)}^{(e)}$	0	$-k_0\frac{a}{2r'}\left(\left(\frac{a}{r'}\right)^2+\left(\frac{r'}{a}\right)^2\right)\sin 2\theta'\sin(k_0 z')$	$-k_0\frac{a}{2r'}\left(\left(\frac{a}{r'}\right)^2-\left(\frac{r'}{a}\right)^2\right)\cos 2\theta'\sin(k_0 z')$
$TEM_0^{(o)}$	0	$k_0\frac{a}{r'}\cos(k_0 z')$	0
$TEM_{1(c)}^{(o)}$	0	$k_0\frac{a}{2r'}\left(\frac{a}{r'}+\frac{r'}{a}\right)\cos\theta'\cos(k_0 z')$	$k_0\frac{a}{2r'}\left(\frac{a}{r'}-\frac{r'}{a}\right)\sin\theta'\cos(k_0 z')$
$TEM_{1(s)}^{(o)}$	0	$k_0\frac{a}{2r'}\left(\frac{a}{r'}+\frac{r'}{a}\right)\sin\theta'\cos(k_0 z')$	$-k_0\frac{a}{2r'}\left(\frac{a}{r'}-\frac{r'}{a}\right)\cos\theta'\cos(k_0 z')$
$TEM_{2(c)}^{(o)}$	0	$k_0\frac{a}{2r'}\left(\left(\frac{a}{r'}\right)^2+\left(\frac{r'}{a}\right)^2\right)\cos 2\theta'\cos(k_0 z')$	$k_0\frac{a}{2r'}\left(\left(\frac{a}{r'}\right)^2-\left(\frac{r'}{a}\right)^2\right)\sin 2\theta'\cos(k_0 z')$
$TEM_{2(s)}^{(o)}$	0	$k_0\frac{a}{2r'}\left(\left(\frac{a}{r'}\right)^2+\left(\frac{r'}{a}\right)^2\right)\sin 2\theta'\cos(k_0 z')$	$-k_0\frac{a}{2r'}\left(\left(\frac{a}{r'}\right)^2-\left(\frac{r'}{a}\right)^2\right)\cos 2\theta'\cos(k_0 z')$

Table 8.2. A set TM, TE and TEM modes of magnetic field. The subscript *s* and *c* denote sine and cosine function for angular dependence. For the TEM modes *(e)* and *(o)* denote even and odd solution with respect to z.

It is further underlined that the selected set of modes is not the only one possible. The general algorithm allows the use of a larger or smaller number of modes provided that a sufficient description of the fields around the wire is given. Intuitively, only low order harmonics should be taken into account. However with 20 modes and only 12 field sample points this system is underdetermined and physical reasoning argues that the modal amplitudes determined are such that the total energy stored in the cell is minimised.

Having obtained the solution for the total electric and magnetic field, the algorithm for interfacing these fields with the numerical network will be presented. However, the aim here is to provide more insight into the implementation, rather than repeating the formulae given in Chapter 3.

As presented in Chapter 3, Equation (3.1), the total fields inside the cell are expressed as:

$$\mathbf{E}=\sum_{n}\mathbf{e}_n X_n=\underline{\mathbf{e}}^T\underline{X} \quad \text{and} \quad \mathbf{H}=\sum_{n}\mathbf{h}_n X_n=\underline{\mathbf{h}}^T\underline{X} \tag{8.10}$$

where the vectors **E, H** consist of components:

$$\mathbf{E}=(E_x,E_y,E_z) \qquad \mathbf{H}=(H_x,H_y,H_z) \tag{8.11}$$

To start with, the fields of the 20 modal solutions are evaluated on each surface of the cubic node at a number of quadrature points. It is clear that in order to utilise the formulae defined in Tables 8.1 and 8.2, the cell coordinate system (x,y,z) must be translated into the wire coordinate system (r',ϕ',z'). This is achieved by using Euler's rotation theorem [8.2] and is mathematically described by:

$$\begin{bmatrix} r' \\ \phi' \\ z' \end{bmatrix} \leftrightarrow \begin{bmatrix} x' \\ y' \\ z' \end{bmatrix} = \begin{bmatrix} & \underline{\underline{A}} & \end{bmatrix} \begin{bmatrix} x \\ y \\ z \end{bmatrix} + \begin{bmatrix} T_x \\ T_y \\ T_z \end{bmatrix} \tag{8.12}$$

where $\underline{\underline{A}}$ is a rotation matrix and $\underline{T} = \left[T_x, T_y, T_z\right]$ is a translation vector. Next, the point (x', y', z') is re-expressed in the polar coordinates (r', ϕ', z') [8.3].

Hence, each quadrature point on the surface of the cell is first re-expressed in terms of the wire coordinate system in which the modal fields are easily evaluated. At each face of the cell the tangential field is calculated and represented in a local Cartesian coordinate system centred on the cell in order to enable straightforward connection with neighbouring nodes.

Prior to the numerical evaluation of the integral appearing in the definition of matrix $\underline{\underline{u}}$ in Equation (3.4) of Chapter 3, a set of basis functions is also evaluated at each point belonging to each surface. Due to the fact that the tangential fields are evaluated in Cartesian system, one of the two unit vectors tangential to the face is used to represent each basis function. These are:

$$\begin{aligned}
&\underline{f}_{1x} = (\bar{x}, 0, 0), \quad \underline{f}_{1y} = (0, \bar{y}, 0) \\
&\underline{f}_{2y} = (0, \bar{y}, 0), \quad \underline{f}_{2z} = (0, 0, \bar{z}) \\
&\underline{f}_{3x} = (\bar{x}, 0, 0), \quad \underline{f}_{3z} = (0, 0, \bar{z}) \\
&\underline{f}_{4y} = (0, \bar{y}, 0), \quad \underline{f}_{4z} = (0, 0, \bar{z}) \\
&\underline{f}_{5x} = (\bar{x}, 0, 0), \quad \underline{f}_{5z} = (0, 0, \bar{z}) \\
&\underline{f}_{6x} = (\bar{x}, 0, 0), \quad \underline{f}_{6y} = (0, \bar{y}, 0)
\end{aligned} \tag{8.13}$$

Integration of the 20 modal solutions over the 6 surfaces with 2 basis functions defined at each of them results in matrix $\underline{\underline{u}}$ of size 12×20. This matrix describes the relationship between 12 port voltages and 20 modal solutions as defined in Chapter 3. The matrix $\underline{\underline{u}}$ is then inverted in a generalised sense using for instance the Singular Value Decomposition (SVD) method [8.5], to construct a matrix $\underline{\underline{w}} = \underline{\underline{u}}^{-1}$ from Equation (3.5). The fact that matrix $\underline{\underline{w}}$ is treated as a general inverse of matrix $\underline{\underline{u}}$ allows to utilise an arbitrary number of modes that provides a sufficient description of the field. As Equation (3.10) of chapter 3 indicates, the expression $\iint_S \underline{e}^* \times \underline{h}^T \cdot dS$ needs to be evaluated which is performed numerically [8.4],

$$\iint_S \underline{\mathbf{e}}^* \times \underline{\mathbf{h}}^T \cdot d\mathbf{S} = \lim_{N \to \infty} \sum_{p=1}^{N} \left(\underline{\mathbf{e}}^* \times \underline{\mathbf{h}}^T \right) \cdot \hat{\mathbf{n}}_p \Delta S_p \tag{8.14}$$

where the normal vectors to the cell faces are defined in a rectangular coordinate system as:

$$\begin{array}{lll} S_1 : \hat{\mathbf{n}}_1 = (0,0,-1), & S_2 : \hat{\mathbf{n}}_2 = (1,0,0), & S_3 : \hat{\mathbf{n}}_3 = (1,0,0), \\ S_4 : \hat{\mathbf{n}}_4 = (-1,0,0), & S_5 : \hat{\mathbf{n}}_5 = (-1,0,0), & S_6 : \hat{\mathbf{n}}_6 = (0,0,1) \end{array} \tag{8.15}$$

The integration defined in Equation (8.14) will result in the matrix $\left[\iint_S \underline{e}^* \times \underline{h}^T \cdot dS \right]$ of size 20×20.

Finally, the eigenvalue problem, Equation (3.11) in Chapter 3

$$\underline{I} = \underline{\underline{w}}^H \left[\iint_S \underline{e}^* \times \underline{h}^T \cdot dS \right] \underline{\underline{w}} \underline{V} = \underline{\underline{\gamma}} \underline{V} \tag{8.16}$$

is solved relating the port voltages to the port currents by an admittance relationship. At this point implementation of the admittance relationship is straightforward and the algorithm to link the solutions obtained with the adjacent nodes of TLM algorithm was studied in Chapter 3 and therefore will not be repeated here. Instead, in the next section the numerical validation will be illustrated.

8.1.1. Numerical Validations

In this section, a number of simple test problems will be investigated to demonstrate the accuracy provided by the new wire nodes. These new nodes are used in conjunction with the conventional SCN node for the remaining problem space. It is emphasised that as only relatively small number of the nodes in the overall simulation are non-standard, the improvements in accuracy incur negligible computational penalty. The results presented in this sub-section were prepared in cooperation with Dr Y. Liu of the GGIEMR at The University of Nottingham.

8.1.1.1. Scattering from Vertical and Straight Dipole

The first example involves a plane wave incident normally upon a straight and slightly tilted wire dipole, which is shown in Figure 8.3. The incident pulse has a Gaussian profile in time of RMS width 6.6 time steps. Initially both the dipole and the vector of incident electric field are orientated in the z-direction and subsequently the dipole is tilted slightly. In the case of a vertical dipole, the ends of the dipole are positioned at the points $(x = 20\text{m}, y = 20\text{m}, z = 0.5\text{m})$ and $(x = 20\text{m}, y = 20\text{m}, z = 1.5\text{m})$, whereas for tilted wire these are $(x = 20\text{m}, y = 20\text{m}, z = 0.5\text{m})$ and $(x = 20.4\text{m}, y = 20.2\text{m}, z = 1.5\text{m})$. A TLM node size, 2Δ, of 0.1m is used and the wire radius is 0.01m. The computational window applied is 60m×60m×3m and the simulation run-time is 512 time-steps. The simulation region forms a TEM waveguide supporting propagation of a plane wave and is truncated by short-circuit, open-circuit and matched boundary conditions on the top and bottom, sides and ends respectively. It is noted that no special treatment is required at the ends of the wire, a conventional TLM node is simply connected to the last wire node.

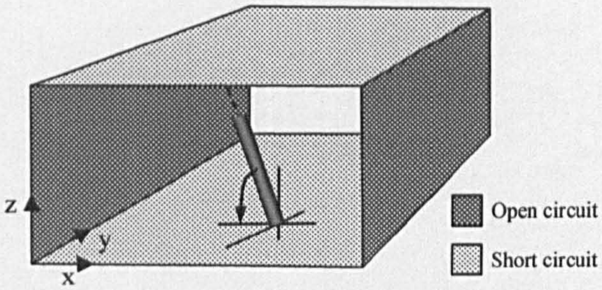

Figure 8.3. A tilted thin wire dipole excited by a vertically polarised plane

Figure 8.4 shows the frequency dependence of the vertically polarised electric field observed 0.2m (2 nodes) in front of the wire for the vertical and tilted dipoles. The frequency is normalised to the maximum frequency of the TLM simulation, i.e. $f_{max} = (2\Delta t)^{-1}$ and $\Delta t = \Delta / c$, c being speed of light in vacuo. For the vertical dipole the TLM results are seen to agree remarkably well with those from a Method of Moments (MoM) solution [8.6], both in terms of the resonant frequency and the shape of the curve.

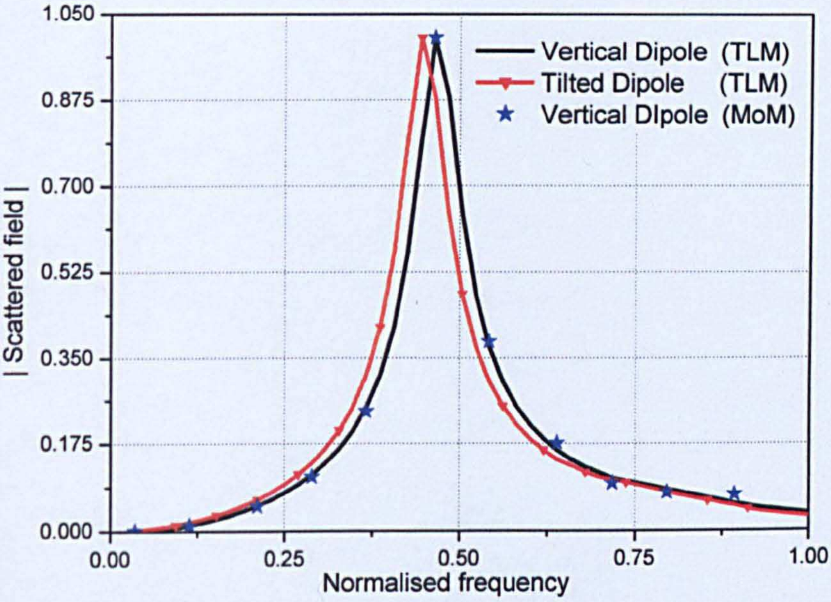

Figure 8.4. Amplitude of the scattered field observed in front of the wire for vertical and tilted dipoles lying in the x-z plane versus the normalised frequency

$$f_{norm} = 2f\Delta t$$

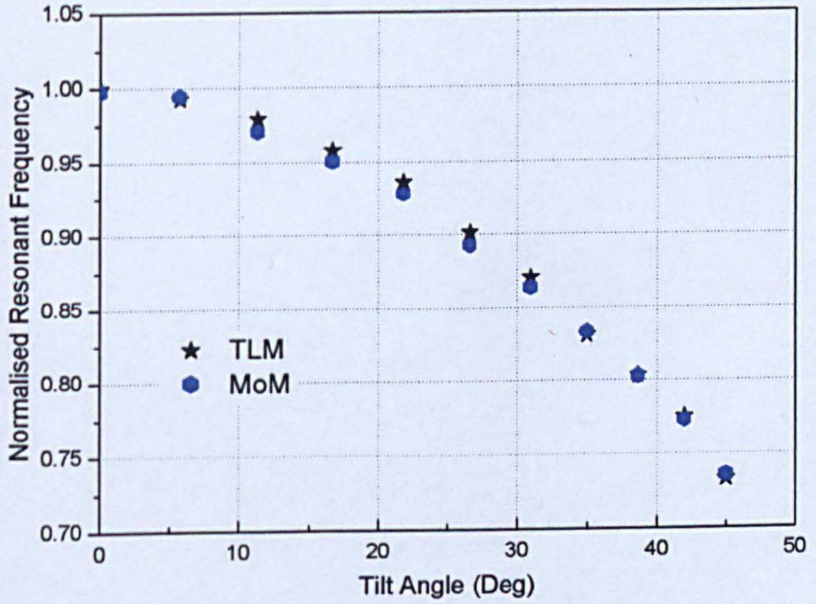

Figure 8.5. Variation of the resonant frequency with the angle of tilt in the x-z plane

The slight increase in the length of the tilted dipole compared to the vertical dipole causes a drop in the resonant frequency and Figure 8.5 shows that this shift compares very well with that predicted from the moments method. This is significant as staircased approximations to tilted wires can often resonate at a frequency corresponding to the total length of the staircase, not the true length of the wire.

8.1.1.2. Scattering from a Circular Wire Loop

In the second example the circular wire loop shown in Figure 8.6 is considered. The loop is placed in the plane y = 15m of a computational region 60m×30m×30m discretised by a TLM mesh of size 0.1m. The same boundary conditions at the edges are assumed as described in the previous test. The loop has a diameter of 1.2m and a wire radius of 0.01m. A plane wave of a Gaussian profile of RMS 6.6 time-steps propagating in the y-direction whose electric field is polarised in the z-direction is incident on the loop and the back-scattered field observed 0.2m in front of the loop.

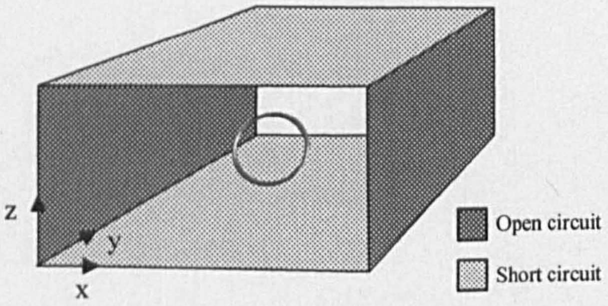

Figure 8.6. A circular wire loop excited by vertically polarised plane wave

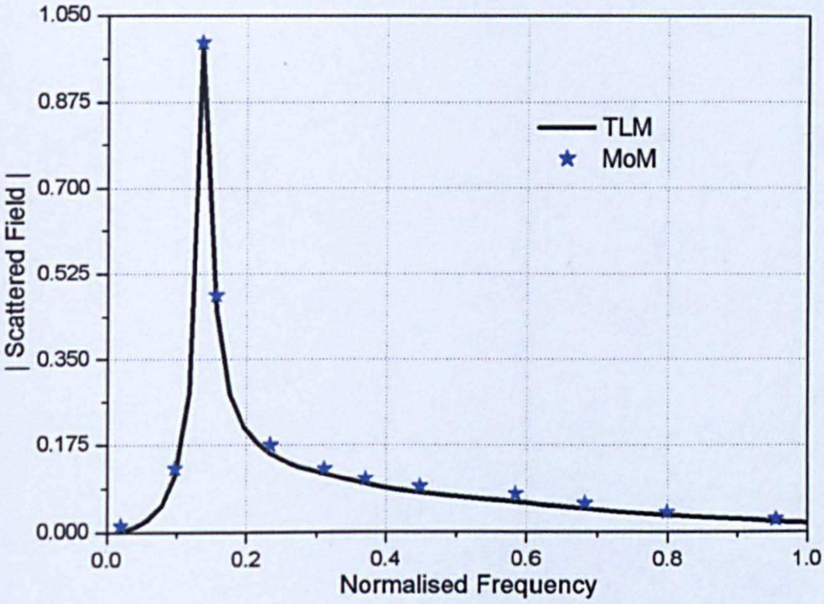

Figure 8.7. The amplitude of the scattered field for a circular wire loop versus normalised frequency

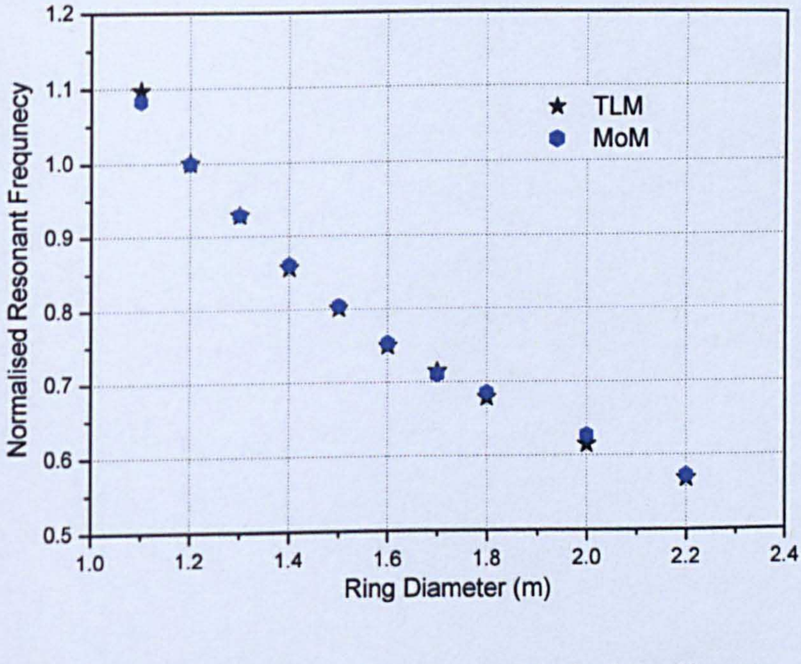

Figure 8.8. Variation of the resonant frequency with the loop diameter; the wire radius $a = 1\,\mathrm{cm}$

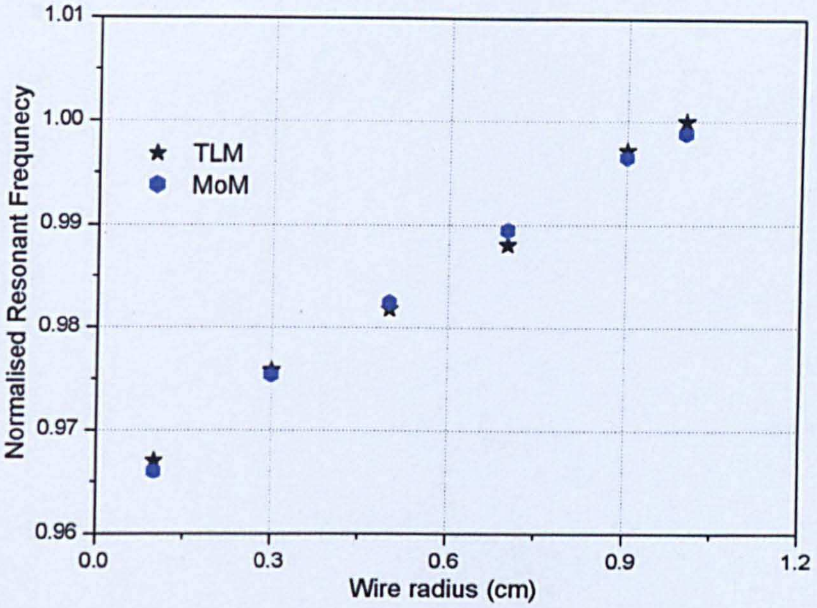

Figure 8.9. Variation of the resonant frequency with the wire radius for a loop diameter $d = 1.2\,\text{m}$

Figure 8.7 shows the frequency dependent scattering from the loop and it is clear that excellent results are provided by the new node. Figure 8.8 and Figure 8.9 show the dependence of the loop's resonant frequency on the radius of the wire and the diameter of the loop, relative to the reference case in Figure 8.7. In both cases, agreement with the moments solution is remarkably close.

As seen, the analytical description of local fields combined with the general procedure of embedding small objects in 3D TLM model gives very good approximation in both cases presented above. In the next section, the procedure to obtain the solutions to local fields by numerical means will be demonstrated.

8.2. Numerical Approximation to Near Field Solutions

A canonical example of a small metal cube embedded into a coarse numerical grid of 3D TLM will be presented in this section. The novelty here lies in the pre-processing stage, in which the numerical approximation is utilised to obtain solutions to the local fields.

Consider a small cubic metal box embedded in a single 3D TLM cell as illustrated in Figure 8.10(a). It is desirable to seek a suitable set of numerical modal solutions to Maxwell's equations which satisfy the boundary conditions on the surface of the scatterer, in this case the conducting box. These solutions come from TLM simulations with the problem space directly meshed by a fine grid, as shown for two-dimensional cross-section position in xz-plane in Figure 8.10(b). The mesh employed must be much smaller or at least, as in our case, of the same size as the conducting cube under consideration. A number of such fine mesh TLM simulations is carried out, each with different field illuminations. Consequently, the problem is excited by a series of plane waves in either direction along each coordinate axis for each of the two orthogonal polarisations in turn. For instance a plane wave is used that propagates in the +z-direction with electric field polarised in x-direction, or a plane wave travelling in +z-direction with electric field vector polarised in the y-direction, etc. This gives a combination of 12 modal solutions in total and for illustration purpose the analytical representation of these plane waves is given in Table 8.3.

	Polarisation	Direction of Propagation	Electric Field Component	Magnetic Field Component
1	x	–z	$E = E_x e^{+jk_0z}$	$H = -\gamma_0 H_y e^{+jk_0z}$
2	x	+z	$E = E_x e^{-jk_0z}$	$H = \gamma_0 H_y e^{-jk_0z}$
3	x	–y	$E = E_x e^{+jk_0y}$	$H = \gamma_0 H_z e^{+jk_0y}$
4	x	+y	$E = E_x e^{-jk_0y}$	$H = -\gamma_0 H_z e^{-jk_0y}$
5	y	–x	$E = E_y e^{+jk_0x}$	$H = -\gamma_0 H_z e^{+jk_0x}$
6	y	+x	$E = E_y e^{-jk_0x}$	$H = \gamma_0 H_z e^{-jk_0x}$
7	y	–z	$E = E_y e^{+jk_0z}$	$H = \gamma_0 H_x e^{+jk_0z}$
8	y	+z	$E = E_y e^{-jk_0z}$	$H = -\gamma_0 H_x e^{-jk_0z}$
9	z	–y	$E = E_z e^{+jk_0y}$	$H = -\gamma_0 H_x e^{+jk_0y}$
10	z	+y	$E = E_z e^{-jk_0y}$	$H = \gamma_0 H_x e^{-jk_0y}$
11	z	–x	$E = E_z e^{+jk_0x}$	$H = \gamma_0 H_y e^{+jk_0x}$
12	z	+x	$E = E_z e^{-jk_0x}$	$H = -\gamma_0 H_z e^{-jk_0x}$

Table 8.3. Analytical representation of the 12 combinations of plane wave used to illuminate the numerical simulation with fine meshes

For each of the possible excitation the fields, e_n and h_n, are recorded at the surfaces 1 to 6 shown in Figure 8.10(a), at frequency much lower than 10% of the maximum frequency available in TLM run. Those six surfaces at which the fields are captured in turn form a coarse node in which the small cube will be modelled in the main coarse mesh TLM simulation, see Figure 8.10(b) for details. The output fields at a chosen frequency are next integrated over the surfaces in a similar fashion to that presented above for the case when the local fields are obtained analytically and the admittance relationship is constructed. The only difference in the approach lies in the number of modal solutions, here 12 instead of 20 modes. At the final stage using the admittance relationship and the scheme presented in Chapter 3, the solution from the fine mesh simulations are embedded into the coarse TLM model. Both results, obtained with an explicitly (fine) meshed node of the cube and the coarse node with small cube embedded within are presented in Figure 8.11.

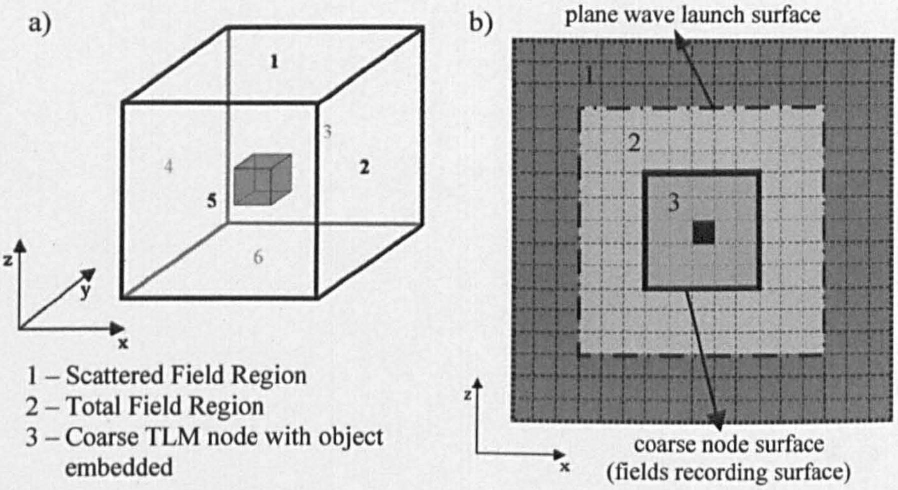

Figure 8.10. The experimental set-up: TLM coarse node with object embedded (a) and computational window for local field pre-processing in xz plane (b)

Figure 8.11 shows the scattered electric field observed at three different locations in front of the x-face of the conducting cube. In this particular case the incident field has a Gaussian profile in time of RMS width 3.6 time steps. The simulations are performed with mesh sizes of 0.3m for the coarse and 0.1m for the fine grid with the calculation area consisting of 33 cells in each direction for the coarse and 99 cells in each direction for the fine mesh respectively. The observation points are placed 13, 10 and 7 nodes for points labelled in Figure 8.11 as 1, 2 and 3 respectively for a coarse mesh and 40, 31 and 22 cells for a fine mesh. This corresponds to a distance from the non-standard node of 4.05m for point 1, 3.15m for point 2 and 2.25m for point 3 in both cases.

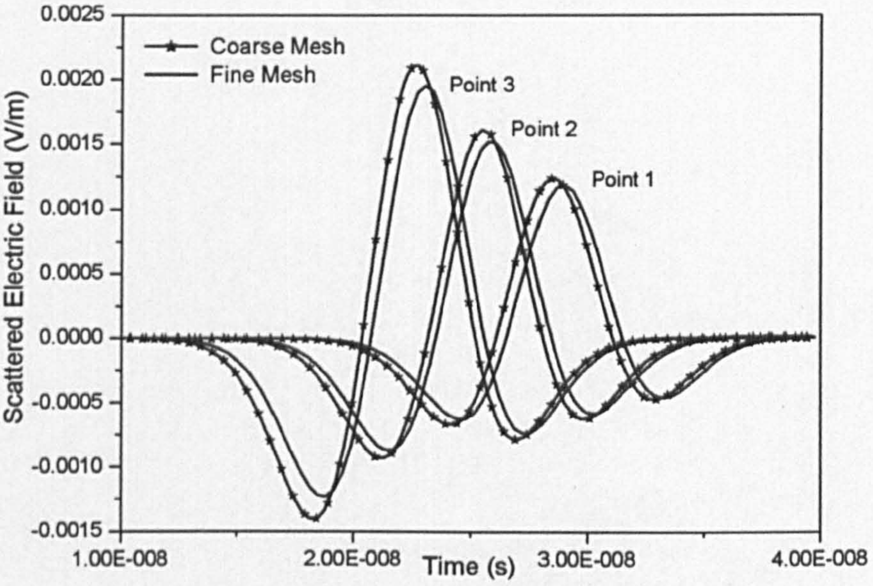

Figure 8.11. Scattered electric field output at three different points in front of the x-face of conducting cube for coarse and fine mesh

Good overall agreement is observed between the two solutions. The far field solution exhibits less error in comparison with the near field results. To explain this it is noted that there will be a contribution to the error from the different dispersion characteristics of the two grid sizes. The small errors in a near field are however compensated by a saving in computational resources. For that particular configuration a run time for a large mesh was decreased by a factor of 20 compared to the fine grid simulation.

8.3. One Point of Integration for 3D Symmetrical Problems

To complete the description of 3D models of objects embedded in a single cell, symmetrical problems will be now considered. In these scenarios, certain simplifications can be adopted and only one point of integration utilised for local field solutions, similarly to the single wire case placed centrally in a 2D cell. This is specifically shown for the example of wave scattering from spherical objects such as conducting and dielectric spheres. In these cases a decomposition of EM field into spherical modes is exploited to developed the spherical node's scattering parameters.

8.3.1. Spherical Modes

Prior to embedding small spherical objects the evaluation of empty non-standard node in spherical coordinate system will be given for comparison. Spherical modes are studied and the impedance relationship between the port voltages and the port currents is evaluated. An expansion of electromagnetic field can be written with reference to the spherical coordinate system shown in section 1 in Appendix E in the following form [8.7]:

$$\begin{aligned} E &= -\sum_{n=1}^{\infty}\sum_{\substack{m=0\\ e,o}}^{n}\left(a_{mn}\overline{m}_{mn} + b_{mn}\overline{n}_{mn}\right)e^{j\omega t} \\ H &= \frac{k}{j\omega\mu}\sum_{n=1}^{\infty}\sum_{\substack{m=0\\ e,o}}^{n}\left(a_{mn}\overline{n}_{mn} + b_{mn}\overline{m}_{mn}\right)e^{j\omega t} \end{aligned} \tag{8.17}$$

where:

$$\begin{aligned} \overline{m}_{mn} = {} & \hat{\mathbf{a}}_{\theta} \times \pm\frac{m}{\sin\theta} z_n(kr) P_n^m(\cos\theta) \substack{\sin\\ \cos} m\phi \\ & \hat{\mathbf{a}}_{\phi} \times -z_n(kr)\frac{\partial}{\partial\theta} P_n^m(\cos\theta) \substack{\cos\\ \sin} m\phi \end{aligned} \tag{8.18}$$

and

$$
\begin{aligned}
\bar{n}_{mn} = \; & \hat{\mathbf{a}}_r \times \frac{n(n+1)}{kr} z_n(kr)\, P_n^m(\cos\theta) \genfrac{}{}{0pt}{}{\cos}{\sin} m\phi \\
& \hat{\mathbf{a}}_\theta \times + \frac{1}{kR}\frac{\partial}{\partial r}\left[r z_n(kr)\right] \frac{\partial}{\partial\theta} P_n^m(\cos\theta) \genfrac{}{}{0pt}{}{\cos}{\sin} m\phi \\
& \hat{\mathbf{a}}_\phi \times \pm \frac{m}{kr\sin\theta}\frac{\partial}{\partial r}\left[r z_n(kr)\right] P_n^m(\cos\theta) \genfrac{}{}{0pt}{}{\sin}{\cos} m\phi
\end{aligned}
\tag{8.19}
$$

and k denotes the wavenumber, that in the present case equals $k = k_0$, $z_n(kr)$ represents a spherical Bessel functions of order *n*, P_n^m denotes Legendre polynomials with respect to the angle dependency with θ and trigonometric functions denote odd and even solutions with respect to the angle dependency with ϕ. The field weighting coefficients *a* and *b* are: $a_{mn} \neq 0$, $b_{mn} = 0$ for TE modes and $b_{mn} \neq 0$, $a_{mn} = 0$ for TM modes.

In order to derive the admittance relationship necessary to link the non-standard node with the real-time numerical network, it is desirable to identify the tangential electric and magnetic field at each face of the cubical node enclosing the volume of empty space. The tangential field components are formulated for both field illuminations, for TE modes:

$$
\begin{aligned}
E_\theta &= -\sum_{n=1}^{\infty}\sum_{\substack{m=0\\ e,o}}^{n}\left(\pm a_{mn}\frac{m}{\sin\theta}z_n(kr)\,P_n^m(\cos\theta)\begin{matrix}\sin\\ \cos\end{matrix}m\phi\right)e^{j\omega t}\\
H_\theta &= \frac{k}{j\omega\mu}\sum_{n=1}^{\infty}\sum_{\substack{m=0\\ e,o}}^{n}\left(a_{mn}\frac{1}{kr}\frac{\partial}{\partial r}\left[rz_n(kr)\right]\frac{\partial}{\partial\theta}P_n^m(\cos\theta)\begin{matrix}\cos\\ \sin\end{matrix}m\phi\right)e^{j\omega t}\\
E_\phi &= \sum_{n=1}^{\infty}\sum_{\substack{m=0\\ e,o}}^{n}\left(a_{mn}z_n(kr)\frac{\partial}{\partial\theta}P_n^m(\cos\theta)\begin{matrix}\cos\\ \sin\end{matrix}m\phi\right)e^{j\omega t}\\
H_\phi &= \frac{k}{j\omega\mu}\sum_{n=1}^{\infty}\sum_{\substack{m=0\\ e,o}}^{n}\left(\pm a_{mn}\frac{m}{kr\sin\theta}\frac{\partial}{\partial r}\left[rz_n(kR)\right]P_n^m(\cos\theta)\begin{matrix}\sin\\ \cos\end{matrix}m\phi\right)e^{j\omega t}
\end{aligned}
\qquad (8.20)
$$

and for TM modes:

$$
\begin{aligned}
E_\theta &= -\sum_{n=1}^{\infty}\sum_{\substack{m=0\\ e,o}}^{n}\left(b_{mn}\frac{1}{kr}\frac{\partial}{\partial r}\left[rz_n(kr)\right]\frac{\partial}{\partial\theta}P_n^m(\cos\theta)\begin{matrix}\cos\\ \sin\end{matrix}m\phi\right)e^{j\omega t}\\
H_\theta &= \frac{k}{j\omega\mu}\sum_{n=1}^{\infty}\sum_{\substack{m=0\\ e,o}}^{n}\left(\pm b_{mn}\frac{m}{\sin\theta}z_n(kr)\,P_n^m(\cos\theta)\begin{matrix}\sin\\ \cos\end{matrix}m\phi\right)e^{j\omega t}\\
E_\phi &= -\sum_{n=1}^{\infty}\sum_{\substack{m=0\\ e,o}}^{n}\left(\pm b_{mn}\frac{m}{kr\sin\theta}\frac{\partial}{\partial r}\left[rz_n(kr)\right]P_n^m(\cos\theta)\begin{matrix}\sin\\ \cos\end{matrix}m\phi\right)e^{j\omega t}\\
H_\phi &= \frac{k}{j\omega\mu}\sum_{n=1}^{\infty}\sum_{\substack{m=0\\ e,o}}^{n}\left(-b_{mn}z_n(kr)\frac{\partial}{\partial\theta}P_n^m(\cos\theta)\begin{matrix}\cos\\ \sin\end{matrix}m\phi\right)e^{j\omega t}
\end{aligned}
\qquad (8.21)
$$

It is clear that in order to employ the scheme presented in Chapter 3 the infinite summation needs be truncated to the lowest order harmonics and can possess only discrete values at the points corresponding to the ports of standard SCN node [8.8]. Due to the character of the problem it is intuitive to seek 12 modal solutions that are symmetrical and also orthogonal, as required by the approach presented in Chapter 3. Taking into account the values and properties of the Legendre polynomials and values of trigonometric functions at the ports, listed in section 2 of Appendix E, twelve low order spherical modes are selected which are illustrated in Figure 8.12.

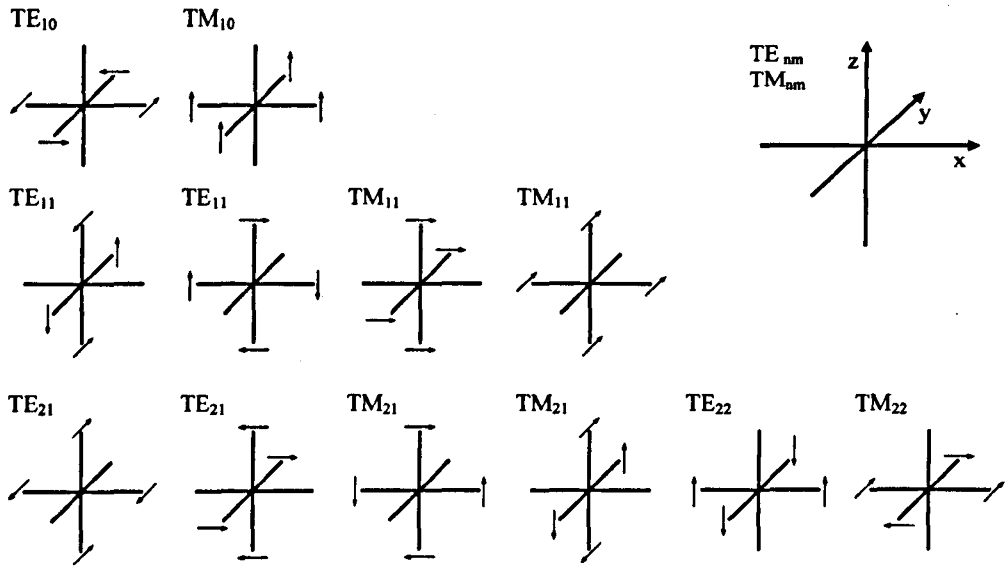

Figure 8.12. A selection of spherical symmetrical modes of the lowest order; the arrows represent the E-field direction

Using this selection the 12-port transformer, presented in Chapter 3, necessary to decompose the incoming voltages into modal amplitudes is constructed as:

$$\underline{\underline{T}}^{T} = 0.5\begin{bmatrix} 0 & 0 & 0 & 0 & 0 & 0 & 0 & 0 & 1 & 1 & 1 & 1 \\ 0 & 0 & 1 & -1 & -1 & 1 & 0 & 0 & 0 & 0 & 0 & 0 \\ 0 & 0 & 0 & 0 & 0 & 0 & 1 & -1 & -1 & 1 & 0 & 0 \\ -1 & 1 & 0 & 0 & 0 & 0 & 0 & 0 & 0 & 0 & 1 & -1 \\ 1 & 1 & 1 & 1 & 0 & 0 & 0 & 0 & 0 & 0 & 0 & 0 \\ 0 & 0 & 0 & 0 & 1 & 1 & 1 & 1 & 0 & 0 & 0 & 0 \\ 0 & 0 & 0 & 0 & -1 & -1 & 1 & 1 & 0 & 0 & 0 & 0 \\ -1 & -1 & 1 & 1 & 0 & 0 & 0 & 0 & 0 & 0 & 0 & 0 \\ -1 & 1 & 0 & 0 & 0 & 0 & 0 & 0 & 0 & 0 & -1 & 1 \\ 0 & 0 & 0 & 0 & 0 & 0 & -1 & 1 & -1 & 1 & 0 & 0 \\ 0 & 0 & 0 & 0 & 0 & 0 & 0 & 0 & -1 & -1 & 1 & 1 \\ 0 & 0 & -1 & 1 & -1 & 1 & 0 & 0 & 0 & 0 & 0 & 0 \end{bmatrix} \qquad (8.22)$$

The values of admittances at the ports are evaluated as $Y = \frac{E_\theta}{H_\phi} = \frac{E_\phi}{H_\theta}$ which by decomposition of the series to particular terms results in:

$$\text{TE: } Y_n^{TE} = \frac{1}{j\omega\mu r}\frac{\frac{\partial}{\partial r}(rj_n(kr))}{j_n(kr)} \tag{8.23}$$

$$\text{TM: } Y_n^{TM} = -\frac{k^2 r}{j\omega\mu}\frac{j_n(kr)}{\frac{\partial}{\partial r}[rj_n(kr)]} \tag{8.24}$$

For an empty space node $z_n(kr) = j_n(k_0 r)$ and the admittances are evaluated at $r = \Delta$, where Δ is the radius of the TLM node.

Using a small value approximation to the Bessel function, detailed in section 3 of Appendix E, it can be demonstrated that those admittances are, for the low order modes, equal to:

$$Y_1^{TE} = \frac{1}{j\omega\mu}\frac{2}{\Delta};\quad Y_2^{TE} = \frac{1}{j\omega\mu}\frac{3}{\Delta};\quad Y_1^{TM} = j\omega\varepsilon\frac{\Delta}{2};\quad Y_2^{TM} = j\omega\varepsilon\frac{\Delta}{3} \tag{8.25}$$

Implementing these values as a scattering relationship on each individual modal line, given in Equation (3.21) in Chapter 3, the time delay from Equation (3.22) can be estimated as:

$$\begin{aligned}
&Y_1^{TE} : -e^{-j\omega\mu y_0\Delta} && \Delta t_1 = \mu y_0 \Delta \\
&Y_2^{TE} : -e^{-\frac{2}{3}j\omega\mu y_0\Delta} && \Delta t_2 = \mu y_0 \Delta \frac{2}{3} \\
&Y_1^{TM} : e^{-j\frac{\omega\varepsilon\Delta}{y_0}} && \Delta t_1 = \frac{\varepsilon\Delta}{y_0} \\
&Y_1^{TM} : e^{-j\frac{2}{3}\frac{\omega\varepsilon\Delta}{y_0}} && \Delta t_2 = \frac{2}{3}\frac{\varepsilon\Delta}{y_0}
\end{aligned} \tag{8.26}$$

where y_0 is the intrinsic admittance of empty space $(\varepsilon = \varepsilon_0, \mu = \mu_0)$.

It should be clear that the lines representing TE mode must use a short-circuit termination and the open-circuited stub is applied for lines corresponding to TM modes. The time-delay for the whole non-standard node can be simplified and made exactly the same as SCN case by approximating the impedance of mode n = 2 to that of line n = 1, analogously to the 2D symmetrical formulation for conducting wires in Chapter 4. It was found that such approximation reduces significantly the computations in the non-standard node without compromising the accuracy. The admittances obtained and the 12-port transformer developed for the non-standard node based on spherical coordinate system can be then embedded into a time-domain TLM model by employing the approach presented in Chapter 3.

8.3.2. Theory of Scattering from a Conductive Sphere

Having established the framework for symmetrical problems described in spherical coordinate system, a simple test is carried out to verify the accuracy of the technique. As a first example, a small conductive sphere is embedded in a coarse mesh of TLM model as shown in Figure 8.13.

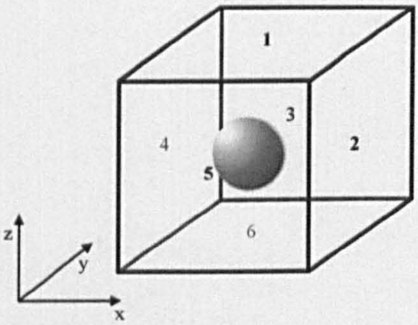

Figure 8.13. Small sphere embedded in a 3D TLM cell

The modal impedances are now modified by taking into account fields scattered from the object and these are

$$Y_l^{TE} = \frac{H_\theta}{E_\phi} = -\frac{H_\phi}{E_\theta} = \frac{1}{j\omega\mu r}\frac{\frac{\partial}{\partial r}\left[r\left(j_l(k_0r)+A_l^{TE}y_l(k_0r)\right)\right]}{j_l(k_0r)+A_l^{TE}y_l(k_0r)} \tag{8.27}$$

$$Y_l^{TM} = -\frac{H_\theta}{E_\phi} = \frac{H_\phi}{E_\theta} = -\frac{k^2r}{j\omega\mu}\frac{j_l(k_0r)+A_l^{TM}y_l(k_0r)}{\frac{\partial}{\partial r}\left[r\left(j_l(k_0r)+A_l^{TM}y_l(k_0r)\right)\right]} \tag{8.28}$$

for TE and TM modes respectively.

On the surface of the conducting sphere the total tangential electric field is forced to zero, thus the scattered field coefficients are calculated as follows:

$$A_l^{TE} = -\left.\frac{j_l(k_0r)}{y_l(k_0r)}\right|_{r=a} \tag{8.29}$$

$$A_l^{TM} = -\left.\frac{\frac{\partial}{\partial r}\left[rj_l(k_0r)\right]}{\frac{\partial}{\partial r}\left[ry_l(k_0r)\right]}\right|_{r=a} = -\frac{j_l(k_0a)+k_0a\,j'_l(k_0a)}{y_l(k_0a)+k_0a\,y'_l(k_0a)} \tag{8.30}$$

where ' denotes the derivative, i.e. $\frac{\partial}{\partial(k_0a)}$ and *a* is the radius of the sphere.

Utilising a small value approximation to Bessel functions it can be shown that at $r=\Delta$ the admittances are: (the complete derivation is given in Appendix E section 4)

$$Y_l^{TE} = \frac{1}{j\omega\mu\Delta}\frac{2\Delta^3+a^3}{\Delta^3-a^3} \tag{8.31}$$

$$Y_l^{TM} = j\omega\varepsilon\frac{\Delta}{2}\frac{\Delta^3+2a^3}{\Delta^3-a^3} \tag{8.32}$$

It is noted that as the sphere radius $a \to 0$, the values of the modal admittances for a conducting sphere will approach the admittances for empty-space node presented in Equation (8.25). It should be clear that the distribution of the modes and the modal transformer remain unchanged compared to the spherical empty-space node. The theory derived above will be now validated for an example of small conducting sphere inserted into a coarse 3D TLM node. The numerical results will be verified against the analytical solution that is given below.

8.3.2.1. Analytical Description

The analytical description for the problem of plane wave scattering from the conducting sphere will be briefly discussed in this sub-section. For detailed information and full derivation the reader is referred to [8.3]. As demonstrated in the reference provided the total field potentials can be formulated as:

$$\begin{aligned} A_r^t &= A_r^i + A_r^s = \frac{\cos\phi}{\omega}\sum_{n=1}^{\infty}\left[a_n\hat{J}_n(kr) + b_n\hat{H}_n^{(2)}(kr)\right]P_n^1(\cos\theta) \\ F_r^t &= F_r^i + F_r^s = \frac{\sin\phi}{\omega\eta}\sum_{n=1}^{\infty}\left[a_n\hat{J}_n(kr) + c_n\hat{H}_n^{(2)}(kr)\right]P_n^1(\cos\theta) \end{aligned} \tag{8.33}$$

where incident field coefficients are $a_n = j^{-n}\dfrac{2n+1}{n(n+1)}$ and $\hat{J}_n(kr), \hat{H}_n^{(2)}(kr)$ are modified Bessel functions defined in Appendix E in section 5. The remaining field components are related by the following sets of equations [8.3]:

$$\begin{aligned} E_r^t &= \frac{1}{j\omega\mu\varepsilon}\left(\frac{\partial^2}{\partial r^2} + k^2\right)A_r^t \\ E_\theta^t &= \frac{1}{j\omega\mu\varepsilon}\frac{1}{r}\frac{\partial^2 A_r^t}{\partial r\partial\theta} - \frac{1}{\varepsilon}\frac{1}{r\sin\theta}\frac{\partial F_r^t}{\partial\phi} \\ E_\phi^t &= \frac{1}{j\omega\mu\varepsilon}\frac{1}{r\sin\theta}\frac{\partial^2 A_r^t}{\partial r\partial\phi} + \frac{1}{\varepsilon}\frac{1}{r}\frac{\partial F_r^t}{\partial\theta} \end{aligned} \tag{8.34}$$

$$\begin{aligned} H_r^t &= \frac{1}{j\omega\mu\varepsilon}\left(\frac{\partial^2}{\partial r^2} + k^2\right)F_r^t \\ H_\theta^t &= \frac{1}{\mu}\frac{1}{r\sin\theta}\frac{\partial A_r^t}{\partial\phi} + \frac{1}{j\omega\mu\varepsilon}\frac{1}{r}\frac{\partial^2 F_r^t}{\partial r\partial\theta} \\ H_\phi^t &= -\frac{1}{\mu}\frac{1}{r}\frac{\partial A_r^t}{\partial\theta} + \frac{1}{j\omega\mu\varepsilon}\frac{1}{r\sin\theta}\frac{\partial^2 F_r^t}{\partial r\partial\phi} \end{aligned} \tag{8.35}$$

To determine the unknown coefficients b_n, c_n the boundary conditions at the surface of the conducting sphere are enforced:

$$\begin{aligned} &E^t_\theta(r = a, 0 \le \theta \le \pi, 0 \le \phi \le 2\pi) = 0 \\ &E^t_\phi(r = a, 0 \le \theta \le \pi, 0 \le \phi \le 2\pi) = 0 \end{aligned} \qquad (8.36)$$

which requires that:

$$b_n = -a_n \frac{\hat{J}'_n(ka)}{\hat{H}'^{(2)}_n(ka)}, \text{ and } c_n = -a_n \frac{\hat{J}_n(ka)}{\hat{H}^{(2)}_n(ka)} \qquad (8.37)$$

Finally the total electric field components, incident and scattered, used for validation purpose in the following sections can be determined as:

incident electric field:

$$\begin{aligned} E^i_r &= -j\cos\phi \sum_{n=1}^{\infty} a_n \left[\hat{J}''_n(kr) + \hat{J}_n(kr)\right] P^1_n(\cos\theta) \\ E^i_\theta &= \frac{\cos\phi}{kr} \sum_{n=1}^{\infty} a_n \left[\left(j\hat{J}'_n(kr)\sin\theta P'^1_n(\cos\theta) - \hat{J}_n(kr)\right) \frac{P^1_n(\cos\theta)}{\sin\theta}\right] \\ E^i_\theta &= \frac{\sin\phi}{kr} \sum_{n=1}^{\infty} a_n \left[j\hat{J}'_n(kr) \frac{P^1_n(\cos\theta)}{\sin\theta} - \hat{J}_n(kr)\sin\theta P'^1_n(\cos\theta)\right] \end{aligned} \qquad (8.38)$$

scattered electric field:

$$\begin{aligned} E^s_r &= -j\cos\phi \sum_{n=1}^{\infty} b_n \left[\hat{H}''^{(2)}_n(kr) + \hat{H}^{(2)}_n(kr)\right] P^1_n(\cos\theta) \\ E^s_\theta &= \frac{\cos\phi}{kr} \sum_{n=1}^{\infty} \left[jb_n \hat{H}'^{(2)}_n(kr)\sin\theta P'^1_n(\cos\theta) - c_n \hat{H}^{(2)}_n(kr) \frac{P^1_n(\cos\theta)}{\sin\theta}\right] \\ E^s_\theta &= \frac{\sin\phi}{kr} \sum_{n=1}^{\infty} \left[jb_n \hat{H}'^{(2)}_n(kr) \frac{P^1_n(\cos\theta)}{\sin\theta} - c_n \hat{H}^{(2)}_n(kr)\sin\theta P'^1_n(\cos\theta)\right] \end{aligned} \qquad (8.39)$$

It is noted that a large number of terms used in the analytical expansion is taken to guarantee the convergence of the series.

8.3.2.2. Numerical Validations

A simple verification test will now be provided for a small conducting sphere embedded within a single TLM cell. The problem is excited by a plane wave with Gaussian profile of 2.5 time-steps RMS width and travelling in the +z direction with +y polarisation. The sphere radius selected for this simulation is $a = 0.5\Delta$ where the radius of the TLM node is $\Delta = 0.05\text{m}$. A perfect TEM waveguide was created to support the plane wave propagation in a computational region of $61 \times 61 \times 61$ numerical nodes, i.e. a short-circuit boundary is assumed at the surfaces 5,3; an open-circuit at 2,4; and a matched boundary is at the surfaces 1,6 from Figure 8.13.

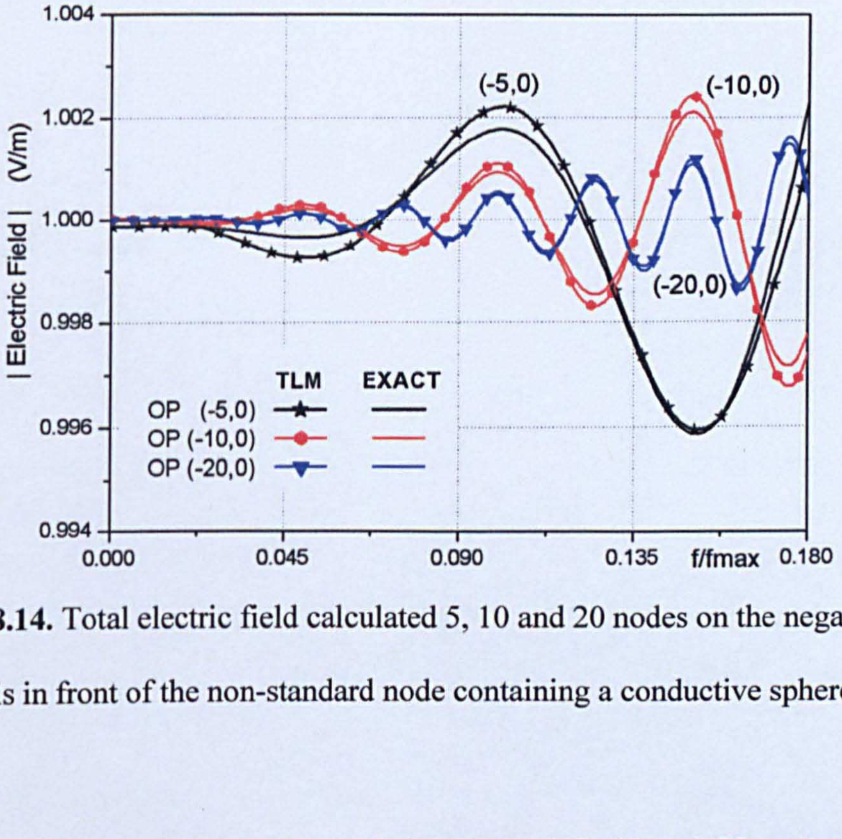

Figure 8.14. Total electric field calculated 5, 10 and 20 nodes on the negative z-axis in front of the non-standard node containing a conductive sphere

Figure 8.14 shows the total electric field observed 5, 10 and 20 nodes on the negative z-axis in front of the non-standard node containing the conducting sphere. The frequency for the experiment is normalised against the maximum frequency of the TLM run, i.e. $f_{max} = (2\Delta t)^{-1}$. Very good agreement is achieved between the analytical solution, labelled as exact, and numerical results for each of the points presented, even beyond the 10% of maximum frequency, the limit below which TLM is regarded as accurate [8.9]. Similarly to the single wire case studied in Chapter 4, the curves representing far field solutions exhibit excellent agreement. This is due to improved numerical resolution at the wavefront curvature that enables the solution to converge rapidly. A slight error is observed for a near field, however, with such weak scattering those errors are negligible when EMC applications are considered.

8.3.3. Scattering from Dielectric Sphere

An extension to the problem of wave scattering from a dielectric sphere is straightforward. It requires updating the values of admittances taking into account a new boundary between air and a dielectric material. At such interfaces it is necessary to maintain continuity of all the tangential electric and magnetic field components. However, the interface considered here is generalised to the boundary between two dielectric materials, one for a medium of $\varepsilon_1 = \varepsilon_0\varepsilon_{r1}$ and the second $\varepsilon_2 = \varepsilon_0\varepsilon_{r2}$ of the object inserted in the medium. This concept covers a much greater range of engineering problems. By simply assuming the permittivity $\varepsilon_{r1} = 1$ and $\varepsilon_{r2} = \varepsilon_r$, where ε_r is the dielectric constant of the sphere, the result for the problem of wave scattered from a dielectric sphere placed in the empty space medium will be generated.

Thus, at the boundary $r = a$, where *a* is the radius of the sphere, the condition of $E_{1\theta}(E_{1\phi}) = E_{2\theta}(E_{2\phi})$ and $H_{1\theta}(H_{1\phi}) = H_{2\theta}(H_{2\phi})$ needs to be satisfied. Expanding those expressions using the field expansions given in Equation (8.20) and (8.21) for TE and TM modes leads to:

for TE modes:

$$A_n^{i1} j_n(k_1 a) + A_n^{s1} y_n(k_1 a) = A_n^{i2} j_n(k_2 a) \tag{8.40}$$

$$\frac{1}{k_1\eta_1}\frac{\partial}{\partial r}\left[r\left(A_n^{i1} j_n(k_1 r) + A_n^{s1} y_n(k_1 r)\right)\right]_{r=a} = \frac{1}{k_2\eta_2} A_n^{i2} \frac{\partial}{\partial r}\left[r j_n(k_2 r)\right]_{r=a} \tag{8.41}$$

and for TM modes:

$$\frac{1}{k_1}\frac{\partial}{\partial r}\left[r(A_n^{i1} j_n(k_1 r) + A_n^{s1} y_n(k_1 r))\right]_{r=a} = \frac{1}{k_2} A_n^{i2} \frac{\partial}{\partial r}\left[r j_n(k_2 r)\right]_{r=a} \tag{8.42}$$

$$\frac{1}{\eta_1}\left(A_n^{i1} j_n(k_1 a) + A_n^{s1} y_n(k_1 a)\right) = \frac{1}{\eta_2} A_n^{i2} j_n(k_2 a) \tag{8.43}$$

where k_1, k_2 are the wavenumbers in the dielectric materials and η_1, η_2 are their intrinsic impedances.

It should be noted that the Neumann function $y_n(k_2 r)$ has been excluded from the solutions, since the fields are required to be finite and continuous and the function $y_n(k_2 r)$ is infinite at $r = 0$. Calculating derivatives in Equation (8.41) and (8.42) yields:

$$\begin{aligned} &\frac{k_2\eta_2}{k_1\eta_1}\left(A_n^{i1}\left(j_n(k_1 a) + k_1 a j'_n(k_1 a)\right) + A_n^{s1}\left(y_n(k_1 a) + k_1 a y'_n(k_1 a)\right)\right) \\ &= A_n^{i2}\left(j_n(k_2 a) + k_2 a j'_n(k_2 a)\right) \end{aligned} \tag{8.44}$$

$$\begin{aligned} &A_n^{i1}\left(j_n(k_1 a) + k_1 a j'_n(k_1 a)\right) + A_n^{s1}\left(y_n(k_1 a) + k_1 a y'_n(k_1 a)\right) \\ &= \frac{k_1}{k_2} A_n^{i2}\left(j_n(k_2 a) + k_2 a j'_n(k_2 a)\right) \end{aligned} \tag{8.45}$$

Dividing simultaneously Equation (8.40) by (8.44) and Equation (8.45) by (8.43) and rearranging the normalised scattering coefficients are obtained in the form, for TE modes:

$$\frac{A_n^{s1}}{A_n^{i1}}=\frac{k_2\eta_2 j_n(k_2a)\left(j_n(k_1a)+k_1a\,j'_n(k_1a)\right)-k_1\eta_1 j_n(k_1a)\left(j_n(k_2a)+k_2a\,j'_n(k_2a)\right)}{k_1\eta_1 y_n(k_1a)\left(j_n(k_2a)+k_2a\,j'_n(k_2a)\right)-k_2\eta_2 j_n(k_2a)\left(y_n(k_1a)+k_1a y'_n(k_1a)\right)} \qquad (8.46)$$

for TM modes:

$$\frac{A_n^{s1}}{A_n^{i1}}=\frac{k_1\eta_2 j_n(k_1a)\left(j_n(k_2a)+k_2a\,j'_n(k_2a)\right)-k_2\eta_1 j_n(k_2a)\left(j_n(k_1a)+k_1a\,j'_n(k_1a)\right)}{k_2\eta_1 j_n(k_2a)\left(y_n(k_1a)+k_1a y'_n(k_1a)\right)-k_1\eta_2 y_n(k_1a)\left(j_n(k_2a)+k_2a\,j'_n(k_2a)\right)} \qquad (8.47)$$

Thus, the scattered field coefficients necessary to evaluate the admittances at the faces of the node, as demonstrated in Equations (8.27) and (8.28) for TE and TM modes respectively are:

$$A_1^{TE}=\frac{A_1^{s1}}{A_1^{i1}}=\frac{k_2\eta_2 j_1(k_2a)\left(j_1(k_1a)+k_1a\,j'_1(k_1a)\right)-k_1\eta_1 j_1(k_1a)\left(j_1(k_2a)+k_2a\,j'_1(k_2a)\right)}{k_1\eta_1 y_1(k_1a)\left(j_1(k_2a)+k_2a\,j'_1(k_2a)\right)-k_2\eta_2 j_1(k_2a)\left(y_1(k_1a)+k_1a y'_1(k_1a)\right)}$$

$$A_1^{TM}=\frac{A_1^{s1}}{A_1^{i1}}=\frac{k_1\eta_2 j_1(k_1a)\left(j_1(k_2a)+k_2a\,j'_1(k_2a)\right)-k_2\eta_1 j_1(k_2a)\left(j_1(k_1a)+k_1a\,j'_1(k_1a)\right)}{k_2\eta_1 j_1(k_2a)\left(y_1(k_1a)+k_1a y'_1(k_1a)\right)-k_1\eta_2 y_1(k_1a)\left(j_1(k_2a)+k_2a\,j'_1(k_2a)\right)}$$

Utilising a small value approximation to Bessel functions detailed in Appendix E section 3 the above can be written as:

$$A_1^{TE}=-\frac{2}{3}k_1^3a^3\left[\frac{k_2\eta_2-k_1\eta_1}{2k_1\eta_1+k_2\eta_2}\right] \qquad (8.48)$$

$$A_1^{TM}=\frac{2}{3}k_1^3a^3\left[\frac{k_1\eta_2-k_2\eta_1}{k_2\eta_1+2k_1\eta_2}\right] \qquad (8.49)$$

Substituting Equation (8.48) and (8.49) into Equation (8.27) and (8.28) respectively and approximating the Bessel functions, the final form of the admittances can be derived. For more details see Appendix E section 6:

$$Y_1^{TE}=\frac{2}{j\omega\mu_1\Delta} \qquad (8.50)$$

$$Y_1^{TM} = j\omega\varepsilon_1 \frac{\Delta}{2} \frac{\varepsilon_{r2}(\Delta^3 + 2a^3) + 2\varepsilon_{r1}(\Delta^3 - a^3)}{\varepsilon_{r2}(\Delta^3 - a^3) + \varepsilon_{r1}(2\Delta^3 + a^3)} \tag{8.51}$$

For the case of waves propagating in air and scattering from a dielectric sphere of permittivity ε_r the admittances are:

$$Y_1^{TE} = \frac{2}{j\omega\mu_0\Delta} \quad \text{and} \quad Y_1^{TM} = j\omega\varepsilon_0 \frac{\Delta}{2} \frac{\varepsilon_r(\Delta^3 + 2a^3) + 2(\Delta^3 - a^3)}{\varepsilon_r(\Delta^3 - a^3) + (2\Delta^3 + a^3)}$$

Having derived the admittances looking into the node centre for both TE and TM modes, the numerical results will be validated against an analytical solution.

8.3.3.1. Numerical Validations

A verification test will be carried out to demonstrate the accuracy of the above description when modelling scattering from a dielectric sphere using coarse meshes. The simulations parameters are chosen as in the previous example when conducting sphere were considered. The sphere consists of material of permittivity $\varepsilon_r = 10$.

Figure 8.15 shows the total field output 5, 10 and 20 nodes in from of the non-standard node with the dielectric sphere and the observation points are positioned on the negative z-axis. It is seen that much weaker scattering is observed when compared to the conducting sphere case. Again the results in the near-field are slightly more in error compared to the far-field results. However, very good overall agreement is achieved between the analytical and numerical solutions.

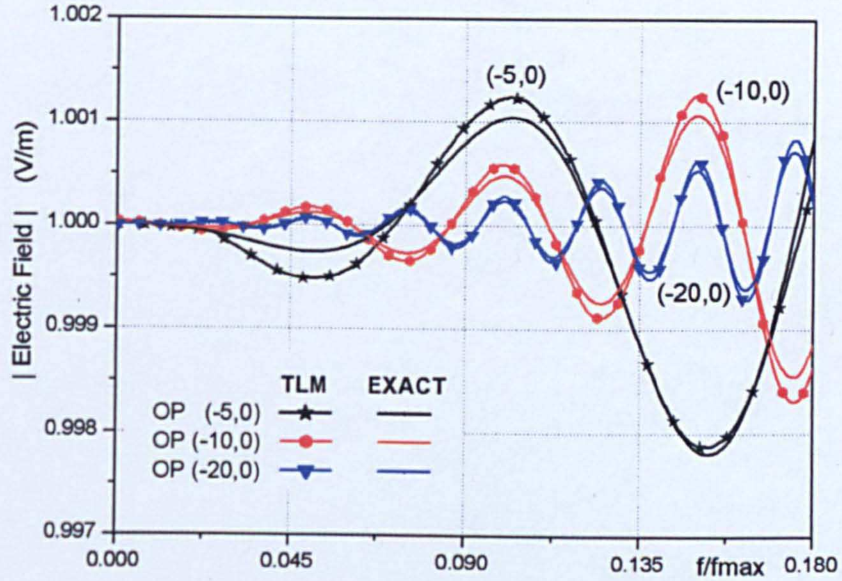

Figure 8.15. Total electric field calculated 5, 10 and 20 nodes on the negative z-axis in front of the node containing a dielectric sphere of $\varepsilon_r = 10$

8.4. Closing Remarks

In this chapter the approach presented in Chapter 3 that allows TLM nodes to be designed in the presence of small-scale scatterers wholly or partially contained within the volume of space the node represents, has been verified by 3D practical tests. Identification of the parameters of the non-standard nodes require local field solutions in the presence of the scatterers and, as was shown, those may be obtained by either exact field analysis or by purely numerical means. Both concepts were investigated. Analytical description of the tilted dipole and the wire loop and numerical approximation to a small conducting cube was used to demonstrate the power of the approach. In both cases excellent agreement with reference results were obtained at a fraction of the computational effort required to directly mesh the specific problems. Finally, a study of spherical geometries was given to present a quick and efficient implementation of our approach to embedding objects analysed in spherical coordinate system.

8.5. References

[8.1] Choong, Y. K., Sewell , P., and Christopoulos , C., *"Accurate modeling of arbitrary placed thin wire in a coarse mesh"*, in Proc. IEE, 4th Int. Conf. Computational Electromagnetics, CEM'02, Bournemouth, U.K., Apr. 8–11, pp. 158-159, 2002

[8.2] http://mathworld.wolfram.com/EulerAngles.html

[8.3] Balanis, C.A., "Advanced Engineering Electromagnetics", John Wiley & Sons, NY, 1989

[8.4] Riley, K.F, Hobson M.P., Bence, S.J., *"Mathematical Methods for Physics and Engineering"*, second edition, Cambridge University Press, UK, 2002

[8.5] Press, W.H., Teukolsky, A.A., Vettering, W.T. and Flannery, B.P. *"Numerical recipes in C: The art of Scientific Computing"*, 2nd Edition, Cambridge University Press, 1992

[8.6] Rockway, J.W., Logan, J. C., Expert MININEC Series, EM Scientific, Inc.

[8.7] Rudge, A.W., Milne, K., Olver, A.D., Knight, P., *"The handbook of Antenna Design"*, Volume 1, Peter Peregrinus Ltd., 1982

[8.8] Johns, P.B., *"A symmetrical condensed node for TLM method"*, IEEE Trans. on Microwave Theory and Tech. Vol.35, No. 4, 370-377, 1987

[8.9] Christopoulos, C., *"The Transmission-Line Modeling Method: TLM"*, Piscataway, NJ: IEEE Press, 1995

Chapter 9

Conclusions

The aim of the work presented in this thesis was to develop techniques that would enable efficient and accurate description of fine features present in multi-scale systems, such as EMC environments within large-scale numerical simulations. The novel approach proposed here provides a stable and robust algorithm that embeds groups of arbitrarily-shaped small objects clustered in close proximity within a single cell of TLM method, or a combination of cells if necessary. Hence, it allows large and highly-integrated platforms such as aircraft and ships to be accurately modelled without utilising explicit fine meshing which is prohibitive in terms of computational requirements. This chapter will review the work presented in this thesis and draw conclusions and suggestions for improvements where appropriate.

Electromagnetic field simulations of multi-scale environments have been proven to be a very challenging task. The difficulty in modelling such systems is due to the large volume of space over which small and large elements interfere and interact with one another, all of them often being equally important from an electromagnetic point of view. Traditional numerical approaches resulting in direct sampling of the problem space with the grid resolution required by the smallest component lead to prohibitive computational demands.

The review of possible practical problems encountered in structures comprising a variety of physical scales was given with the main focus being placed on EMC applications. In the realm of EMC, the prediction of fields scattered from thin wires is of great importance. Such features are fundamental components of a wide range of antennas and are commonly used in cables and bundles that link and provide communication between elements and systems. In order to familiarise the reader with the impact that radiated or scattered fields from thin wires have on surrounding systems, the necessary background electromagnetic theory was provided. A detailed description of the field behaviour in the presence of such cylindrical scatterers was also given.

Several different attempts were proposed in the past to model thin wires. These were discussed and the pros and cons of their application to EMC problems were highlighted. One of the particular techniques based on a sub-cell approach utilises the so called macro-node [9.1-9.3]. In this concept the problem space is discretised with a coarse mesh and the response of a large computational cell is engineered to mimic the behaviour of the fine feature enclosed within it. This results in a significant reduction in computational memory requirements and simulation run-times, as the number of those non-standard nodes containing wires is relatively small compared to the total number of spatial cells. The macro-node approach is stable and robust. It utilises known analytical solutions for the fields around the wire to account for the presence of such a feature and is not based on any empirical factors. However, before this work it was limited to embedding only one wire that is placed at the centre of numerical cell which restricts its applicability to modeling fine features clustered together. Such scenarios are often encountered when modelling for EMC and would again necessitate the use of relatively small grids.

Consequently, a novel extension to this approach was presented that removes the limitations of its predecessor. In the proposed method no restriction is placed upon the geometry of the object or its position and orientation within the cell. In addition, the fine feature may be wholly enclosed within a single cell or pass across several cells. A significant improvement was made so that the algorithm accounts also for multiple objects/wires inserted into one TLM cell coupled by their near fields with each other and the surrounding space. Furthermore, the local field solutions around the features that form a key component of the algorithm, do not have to be calculated analytically. They can alternatively be obtained from numerical simulations or simply measurements thus ensuring the versatility of the approach and its applicability to many engineering problems for which an analytical solution is intractable.

Initially, the accuracy of the approach was verified for a two-dimensional problem of wave scattering from a single conducting wire placed centrally in the cell. A comparison was made with analytical solutions, the multi-feature node yielding very good agreement for the field intensity in both the near and far-field regions.

Furthermore, the approach was applied to modelling a cluster of conducting wires in a single TLM cell. Again, very good agreement was found with the exact solution. As was shown this good accuracy even goes beyond the 10% of the maximum simulation frequency, a limit that guarantees almost dispersionless operation of schemes such as TLM [9.4]. The wire model presented here can be widely utilised in many examples, for instance to model linear array antennas with the flexibility of employing different mesh periodicity compared to the periodicity of antenna's elements.

Of great importance in EMC simulations is the modelling of wire bundles and cables comprising conducting wires, dielectric rods and wires coated with dielectric insulation. Examples of such features embedded in TLM cells were also investigated and again very good agreement with the known behaviour of the scattered field was found. As discussed, the approach allows use of a cell that contains cylindrical structures of different material characteristics. This is implemented by simply applying the appropriate boundary conditions at the surface of the cylinders in the pre-processing stage. Similarly, losses can be incorporated in the system as was demonstrated when a single lossy wire was studied.

Models of conducting thin strips or narrow slots in conducting planes embedded in a single 2D cell were also examined. Here, the fields in the vicinity of the feature were decomposed into elliptical harmonics which were in turn used to construct the admittance relationship between the magnetic and electric field necessary to connect the multi-feature node with the rest of the numerical grid. The node with such features performed exceedingly well when validated against analytical solutions.

It was also shown that not only EMC predictions can benefit from the advantages the proposed technique offers. As presented, it was successfully employed in photonics where the macroscopic behaviour of microstructure photonic band-gap materials were easily estimated without the need to grade the mesh so that it characterised in detail every single feature of the photonic lattice. This is especially practically important when a high degree of integration of devices on a single substrate is involved.

It is observed that the 2D models reviewed above were developed for EMC applications, hence only second order accuracy was considered. However, for certain areas such accuracy may not be sufficient. In this case the methodology needs to be adjusted to include a higher order scheme. One possible concept for achieving higher accuracy is to replace the traditional communication between the nodes that is conventionally conducted through one point, with two points on each edge of the 2D node. Hence, the new 2D node would consist of eight ports in total. Such a configuration would allow incorporating higher order harmonics, up to eight, and the near fields around the wires would be approximated by eight points instead of four. This would increase the accuracy of the approach, however at the cost of computational resources, as the number of variables stored per cell, with or without objects inside, would double. Nevertheless such a trade-off may be profitable when better resolution is required and only a part of a large system is analysed so that the volume of space that needs to be discretised is reasonably small.

Another area where the approach could be employed is a modelling of materials with complex frequency-dependent characteristics. As far as the geometry is concerned, special attention is placed upon cylindrical nanowires [9.5] and the phenomenon of surface plasmons [9.6] that are excited in response to applied electromagnetic field whenever such nanoparticles are placed in closed proximity. Preliminary calculations revealed that the admittances obtained from the general eigenvalue problem representing relationship between the tangential electric and magnetic field at the edges of the node possess complex frequency-dependent characteristics. They are no longer simply proportional or inversely proportional to frequency due to the material, silver for example [9.7]. Therefore the equivalent circuit model is no longer valid and cannot be used to implement the admittance relationship into the time-domain method. Instead digital filters [9.8] can be utilised to enable the frequency-dependent characteristics of the admittances to be embedded in TLM. In order to conduct such a process the admittance characteristics have to be represented in a form of a Padé approximation [9.8]. Hence, the vector fitting technique [9.9] or Prony's method [9.10] can be used to identify the necessary poles and zeros and construct formulae that can be applied in time domain schemes by the means of $Z-$transform [9.8].

The true potential and power of the approach was presented in 3D simulations. Thin dipoles obliquely orientated to the nodal axes as well as circular thin wire loops evaluated by linear piecewise approximation were considered. In both cases excellent agreement with reference results were obtained. Not only are these examples suitable test problems for the general approach, but also important practical configurations in their own right. In both those tests the fields around the features were still calculated using analytical expansion in terms of cylindrical harmonics. However, as pointed out at the pre-processing stage, a numerical approximation can be used to estimate such fields. This was shown for fields scattered from a small cube. Very good agreement was achieved between fine mesh simulations and coarse mesh results. For that particular configuration the run time for a large mesh was reduced by a factor of 20 compared to the fine grid simulation. Finally, the possibility of embedding objects characterised by a spherical coordinates was demonstrated. The results of numerical simulations of field scattered from small conducting or dielectric spheres matched very well with the analytical solutions, again well beyond 10% of the maximum frequency.

The 3D approach could be easily extended to account for multiple wires passing through a cell as was done for the two-dimensional case. However, it should be recognized that a number of independent wire-to-wire voltages will exist and that these ought to be explicitly present in the algorithm to allow interfacing with lumped circuit components. This is achieved by simply choosing sufficient additional ports on the appropriate cell surfaces each of which represents an independent local, quasi-static field that gives rise to inter-wire voltages. This would necessitate an increase in the number of basis functions $\underline{\mathbf{f}}_p$ on each surface of the cell to remain consistent with the boundary conditions placed on the tangential electric field around the wires and ensure continuity of the fields at the interface.

In summary, this thesis presented a stable and robust approach to model sub-wavelength features in a coarse grid simulation without placing any restriction on the geometry or position of the object(s) inside the cell. The technique was successfully implemented to many practical problems and the results verified showing second order accuracy.

References

[9.1] Choong, Y. K., Sewell, P., and Christopoulos, C., *"Accurate wire representation in numerical models for high-frequency simulation"*, Electron. Lett., Vol. 37, No. 5, pp. 280–282, 2001

[9.2] Choong, Y. K., Sewell, P., and Christopoulos, C., *"New thin-wire formulation for time-domain differential-equation models"*, in Proc. 4th Int. Workshop Computational Electromagnetics, U.K.: Univ. Nottingham, Sept. 17–19, pp. 187–194, 2001

[9.3] Choong, Y. K., Sewell, P., and Christopoulos, C., "Accurate modeling of arbitrary placed thin wire in a coarse mesh", in Proc. IEE, 4th Int. Conf. Computational Electromagnetics, CEM'02, Bournemouth, U.K., Apr. 8–11, pp. 158-159, 2002

[9.4] Christopoulos, C., *"The Transmission-Line Modeling Method: TLM"*. Piscataway, NJ: IEEE Press, 1995

[9.5] Kottoman, J.P., Martin, O.J.F., *"Plasmon resonances of silver nanowires with a nonregular cross section"*, Physical Review B, Vol. 64, pp. 235-402, 2001

[9.6] Ebbesen, T.W., Lezec, H.J., Ghaemi, H.F., Thio, T. and Wolff, P.A., *"Extraordinary optical transmission through sub-wavelength hole arrays"*, Nature, Vol. 391, pp. 667-669, 1998

[9.7] Johnson, P.B. and Christy R.W., "Optical Constant of the Noble Metals", Physical Review B, Vol. 6, No. 12, pp. 4371-4379, 1972

[9.8] Paul, J., Podlozny, D., Thomas, D.W.P., Christopoulos, C., *"Time-Domain Simulation of Thin Metal Boundaries and Thins Panels Using Digital Filters in TLM"*, Turkish Journal of Electrical Engineering and Computer Sciences, Vo. 10, No. 2, pp. 185-198, 2002

[9.9] Gustavsen, B., Semlyen, A., *"Rational Approximation of Frequency Domain Responses by Vector Fitting"*, IEEE Trans. on Power Delivery, Vol. 14, No. 3, pp.1052-1061, 1999

[9.10] Parks, T.W., and C.S. Burrus, *"Digital Filter Design"*, John Wiley & Sons, 1987

Appendix A

1. Vector Formulae

$$\nabla \times \nabla \times \mathbf{A} = \nabla(\nabla \cdot \mathbf{A}) - \nabla^2 \mathbf{A} \tag{A.1}$$

$$\nabla \cdot (\psi \mathbf{A}) = \mathbf{A} \cdot \nabla \psi + \psi \nabla \cdot \mathbf{A} \tag{A.2}$$

2. Vector Differential Operations in Rectangular Coordinates

Assuming a rectangular coordinate system (x,y,z) and defining a scalar function $\Phi = \Phi(x,y,z)$ and a vector $\mathbf{A} = \hat{\mathbf{x}}A_x + \hat{\mathbf{y}}A_y + \hat{\mathbf{z}}A_z$ the following can be written.:

$$\nabla \Phi = \hat{\mathbf{x}}\frac{\partial \Phi}{\partial x} + \hat{\mathbf{y}}\frac{\partial \Phi}{\partial y} + \hat{\mathbf{z}}\frac{\partial \Phi}{\partial z} \tag{A.3}$$

$$\nabla \cdot \mathbf{A} = \frac{\partial A_x}{\partial x} + \frac{\partial A_y}{\partial y} + \frac{\partial A_z}{\partial z} \tag{A.4}$$

$$\nabla \times \mathbf{A} = \hat{\mathbf{x}}\left[\frac{\partial A_z}{\partial y} - \frac{\partial A_y}{\partial z}\right] + \hat{\mathbf{y}}\left[\frac{\partial A_x}{\partial z} - \frac{\partial A_z}{\partial x}\right] + \hat{\mathbf{z}}\left[\frac{\partial A_y}{\partial x} - \frac{\partial A_x}{\partial y}\right] \tag{A.5}$$

$$\nabla^2 \Phi = \frac{\partial^2 \Phi}{\partial x^2} + \frac{\partial^2 \Phi}{\partial y^2} + \frac{\partial^2 \Phi}{\partial z^2} \tag{A.6}$$

$$\nabla^2 \mathbf{A} = \hat{\mathbf{x}}\nabla^2 A_x + \hat{\mathbf{y}}\nabla^2 A_y + \hat{\mathbf{z}}\nabla^2 A_z \tag{A.7}$$

3. Vector Differential Operations in Cylindrical Coordinates

Assuming a cylindrical coordinate system (r,ϕ,z) and defining a scalar function $\Phi=\Phi(r,\phi,z)$ and a vector $\mathbf{A}=\hat{r}A_r+\hat{\phi}A_\phi+\hat{z}A_z$ the following can be written.:

$$\nabla\Phi=\hat{r}\frac{\partial\Phi}{\partial r}+\hat{\phi}\frac{\partial\Phi}{\partial\phi}+\hat{z}\frac{\partial\Phi}{\partial z} \tag{A.8}$$

$$\nabla\cdot\mathbf{A}=\frac{1}{r}\frac{\partial(rA_r)}{\partial r}+\frac{1}{r}\frac{\partial A_\phi}{\partial\phi}+\frac{\partial A_z}{\partial z} \tag{A.9}$$

$$\nabla\times\mathbf{A}=\hat{r}\left[\frac{1}{r}\frac{\partial A_z}{\partial\phi}-\frac{\partial A_\phi}{\partial z}\right]+\hat{\phi}\left[\frac{\partial A_r}{\partial z}-\frac{\partial A_z}{\partial r}\right]+\hat{z}\left[\frac{1}{r}\frac{\partial(rA_\phi)}{\partial r}-\frac{1}{r}\frac{\partial A_r}{\partial\phi}\right] \tag{A.10}$$

$$\nabla^2\Phi=\frac{1}{r}\frac{\partial}{\partial r}\left(r\frac{\partial\Phi}{\partial r}\right)+\frac{1}{r}\frac{\partial^2\Phi}{\partial\phi^2}+\frac{\partial^2\Phi}{\partial z^2} \tag{A.11}$$

$$\nabla^2\mathbf{A}=\hat{r}\left(\nabla^2A_r-\frac{2}{r^2}\frac{\partial A_\phi}{\partial\phi}-\frac{A_r}{r^2}\right)+\hat{\phi}\left(\nabla^2A_\phi+\frac{2}{r^2}\frac{\partial A_r}{\partial\phi}-\frac{A_\phi}{r^2}\right)+\hat{z}\left(\nabla^2A_z\right) \tag{A.12}$$

4. Maxwell's Equations in Rectangular Coordinates

In a homogenous, source-free and isotropic medium described via rectangular coordinate system Maxwell's equations are:

$$\nabla\times\mathbf{E}=-\mu\frac{\partial\mathbf{H}}{\partial t}\qquad\qquad\nabla\times\mathbf{H}=\varepsilon\frac{\partial\mathbf{E}}{\partial t}$$

$$\begin{aligned}
\frac{\partial E_z}{\partial y}-\frac{\partial E_y}{\partial z}&=-\mu\frac{\partial H_x}{\partial t} &\qquad \frac{\partial H_z}{\partial y}-\frac{\partial H_y}{\partial z}&=\varepsilon\frac{\partial E_r}{\partial t}\\
\frac{\partial E_x}{\partial z}-\frac{\partial E_z}{\partial x}&=-\mu\frac{\partial H_y}{\partial t} &\qquad \frac{\partial H_x}{\partial z}-\frac{\partial H_z}{\partial x}&=\varepsilon\frac{\partial E_\theta}{\partial t}\\
\frac{\partial E_y}{\partial x}-\frac{\partial E_x}{\partial y}&=-\mu\frac{\partial H_z}{\partial t} &\qquad \frac{\partial H_y}{\partial x}-\frac{\partial H_x}{\partial y}&=\varepsilon\frac{\partial E_z}{\partial t}
\end{aligned} \tag{A.13}$$

5. Maxwell's Equations in Cylindrical Coordinates

In a homogenous, source-free and isotropic medium described via cylindrical coordinate system Maxwell's equations are:

$$\nabla \times \mathbf{E} = -j\omega\mu\mathbf{H} \qquad\qquad \nabla \times \mathbf{H} = j\omega\varepsilon\mathbf{E}$$

$$\begin{aligned}
\frac{1}{r}\frac{\partial E_z}{\partial \phi} - \frac{\partial E_\phi}{\partial z} &= -j\omega\mu H_r & \qquad \frac{1}{r}\frac{\partial H_z}{\partial \phi} - \frac{\partial H_\phi}{\partial z} &= j\omega\varepsilon E_r \\
\frac{\partial E_r}{\partial z} - \frac{\partial E_z}{\partial r} &= -j\omega\mu H_\phi & \qquad \frac{\partial H_r}{\partial z} - \frac{\partial H_z}{\partial r} &= j\omega\varepsilon E_\phi \\
\frac{1}{r}\frac{\partial}{\partial r}\left(rE_\phi\right) - \frac{1}{r}\frac{\partial E_r}{\partial \phi} &= -j\omega\mu H_z & \qquad \frac{1}{r}\frac{\partial}{\partial r}\left(rH_\phi\right) - \frac{1}{r}\frac{\partial H_r}{\partial \phi} &= j\omega\varepsilon E_z
\end{aligned} \tag{A.14}$$

6. Jacobi-Anger Expansion

$$e^{-js\cos\phi} = \sum_{n=-\infty}^{\infty} (-j)^n J_n(s) e^{-jn\phi} \tag{A.15}$$

Appendix B

1. Bessel's function properties

$$J_{-n}(z)=(-1)^n J_n(z) \text{ for } n=0,1,2,.... \tag{B.1}$$

2. Bessel Wronskian

$$\begin{aligned}
&J_n(z)\cdot\frac{\partial}{\partial z}H_n^{(2)}(z)-H_n^{(2)}(z)\cdot\frac{\partial}{\partial z}J_n(z)= \\
&=J_n(z)\cdot\frac{\partial}{\partial z}\left(J_n(z)-j\cdot N_n(z)\right)-\frac{\partial}{\partial z}J_n(z)\cdot\left(J_n(z)-j\cdot N_n(z)\right) \\
&=-j\left(J_n(z)\frac{\partial}{\partial z}N_n(z)-N_n(z)\frac{\partial}{\partial z}J_n(z)\right)=-j\frac{2}{\pi z}
\end{aligned} \tag{B.2}$$

3. Small Argument Approximation to Cylindrical Bessel's Functions

$$\begin{aligned}
&\text{for } n\neq 0 \quad J_n(z)=\frac{1}{2^n\left|n\right|!}z^{|n|} \quad \text{and} \quad N_n(z)=-\frac{(|n|-1)!}{\pi}\frac{2^{|n|}}{z^{|n|}} \\
&\text{for } n=0 \quad J_0(z)=1-\frac{z^2}{4} \quad \text{and} \quad N_0(z)=\frac{2}{\pi}\ln\left(\gamma z/2\right)
\end{aligned} \tag{B.3}$$

4. A Derivation of Modal Admittances for a Single Wire

4.1. TM polarisation

Form Equation (4.61) for a TM polarised single wire the admittance relationship can be formulated as follows.

$$Y_n=\frac{k_0}{j\omega\mu_0}\frac{J'_n(k_0r)+X_{sn}^{TM}N'_n(k_0r)}{J_n(k_0r)+X_{sn}^{TM}N_n(k_0r)}\text{, where } X_{sn}^{TM}=-\frac{J_n(k_0a)}{N_n(k_0a)}$$

Utilising the small argument approximation to the Bessel functions detailed in the section above yields;

for $n=0$

$$X_{s0}^{TM} = -\frac{1-\dfrac{k_0^2a^2}{4}}{\dfrac{2}{\pi}\ln(\gamma k_0 a/2)} = -\frac{\pi(4-k_0^2a^2)}{8\ln(\gamma k_0^2 a/2)}$$

and

$$Y_0 = \frac{1}{j\omega\mu_0}\frac{-\dfrac{1}{2}k_0^2\Delta - \dfrac{\pi(4-k_0^2a^2)}{8\ln(\gamma k_0 a/2)}\dfrac{2}{\pi\Delta}}{1-\dfrac{k_0^2\Delta^2}{4}-\dfrac{\pi(4-k_0^2a^2)}{8\ln(\gamma k_0 a/2)}\dfrac{2}{\pi}\ln(\gamma k_0\Delta/2)} =$$

$$\frac{1}{j\omega\mu_0}\frac{\dfrac{-2k_0^2\Delta^2\ln(\gamma k_0 a/2)-(4-k_0^2a^2)}{4\Delta\ln(\gamma k_0 a/2)}}{\dfrac{(4-k_0^2\Delta^2)\ln(\gamma k_0 a/2)-(4-k_0^2a^2)\ln(\gamma k_0\Delta/2)}{4\ln(\gamma k_0 a/2)}} =$$

$$\frac{1}{j\omega\mu_0\Delta}\frac{-2k_0^2\Delta^2\ln(\gamma k_0 a/2)-(4-k_0^2a^2)}{(4-k_0^2\Delta^2)\ln(\gamma k_0 a/2)-(4-k_0^2a^2)\ln(\gamma k_0\Delta/2)} =$$

$$\frac{1}{j\omega\mu_0\Delta}\frac{-2k_0^2\Delta^2\ln(\gamma k_0 a/2)-4+k_0^2a^2}{4\ln(\gamma k_0 a/2)-k_0^2\Delta^2\ln(\gamma k_0 a/2)-4\ln(\gamma k_0\Delta/2)+k_0^2a^2\ln(\gamma k_0\Delta/2)}$$

$$\frac{1}{j\omega\mu_0\Delta}\frac{-2k_0^2\Delta^2\ln(\gamma k_0 a/2)-4+k_0^2a^2}{4\ln(\gamma k_0 a/2)-k_0^2\Delta^2\ln(\gamma k_0 a/2)-4\ln(\gamma k_0\Delta/2)+k_0^2a^2\ln(\gamma k_0\Delta/2)} =$$

$$\frac{1}{j\omega\mu_0\Delta}\frac{-2k_0^2\Delta^2\ln(\gamma k_0 a/2)-4+k_0^2a^2}{-4\ln(\Delta/a)+k_0^2\left[a^2\ln(\gamma k_0\Delta/2)-\Delta^2\ln(\gamma k_0 a/2)\right]} \approx \frac{1}{j\omega\mu_0}\frac{1}{\Delta\ln(\Delta/a)}$$

for $n \neq 0$

$$X_{sn}^{TM} = -\frac{\dfrac{(k_0a)^{|n|}}{2^{|n|}|n|!}}{-\dfrac{2^{|n|}(|n|-1)!}{\pi(k_0a)^{|n|}}} = \frac{\pi(k_0a)^{2|n|}}{2^{2|n|}|n|!(|n|-1)!}$$

and

$$Y_n = \frac{1}{j\omega\mu_0}\frac{\dfrac{k_0(k_0\Delta)^{|n|-1}}{2^{|n|}(|n|-1)!}+\dfrac{\pi(k_0a)^{2|n|}}{2^{2|n|}|n|!(|n|-1)!}\dfrac{k_0 2^{|n|}|n|!}{\pi(k_0\Delta)^{|n|+1}}}{\dfrac{(k_0\Delta)^{|n|}}{2^{|n|}|n|!}-\dfrac{\pi(k_0a)^{2|n|}}{2^{2n}|n|!(|n|-1)!}\dfrac{2^{|n|}(|n|-1)!}{\pi z^{|n|}}} =$$

$$\frac{1}{j\omega\mu_0}\frac{\dfrac{k_0(k_0\Delta)^{|n|-1}}{2^{|n|}(|n|-1)!}+\dfrac{(k_0a)^{2|n|}}{2^{|n|}(|n|-1)!}\dfrac{k_0}{(k_0\Delta)^{|n|+1}}}{\dfrac{(k_0\Delta)^{|n|}}{2^{|n|}|n|!}-\dfrac{(k_0a)^{2|n|}}{2^{|n|}|n|!}\dfrac{1}{(k_0\Delta)^{|n|}}} =$$

$$\frac{1}{j\omega\mu_0}\frac{\dfrac{k_0(k_0\Delta)^{2|n|}}{2^{|n|}(|n|-1)!(k_0\Delta)^{n+1}}+\dfrac{(k_0a)^{2|n|}}{2^{|n|}(|n|-1)!}\dfrac{k_0}{(k_0\Delta)^{|n|+1}}}{\dfrac{(k_0\Delta)^{|n|}(k_0\Delta)^{n}}{2^{|n|}|n|!(k_0\Delta)^{n}}-\dfrac{(k_0a)^{2|n|}}{2^{|n|}|n|!}\dfrac{1}{(k_0\Delta)^{|n|}}} =$$

$$\frac{1}{j\omega\mu_0}\frac{\dfrac{k_0^{2|n|+1}(\Delta^{2|n|}+a^{2|n|})}{2^{|n|}(|n|-1)!(k_0\Delta)^{|n|+1}}}{\dfrac{k_0^{2|n|}(\Delta^{2|n|}-a^{2|n|})}{2^{|n|}|n|!(k_0\Delta)^{|n|}}} = \frac{1}{j\omega\mu_0}\frac{|n|}{\Delta}\frac{(\Delta^{2|n|}+a^{2|n|})}{(\Delta^{2|n|}-a^{2|n|})}$$

4.2. TE polarisation

Form Equation (4.62) for a TE polarised single wire the admittance relationship can be formulated as follows.

$$Y_n = -\frac{j\omega\varepsilon}{k_0}\frac{J_n(k_0r)+X_{sn}^{TE}N_n(k_0r)}{J'_n(k_0r)+X_{sn}^{TE}N'_n(k_0r)},\ \text{where}\ X_{sn}^{TM} = -\frac{J'_n(k_0a)}{N'_n(k_0a)}$$

Utilising the small argument approximation to the Bessel functions leads to:

for $n = 0$

$$X_{s0}^{TM} = -\frac{-\dfrac{1}{2}k_0a}{\dfrac{2}{\pi k_0a}} = \frac{k_0a}{2}\frac{\pi k_0a}{2} = \frac{\pi(k_0a)^2}{4}$$

and

$$Y_0 = \frac{j\omega\varepsilon_0}{k_0}\frac{J_0(k_0r)+X_{s0}^{TE}N_0(k_0r)}{J'_0(k_0r)+X_{s0}^{TE}N'_0(k_0r)} = j\omega\varepsilon_0\frac{1-\frac{(k_0\Delta)^2}{4}+\frac{\pi(k_0a)^2}{4}\frac{2}{\pi}\ln(\gamma k_0\Delta/2)}{-\frac{1}{2}k_0^2\Delta+\frac{\pi(k_0a)^2}{4}\frac{2}{\pi\Delta}} =$$

$$j\omega\varepsilon_0\frac{1-\frac{(k_0\Delta)^2}{4}+\frac{(k_0a)^2}{2}\ln(\gamma k_0\Delta/2)}{-\frac{1}{2}k_0^2\Delta+\frac{(k_0a)^2}{2}\frac{1}{\Delta}} = j\omega\varepsilon_0\frac{1-\frac{k_0^2\left(\Delta^2+a^2\ln(\gamma k_0\Delta/2)\right)}{4}}{\frac{k_0^2(a^2-\Delta^2)}{2\Delta}} =$$

$$j\omega\varepsilon_0\frac{4-k_0^2\left(\Delta^2+a^2\ln(\gamma k_0\Delta/2)\right)}{2}\frac{\Delta}{k_0^2(a^2-\Delta^2)} \approx j\omega\varepsilon_0\frac{2\Delta}{k_0^2(a^2-\Delta^2)} =$$

$$-j\omega\varepsilon_0\frac{2\Delta}{k_0^2(\Delta^2-a^2)} = \frac{1}{j\omega\mu_0}\frac{2\Delta}{(\Delta^2-a^2)}$$

for $n \neq 0$

$$X_{sn}^{TM} = -\frac{\frac{1}{2^{|n|}(|n|-1)!}(k_0a)^{|n|-1}}{\frac{2^{|n|}|n|!}{\pi(k_0a)^{|n|+1}}} = -\frac{(k_0a)^{|n|-1}}{2^{|n|}(|n|-1)!}\frac{\pi(k_0a)^{|n|+1}}{2^{|n|}|n|!} = -\frac{\pi}{|n|!(|n|-1)!}\frac{(k_0a)^{2|n|}}{2^{2|n|}}$$

and

$$Y_n = \frac{j\omega\varepsilon_0}{k_0}\frac{J_n(k_0r)+X_{sn}^{TE}N_n(k_0r)}{J'_n(k_0r)+X_{sn}^{TE}N'_n(k_0r)} =$$

$$j\omega\varepsilon_0\frac{\frac{1}{2^{|n|}|n|!}(k_0\Delta)^{|n|}+\frac{\pi}{|n|!(|n|-1)!}\frac{(k_0a)^{2|n|}}{2^{2|n|}}\frac{2^{|n|}(|n|-1)!}{\pi(k_0\Delta)^{|n|}}}{k_0\frac{(k_0\Delta)^{|n|-1}}{2^{|n|}(|n|-1)!}-\frac{k_0\pi}{|n|!(|n|-1)!}\frac{(k_0a)^{2|n|}}{2^{2|n|}}\frac{2^{|n|}|n|!}{\pi(k_0\Delta)^{|n|+1}}}$$

$$j\omega\varepsilon_0\frac{\frac{(k_0\Delta)^{2|n|}+(k_0a)^{2|n|}}{2^{|n|}|n|!(k_0\Delta)^{|n|}}}{\frac{k_0(k_0\Delta)^{|n|-1}(k_0\Delta)^{|n|+1}-k_0(k_0a)^{2|n|}}{2^{|n|}(|n|-1)!(k_0\Delta)^{|n|+1}}} =$$

$$j\omega\varepsilon_0\frac{\frac{k_0^{2|n|}(\Delta^{2|n|}+a^{2|n|})}{2^{|n|}|n|!(k_0\Delta)^{|n|}}}{\frac{k_0^{2|n|+1}(\Delta^{2|n|}-a^{2|n|})}{2^{|n|}(|n|-1)!(k_0\Delta)^{|n|+1}}} = j\omega\varepsilon_0\frac{\Delta}{|n|}\frac{(\Delta^{2|n|}+a^{2|n|})}{(\Delta^{2|n|}-a^{2|n|})}$$

Appendix C

The input admittance of a transmission line of characteristic admittance Y, length Δ and terminated by a conductance G is:

$$\begin{aligned} Y_{\text{input}} &= Y\frac{G + jY\tan(k\Delta)}{Y + jG\tan(k\Delta)}\frac{Y - jG\tan(k\Delta)}{Y - jG\tan(k\Delta)} \\ &= Y\frac{GY + jY^2\tan(k\Delta) - jG^2\tan(k\Delta) + YG\tan^2(k\Delta)}{Y^2 + G^2\tan^2(k\Delta)} \end{aligned} \tag{C.1}$$

For low frequencies, so that the argument of the tangent function is small, this can be approximated to second order accuracy as:

$$\begin{aligned} Y_{\text{input}} &\approx G + jY\tan(k\Delta) - j\frac{G^2}{Y}\tan(k\Delta) \\ &= G + jG\tan(k\Delta)\left(\frac{Y}{G} - \frac{G}{Y}\right) \\ &= G + jk\Delta G\left(\frac{Y}{G} - \frac{G}{Y}\right) \end{aligned} \tag{C.2}$$

Appendix D

The elliptical coordinate system is defined with reference to Figure 7.1 of Chapter 7 as:

$$\begin{aligned} x &= \frac{d}{2}\cosh u \cos v \\ y &= \frac{d}{2}\sinh u \sin v \\ z &= z \end{aligned} \tag{D.1}$$

Form the above Equations the following can be formulated:

$$\cos^2 v = \frac{4x^2}{d^2 \cosh^2 u} \qquad \sin^2 v = \frac{4y^2}{d^2 \sinh^2 u} \tag{D.2}$$

Using the properties of trigonometric functions:

$$\frac{4x^2}{d^2 \cosh^2 u} + \frac{4y^2}{d^2 \sinh^2 u} = 1 \tag{D.3}$$

Rearranging,

$$d^2 \sinh^4 u + (d^2 - 4x^2 - 4y^2)\sinh^2 u - 4y^2 = 0 \tag{D.4}$$

One of the solutions to the quadratic equations is given by:

$$\sinh u = \sqrt{\frac{4x^2 + 4y^2 - d^2 + \sqrt{(d^2 - 4x^2 - 4y^2)^2 + 16y^2d^2}}{2d^2}} \tag{D.5}$$

Define

$$A = \frac{4x^2 + 4y^2 - d^2 + \sqrt{(d^2 - 4x^2 - 4y^2)^2 + 16y^2d^2}}{2d^2} \tag{D.6}$$

Thus, Equation (D.5) is in the form:

$$\sinh u = \sqrt{A} \tag{D.7}$$

Therefore the variable *u* is obtained as:

$$u = \operatorname{arc\,sinh}\sqrt{A} = \ln\left(\sqrt{A} + \sqrt{A+1}\right) \tag{D.8}$$

The derivatives $\frac{\partial u}{\partial x}$ and $\frac{\partial u}{\partial y}$ are calculated as follows:

$$\frac{\partial u}{\partial x} = \frac{\partial u}{\partial A}\frac{\partial A}{\partial x}\left(\frac{1}{\sqrt{A}+\sqrt{A+1}}\cdot\frac{1}{2\sqrt{A}} + \frac{1}{2\sqrt{A+1}}\right)\frac{\partial A}{\partial x} = \frac{1}{2\sqrt{A(A+1)}}\frac{\partial A}{\partial x} \tag{D.9}$$

$$\frac{\partial u}{\partial y} = \frac{\partial u}{\partial A}\frac{\partial A}{\partial y} = \frac{1}{2\sqrt{A(A+1)}}\frac{\partial A}{\partial y} \tag{D.10}$$

where

$$\frac{\partial A}{\partial x} = \frac{4x}{d^2} + \frac{-4(d^2 - 4x^2 - 4y^2)x}{d^2\sqrt{(d^2 - 4x^2 - 4y^2) + 16y^2d^2}} \tag{D.11}$$

$$\frac{\partial A}{\partial y} = \frac{4y}{d^2} + \frac{4y(d^2 + 4x^2 + 4y^2)}{d^2\sqrt{(d^2 - 4x^2 - 4y^2)^2 + 16y^2d^2}} \tag{D.12}$$

From Equation (D.1) the following can be formulated:

$$\cosh^2 u = \frac{4x^2}{d^2\cos^2 v} \qquad \sinh^2 u = \frac{4y^2}{d^2\sin^2 v} \tag{D.13}$$

Using the $\cosh^2 u - \sinh^2 u = 1$ leads to:

$$\frac{4x^2}{d^2\cos^2 v} - \frac{4y^2}{d^2\sin^2 v} = 1 \tag{D.14}$$

This after some mathematical rearrangements yields:

$$d^2\sin^4 v + (4x^2 + 4y^2 - d^2)\sin^2 v - 4y^2 = 0 \tag{D.15}$$

One of the solutions to the above quadratic equations can be found as follows:

$$\sin v = \sqrt{\frac{d^2 - 4x^2 - 4y^2 + \sqrt{(4x^2 + 4y^2 - d^2)^2 + 16y^2d^2}}{2d^2}} \tag{D.16}$$

Define

$$B = \frac{d^2 - 4x^2 - 4y^2 + \sqrt{(4x^2 + 4y^2 - d^2)^2 + 16y^2d^2}}{2d^2} \qquad (D.17)$$

Equation (D.16) can be written as:

$$\sin v = \sqrt{B} \qquad (D.18)$$

From Equation (D.18) the variable *v* can be calculated in the form:

$$v = \arcsin\sqrt{B} \qquad (D.19)$$

Thus, the derivatives $\frac{\partial v}{\partial x}$ and $\frac{\partial v}{\partial y}$ are found from:

$$\frac{\partial v}{\partial x} = \frac{\partial v}{\partial B}\frac{\partial B}{\partial x} \frac{1}{2\sqrt{B(1-B)}}\frac{\partial B}{\partial x} \qquad (D.20)$$

$$\frac{\partial v}{\partial y} = \frac{\partial v}{\partial B}\frac{\partial B}{\partial y} \frac{1}{2\sqrt{B(1-B)}}\frac{\partial B}{\partial y} \qquad (D.21)$$

where

$$\frac{\partial B}{\partial x} = \frac{4x(4x^2 + 4y^2 - d^2)}{d^2\sqrt{(4x^2 + 4y^2 - d^2)^2 + 16y^2d^2}} - \frac{4x}{d^2} \qquad (D.22)$$

$$\frac{\partial B}{\partial y} = \frac{4y(4x^2 + 4y^2 + d^2)}{d^2\sqrt{(4x^2 + 4y^2 - d^2)^2 + 16y^2d^2}} - \frac{4y}{d^2} \qquad (D.23)$$

Appendix E

1. Spherical Coordinate System

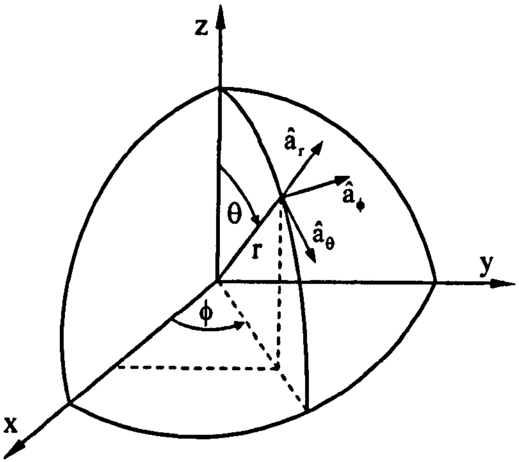

2. Possible Combinations of Spherical Modes.

The discrete values of angles at the points corresponding to the ports on each of the 6 surfaces of the cubic TLM node.

$$S_1:(\theta=\pi);\ \ S_2:(\theta=\pi/2,\phi=0);\ \ S_3:(\theta=\pi/2,\phi=\pi/2);$$
$$S_4:(\theta=\pi/2,\phi=\pi)\ \ S_5:(\theta=\pi/2,\phi=3\pi/2);\ \ S_6:(\theta=0) \tag{E.1}$$

The fields at the ports are either proportional to *A* or *B*, where $A=\dfrac{m}{\sin\theta}P_n^m(\cos\theta)$

and $B=\dfrac{\partial}{\partial\theta}P_n^m(\cos\theta)$

The values of *A* and *B* for the lowest order harmonics are given as:

A	m = 0	m = 1	m = 2
n = 1	0	1	0
n = 2	0	3cosθ	6sinθ

B	m = 0	m = 1	m = 2
n = 1	-sinθ	cosθ	0
n = 2	-3/2sin2θ	3cos2θ	3sin2θ

It should be noted that

$$P_n^m(x) = 0 \qquad m > n \tag{E.2}$$

3. Small Argument Approximation to Spherical Bessel Functions

for $x \ll 1$

$$j_n(x) \approx \frac{x^n}{1\cdot 3\cdot 5\cdot \ldots \cdot (2n+1)} \quad \text{and} \quad y_n(x) \approx \frac{-1\cdot 3\cdot 5\cdot \ldots \cdot (2n-1)}{x^{n+1}} \tag{E.3}$$

4. Derivation of Admittances for a Conductive Sphere

$$A_1^{TE} = \frac{(ka)^3}{3}\ \text{, and} \qquad A_1^{TM} = -\frac{\dfrac{k_0 a}{3} + \dfrac{1}{3}k_0 a}{\dfrac{-1}{k_0{}^2 a^2} + \dfrac{2k_0 a}{k_0{}^3 a^3}} = -\frac{2}{3}(k_0 a)^3$$

$$\begin{aligned}
Y_1^{TE} &= \frac{1}{j\omega\mu\Delta}\frac{\left(j_1(k_0\Delta) + A_1^{TE} y_1(k_0\Delta)\right) + kR\left(j'_1(k_0\Delta) + A_1^{TE} y'_1(k_0\Delta)\right)}{j_1(k_0\Delta) + A_1^{TE} y_1(k_0\Delta)} = \\
&\frac{1}{j\omega\mu\Delta}\frac{\left(\dfrac{1}{3}k_0 R - \dfrac{(k_0 a)^3}{3}\dfrac{1}{(k_0\Delta)^2}\right) + k_0\Delta\left(\dfrac{1}{3} + \dfrac{(k_0 a)^3}{3}\dfrac{2}{(k_0\Delta)^3}\right)}{\dfrac{1}{3}k_0\Delta - \dfrac{(k_0 a)^3}{3}\dfrac{1}{(k_0\Delta)^2}} = \\
&\frac{1}{j\omega\mu\Delta}\frac{\dfrac{1}{3}k_0\Delta\left(1 - \dfrac{a^3}{\Delta^3}\right) + \dfrac{1}{3}k_0\Delta\left(1 + 2\dfrac{a^3}{\Delta^3}\right)}{\dfrac{1}{3}k_0\Delta\left(1 - \dfrac{a^3}{\Delta^3}\right)} = \frac{1}{j\omega\mu\Delta}\frac{\left(2 + \dfrac{a^3}{\Delta^3}\right)}{\left(1 - \dfrac{a^3}{\Delta^3}\right)} = \\
&\frac{1}{j\omega\mu\Delta}\frac{\left(2\Delta^3 + a^3\right)}{\left(\Delta^3 - a^3\right)}
\end{aligned}$$

$$Y_1^{TM} = -\frac{k_0^2\Delta}{j\omega\mu}\frac{j_1(k_0\Delta)+A_1^{TM}y_1(k_0\Delta)}{j_1(k_0\Delta)+A_1^{TM}y_1(k_0\Delta)+k_0\Delta\left[j'_1(k_0\Delta)+A_1^{TM}y'_1(k_0\Delta)\right]}$$

$$= j\omega\varepsilon\Delta\frac{\frac{1}{3}k_0\Delta+\frac{2}{3}(k_0a)^3\frac{1}{(k_0\Delta)^2}}{\frac{1}{3}k_0\Delta+\frac{2}{3}(k_0a)^3\frac{1}{(k_0\Delta)^2}+k_0\Delta\left[\frac{1}{3}-\frac{2}{3}(k_0a)^3\frac{2}{(k_0\Delta)^3}\right]}$$

$$= j\omega\varepsilon\Delta\frac{\frac{1}{3}k_0\Delta\left(1+2\frac{a^3}{R^3}\right)}{\frac{1}{3}k_0\Delta\left(1+2\frac{a^3}{R^3}\right)+\frac{1}{3}k_0\Delta\left[1-4\frac{a^3}{R^3}\right]} = j\omega\varepsilon\frac{\Delta}{2}\frac{\Delta^3+2a^3}{\Delta^3-a^3}$$

5. Modified Bessel Function

$$\hat{Z}_n(kr) = kr\,z_n(kr) = kr\sqrt{\frac{\pi}{2kr}}Z_{n+1/2}(kr) = \sqrt{\frac{\pi kr}{2}}Z_{n+1/2}(kr) \qquad (E.4)$$

where $z_n(kr)$ is a spherical and $Z_n(kr)$ a cylindrical Bessel function.

6. Derivation of Admittances for a Dielectric Sphere

For TE mode

$$Y_1^{TE} = \frac{1}{j\omega\mu_1\Delta}\frac{\left(j_1(k_1\Delta)+k_1\Delta j'_1(k_1\Delta)\right)+A_1^{TE}\left(y_1(k_1\Delta)+k\Delta y'_1(k_1\Delta)\right)}{j_1(k_1\Delta)+A_1^{TE}y_1(k_1\Delta)}$$

$$= \frac{1}{j\omega\mu_1\Delta}\frac{\frac{2}{3}k_1\Delta+A_1^{TE}\frac{1}{k_1^2\Delta^2}}{\frac{1}{3}k_1\Delta-A_1^{TE}\frac{1}{k_1^2\Delta^2}} = \frac{\frac{2}{3}k_1^3\Delta^3+A_1^{TE}}{\frac{1}{3}k_1^3\Delta^3-A_1^{TE}}$$

where $A_1^{TE} = -\frac{2}{3}k_1^3a^3\left[\frac{k_2\eta_2-k_1\eta_1}{2k_1\eta_1+k_2\eta_2}\right]$, thus

$$Y_1^{TE} = \frac{2}{j\omega\mu_1\Delta}\frac{k_1\eta_1(2\Delta^3+a^3)+k_2\eta_2(\Delta^3-a^3)}{k_1\eta_1(2\Delta^3-2a^3)+k_2\eta_2(\Delta^3+2a^3)} = \frac{2}{j\omega\mu_1\Delta}$$

For TM mode

$$Y_1^{TM} = -\frac{k_1^2\Delta}{j\omega\mu_1}\frac{j_1(k_1\Delta)+A_1^{TM}y_1(k_1\Delta)}{\left(j_1(k_1\Delta)+k_1\Delta j'_1(k_1\Delta)\right)+A_1^{TM}\left(y_1(k_1\Delta)+k_1\Delta y'_1(k_1\Delta)\right)}$$

$$= j\omega\varepsilon_1\Delta\frac{\frac{1}{3}k_1^3\Delta^3 - A_1^{TM}}{\frac{2}{3}k_1^3\Delta^3 + A_1^{TM}}$$

where $A_1^{TM} = \frac{2}{3}k_1^3a^3\left[\frac{k_1\eta_2 - k_2\eta_1}{k_2\eta_1 + 2k_1\eta_2}\right]$, thus

$$Y_1^{TM} = j\omega\varepsilon_1\frac{\Delta}{2}\frac{k_2\eta_1(\Delta^3+2a^3)+2k_1\eta_2(\Delta^3-a^3)}{k_2\eta_1(\Delta^3-a^3)+k_1\eta_2(2\Delta^3+a^3)}$$

$$= j\omega\varepsilon_1\frac{\Delta}{2}\frac{\varepsilon_2(\Delta^3+2a^3)+2\varepsilon_1(\Delta^3-a^3)}{\varepsilon_2(\Delta^3-a^3)+\varepsilon_1(2\Delta^3+a^3)}$$